ORSAY
n° d'ordre :

LAL 97–18
Avril 1997

UNIVERSITÉ DE PARIS-SUD
Centre d'Orsay

THÈSE

présentée
pour obtenir

le grade de DOCTEUR EN SCIENCES PHYSIQUES

de l'Université de Paris XI Orsay

par

Andreas Höcker

Mesure des fonctions spectrales du lepton τ et applications à la chromodynamique quantique

soutenue le 18 avril 1997 devant la Commission d'Examen

MM.	J.	LEFRANCOIS	Président
	M.	DAVIER	
	A.	PICH	
	L.	ROLANDI	
	A.	ROUGÉ	
	R.	STROYNOWSKI	

Abstract

This thesis presents measurements of the τ vector (V) and axial-vector (A) hadronic spectral functions and phenomenological studies in the framework of quantum chromodynamics (QCD). The analysis is based on a data sample accumulated during the years 1991–1994 by the ALEPH detector at the e^+e^- collider LEP. In order to obtain the physical hadronic invariant mass spectra (which determine the spectral functions), the spectra are unfolded from detector effects using a new method based on an inversion of the regularized detector reponse matrix. Systematic effects from the measurement procedure and the unfolding are studied and the corresponding uncertainties are evaluated.

Using the hypothesis of conserved vector currents (CVC), the dominant two- and four-pion vector spectral functions are compared to the corresponding cross sections from e^+e^- annihilation. A combined fit of the pion form factor from τ decays and e^+e^- data is performed using different parametrizations. The mass and the width of the $\rho^\pm(770)$ and the $\rho^0(770)$ are separately determined in order to extract possible isospin violating effects. The mass and width differences are measured to be $M_{\rho^\pm(770)} - M_{\rho^0(770)} = (0.0 \pm 1.0)\ \mathrm{MeV}/c^2$ and $\Gamma_{\rho^\pm(770)} - \Gamma_{\rho^0(770)} = (0.1 \pm 1.9)\ \mathrm{MeV}/c^2$.

Several QCD chiral sum rules involving the difference $(V - A)$ of the spectral functions are compared to their measurements. The Borel-transformed Das-Mathur-Okubo sum rule is used to measure the pion polarizability to be $\alpha_\mathrm{E} = (2.68 \pm 0.91) \times 10^{-4}\ \mathrm{fm}^3$.

The τ vector and axial-vector hadronic widths and certain spectral moments are exploited to measure α_s and non-perturbative contributions at the τ mass scale. The best, and experimentally and theoretically most robust, determination of $\alpha_s(M_\tau)$ is obtained from the inclusive $(V + A)$ fit that yields $\alpha_s(M_\tau) = 0.348 \pm 0.017$ giving $\alpha_s(M_\mathrm{Z}) = 0.1211 \pm 0.0021$ after the evolution to the mass of the Z boson. The approach of the Operator Product Expansion (OPE) is tested experimentally by means of an evolution of the τ hadronic width to masses smaller than the τ mass. Using the difference $(V - A)$ of the spectral functions allows one to directly measure the dominant non-perturbative OPE dimension to be $D = 6.9 \pm 0.5$.

As additional applications, the vector spectral functions are used to improve the precision of the experimental determination of the hadronic contribution to the anomalous magnetic moment of the muon $a_\mu = (g-2)/2$ and to the running of the QED fine structure constant $\alpha_\mathrm{QED}(M_\mathrm{Z}^2)$ at the Z mass. They are found to be $a_\mu^\mathrm{had} = (701.1 \pm 9.4) \times 10^{-10}$ and $\Delta\alpha_\mathrm{had}(M_\mathrm{Z}^2) = (281.7 \pm 6.2) \times 10^{-4}$, where the latter leads to $\alpha^{-1}(M_\mathrm{Z}^2) = 128.878 \pm 0.085$.

Key words:
LEP
ALEPH
Tau lepton
Unfolding
Spectral function
CVC
Pion form factor
Anomalous magnetic moment of the muon
Fine structure constant
Strong interaction (QCD)
Chiral sum rules
Operator Product Expansion (OPE)
Strong coupling constant
Running of α_s

ORSAY
n° d'ordre :

LAL 97–18
Avril 1997

UNIVERSITÉ DE PARIS-SUD
Centre d'Orsay

THÈSE

présentée
pour obtenir

le grade de DOCTEUR EN SCIENCES PHYSIQUES

de l'Université de Paris XI Orsay

par

Andreas Höcker

Mesure des fonctions spectrales du lepton τ et applications à la chromodynamique quantique

soutenue le 18 avril 1997 devant la Commission d'Examen

MM. J. LEFRANCOIS Président
M. DAVIER
A. PICH
L. ROLANDI
A. ROUGÉ
R. STROYNOWSKI

Contents

Introduction

Since the discovery of the heavy lepton τ through the observation of e-μ events originating from τ pairs [1], the study of τ pair production and decays has evolved in many different ways. The research was propelled by the prophetic paper of Y. S. Tsai [2], which anticipated almost the whole range of physics of leptons that are heavy enough to decay into hadrons. This property of the τ is of particular interest, as it provides a new laboratory to study the gauge theory of strong interactions (QCD) at an energy scale where non-perturbative effects come into play. The subject of this thesis is the analysis of hadronic τ decays measured during the years 1991 to 1994 by the ALEPH detector at the *Large Electron-Positron Collider* (LEP) at CERN.

The natural observables that give access to the inner structure of the hadronic τ decays are the so-called *spectral functions.* These essentially consist of the invariant mass spectra of the hadronic final states, normalised to their respective branching ratios and corrected for the τ decay phase space and decay kinematics. As a consequence of the weak leptonic decays occurring through the exchange of a maximal parity violating virtual W boson, the τ spectral functions have both *vector* and *axial-vector* contributions. Any difference in the normalisation (branching ratios) or the shape between vector and axial-vector spectral functions is necessarily generated by non-perturbative QCD as, *e.g.*, long distance resonance phenomena. Among those resonances the most prominent of are the well-known $\rho(770)$ — vector — and $a_1(1260)$ — axial-vector — mesons. For non-perturbative effects to be studied, a clear experimental separation of the hadronic τ decay channels into vector and axial-vector states is necessary. Conceptional ambiguities and experimental problems concerning this separation are discussed in detail in the framework of this work.

The τ vector spectral functions have their counterparts in the low energy e^+e^- annihilation cross section into isovector hadronic final states allowing isospin invariance of the hadronic currents (*Conserved Vector Current* property — CVC) to be tested. Extended comparisons of the two- and four-pion final states, as well as the sum of all vector current isovector final states, between τ spectral functions and e^+e^- cross sections are presented. This includes a combined fit to the electromagnetic and weak pion form factors.

Several spectral function analyses have been already performed along these lines. In 1987, the ARGUS Collaboration published the spectral function of the decay $\tau^- \to 2\pi^-\pi^+\pi^0\nu_\tau$ [3]. The CLEO Collaboration compared the e^+e^- results via CVC to the corresponding invariant mass spectra of the τ final states $2\mathrm{h}^-\mathrm{h}^+\pi^0$ and $3\mathrm{h}^-2\mathrm{h}^+\pi^0$ [4]. Recently, the ALEPH Collaboration published a study of τ decays into η and ω mesons [5], in which the final states $\pi^-\pi^0\eta$ and $\pi^-\omega$ were found to be in good agreement with e^+e^- data.

The high precision of the new τ data, in particular of the two-pion spectral function, can be exploited to improve the determination of the hadronic contribution to the muon anomalous magnetic moment $(g-2)_\mu$ and to the running of the electromagnetic coupling constant α at the mass of the Z boson. Both quantities are largely dominated by the uncertainties of virtual quark-loop contributions, that are not calculable within perturbative

QCD. Reducing these uncertainties permits one to use the muonic $(g-2)_\mu$ (which can be measured very accurately) in interesting tests of higher order electroweak interaction and in the search for new physics. In the case of the running α, it is of crucial importance to know precisely $\alpha(M_Z^2)$ as its uncertainty limits the logarithmic constraint on the mass of the Higgs boson (obtained from an overall electroweak fit). Although not calculable theoretically, the hadronic loop contributions can be obtained via dispersion relations from an integral over experimental data, convoluted with the corresponding QED kernel function. The resulting analysis using τ and e^+e^- data is presented in this thesis.

QCD sum rules, involving the difference of vector and axial-vector spectral functions, are calculable perturbatively in the framework of *Chiral Perturbation Theory* (ChPT) where the masses of the light quarks u, d, s are neglected. The most famous chiral sum rules, like the Das-Mathur-Okubo [6], and the first and second Weinberg sum rules [7], are examined using τ data. Finite energy sum rule techniques are employed in order to measure the polarisability of the pion.

Another important topic of Quantum Chromodynamics considered in this work is the measurement of the running strong coupling constant, α_s, at the scale of the τ mass. Such measurements were carried out for the first time time by ALEPH [8] and CLEO [9] (see also [10]). Using the *Operator Product Expansion* (OPE) [11], a theoretical prediction of the inclusive vector/axial-vector τ hadronic width as a function of both α_s and non-perturbative phenomenological operators has become available [12]. These operators are part of a power series in the mass of the τ. They absorb unpredictable long-distance effects and are determined experimentally [13]. In this thesis, the consistency of the OPE ansatz and the stability of the α_s measurement are studied by comparing of the theoretical prediction of the evolved τ hadronic width obtained for masses smaller than the τ mass to the corresponding measurement.

This thesis is organised as follows: in Part I, the theoretical and phenomenological basis of the τ spectral function analysis is presented, including a brief description of the τ pair production and their decays in the framework of the Standard Model (SM) of electroweak interactions, as well as general considerations of hadronic interactions. Part II deals with the actual τ spectral functions measurements, giving an overview of the measurement facilities and of the selection and classification procedure of the τ decays. A comprehensive presentation is given of the unfolding method employed in this thesis. The unfolding of detector effects is an important step of the analysis and requires particular care. A detailed description of systematic effects affecting the measurements follows. In Part III the applications of the measurements to the QCD phenomenology are presented: the comparison of the vector spectral functions to e^+e^- cross sections, the measurement of $(g-2)_\mu$ and $\alpha(M_Z^2)$, as well as the QCD sum rule tests and the measurement of $\alpha_s(M_\tau)$.

Part I

Theoretical Framework

Chapter 1

Production of τ Pairs at LEP and τ Decays

The present analysis is based on data from Z boson decays into τ pairs. Due to the short lifetime of the produced τ's, they decay still inside the primary detector elements into its leptonic and semileptonic final states. The following sections give a brief introduction into the phenomenology of τ pair production at LEP and their decays.

1.1 The Standard Model of $e^+e^- \rightarrow \tau^+\tau^-$ at $q^2 = M_{\mathrm{Z}}^2$

The theory of electroweak interactions, in conjunction with the Quantum Chromodynamics, the fundament of the Standard Model (SM), grounds on models which were developed thirty years ago by S.L. Glashow, S. Weinberg and A. Salam [14]. It is based on the unified gauge symmetry $SU(2) \times U(1)$, which is the smallest symmetry group to be invariant under weak isospin and weak hypercharge transformations. The renormalisable electroweak theory incorporates the massive gauge bosons $\mathrm{W}^{\pm}$, Z which is achieved by spontaneously breaking the local gauge symmetry. This so-called Higgs mechanism generates the masses of the gauge bosons as well as those of leptons and quarks. It requires the introduction of at least one additional complex Higgs doublet ϕ. The physical neutral Higgs scalar H is the only remaining part of ϕ after spontaneous symmetry breaking. Its mass is not predicted by the model. Nevertheless, constraints on M_{H} can be obtained from global electroweak fits using all accessible experimental information to the SM in which the mass of the Higgs boson intervenes logarithmically through higher order loops.

In the SM, the fields of matter are fermions organised in three hierarchic generations of leptons and quarks with increasing masses. The τ lepton as the heaviest lepton belongs to the third generation. Left-handed fermions transform as weak isospin doublets under $SU(2)$, whereas right-handed fermions are singlets. The mass- and chargeless neutrinos are always left-handed and couple to the weak gauge bosons. The quark mass eigenstates (d, s, b) are not the same as the weak eigenstates (d', s', b'). Both bases are related via the unitary Cabibbo-Kobayashi-Maskawa (CKM) mixing matrix [15]

$$\begin{pmatrix} d' \\ s' \\ b' \end{pmatrix} = \begin{pmatrix} V_{ud} & V_{us} & V_{ub} \\ V_{cd} & V_{cs} & V_{cb} \\ V_{td} & V_{ts} & V_{tb} \end{pmatrix} \begin{pmatrix} d \\ s \\ b \end{pmatrix} , \tag{1.1}$$

where by convention the three charge 2/3 quarks (u, c, t) are unmixed.

The coupling of a fermion f to the weak bosons has the form

$$\gamma_\mu \frac{1}{2}(v_f - a_f\gamma_5)$$

with the vector (V) and axial-vector (V) coupling constants $v_f = I_3^f - 2Q_f \sin^2\theta_\mathrm{W}$, $a_f = I_3^f$ which read $I_3^f = 1/2$ for ν_e, ν_μ, ν_τ neutrinos and u, c, t quarks, $I_3^f = -1/2$ for e, μ, τ neutrinos and d, s, b quarks in the neutral sector (Z). The coupling in the charged sector $(\mathrm{W}^\pm)$ is a maximal parity violating $V - A$ coupling, *i.e.*, the coupling constants read $v_f = a_f = 1$. The experimental value of the weak mixing angle depends on the electroweak renormalisation scheme. In $\overline{\mathrm{MS}}$ one obtains from the measurement of the leptonic and the hadronic asymmetries the combined result $\sin^2\theta_\mathrm{W} = 0.23165 \pm 0.00024$ (LEP and SLD (at SLAC) data) [16] with a $\chi^2 = 12.8$ for 6 degrees of freedom (d.o.f). For momenta small compared to M_W (strong virtuality), the charged current coupling of a W to a fermion and its isopartner gives rise to the effective four-fermion interaction with $G_\mathrm{F}/\sqrt{2} = g^2/8M_\mathrm{W}^2$, with the Fermi constant $G_\mathrm{F} = 1.16639 \times 10^{-5}\ \mathrm{GeV}^{-2}$ [17], obtained from the accurate measurement of the muon lifetime. The electroweak theory provides precise relations between the masses of the gauge bosons and $\sin^2\theta_\mathrm{W}$, given at tree level, *e.g.*, by the equivalent expressions

$$\begin{aligned} \sin^2\theta_\mathrm{W} &= 1 - \frac{M_\mathrm{Z}^2}{M_\mathrm{W}^2} , \\ \sin^2\theta_\mathrm{W} &= \frac{\pi\alpha}{\sqrt{2}M_\mathrm{W}^2 G_\mathrm{F}} , \\ \sin^2\theta_\mathrm{W} &= \frac{1}{4}\left(1 - \frac{v_f}{a_f}\right) . \end{aligned}$$

Radiative corrections involving the running of $\alpha(s)$ and electroweak loop contributions affect these tree-level relations and renormalised couplings have to be introduced. It is possible to a good approximation to keep the lowest order formulae in terms of the renormalised couplings (the so-called improved Born approximation).

The total cross section $\sigma_{f\bar{f}}$ of the reaction $e^+e^- \to \mathrm{Z} \to f\bar{f}$ at tree level is parametrised by the Breit-Wigner resonance

$$\sigma_{f\bar{f}} = \frac{12\pi}{M_Z^2}\frac{\Gamma_e\Gamma_f}{\Gamma_Z^2}\frac{s\Gamma_Z^2}{(s - M_Z^2)^2 + M_Z^2\Gamma_Z^2} , \tag{1.2}$$

with the Z mass $M_Z = (91.1863 \pm 0.0020)\ \mathrm{GeV}/c^2$ and its width $\Gamma_Z = (2.4946 \pm 0.0027)\ \mathrm{GeV}/c^2$, taken from the combination of the fit results of all four LEP experiments [16]. At tree level and neglecting lepton masses, the partial width of the Z boson for the production of lepton pairs is given by

$$\Gamma_\ell = \frac{G_F M_Z^3}{6\pi\sqrt{2}}(a_\ell^2 + v_\ell^2) = 83.4 \text{ MeV}/c^2 . \tag{1.3}$$

It has been measured to be (assuming e-μ-τ universality) $\Gamma_\ell = (83.91 \pm 0.011)$ MeV/c^2 [17] to be compared to the tree level result (1.3) which is already a good approximation. The Z hadronic decay width, precisely obtained from the measurement of the total leptonic width ($\Gamma_{\text{had}}^{\text{tot}} + \Gamma_\ell^{\text{tot}} = \Gamma_Z$), receives a 4% contribution from higher order quark loop corrections, governed by perturbative QCD. The theoretical prediction can be used to extract a value for $\alpha_s(M_Z)$ (see Section 2.6 for more information).

The parity violating $V - A$ type coupling of the neutral current gives rise to a forward-backward asymmetry of the fermion anti-fermion cross section in forward ($\cos\theta_{\text{polar}} > 0$) and backward ($\cos\theta_{\text{polar}} < 0$) direction:

$$A_{\text{FB}}^{f\bar{f}} = \frac{\sigma(\text{forward}) - \sigma(\text{backward})}{\sigma(\text{forward}) + \sigma(\text{backward})} = \frac{3}{4} A_e A_f , \tag{1.4}$$

where the r.h.s. holds for tree level only and $A_f = 2a_f v_f/(a_f^2 + v_f^2)$. The measurement of $A_{\text{FB}}^{f\bar{f}}$ determines $\sin^2\theta_{\text{W}}$.

1.2 Properties of the τ Lepton

The τ lepton was discovered in 1975 by M. Perl *et al.* [1] using the MARK I detector at the e^+e^- collider SPEAR at SLAC. The $e^+e^- \to \tau^+\tau^-$ cross section behaviour and magnitude showed consistency with the production of pointlike spin 1/2 Dirac particles. It was the first evidence for a third generation of elementary fermions. Since then, the precision in the measurements of its properties increased impetuously, drawing in part near the three per mille limit of precision as, *e.g.*, for the leptonic branching ratios and the τ lifetime. The most important properties and their measurements are briefly collected in the following paragraphs.

1.2.1 The τ Mass

The by far most precise measurement of the τ mass is provided by the BES Collaboration by means of a maximum likelihood fit of the $e^+e^- \to \tau^+\tau^-$ production cross section given at threshold energies by

$$\sigma_{\tau^+\tau^-} = \frac{4\pi\alpha^2}{3s}\frac{\beta(3-\beta^2)}{2} F_c . \tag{1.5}$$

with $\beta = (1 - 4M_\tau^2/s)^{1/2}$ and $F_c \sim \pi\alpha/\beta(1 - \exp(-\pi\alpha/\beta))$ which is caused by the Coulomb attraction between the τ^+ and the τ^- [18] (this produces a non-vanishing threshold cross section of $\sigma_{\tau^+\tau^-}(\beta = 0) \sim 0.23$ nb). The fit results in a τ mass of [19]

$$M_\tau = 1776.96^{+0.18}_{-0.21}{}^{+0.25}_{-0.17} \text{ MeV}/c^2 .$$

Another method, employed at higher energies for the first time by the ARGUS Collaboration [20], uses a kinematic reconstruction of the decay cone of three-prong hadronic decays to constrain the τ mass.

1.2.2 The τ Lifetime

By virtue of the high resolution of their silicon vertex detectors, the LEP experiments dominate the measurements of the τ lifetime in the world average. All methods employed use a reconstruction of the τ decay vertex which, at LEP energy, is displaced by an average of 2.2 mm from the $\tau^+\tau^-$ production vertex. Five different analyses have been performed by the ALEPH Collaboration [21]:

> the first uses the momentum-dependent impact parameter sum method (MIPS) analyses 1-1 topology events in which the mean lifetime is extracted from the impact parameter sum distribution. The impact parameter sum is essentially the distance of the two daughter tracks at their points of closest approach to the beam axis.
>
> In the impact parameter sum analysis (IPS) the daughter track directions are considered in addition to the impact parameter sum in the fit to the mean τ lifetime. The sphericity axis, calculated for each event from the charged and neutral decay products is used as an estimate of the τ production axis. As an advantage, the uncertainty of the primary vertex position vanishes in the impact parameter sum methods.
>
> The impact parameter difference analysis (IPD) of 1-1 topology events uses a fit to the difference between the impact parameters of positive and negative tracks as a function of their acollinearity and polar angle. This method is somewhat complementary to the IPS methods used as it is independent from the impact parameter resolution and the τ flight direction.
>
> The most classical approach is the decay length or vertex method (DL) in which the lifetime of τ's decaying into three charged tracks is measured by means of a constrained fit to the secondary vertex.
>
> Finally, the three dimension impact parameter method exploits the three dimensional space resolution of the vertex detector in conjunction with a complete kinematic reconstruction of the τ flight direction. The method combines the advantages of the IPS and IPD procedures and provides therefore the most competitive result.

All methods are still statistically limited. The combined results of 1991 to 1994 ALEPH data yield the preliminary value of

$$\tau_\tau = (291.2 \pm 2.0 \pm 1.2) \text{ fs} .$$

The combination of the results presented at the Fourth International Workshop on Tau Lepton Physics (TAU'96), Colorado 1996, gives [22]

$$\tau_\tau = (290.2 \pm 1.2) \text{ fs} . \tag{1.6}$$

1.2.3 The τ Branching Ratios

A crucial point of the spectral function analysis is a good knowledge of the branching fractions of the exclusive τ decays modes. Their measurement requires the identification of a charged track in (essentially) one-prong decays as an electron, muon or hadron. The further classification of hadronic channels is based on the number of reconstructed charged and neutral hadrons, as well as the determination of the pion and kaon fraction in charged tracks. The analysis techniques used for the ALEPH measurements of the leptonic [23] and hadronic [24] branching ratios and for the measurement of the τ spectral functions are essentially the same and will be presented in detail in Part II of this work.

The combined result of the measurements of leptonic branching ratios presented at the TAU'96 workshop are[1]

$$\begin{aligned} B(\tau^- \to e^-\bar{\nu}_e\nu_\tau) &= (17.786 \pm 0.072)\,\% && (1.7)\\ B(\tau^- \to \mu^-\bar{\nu}_\mu\nu_\tau) &= (17.317 \pm 0.078)\,\% && (1.8)\end{aligned}$$

with a clear evidence of a smaller branching ratio for the heavier muon due to phase space suppression:

$$\frac{B(\tau^- \to \mu^-\bar{\nu}_\mu\nu_\tau)}{B(\tau^- \to e^-\bar{\nu}_e\nu_\tau)} = 0.9736 \pm 0.0059 \; . \qquad (1.9)$$

The Standard Model predicts for the total width of the $B(\tau^- \to \ell^-\bar{\nu}_\ell\nu_\tau)$ decay, including electroweak radiative corrections [25],

$$\Gamma_{\rm SM}(\tau^- \to \ell^-\bar{\nu}_\ell\nu_\tau) = \frac{G_{\rm F}^2 M_\tau^5}{192\pi^3}\, f\!\left(\frac{m_\ell^2}{M_\tau^2}\right)\left(1 + \frac{3}{5}\frac{M_\tau^2}{M_{\rm W}^2}\right)\left[1 + \frac{\alpha(M_\tau)}{2\pi}\left(\frac{25}{4} - \pi^2\right)\right] , \qquad (1.10)$$

with $f(y) = 1 - 8y + 8y^3 - 12y^2 \ln y$. This yields

$$\frac{\Gamma_{\rm SM}(\tau^- \to \mu^-\bar{\nu}_\mu\nu_\tau)}{\Gamma_{\rm SM}(\tau^- \to e^-\bar{\nu}_e\nu_\tau)} = 0.972565 \pm 0.000009 \; , \qquad (1.11)$$

in agreement with (1.9).

1.2.4 Universality Between the Lepton Families

The hypothesis of e-μ-τ universality of the electroweak interaction relates masses, lifetimes and branching ratios between the leptons. Any deviation from universality would be direct evidence for new physics beyond the Standard Model. The ratios of $e\bar{\nu}_e$ and $\mu\bar{\nu}_\mu$ couplings $g_e^{T/L}$, $g_\mu^{T/L}$ to the W boson follow from comparisons of τ branching ratios to e and μ and from the ratio of pion decay branching fractions. The two comparisons probe separately the couplings to transverse ($J_{\tau+\nu_\tau} = 1$) or longitudinal ($J_\pi = 0$) W's. Recent results for the respective ratios are [22]

$$\frac{g_\mu^T}{g_e^T} = 1.0008 \pm 0.0028 \; ,$$

---

[1] Throughout this thesis, charge conjugate states are implied.

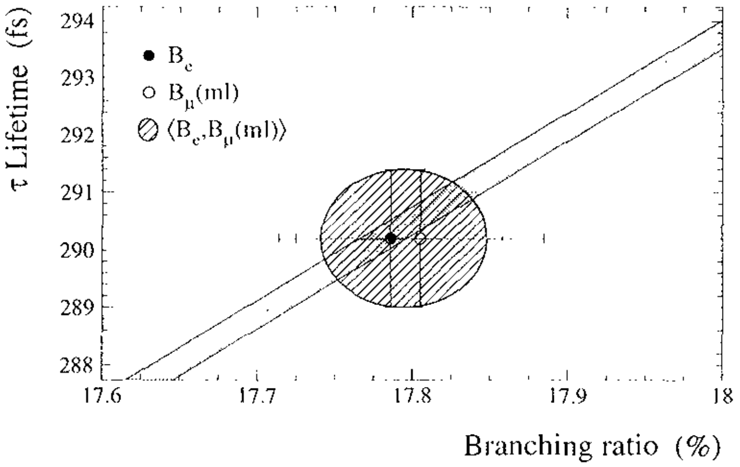

Figure 1.1: *Universality relation between τ_τ and the electronic and muonic branching ratios (shaded band). The points show the corresponding measurements.*

$$
\begin{aligned}
\frac{g_\mu^L}{g_e^L} &= 1.0012 \pm 0.0015 \; , \\
\frac{g_\tau^T}{g_\mu^T} &= 1.0003 \pm 0.0029 \; , \\
\frac{g_\tau^L}{g_\mu^L} &= 1.0067 \pm 0.0064 \; ,
\end{aligned}
$$

all in agreement with universality. The assumption of universality can be used to improve significantly the precision of the $B(\tau^- \to e^-\bar{\nu}_e\nu_\tau)$ branching ratio. Using the relations (1.11) and

$$B(\tau^- \to e^-\bar{\nu}_e\nu_\tau) = \frac{1}{(1632.1 \pm 1.4)\ \mathrm{fs}}\,\tau_\tau \tag{1.12}$$

where the error comes from the uncertainty on M_τ with the previously quoted values for $B(\tau^- \to \mu^-\bar{\nu}_\mu\nu_\tau)$ and τ_τ, one obtains for the electron branching ratio with universality

$$B(\tau^- \to e^-\bar{\nu}_e\nu_\tau) = (17.789 \pm 0.043)\,\% \; , \tag{1.13}$$

with $\chi^2/\mathrm{d.o.f.} = 0.06/2$. Fig. 1.1 shows the τ lifetime versus the electronic (B_e) and muonic (B_μ(ml). "ml" means massless: $B_\mu(\mathrm{ml}) = B_\mu/0.9725\ldots$) branching ratios as well as the weighted average of both (assuming universality). The shaded band depicts the universality relation (1.12) where the uncertainty stems from the error on M_τ.

A test of charged lepton universality in the neutral current sector is provided by the measurement of the angular asymmetries in $\mathrm{Z} \to \ell^+\ell^-$ decays. The combination of LEP and SLD data yields for the ratios of the respective vector and axial-vector couplings to the Z boson

$$\frac{v_\mu}{v_e} = 0.935 \pm 0.085 \; ,$$

$$\begin{aligned}\frac{v_\tau}{v_e} &= 0.959 \pm 0.046\ ,\\ \frac{a_\mu}{a_e} &= 0.9993 \pm 0.0017\ ,\\ \frac{a_\tau}{a_e} &= 1.0000 \pm 0.0019\ ,\end{aligned}$$

as in the charged current sector, in agreement with universality. The good precision of the v_τ/v_e ratio compared to v_μ/v_e is provided by the measurement of the final state polarisation which is only possible for the unstable τ lepton (see following section).

1.2.5 The τ Polarisation

Another effect of the parity violating neutral current (besides the forward-backward asymmetry) is the fact that the fermions produced in Z decays have a non-zero average helicity. The amount of this asymmetry, the polarisation P, depends on the polar angle of the lepton flight direction, *i.e.*, is forward-backward asymmetric. Both, the polarisation and its forward-backward asymmetry are related to $A_{\mathrm{FB}}^{f\bar{f}}$ and serve therefore as additional sensitive sources to measure the weak mixing angle $\sin^2\theta_{\mathrm{W}}$. At LEP there is no experimental access to the helicity states of the "stable" e and μ pairs. However, in the τ case, the helicity information is contained in the energies and momenta of the τ decay products so that their reconstruction permits the inference of the original τ spin. Newer analyses of the τ polarisation use so-called optimal observables [26] with highest possible sensitivity on the basis of a complete kinematic reconstruction of the τ rest frame, taking into account the correlation between the τ hemispheres [27], and the corresponding τ decay matrix element. The combination of all LEP results for the τ polarisation on the Z peak yields [16]

$$P_\tau = (-14.01 \pm 0.67)\,\%\ .$$

1.2.6 CP Violation

The existence of CP violation in the neutral kaon sector, discovered by Christenson *et al.* [28], has been an experimental fact for a long time. It is introduced into the Standard Model by complex Yukawa couplings which generate a non-vanishing phase in the unitary CKM mixing matrix. On the other hand, any CP violation in the leptonic sector would as non-zero neutrino masses signify new physics. The authors of Ref. [29] suggested a model independent ansatz to extend the SM Lagrangian by an effective CP violating term, where the strength of this new coupling is governed by a q^2 dependent complex form factor, called the weak dipole moment d_τ^w in the case of $e^+e^- \rightarrow \tau^+\tau^-$ production at $q^2 = M_Z$. CP violation is measured at LEP using CP-odd observables which mean values are proportional to the CP violation generating weak dipole moment. The existence of the additional coupling influences the spin-momentum correlation of the τ pair and can therefore only be measured in the τ sector where the τ spin can be reconstructed through the measurement of its decays. Equivalent to the polarisation measurement, the phenomenological knowledge of the CP violating $\tau^+\tau^-$ production matrix as well as the dynamics of the τ decays considered allows the development of optimal observables, which depend on the respective τ final state [30]. The combination of recent LEP results yields the upper limits [31]

$$\begin{aligned} |\mathrm{Re}(d_\tau^w)| &< 3.6 \times 10^{-18}\ e\,\mathrm{cm}\ , \\ |\mathrm{Im}(d_\tau^w)| &< 1.1 \times 10^{-17}\ e\,\mathrm{cm}\ , \\ |d_\tau^w| &< 1.2 \times 10^{-17}\ e\,\mathrm{cm}\ , \end{aligned}$$

at 95% confidence level (CL). Optimistic theoretical expectations of $|d_\tau^w|$ from multi-Higgs models, supersymmetry or massive Majorana neutrinos reach the level of a few times 10^{-20} $e\,$cm, while lepto-quark models might generate a weak dipole moment of up to 3×10^{-19} $e\,$cm [31].

1.2.7 The Lorentz Structure of the Charged Currents

The Standard Model presupposes a pure $V-A$ structure of the charged current propagated by the W boson. A general coupling ansatz which involves additional V, A, $V+A$ and scalar (S), pseudoscalar (P) and tensor (T) couplings is proposed by Bouchiat and Michel [32]. The linear independent basis of this representation are the so-called Michel parameters in which the differential leptonic decay width of the τ has the form

$$\begin{aligned} \frac{d\Gamma(\tau^- \to \ell^- \bar{\nu}_\ell \nu_\tau)}{d\Omega\, dx} \propto\ & \beta x^2 \left\{ 3(1-x) + 2\rho\left(\frac{4}{3}x - 1 - \frac{m_\ell^2}{3\omega^2 x}\right) + 6\eta \frac{m_\ell}{M_\tau}\frac{1-x}{x} \right. \\ & \left. - P_\tau\, \xi \cos\theta_\ell \left[1 - x + 2\delta\left(\frac{4}{3}x - 1\right)\right] \right\} . \qquad (1.14) \end{aligned}$$

Here, θ_ℓ is the angle between the τ spin and the momentum of the lepton, $\beta = p_\ell/E_\ell$, $x = E_\ell/\omega$ and $\omega = (M_\tau^2 + m_\ell^2)/2M_\tau$. The SM values for the Michel parameters are: $\rho = \delta = 3/4$, $\eta = 0$ and $\xi = 1$. For example, the parameter ρ would be 3/8 for pure V or A and zero in the case of a right-handed $V+A$ coupling at the τ-ν_τ-W vertex. Precise recent experimental results from the CLEO Collaboration are (universality assumed) [33]

$$\begin{aligned} \rho_{e,\mu} &= 0.735 \pm 0.0013 \pm 0.008\ , \\ \eta_{e,\mu} &= -0.015 \pm 0.061 \pm 0.065\ , \\ \xi_{e,\mu} &= 1.007 \pm 0.040\ , \\ (\xi\delta)_{e,\mu} &= 0.745 \pm 0.026\ , \end{aligned}$$

all in agreement with the SM. The values for $\xi_{e,\mu}$ and $(\xi\delta)_{e,\mu}$ are preliminary and given with statistical errors only.

1.2.8 The τ Neutrino

The τ neutrino ν_τ is the only elementary fermion of the Standard Model which has not been discovered yet. Efforts towards its detection are presently undertaken by the CHORUS [34] and NOMAD [35] Collaborations at CERN who attempt to tag ν_τ's (by means of a τ signal) originating from $\nu_\mu \to \nu_\tau$ oscillations which occur if the neutrino masses are non-zero. This phenomena is equivalent to the mixing of massive quarks, described by the CKM mixing matrix.

Although the ν_τ has not directly been detected, it influences significantly the kinematic of τ decays and the τ branching itself. The energy-momentum conservation of $\tau(k) \rightarrow X(p_X) + \nu(p_\nu)$ reads $k = p_X + p_\nu$ or its square $M_\tau^2 = m_X^2 + m_\nu^2 + 2E_X E_\nu - 2|\vec{p_X}||\vec{p_\nu}|\cos\theta_{X,\nu}$. The existence of an invisible light particle (missing energy but small missing mass) can then readily be inferred. *e.g.*, from the E_X spectrum. But could this invisible particle not be an electron or muon neutrino ? In such a case one would assume that the τ itself is of electron or muon type, *e.g.*, an excited state of those, which certainly would cause transitions like $\tau \rightarrow e\gamma$ and $\tau \rightarrow \mu\gamma$, respectively, without missing energy. It would furthermore yield a breakdown of the universality relation between M_τ, B_e, B_μ and τ_τ. In fact, universality between all lepton couplings is *the* evidence for a left-handed τ, ν_τ isospin doublet.

Up to now, all observations carried out (including the Z width consistent with $N_\nu = 3$ ($N_\nu = 2.989 \pm 0.012$ [16])) support the existence of a light (or massless), exclusively weak interacting, left-handed particle of a third generation, *i.e.*, different from ν_e and ν_μ: the τ neutrino ν_τ.

The indirect kinematic evidence for its existence is exploited by the experiments to constrain the neutrino mass M_{ν_τ}. The sensitivity of such constraint fits increases with the amount of kinematical information used. It is good for high-multiplicity hadronic final states and worse in the leptonic decay modes due to the additional $\bar{\nu}_\ell$ which gets lost. Several reconstruction methods have been applied by different collaborations all dealing with the three or five-prong τ final states. No evidence for a non-zero mass has been found. The following limits are given at 95% confidence level:

> CLEO, OPAL and ALEPH used a two-dimensional likelihood fit to the energy and the invariant mass of the $\tau^- \rightarrow (5\text{h})^- \nu_\tau$ final state (ALEPH: $\tau^- \rightarrow (5\text{h})^- (\pi^0)\, \nu_\tau$). They obtained the results: CLEO $M_{\nu_\tau} < 32.6$ MeV/c^2 [36], OPAL (1992 data) $M_{\nu_\tau} < 74$ MeV/c^2 [37] and ALEPH (1991–93) $M_{\nu_\tau} < 23.1$ MeV/c^2 [38].
>
> OPAL used the correlation of the two τ hemispheres (ideally, they are emitted back-to-back) to infer an upper limit for M_{ν_τ} requiring three-prong candidates in both cones. They found $M_{\nu_\tau} < 35.3$ MeV/c^2 [39]. An improvement of this method using an optimal exploitation of the available kinematic information is presented in Ref. [40].
>
> DELPHI used a fit to the invariant mass spectrum of the $\tau^- \rightarrow (3\pi)^- \nu_\tau$ decay which is dominated by the $a_1(1260)$ resonance. They obtained $M_{\nu_\tau} < 29.3$ MeV/c^2 [41].
>
> In a second analysis ALEPH applied the same method as for the $(5\text{h})^- (\pi^0)\, \nu_\tau$ final states on $\tau^- \rightarrow (3\pi)^- \nu_\tau$ decays which occur much more frequently (about a factor of 100) but is less sensitive to M_{ν_τ}. The upper limit is found to be $M_{\nu_\tau} < 25.7$ MeV/c^2 [42].

The best limit is derived from a combined likelihood of both ALEPH measurements taking into account the correlations between systematic errors [42]:

$$M_{\nu_\tau} \; < \; 18.2 \ \mathrm{MeV}/c^2 \ ,$$

at 95% confidence level.

1.3 Hadronic τ Decays and CVC

The τ is the only lepton of the three known generations heavy enough to decay into hadrons. The very clean conditions at LEP energies, where the $Z \rightarrow q\bar{q}$ background is easy to separate due to the high multiplicity of its final states, render hadronic τ decays an ideal laboratory for studying the hadronic charged currents and QCD.

In analogy to purely leptonic τ decays, the invariant amplitude for the hadronic (semileptonic) decays can be written in form of a current-current interaction

$$\mathcal{M}(\tau^- \rightarrow \mathrm{hadrons}^- \nu_\tau) \; = \; \frac{G_\mathrm{F}}{\sqrt{2}} |V| l_\mu J^\mu \ , \tag{1.15}$$

with the corresponding non-strange or strange CKM matrix element $|V|$. l_μ describes the $V - A$ current

$$l_\mu \; = \; \bar{\nu}_\tau \gamma_\mu (1 - \gamma_5) \tau \ . \tag{1.16}$$

The hadronic transition current J_μ is the piece of interest here. It probes the matrix element of the left handed charged current between the vacuum and the hadronic final state. Restricting to a $V - A$ structure, one can write [43]

$$J_\mu \; = \; \langle \mathrm{hadrons} | V_\mu(0) - A_\mu(0) | 0 \rangle \ . \tag{1.17}$$

With a non-strange current, hadronic systems of spin-parity $J^P = 0^-, 0^+, 1^-, 1^+$ can be produced. The differential τ hadronic width can be expressed in the general ansatz [44]

$$d\Gamma(\tau^- \rightarrow \mathrm{hadrons}^- \nu_\tau) \; = \; \frac{G_\mathrm{F}^2}{4 M_\tau} |V|^2 L_{\mu\nu} H^{\mu\nu} \, d\mathrm{PS} \ , \tag{1.18}$$

with the leptonic (hadronic) tensor $L_{\mu\nu}$ ($H_{\mu\nu}$) and the Lorentz invariant phase space element dPS. Seen from the hadronic rest system, the tensor product simplifies to a sum over so-called structure functions and kinematic factors [44].

For the most simple hadronic decay modes $\tau \rightarrow \mathrm{h}^- \nu_\tau$ (h$\equiv \pi$, K), the structure functions reduce to δ-functions. Including short distance electroweak radiative corrections to the one loop level and non-logarithmic terms, and integrating over the τ phase space, its decay width is given by [25, 45]

$$\Gamma(\tau^- \rightarrow \mathrm{h}^- \nu_\tau) \; = \; \frac{G_\mathrm{F}^2 f_\mathrm{h}^2 |V|^2}{8\pi} M_\tau^3 \left(1 - \frac{m_\mathrm{h}^2}{M_\tau^2}\right)^2 \left(1 + \frac{\alpha}{2\pi} \left(\ln \frac{M_Z}{M_\tau} + \frac{5}{6}\right)\right) \ . \tag{1.19}$$

with the pion decay constant[2] $f_\pi = (92.4 \pm 0.26)$ MeV [17] measured in the decays $\pi^- \rightarrow \mu^- \bar{\nu}_\mu$ and $\pi^- \rightarrow \mu^- \bar{\nu}_\mu \gamma$, the kaon decay constant $f_\mathrm{K} = (113.0 \pm 1.0)$ MeV [17] measured

---

[2] The definition of f_π and f_K adopted here differs from the one used in [17] by a factor of $\sqrt{2}$.

similarly in $K^- \to \mu^-\bar{\nu}_\mu$, $\mu^-\bar{\nu}_\mu\gamma$ decays and the respective CKM matrix elements $|V_{ud}| = 0.9752 \pm 0.0007$ [17] and $|V_{us}| = 0.221 \pm 0.003$[3], respectively. Using (1.13) and $B(\tau^- \to \pi^-\nu_\tau) = (11.23 \pm 0.16)\%$ [46], $B(\tau^- \to K^-\nu_\tau) = (0.691 \pm 0.030)\%$ [47], one obtains

$$\begin{aligned} \frac{B(\tau^- \to \pi^-\nu_\tau)}{B(\tau^- \to e^-\bar{\nu}_e\nu_\tau)} &= 0.6313 \pm 0.0091 \ , \qquad (1.20) \\ \frac{B(\tau^- \to K^-\nu_\tau)}{B(\tau^- \to e^-\bar{\nu}_e\nu_\tau)} &= 0.0389 \pm 0.0017 \ , \qquad (1.21) \end{aligned}$$

compared to the ratio of (1.19) to (1.10) which gives 0.6280 (π) and 0.0416 (K) in agreement with (1.20) and (1.21).

1.3.1 Vector and Axial-Vector Spectral Functions

The quantum number corresponding to the (conserved) vector and axial-vector currents is the so-called isotopic parity, the G-parity. It is a generalized multiplicative symmetry of multi-pion systems under the successive operations C and R, where C conjugates the charge and R rotates the system around the second axis in $I = 1$ isospace:

$$(\mathrm{G} \equiv \mathrm{CR}) \begin{pmatrix} \frac{1}{\sqrt{2}}(\pi_1 + i\pi_2) \\ \frac{1}{\sqrt{2}}(\pi_1 - i\pi_2) \\ \pi_3 \end{pmatrix} = -\mathrm{C} \begin{pmatrix} \frac{1}{\sqrt{2}}(\pi_1 - i\pi_2) \\ \frac{1}{\sqrt{2}}(\pi_1 + i\pi_2) \\ \pi_3 \end{pmatrix} = - \begin{pmatrix} \frac{1}{\sqrt{2}}(\pi_1 + i\pi_2) \\ \frac{1}{\sqrt{2}}(\pi_1 - i\pi_2) \\ \pi_3 \end{pmatrix} ,$$

with $\pi^\pm = (\pi_1 \pm i\pi_2)/\sqrt{2}$ and $\pi^0 = \pi_3$. The measurement of the non-strange τ vector (axial-vector) current spectral functions requires the selection and identification of τ decay modes with a defined G-parity G=+1 (G=−1) and therefore hadronic channels with an even (odd) number of neutral *or* charged pions (G is a multiplicative quantum number). In a neutral system, like in e^+e^- annihilation, the G-parity is related to the isospin I of the final state via $\mathrm{G} = \mathrm{C}\,(-1)^I$. Thus, owing to $\mathrm{C}_\gamma = -1$, one has $I_{2n\pi} = 1$ and $I_{(2n-1)\pi} = 0$ for $n = 1, 2, \ldots$. Isospin violating electromagnetic decays do not respect this relation. A prominent candidate is the $I = 0$ decay $\omega \to \pi^+\pi^-$ which occurs in 2.2% of all ω decays. Since hadronic final states of different G-parity differ also in J^P quantum numbers, there is no interference between these two states. Thus the total hadronic width separates into $\Gamma_{\mathrm{tot}} = \Gamma_V + \Gamma_A$.

The isovector spectral function v_{1,V^-} (a_{1,A^-}) of a non-strange vector (axial-vector) τ decay channel $V^-\nu_\tau$ ($A^-\nu_\tau$) is obtained by dividing the normalised invariant mass-squared distribution $(1/N_{V/A^-})(dN_{V/A^-}/ds)$ for a given hadronic mass $\sqrt{s}$ by the appropriate kinematic factor:

$$\begin{aligned} v_{1,V^-}/a_{1,A^-}(s) &= \frac{M_\tau^2}{6\,|V_{ud}|^2\,S_{\mathrm{EW}}}\,\frac{B(\tau^- \to V^-/A^-\,\nu_\tau)}{B(\tau^- \to e^-\,\bar{\nu}_e\nu_\tau)} \\ &\quad \times \frac{dN_{V/A^-}}{N_{V/A^-}\,ds}\left[\left(1 - \frac{s}{M_\tau^2}\right)^2\left(1 + \frac{2s}{M_\tau^2}\right)\right]^{-1} . \qquad (1.22) \end{aligned}$$

---

[3] Unitarity of the CKM matrix requires $V_{ud}^2 + V_{us}^2 + V_{ub}^2 = 1$. Estimating the u,b-mixing to be smaller than 0.005 (68%CL) [17] one obtains the value quoted for $|V_{us}|$.

where again $|V_{ud}| = 0.9752 \pm 0.0007$ [17] denotes the CKM weak mixing matrix element and $S_{\mathrm{EW}} = 1.0194 \pm 0.0040$ accounts for electroweak second order corrections [25] (see next paragraph). The spectral functions are normalised by the ratio of the respective vector/axial-vector branching fraction $B(\tau^- \to V^-/A^-\,\nu_\tau)$ to the branching fraction of the electron channel (1.13), the latter improved by universality assumption. Note that this definition of the τ spectral functions differs from the one used in [48] by an additional factor $4\pi^2$.

With the definition of Eq. (1.22) the differential τ decay rate into non-strange hadrons reads [2]

$$\frac{d\Gamma\left(\tau^- \to \nu_\tau (V^-/A^-)\right)}{ds} = \frac{G_{\mathrm{F}}^2 |V_{ud}|^2 S_{\mathrm{EW}} M_\tau^3}{32\pi^3} \left(1 - \frac{s}{M_\tau^2}\right)^2 \left(1 + \frac{2s}{M_\tau^2}\right) v_{1,V^-}/a_{1,A^-}(s) \,, \tag{1.23}$$

which corresponds to the standard relation between hadronic width and branching ratio

$$\Gamma(\tau \to \nu_\tau \text{ hadrons}) = \frac{G_{\mathrm{F}}^2 M_\tau^5}{192\pi^3} \, \frac{B(\tau \to \nu_\tau \text{ hadrons})}{B(\tau \to e\bar{\nu}_e\nu_\tau)} \,, \tag{1.24}$$

from $\Gamma_\tau = \tau_\tau^{-1}$.

1.3.2 Electroweak Radiative Corrections

The dominant contribution from electroweak radiative corrections to the hadronic decay width comes from the short distance correction to the effective four-fermion coupling $\tau \to (d\bar{u})^- \nu_\tau$ leading to the fractional logarithmic term $(\alpha(M_\tau)/2\pi)(4\ln(M_{\mathrm{Z}}/M_\tau) + 5/6)$ [45], which vanishes due to their integer charges in leptonic τ decays. This short distance correction can be absorbed into an overall multiplicative electroweak correction S_{EW} introduced in Eq. (1.22). The resummation of higher-order electroweak logarithms using the renormalisation group yields [12, 25]

$$S_{\mathrm{EW}} = \left(\frac{\alpha(m_b)}{\alpha(M_\tau)}\right)^{\frac{9}{19}} \times \left(\frac{\alpha(M_{\mathrm{W}})}{\alpha(m_b)}\right)^{\frac{9}{20}} \times \left(\frac{\alpha(M_{\mathrm{Z}})}{\alpha(M_{\mathrm{W}})}\right)^{\frac{36}{17}} = 1.0194 \,, \tag{1.25}$$

while remaining perturbative electroweak corrections are of order $\alpha^n(M_\tau)\ln^{n-1}(M_{\mathrm{Z}}/M_\tau)$ which is safe to ignore. The subleading non-logarithmic short distance correction, calculated to order $O(\alpha)$ at quark level: $5\alpha(M_\tau)/12\pi \simeq 0.0010$ [45] turns out to be small. Additional long-distance corrections are expected to be final state dependent. They have only been computed for the $\tau^- \to \pi^- \nu_\tau$ decay leading to a total radiative correction of 2.03% [49] which is dominated by the leading logarithm from the short distance contribution. The experimental value of the ratio (1.20) shows good agreement with the theoretical prediction obtained from the formulae given in Ref. ([25]). The evaluation of (1.25) neglects radiative corrections from additional gluon exchange between the final state quarks.

To be safe [50], the uncertainty of S_{EW} in (1.25) is estimated to be $\Delta S_{\mathrm{EW}} = 0.0040$.

1.3.3 τ Spectral Functions and CVC

Assuming unitarity and analyticity to hold, the spectral functions of hadronic τ decays are proportional to the imaginary part of the two-point correlation (or: hadronic vacuum polarisation) functions [12, 51]

$$\begin{aligned} \Pi^{\mu\nu}_{ij,U}(q) &\equiv i \int d^4x\, e^{iqx} \langle 0|T(U^{\mu}_{ij}(x)U^{\nu}_{ij}(0)^{\dagger})|0\rangle \\ &= (-g^{\mu\nu}q^2 + q^{\mu}q^{\nu})\,\Pi^{(1)}_{ij,U}(q^2) + q^{\mu}q^{\nu}\,\Pi^{(0)}_{ij,U}(q^2) \end{aligned} \tag{1.26}$$

of vector ($U^{\mu}_{ij} \equiv V^{\mu}_{ij} = \bar{q}_j\gamma^{\mu}q_i$) or axial-vector ($U^{\mu}_{ij} \equiv A^{\mu}_{ij} = \bar{q}_j\gamma^{\mu}\gamma_5 q_i$) colour-singlet quark currents in corresponding quantum states and for time-like momenta-squared $q^2 > 0$. The Lorentz decomposition is used in Eq. (1.26) to separate the correlator into its transverse $\Pi^{(1)}_{ij,U}(q^2)$ and longitudinal $\Pi^{(0)}_{ij,U}(q^2)$ parts. Thus, using the definition (1.22), one identifies for non-strange quark currents

$$\frac{1}{\pi}\mathrm{Im}\left[\Pi^{(1)}_{\bar{u}d,V/A}(s) + \Pi^{(0)}_{\bar{u}d,V/A}(s)\right] = \frac{1}{2\pi^2}v_1/a_1(s)\ . \tag{1.27}$$

Using Cauchy's integration formula, the analytic vacuum polarisation function $\Pi^{(J)}(q^2)$ obeys the dispersion relation

$$\Pi^{(J)}(q^2) = \frac{1}{\pi}\int\limits_0^{\infty} ds\, \frac{\mathrm{Im}\Pi^{(J)}(s)}{s - q^2} + \text{subtractions}\ . \tag{1.28}$$

where the unknown but in general irrelevant subtraction constants can be removed by taking the derivative of $\Pi(q^2)$. The imaginary part $\mathrm{Im}\Pi^{(J)}(s)$ is proportional to the τ spectral functions or the hadronic cross section in e^+e^- annihilation. The above dispersion relation allows one to connect experimentally measurable quantities to the correlation functions $\Pi^{(J)}(q^2)$ calculable with QCD techniques. This point will be rediscussed in more detail in section 2.5.

The vacuum polarisation functions (1.26) for various types of quark currents ij are crucial in the theoretical evaluation of total cross sections and decay widths. In an equivalent consideration one can relate the cross section of e^+e^- annihilation $\sigma(e^+e^- \to V_{I=0,1})$ to the imaginary part of the corresponding vacuum polarisation function (optical theorem), where the photon propagator allows only vector final states here. Then, using isospin rotation, the spectral function of a vector τ decay mode $X^-\nu_\tau$ in a given isospin state for the hadronic system is related to the e^+e^- annihilation cross section of the corresponding isovector final state X^0:

$$\sigma^{I=1}_{e^+e^-\to X^0}(s) = \frac{4\pi\alpha^2}{s}\, v_{1,X^-}(s)\ . \tag{1.29}$$

For the two-body hadronic final state $X^- \equiv \pi^-\pi^0$ in τ decays it is customary to introduce a weak pion form factor $\tilde{F}^{I=1}_{\pi}$ to describe phenomenologically the probability density of the transition $W^- \to \pi^-\pi^0$:

$$|\tilde{F}^{I=1}_{\pi}(s)|^2 = \frac{12}{\beta^3_{\pi}(s)}\, v_{1,\pi^-\pi^0}(s)\ , \tag{1.30}$$

where $\beta_\pi(s) = (1 - 4m_\pi^2/s)^{1/2}$ is the pion velocity in the hadronic centre of mass. The weak pion form factor can be identified via CVC with the isovector electromagnetic form factor, given by

$$|F_\pi^{I=1}(s)|^2 = \frac{3}{\pi}\frac{s}{\alpha^2\,\beta_\pi^3(s)}\,\sigma^{I=1}_{e^+e^-\to\pi^+\pi^-}(s)\;, \tag{1.31}$$

which implies Eq.(1.29). In order to complete the formula package, one may relate the τ vector spectral function to the total hadronic cross section

$$R(s) = \frac{\sigma^{\rm tot}_{e^+e^-\to\,\rm hadrons}}{\sigma_{e^+e^-\to\mu^+\mu^-}}\;, \tag{1.32}$$

so that with $\sigma_{e^+e^-\to\mu^+\mu^-} = 4\pi\alpha^2/3s$ and Eq. (1.29) one obtains

$$R(s) = 3\times v_1(s)\;. \tag{1.33}$$

The above equations relate hadronic spectral functions from τ decays to isovector vacuum polarisation currents. For this purpose one has to worry whether the breakdown of CVC due to chiral symmetry violating effects or electromagnetic vertex corrections has non-negligible contributions within the present accuracy. A detailed discussion of this point is given in Chapter 9, Section 9.1.

1.4 Classification of Many Pion Systems

Abraham Pais [52] introduced in 1960 a classification of N-pions states with total isospin $I = 0, 1$. The basis of isospin wave functions of the system belongs to irreducible representations of the corresponding symmetry group which are characterized by three integer quantum numbers (partitions of N) N_1, N_2, N_3 obeying the relations

$$\begin{aligned} N_1 \geq N_2 \geq N_3 \geq 0\;, \\ N_1 + N_2 + N_3 = N \quad . \end{aligned} \tag{1.34}$$

Each state (N_1, N_2, N_3) of a partition class $\{N_1, N_2, N_3\}$ is characterized by its symmetry property under the exchange of some of the momenta $p_a, \ldots, p_N$. Such a state is constructed with the help of a Young tableau. A construction prescription on how to obtain specific classes from Young tableaux is given in Ref. [53]. A brief review of the Pais classification concerning explicitly τ final states is presented in Ref. [54].

The authors of Ref [53] give a certain number of properties shared by all states of a given class of partitions N_1, N_2, N_3:

> the total isospin $I_{N\pi}$ of the N-pion system is determined uniquely and
>
> it holds $I_{N\pi} = 0$ ($I_{N\pi} = 1$), if $N_1 - N_2$ and $N_2 - N_3$ are both even (odd).
>
> States (N_1, N_2, N_3) are composed by N_3 isoscalar subsystems of three pions, $N_2 - N_3$ isovector subsystems of two pions and N_1 (isovector) single pions.

$N=2$	e^+e^- $(I=1)$	τ^- $(I=1)$
$\{\text{Class}\}_I$	$\pi^+\pi^-$	$\pi^-\pi^0$
$\{110\}_1$	1	1

$N=3$	e^+e^- $(I=0)$	τ^- $(I=1)$	
$\{\text{Class}\}_I$	$\pi^+\pi^-\pi^0$	$2\pi^-\pi^+$	$\pi^-2\pi^0$
$\{300\}_1$	–	4/5	1/5
$\{210\}_1$		1/2	1/2
$\{111\}_0$	1	–	–

$N=4$	e^+e^- $(I=1)$		τ^- $(I=1)$	
$\{\text{Class}\}_I$	$2\pi^+2\pi^-$	$\pi^+\pi^-2\pi^0$	$2\pi^-\pi^+\pi^0$	$\pi^-3\pi^0$
$\{310\}_1$	4/5	1/5	3/5	2/5
$\{211\}_1$	0	1	1	0

$N=5$	e^+e^- $(I=0)$		τ^- $(I=1)$		
$\{\text{Class}\}_I$	$2\pi^+2\pi^-\pi^0$	$\pi^+\pi^-3\pi^0$	$3\pi^-2\pi^+$	$2\pi^-\pi^+2\pi^0$	$\pi^-4\pi^0$
$\{500\}_1$		–	24/35	8/35	3/35
$\{410\}_1$			4/10	3/10	3/10
$\{320\}_1$		–	2/5	3/5	0
$\{311\}_0$	2/3	1/3	–	–	–
$\{221\}_1$	–	–	0	1	0

$N=6$	e^+e^- $(I=1)$			τ^- $(I=1)$		
$\{\text{Class}\}_I$	$3\pi^+3\pi^-$	$2\pi^+2\pi^-2\pi^0$	$\pi^+\pi^-4\pi^0$	$3\pi^-2\pi^+\pi^0$	$2\pi^-\pi^+3\pi^0$	$\pi^-5\pi^0$
$\{510\}_1$	24/35	8/35	3/35	16/35	10/35	9/35
$\{411\}_1$	0	2/5	3/5	4/5	1/5	0
$\{330\}_1$	3/5	2/5	0	1/5	4/5	0
$\{321\}_1$	0	1	0	1/2	1/2	0

Table 1.1: *Decomposition of e^+e^- annihilation and τ final states in linear independent classes using the Pais description* [52]. *The values given are explicitly cross sections and partial decay widths, respectively.*

According to the CVC hypothesis, the amplitudes of τ vector final states with an even number of pions are related to isovector amplitudes of e^+e^- annihilation final states by isospin rotation. Table 1.1 compiles the Pais classification for e^+e^- annihilation and τ final states containing $N = 2, \ldots, 6$ pions. Most relations shown are taken from Ref. [54] (see also Ref. [55]).

Upper Bounds for Unmeasured Final States

A very useful property of the rigorous isospin classification which is extensively used in this thesis is the possibility to constrain cross sections (branching fractions) of unmeasured e^+e^- (τ) final states from measured ones.

The approach used is always the same and will in the following be demonstrated for the case of the five-pion τ final state where the $\pi^-4\pi^0\nu_\tau$ mode has indeed been measured but its precision is rather weak. The world average for the branching ratio is

$B(\tau^- \to \pi^- 4\pi^0 \nu_\tau) = (0.12 \pm 0.06)\%$ [17]. Using the decomposition of Tab. 1.1

$$\begin{aligned}
\Gamma_{5\pi^\pm} &= \frac{24}{35}\Gamma_{500} + \frac{2}{5}\Gamma_{410} + \frac{2}{5}\Gamma_{320} \ , && (1.35)\\
\Gamma_{3\pi^\pm 2\pi^0} &= \frac{8}{35}\Gamma_{500} + \frac{3}{10}\Gamma_{410} + \frac{3}{5}\Gamma_{320} + \Gamma_{221} \ , && (1.36)\\
\Gamma_{\pi^\pm 4\pi^0} &= \frac{3}{35}\Gamma_{500} + \frac{3}{10}\Gamma_{410} \ , && (1.37)
\end{aligned}$$

one obtains two distinct upper limits for $\Gamma_{\pi^\pm 4\pi^0}$ from the assumption of dominant $\{500\}$ and $\{410\}$ classes, respectively. Dominant Γ_{500} leads to the upper limits

$$\begin{aligned}
\Gamma_{\pi^\pm 4\pi^0} &\le \frac{1}{8}\Gamma_{5\pi^\pm} \ , && (1.38)\\
\Gamma_{\pi^\pm 4\pi^0} &\le \frac{3}{8}\Gamma_{3\pi^\pm 2\pi^0} \ , && (1.39)
\end{aligned}$$

while a dominant Γ_{410} yields

$$\begin{aligned}
\Gamma_{\pi^\pm 4\pi^0} &\le \frac{3}{4}\Gamma_{5\pi^\pm} \ , && (1.40)\\
\Gamma_{\pi^\pm 4\pi^0} &\le \Gamma_{3\pi^\pm 2\pi^0} \ . && (1.41)
\end{aligned}$$

Using the branching ratios given in Tab. 6.2 of Chapter 6, $B_{5\pi^\pm} = (0.066 \pm 0.008)\%$ and $B_{3\pi^\pm 2\pi^0} = (0.43 \pm 0.10)\%$, with $B_{5\pi^\pm}/B_{3\pi^\pm 2\pi^0} = 0.15 \pm 0.04$, one can already exclude a $\{410\}$ dominance which predicts the ratio to be $B_{5\pi^\pm}/B_{3\pi^\pm 2\pi^0} = 4/3$. In fact, one concludes from the decomposition (1.36) that the high $B_{3\pi^\pm 2\pi^0}$ is created by a dominant $\{221\}$ contribution which should be largely saturated by the well known $\omega\,\pi^-\pi^0$ intermediate state with $B_{\omega\,\pi^-\pi^0} = (0.38 \pm 0.11)\%$ of which 88.8% decay into $3\pi^\pm 2\pi^0$.

Using the "best",*i.e.*, lowest upper limit from Eqs. (1.38) and (1.40) which is $\Gamma_{\pi^\pm 4\pi^0} \le \frac{3}{4}\Gamma_{5\pi^\pm}$ one obtains

$$B_{\pi^\pm 4\pi^0} \le 0.054\,\% \ ,$$

with 68% confidence level. As corresponding value one may take $B_{\pi^\pm 4\pi^0} = 0.027 \pm 0.027$, providing a two times better accuracy than the measurement.

Chapter 2

Hadronic τ Decays and QCD

A decisive role in the construction of SM has been played by the experimental studies of inclusive processes, in particular e^+e^- annihilation into hadrons, and deep inelastic e-p scattering. The discovery of scaling of deep inelastic structure functions [56] led to the parton model [57]. Finally, the discovery of asymptotic freedom in non-abelian gauge field models [58] together with the conception of spin 1/2, fractionally electric charged elementary constituents of hadrons – quarks [59] with an additional quantum number colour, interacting via 8 massless, non-abelian, *i.e.*, self-interacting gauge bosons – gluons caused the creation of Quantum Chromodynamics (QCD) [60]. The existence of gluons was first inferred from the observation of scaling violation in deep inelastic lepton-nucleon scattering. In 1979, (radiative) gluons were directly observed in 3-jet final states of e^+e^- annihilation [61]. A historical review of QCD can be found, *e.g.*, in Ref. [62].

2.1 The QCD Lagrangian

QCD is a renormalisable quantum field theory based on the local $SU_C(3)$ colour symmetry group, which implies the minimal locally gauge invariant Lagrangian density [63]

$$\begin{aligned}\mathcal{L}_{\mathrm{QCD}} &= -\frac{1}{4}(\partial^\mu G^\nu_a - \partial^\nu G^\mu_a)(\partial_\mu G^a_\nu - \partial_\nu G^a_\mu) + \sum_f \bar{q}^\alpha_f (i\gamma^\mu\partial_\mu - m_f)q^\alpha_f \\ &+ g_s G^\mu_a \sum_f \bar{q}^\alpha_f \gamma_\mu t^a_{\alpha\beta} q^\beta_f \\ &- \frac{g_s}{2} f^{abc}(\partial^\mu G^\nu_a - \partial^\nu G^\mu_a)G^b_\mu G^c_\nu - \frac{g_s^2}{4} f^{abc} f_{ade} G^\mu_b G^\nu_c G^d_\mu G^e_\nu \,, \end{aligned} \tag{2.1}$$

with the quark fields q^α_f (six flavours: $f = u, d, s, c, b, t$, and three colours: $\alpha = r, g, b$), the gluon fields G^μ_a, the unique *strong coupling constant* g_s and the 8 generator matrices of $SU_C(3)$, t^a $(a = 1, \ldots, 8)$ which obey the commutation relations $[t^a, t^b] = i f^{abc} t^c$ with the real, totally antisymmetric structure constants f^{abc}. The tensor $G^{\mu\nu}_a = \partial^\mu G^\nu_a - \partial^\nu G^\mu_a + g_s f^{abc} G^\mu_b G^\nu_c$ gives the strength of the Yang-Mills fields [64]. The first line in Eq. (2.1) contains the kinetic terms for the respective fields; the colour interaction between quarks and gluons is given by the second line and the third line describes the gluon-gluon interaction owing to the non-abelian character of the theory.

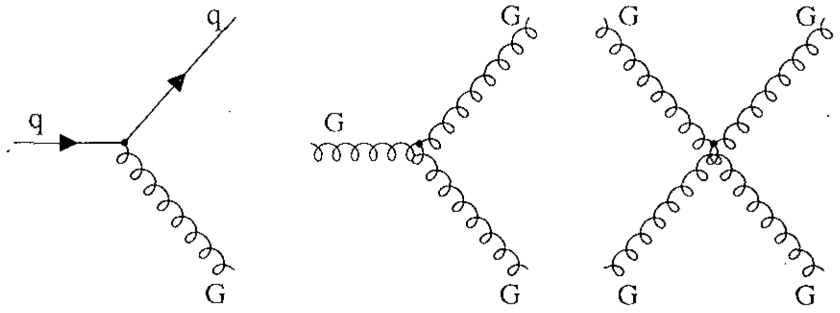

(a) (b) (c)

Figure 2.1: *Elementary vertices of QCD: (a) quark-gluon vertex, (b) triple gluon vertex, and (c) four-gluon vertex.*

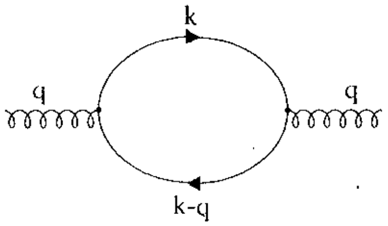

Figure 2.2: *Gluon self-energy diagram corresponding to the correlator Eq.* (2.5).

The above QCD Lagrangian leads to the three elementary vertices shown in Fig. 2.1. The amplitudes for the $q\bar{q}G$ and GGG vertices — Figs. 2.1(a) and (b) — are linear in the coupling g_s, whereas the four-gluon vertex 2.1(c) is proportional to g_s^2. The sum over the possible colour combinations for final state partons yields the following *colour factors*:

$$\mathrm{Tr}\, t^a t^b = T_F \delta^{ab} \implies T_F = \frac{1}{2} \tag{2.2}$$

$$t^a_{\alpha\beta} t^b_{\beta\gamma} = C_F \delta_{\alpha\gamma} \implies C_F = \frac{N_C^2 - 1}{2N_C} = \frac{4}{3} \tag{2.3}$$

$$f^{abc} f^{abd} = C_A \delta^{cd} \implies C_A = N_C = 3 \,, \tag{2.4}$$

where the last identity on the r.h.s. accounts for $SU_C(N_C)$, $N_C = 3$. The colour factors are the eigenvalues of the Casimir operators. They are proportional to the probabilities of the transitions: $G \to q\bar{q}$ (T_F), $q \to qG$ (C_F) and $G \to GG$ (C_A).

2.2 Renormalisation

QCD higher order graphs give rise to divergences which must be regularised. There are two kind of divergences: one, the so-called ultraviolet divergence is due to large integration momenta as can easily be seen in the two-point correlation function [63] of the gluon self energy loop shown in Fig. 2.2:

$$\Pi^{\mu\nu}_{ab} \;=\; i\delta_{ab} g_s^2 T_F \int \frac{d^4k}{(2\pi)^4} \frac{\mathrm{Tr}\left[\gamma^\mu \not{k} \gamma^\nu (\not{k} - \not{q}\right]}{k^2(k-q)^2} \;, \tag{2.5}$$

which diverges as $\int d^4k/k^2 = \infty$. The other one, the infrared divergence, is associated with the small integration momenta in the massless limit. It has been conventional to define the loop integrals through dimensional regularisation [65], where the four dimensional space-time is replaced by $D = 4 + 2\epsilon$. The integration (2.5) can then be performed and the solution is proportional to [63]

$$\left(\frac{-q^2}{4\pi}\right)^{\epsilon} \left(-\frac{1}{\epsilon} - \gamma_{\mathrm{E}} + \mathcal{O}(\epsilon^2)\right) \stackrel{\epsilon \to 0}{=} \mu^{2\epsilon} \left[-\frac{1}{\epsilon} - \gamma_{\mathrm{E}} + \ln 4\pi - \ln(-q^2/\mu^2) + \mathcal{O}(\epsilon)\right] \;. \tag{2.6}$$

where $\gamma_{\mathrm{E}} = 0.57722$ is the Euler constant. The ultraviolet divergence of the loop appears through the pole $1/\epsilon$ for $D \to 4$. Since q^2 has a dimension, an arbitrary energy scale μ^2 is introduced on the r.h.s. of Eq. (2.6) in order to guarantee a dimensionless argument of the logarithm, while of course the expression stays independent of μ. The correlator (2.5) finally reads

$$\begin{aligned} \Pi^{\mu\nu}_{ab} &= \delta_{ab} \left(-q^2 g^{\mu\nu} + q^\mu q^\nu\right) \Pi(q^2) \;, \\ \Pi(q^2) &= -\frac{4}{3} T_F \left(\frac{g_s \mu^\epsilon}{4\pi}\right)^2 \left[\frac{1}{\epsilon} + \gamma_{\mathrm{E}} - \ln 4\pi + \ln(-q^2/\mu^2) - \frac{5}{3} + \mathcal{O}(\epsilon)\right] \end{aligned} \tag{2.7}$$

where the limit $\epsilon \to 0$ defines the counterterms of the regularisation. After fixing $\Pi(q^2)$ at given reference energy $q^2 = \Lambda^2$ (for example through a measurement), one obtains the regularised expression

$$\Pi(q^2) \;=\; \Pi(\Lambda^2) - \frac{4}{3} T_F \left(\frac{g_s}{4\pi}\right)^2 \ln\left(\frac{q^2}{\Lambda^2}\right) \;, \tag{2.8}$$

which governs the evolution of $\Pi(q^2)$. One may now split the self-energy contribution into a meaningless divergent piece $\Pi_\epsilon(\mu^2)$ which does not depend on q^2, and a finite term: $\Pi(q^2) = \Pi_\epsilon(\mu^2) + \Pi_R(q^2/\mu^2)$ [63], where the choice of $\Pi_\epsilon(\mu^2)$ (the renormalisation scheme) is ambiguous and depends on the specific problem. All formulae given in this work refer to the *modified minimal subtraction scheme* ($\overline{\mathrm{MS}}$) [66], defined, *e.g.*, for the diagram of Fig. 2.2 by

$$\Pi_\epsilon(\mu^2) \;=\; -\frac{T_F}{3\pi} \frac{g_s^2}{4\pi} \mu^{2\epsilon} \left(\frac{1}{\epsilon} + \gamma_{\mathrm{E}} - \ln 4\pi\right) \;, \tag{2.9}$$

$$\Pi_R(q^2/\mu^2) \;=\; -\frac{T_F}{3\pi} \frac{g_s^2}{4\pi} \left(\ln(-q^2/\mu^2) - \frac{5}{3}\right) \;. \tag{2.10}$$

The "modification" concerns the constant term $\gamma_{\mathrm{E}} - \ln 4\pi$, which in the minimal subtraction scheme (MS) is kept in the finite term $\Pi_R(q^2/\mu^2)$.

2.2.1 The Renormalisation Group Equations

In a more general way, following the QED pattern, one can say that the subtraction of divergences is equivalent to the renormalisation of the parameters coupling ($\alpha_s \equiv g_s^2/4\pi$), quark mass ($m_q$), etc, and fields in the original bare (superscript B) Lagrangian such as $\alpha_s^B = \mu^{2\epsilon} Z_{\alpha_s} \alpha_s$, $m_q^B = Z_m m_q$, etc. The parameter μ^2 entered through the renormalisation and hence the unrenormalised quantities are independent of μ^2. This leads to the differential *Renormalisation Group Equations* (RGE)

$$\begin{aligned} \mu \frac{\partial \alpha_s}{\partial \mu} &= \beta(\alpha_s)\alpha_s = -\frac{\beta_0}{2\pi}\alpha_s^2 - \frac{\beta_1}{4\pi^2}\alpha_s^3 - \frac{\beta_2}{64\pi^3}\alpha_s^4 - \frac{\beta_3}{128\pi^4}\alpha_s^5 - \ldots , && (2.11) \\ \frac{\mu}{m_q}\frac{\partial m_q}{\partial \mu} &= -\gamma(\alpha_s) . && (2.12) \end{aligned}$$

The solution of Eq. (2.11) including the three-loop level as an expansion of inverse powers of $\ln(\mu^2)$ reads in $\overline{\mathrm{MS}}$ [17]

$$\begin{aligned} \alpha_s(\mu) &= \frac{4\pi}{\beta_0 \ln(\mu^2/\Lambda^2_{\overline{\mathrm{MS}}})}\left\{1 - \frac{2\beta_1}{\beta_0^2}\frac{\ln\left[\ln(\mu^2/\Lambda^2_{\overline{\mathrm{MS}}})\right]}{\ln(\mu^2/\Lambda^2_{\overline{\mathrm{MS}}})} + \frac{4\beta_1^2}{\beta_0^4 \ln^2(\mu^2/\Lambda^2_{\overline{\mathrm{MS}}})}\right. \\ &\qquad \left. \times \left(\left(\ln\left[\ln(\mu^2/\Lambda^2_{\overline{\mathrm{MS}}})\right] - \frac{1}{2}\right)^2 + \frac{\beta_0\beta_2}{8\beta_1^2} - \frac{5}{4}\right)\right\} , && (2.13) \end{aligned}$$

where

$$\begin{aligned} \beta_0 &= 11 - \frac{2}{3}n_f , \\ \beta_1 &= 51 - \frac{19}{3}n_f , \\ \beta_2 &= 2857 - \frac{5033}{9}n_f + \frac{325}{27}n_f^2 , && (2.14) \end{aligned}$$

obtained from the calculation of the corresponding Feynman diagrams. The renormalisation scheme dependent dimensional parameter $\Lambda_{\overline{\mathrm{MS}}}$ enters through the integration of the differential equation (2.11). It is fixed by the starting conditions of the problem, *e.g.*, a measurement of $\alpha_s(\mu)$ at given scale μ. Eq. (2.13) illustrates the asymptotic freedom property of the non-abelian QCD: $\mu \to \infty$ implies $\alpha_s \to 0$. On the other hand, the value of $\alpha_s(\mu)$ diverges for $\mu \to \Lambda_{\overline{\mathrm{MS}}}$ giving rise to non-perturbative quark confinement effects. The evolution of α_s on the basis of the RGE including fourth order β_3 will be discussed in the following paragraph.

As solution of Eq. (2.12) one obtains the running quark masses $m_i(\mu)$, expressed in terms of the scale invariant parameter $\hat{m}_i$ as follows [12]:

$$\begin{aligned} m_i(\mu) &= \hat{m}_i \left(\frac{\beta_0}{2}\frac{\alpha_s(\mu^2)}{\pi}\right)^{2\gamma_0/\beta_0} \left\{1 + \frac{\beta_1}{\beta_0}\left(\frac{\gamma_1}{\beta_1} - \frac{\gamma_0}{\beta_0}\right)\frac{\alpha_s(\mu^2)}{\pi}\right. \\ &+\frac{1}{2}\left[\frac{\beta_1^2}{\beta_0^2}\left(\frac{\gamma_1}{\beta_1} - \frac{\gamma_0}{\beta_0}\right)^2 - \frac{\beta_1^2}{2\beta_0^2}\left(\frac{\gamma_1}{\beta_1} - \frac{\gamma_0}{\beta_0}\right) + \frac{\beta_2}{16\beta_0}\left(\frac{\gamma_2}{\beta_2} - \frac{\gamma_0}{\beta_0}\right)\right]\left(\frac{\alpha_s(\mu^2)}{\pi}\right)^2 \\ &\left. +\mathcal{O}(\alpha_s^3)\right\} && (2.15) \end{aligned}$$

with the γ_i coefficients

$$\begin{aligned}
\gamma_0 &= 2 \\
\gamma_1 &= \frac{101}{6} - \frac{5}{9} n_f \, , \\
\gamma_2 &= \frac{1}{3}\left[3747 - \left(192.3291 + \frac{2216}{27}\right) n_f - \frac{140}{27} n_f^2\right] \, . \qquad (2.16)
\end{aligned}$$

2.2.2 The Evolution of $\alpha_s(\mu)$

One major aim of the QCD analysis with τ data is the precise measurement of α_s at the scale M_τ^2. However, in order to test the compatibility of the result one crucially relies on the evolution $\alpha_s(M_\tau) \longrightarrow \alpha_s(M_Z)$ governed by the RGE (2.11). A difficulty arises from the quark thresholds: as MS schemes employ mass-independent renormalisations, the MS-renormalised QCD coupling α_s does not depend on a particular vertex function. This simplifies the calculation of QCD corrections beyond the one-loop level. On the other hand, decoupling of heavy quarks [67] is not manifest in each order of perturbation theory [68]. A heavy quark decoupling is realized in so-called momentum-space dependent renormalisation schemes (MO). The RGE in a MO scheme involves the scaling-function $\beta_{\rm MO} = \beta(\alpha_s', m_i', a')$ which depends on the coupling $\alpha_s'(\mu)$, the quark masses $m_i'(\mu)$ and a gauge parameter $a'(\mu)$ where the primes denotes the scheme dependence of the parameters. Quark loop calculations in this scheme appear rather complicated, however, the mass dependence of the β-function provides a suppression of heavy-quark effects at scales much smaller than the masses of these quarks, *i.e.*, it decouples heavy quarks from light-particle Green's function to each order in perturbation theory.

To obtain decoupling in MS schemes, one builds in the decoupling region, $\mu \ll m^{(f)}(\mu)$, where $m^{(f)}(\mu)$ is the mass of the heavy-quark with flavour f, an effective field theory that behaves as if only light quarks up to flavour $f-1$ were present. Matching conditions connect the parameters of the low energy effective Lagrangian to the full theory. The coupling constant of the effective theory can then be expressed as a power series of the coupling constant of the full theory with coefficients that depend on $x = \ln(m^{(f)}(\mu)/\mu)$. Doing so one obtains for the matching of α_s and the light quark masses between the "light" flavour $f-1$ and the heavy-quark flavour f [69][1]:

$$\begin{aligned}
\alpha_s^{(f-1)}(\mu) &= \alpha_s^{(f)}(\mu)\left[1 + \frac{x}{6}\frac{\alpha_s^{(f)}(\mu)}{\pi} + \left(\frac{1}{36}x^2 + \frac{11}{24}x + \frac{11}{72}\right)\left(\frac{\alpha_s^{(f)}(\mu)}{\pi}\right)^2\right] \, , \qquad (2.17) \\
m_{f'}^{(f-1)}(\mu) &= m_{f'}^{(f)}(\mu)\left[1 + \frac{1}{12}\left(x^2 + \frac{5}{3}x + \frac{89}{36}\right)\left(\frac{\alpha_s^{(f)}(\mu)}{\pi}\right)^2\right] \, . \qquad (2.18)
\end{aligned}$$

There is no straightforward argument for the choice of the matching scale μ. Keeping in mind the consideration of quark loops makes the setting $\mu = 2m_f$ quite meaningful (see

---

[1] There is a (numerically insignificant) misprint in the original paper by Bernreuther and Wetzel [69]. The coefficient "7/72" of $(\alpha_s^{(f)})^2$ in the matching condition between different active flavours at the quark thresholds must be "11/72" [70, 71].

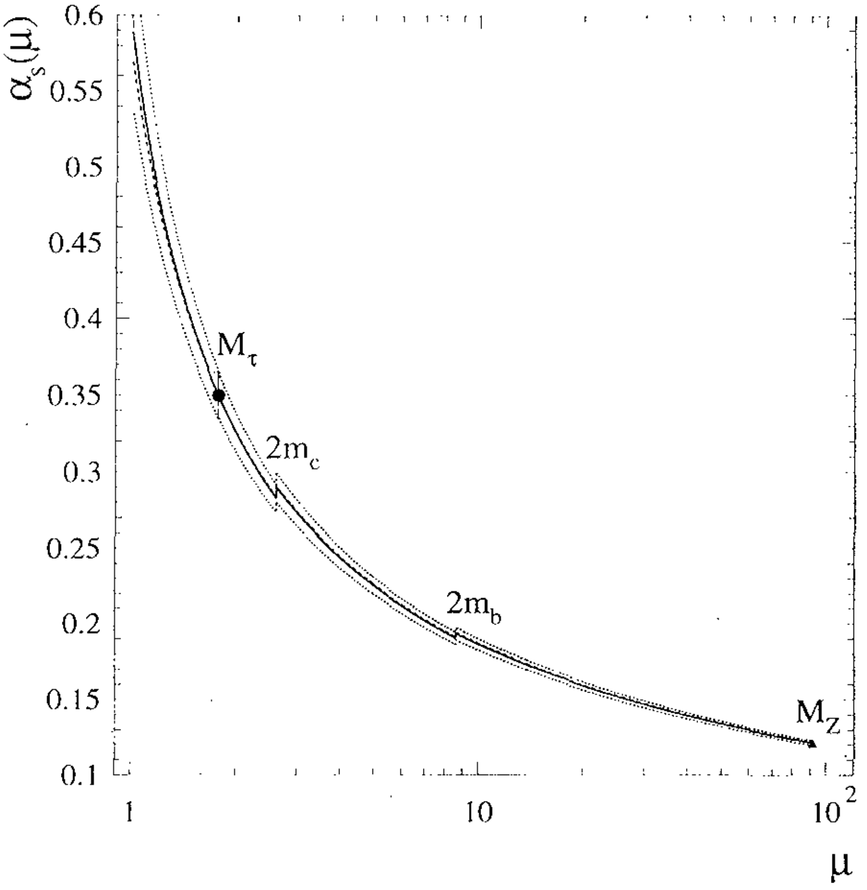

Figure 2.3: *Evolution of typical* $\alpha_s(M_\tau) = 0.350 \pm 0.015$ *to higher and lower energy scales* μ. *The solid line depicts the numerical solution including fourth order* β*-function with error bars (dotted lines). The dashed-dotted line (almost identical with the dashed line) shows the numerical solution to third order only, and the dashed line is the result from the analytical approximation.*

the end of this paragraph for the discussion of the theoretical uncertainties related to this ambiguity).

There exists two different approaches to solve the RGE (2.11). The first deals with an analytical approximation of the exact solution to three loop order which leads to Expression (2.13), whereas the second employs a numerical computation of the differential equation using the CERNLIB routine `DRKSTP` based on Runge-Kutta integration [72] which performs the evolution in infinitesimal steps. Fig. 2.3 depicts the two solutions as a function of μ where both are fixed at $\mu = M_\tau$ to $\alpha_s(M_\tau) = 0.35$. Additionally showed (solid line) is the numerical solution using the four-loop β-function

$$\begin{aligned}\beta_3 &= \left(\frac{149753}{6} + 3564\,\zeta_3\right) - \left(\frac{1078361}{162} + \frac{6508}{27}\zeta_3\right) n_f \\ &\quad + \left(\frac{50065}{162} + \frac{6472}{81}\zeta_3\right) n_f^2 + \frac{1093}{729} n_f^3 \,, \qquad (2.19)\end{aligned}$$

with $\zeta_3 = 1.2020569\ldots$, recently calculated in Ref. [73]. The dotted lines show the errors assuming a typical experimental uncertainty for $\alpha_s(M_\tau)$ of 0.015. All curves are in very good agreement. The difference between the third and fourth order numerical evolution from M_τ to M_Z assuming $\alpha_s(M_\tau) = 0.35$ is $\alpha_s(M_Z)_{3.\,\mathrm{order}} - \alpha_s(M_Z)_{4.\,\mathrm{order}} = 0.00034$ which is negligible compared to typical experimental and theoretical uncertainties in the $\alpha_s(M_Z)$ determination of 0.0020 0.0060.

The major evolution uncertainty left stems from the scale ambiguity of the matching of the quark flavours. The variation of the quark thresholds $m_c = 1.3\ldots2.6$ and $m_b = 4.3\ldots9.6$ yields the systematic evolution error of

$$\Delta^{\mathrm{evol}}\alpha_s(M_Z) \;=\; 0.0010\;. \tag{2.20}$$

2.3 Perturbative and Non-Perturbative QCD

Due to the non-abelian character of QCD, the strong coupling constant α_s diverges at very low energy: starting from the asymptotic side, *i.e.*, at short distances and moving to larger distances where confinement effects become important, asymptotic freedom starts to break down and resonances emerge as a reflection of the fact that quarks and gluons are permanently confined within hadrons. The breakdown of asymptotic freedom, *i.e.*, perturbative QCD, is signalled by the emergence of power corrections due to non-perturbative effects in the QCD vacuum. These are introduced via non-vanishing vacuum expectation values originating from quark and gluon condensation

$$\langle m_j\bar{q}_i q_i\rangle\;, \qquad \langle\frac{\alpha_s}{\pi}GG\rangle\;. \tag{2.21}$$

A very prominent example of non-vanishing quark condensates is given by the physical states ρ (vector) and π/a_1 (axial-vector). The vacuum polarization induced by the corresponding vector and axial-vector currents is degenerated order by order in perturbation theory (neglecting u, d quark masses which is a good approximation). From the dimensional point of view, non-vanishing vacuum expectation values should lead to power corrections compared to the logarithmic behaviour of perturbative contribution [74].

2.3.1 Operator Product Expansion (OPE)

It was the approach of the authors of Ref. [11] to use the OPE in ambivalent energy regions where non-perturbative effects come into play but still perturbative QCD dominates. As shown by the same authors, there exist critical dimensions, *i.e.*, energies at which non-perturbative effects cause OPE to break down. In τ decays, one expects the energy scale of the break down on its best at about 800 MeV where the $\rho(770)$ resonance becomes important.

The OPE of a two-point corelation function $\Pi^{(J)}(s)$ takes the form [12]

$$\Pi^{(J)}(s) \;=\; \sum_{D=0,2,4,\ldots}\frac{1}{(-s)^{D/2}}\sum_{\dim\mathcal{O}=D}C^{(J)}(s,\mu)\langle\mathcal{O}(\mu)\rangle\;, \tag{2.22}$$

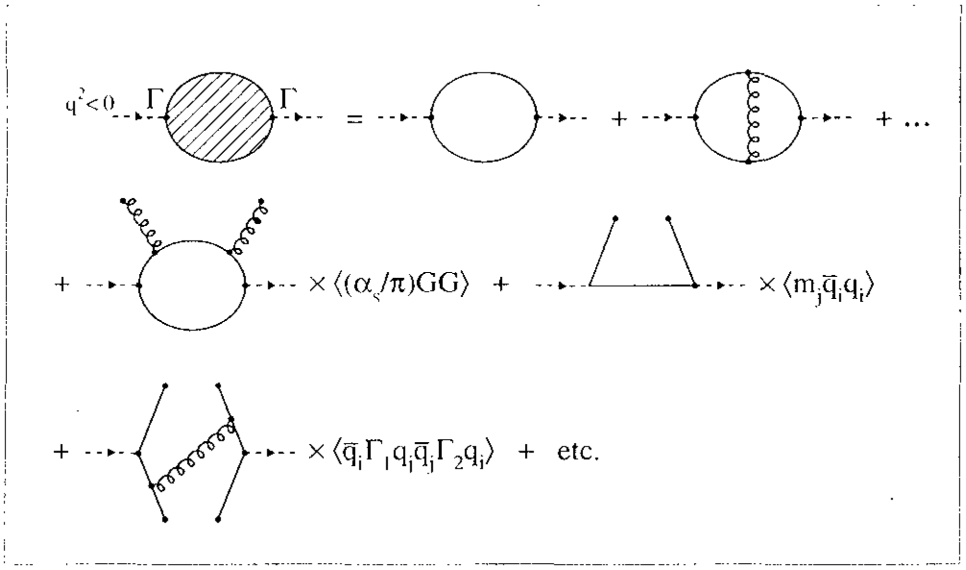

Figure 2.4: *Diagrammatic presentation of the vacuum polarisation for light quarks. The first line depicts the perturbative series (up to first order in α_s shown), the second (third) line gives the $D = 4$ ($D = 6$) non-perturbative contribution, separated in short-distance (loops) and long-distance (vacuum expectation operators) pieces.*

where the inner sum is over the operators of dimension D. The parameter μ is arbitrary. It separates the long-distance non-perturbative effects, absorbed into the vacuum expectation elements $\langle \mathcal{O}(\mu) \rangle$, from the short-distance effects which are included in the Wilson coefficient [75] $C^{(J)}(s, \mu)$. Since the operator $\langle \mathcal{O}(\mu) \rangle$ contains vacuum expectation values, only those with spin zero (scalar) need to be considered: the operator of dimension $D = 0$ is the unit operator (perturbative series). Treating running quark masses as operators classes them as dimension $D = 2$ operators of the form $m_i(\mu) m_j(\mu)$. The first dynamical operators the quark and the gluon condensates (2.21) appear at dimension $D = 4$. They not depend on the separation scale μ. The dominant contribution to the dimension $D = 6$ operators carries non-trivial four-quark dynamical effects of the form $\bar{q}_i \Gamma_1 q_j \bar{q}_k \Gamma_2 q_l$, where Γ is the general current vertex determined by the respective quark current $\bar{q}_i \Gamma q_j$. Additional contributions to $D = 6$ from a mixed quark-gluon condensate as well as a triple gluon condensate are assumed to be small [12]. The strength of the dimension $D = 8$ term is poorly known as it involves a large number of operators. Some of its effects have been studied in Ref. [76].

Fig. 2.4 depicts the diagrams for a two-point vacuum polarisation function for light quarks [74]. The momentum transfer $-q^2$ is large and all propagators in the diagrams which represent the Wilson coefficients carry large momenta while the momenta of the quark and the gluon contributions which disappear into the vacuum go to zero.

2.3.2 The Borel Transformation of Correlators

In order to pick out the lowest resonance (ground state) in a particular channel one can define moments of derivatives of the correlator $\Pi^{(J)}(q^2)$ [11]:

$$M_n^{(J)}(Q_0^2) \;=\; \frac{1}{n!}\left((-)^n \frac{d^n \Pi^{(J)}(Q^2)}{d(Q^2)^n}\bigg|_{Q^2=-Q_0^2}\right) \;=\; \frac{1}{\pi}\int\limits_{s_0}^{\infty} ds\, \frac{\mathrm{Im}\Pi^{(J)}(s)}{(s+Q_0^2)^{n+1}}\;, \tag{2.23}$$

with $Q^2 = -q^2$. The dispersion relation (1.28) is used to obtain the second identity. Inserting a narrow width resonance approximation parametrised through a $\delta(s - M_R^2)$ function as corresponding spectral function into $\mathrm{Im}\Pi^{(J)}(s)$ and taking the ratios of adjacent moments yields for large derivatives n

$$\frac{M_n^{(J)}(Q_0^2)}{M_{n-1}^{(J)}(Q_0^2)} \;\simeq\; (M_R^2 + Q_0^2)^{-1}\;, \tag{2.24}$$

which gives the mass of the lowest resonance.

The use of the moments (2.23) is only valid for heavy quark systems where vacuum condensates are negligible. Applied to light quark systems, higher non-perturbative dimensions come into play. The moments can still be used at large momentum scales Q^2 where all corrections are small. The critical momentum scale of minimum Q^2 increases with the number of derivatives used, *i.e.*, with the projection strength on the lowest resonance. In the limit $Q^2 \to \infty$, $n \to \infty$ and $Q^2/n = M^2$ fixed, the evaluation of the moments is reliable. This corresponds to introducing the Borel transform (also called: Laplace transform [77]) of the correlator $\Pi^{(J)}(Q^2)$ with the Borel parameter M^2 [11]:

$$L_M\Pi^{(J)}(Q^2) \;=\; \lim_{Q^2,n\to\infty} \frac{1}{(n-1)!}(Q^2)^n(-)^n \frac{d^n\Pi^{(J)}(Q^2)}{d(Q^2)^n} \quad \text{with} : Q^2/n = M^2\;, \tag{2.25}$$

which improves OPE as it appears that an operator of dimension D is suppressed by a factor $1/(D/2-1)!$ [74]. Using again the dispersion relation (1.28), one obtains for the Borel transformed correlator

$$L_M\Pi^{(J)}(Q^2) \;=\; \frac{1}{\pi M^2}\int ds\, e^{-s/M^2}\mathrm{Im}\Pi^{(J)}(s)\;, \tag{2.26}$$

where subtractions cancel in the derivatives.

The Borel transform of correlators is a powerful tool to improve the convergence (saturation) of the integral (2.26). This is of particular importance as experiments cover only limited energy regions. The feasibility of QCD checks on the basis of finite energy dispersion relations using spectral functions or e^+e^- cross sections from the experiment depends therefore crucially on the saturation of the dispersion integral. A second important point, specifically related to τ data, is the higher quality of τ spectral functions at lower mass-squared owing to the phase space suppression factor which limits statistics at high masses. The Borel transformation improves significantly the precision of the measurement of so-called *chiral sum rules* (see following section) which involve $V-A$ spectral functions from τ decays.

2.4 Chiral Symmetry and QCD Sum Rules

In the limit of n_f massless quarks ($m_i = 0$, $i = u, d, \ldots$), the QCD Lagrangian (2.1) possesses a global $SU_L(n_f) \times SU_R(n_f)$ chiral symmetry between the left- and right-handed quarks in flavour space. The associated Noether currents (from Noether's theorem: every symmetry-transformation of a field theory implies a conserved current) are the vector (V^μ) and axial-vector (A^μ) quark currents [78]. The vector and axial-vector charges

$$Q_{V/A} = \int d^3x \, V^0/A^0(x) \; . \tag{2.27}$$

are the generators of the symmetry group. For a state $|\phi\rangle$ which is symmetric under $SU(3)_L \times SU(3)_R$ one then must have [79][2]

$$\langle\phi|A^a_\mu(x)A^b_\mu(y)|\phi\rangle = \langle\phi|V^a_\mu(x)V^b_\mu(y)|\phi\rangle \qquad (a, b =, 1, \ldots, 8) \; , \tag{2.28}$$

which requires that for every contribution on the r.h.s. of Eq. (2.28) ($J^P = 0^+$ or 1^-) there exists a mass degenerate partner on the l.h.s. ($J^P = 0^-$ or 1^+). However, chiral symmetry which should be a good symmetry for the light u, d, s quarks is not observed in the low energy hadronic spectra of e^+e^- annihilation or τ spectral functions. In order to be consistent with this experimental fact, the chiral flavour group $SU(3)_L \times SU(3)_R$ is assumed to be spontaneously broken by non-vanishing light quark masses down to $SU(3)_{L+R}$ where the vacuum expectation values are symmetrical:

$$\langle m\,\bar{u}u\rangle = \langle m\,\bar{d}d\rangle = \langle m\,\bar{s}s\rangle \neq 0 \; . \tag{2.29}$$

Goldstone's theorem states [80]: if a generator T^a of the symmetry group produces non-zero vacuum expectation values, the physically state $T^a|0\rangle$ (which must exist) is a massless scalar, if T^a is a vector charge; it is a massless pseudoscalar, if T^a is an axial-vector charge.

The spontaneously symmetry breaking of the axial charge generates an octet of massless pseudoscalar mesons which is identified with the 8 lightest hadronic states: π^+, π^0, π^-, η, K$^+$, K$^-$, K^0 and $\bar{\text{K}}^0$. In this case, the axial-vector current is non-conserved and its divergence reads:

$$\partial_\mu A^\mu_{ij} = (m_i + m_j)\bar{q}_i(i\gamma_5)q_j \; , \tag{2.30}$$

associated with the decay constant f_P of a pseudoscalar meson P with four momentum q_μ, defined as:

$$\langle 0|\partial_\mu A^\mu_P|P\rangle = \sqrt{2}f_P m_P^2 \qquad \text{or} : \quad \langle 0|A^\mu_P|P\rangle = \sqrt{2}f_P q^\mu . \tag{2.31}$$

The non-vanishing physical masses of the pseudoscalars reflect the fact that QCD is not really a chiral theory. True zero u, d, s quark masses would generate massless pseudoscalar mesons. Explicit mass formulae for the pseudoscalars can be deduced from Chiral Perturbation Theory (ChPT) which is, in principle, a perturbative expansion in powers of

---

[2] The conserved right- ($R = V + A$) and left-handed ($L = V - A$) currents under $SU(3)_L \times SU(3)_R$ transform like ($\underline{8}$, $\underline{1}$) and ($\underline{1}$, $\underline{8}$), respectively. If $|\phi\rangle$ is invariant then $\langle\phi|RL|\phi\rangle = 0 \Rightarrow \langle\phi|V^2 - A^2|\phi\rangle = 0$ which is Eq. (2.28).

quark masses (for an introduction see, *e.g.*, Ref. [81]). Such formulae carry direct proportionalities to the quark masses (not including electromagnetic mass symmetry breaking):

$$
\begin{aligned}
m_{\pi^\pm}^2 &\sim m_u + m_d \;, \\
m_{\pi^0}^2 &\sim m_u + m_d - \mathcal{O}\left(\frac{(m_u+m_d)^2}{m_s-(m_u-m_d)/2}\right) \;, \\
m_{\mathrm{K}^\pm}^2 &\sim m_u + m_s \;, \\
m_{\mathrm{K}^0}^2 &\sim m_d + m_s \;, \\
m_{\eta^0}^2 &\sim m_u + m_d + 4m_s + \mathcal{O}\left(\frac{(m_u+m_d)^2}{m_s-(m_u-m_d)/2}\right) \;.
\end{aligned}
\qquad (2.32)
$$

There is no indication of spontaneously symmetry breaking of the vector charge (the vector charge operators "annihilate" the vacuum): no light scalars have been found experimentally, vector mesons can well be classified in degenerate multiplets which are $SU(3)_V$ representations. The longitudinal part of the vector correlator in Eq. (1.26) then vanishes: $\Pi^{(0)}_{ij,V}(q^2) = 0$.

2.4.1 Spectral Sum Rules

Reducing chiral symmetry to the non-strange sector, *i.e.*, $SU(2)_L \times SU(2)_R$, one has the two-point correlator [78]

$$
\begin{aligned}
\Pi^{\mu\nu}_{\bar{u}d,LR}(q) &= i\int d^4x\, e^{iqx}\langle 0|T(L^\mu(x)R^\nu(0)^\dagger)|0\rangle \\
&= (-g^{\mu\nu}q^2 + q^\mu q^\nu)\,\Pi^{(1)}_{\bar{u}d,LR}(q^2) \;+\; q^\mu q^\nu\,\Pi^{(0)}_{\bar{u}d,LR}(q^2) \;,
\end{aligned}
\qquad (2.33)
$$

where L^μ and R^μ are the left and right-handed quark currents

$$
L^\mu \;=\; \bar{u}\gamma^\mu(1-\gamma_5)d \;, \qquad R^\mu \;=\; \bar{u}\gamma^\mu(1+\gamma_5)d \;. \qquad (2.34)
$$

With Eqs. (2.33), (2.34) and the correlators for vector and axial-vector currents (1.26) one identifies

$$
\Pi^{\mu\nu}_{\bar{u}d,LR}(q) \;=\; \Pi^{\mu\nu}_{\bar{u}d,V}(q) \;-\; \Pi^{\mu\nu}_{\bar{u}d,A}(q) \;. \qquad (2.35)
$$

The correlator $\Pi^{\mu\nu}_{\bar{u}d,LR}(q)$ vanishes in the chiral or in the asymptotic $q^2 \to \infty$ limits (which again implies the degeneracy of Eq. (2.28)). Using the dispersion relation (1.28) one obtains the two famous Weinberg sum rules (WSR) [7, 78] for u, d quark correlators from the comparison of the $q^\mu q^\nu$ and the q^2 terms in Eq. (2.33):

$$
\text{1. WSR :} \quad \int\limits_0^\infty ds\, \mathrm{Im}\left[\Pi^{(1)}_{\bar{u}d,V}(s) - \Pi^{(1)}_{\bar{u}d,A}(s) + \Pi^{(0)}_{\bar{u}d,V}(s) - \Pi^{(0)}_{\bar{u}d,A}(s)\right] \;=\; 0 \;; \qquad (2.36)
$$

$$
\text{2. WSR :} \quad \int\limits_0^\infty ds\, s\, \mathrm{Im}\left[\Pi^{(1)}_{\bar{u}d,V}(s) - \Pi^{(1)}_{\bar{u}d,A}(s)\right] \;=\; 0 \;. \qquad (2.37)
$$

The first WSR can be simplified using the pion decay constant f_π defined in Eq. (2.31) which fixes the integral $\int_0^\infty ds\, \mathrm{Im}\Pi^{(0)}_{\bar{u}d,A}(s) = f_\pi^2$, and the fact the longitudinal vector correlator vanishes. When switching quark masses on, only the first WSR remains valid while the second WSR breaks down due to contributions from the difference of non-conserved vector and axial-vector currents of order m_q^2/s, leading to a quadratic divergence of the integral [77]. However, convergence can be recovered by considering a Borel transformed version of the second WSR where the result is expressed as a function of the Borel parameter M^2 and the u, d running quark masses at scale M^2 and quark condensates in powers of $1/M^0$, $1/M^2$, ... [77, 11, 82].

Assuming narrow-width approximation for the resonances and a saturation of the corresponding vector, axial-vector spectral functions by the π, $\rho(770)$ and $a_1(1260)$, Weinberg deduced from his sum rules the mass formula [7]

$$M_{a_1}/M_\rho \simeq 1.41 , \qquad (2.38)$$

which is not so bad compared to $M_{a_1}/M_\rho = 1.60 \pm 0.05$ [17] and keeping in mind the coarseness of the approximations used.

Das, Mathur and Okubo (DMO) [6] showed that the derivative of the vector minus axial-vector correlator $\Pi_{\bar{u}d,V-A}(q^2)$ taken at $q^2 = 0$ is connected with the radiative $\pi^- \to \ell^- \bar{\nu}_\ell \gamma$ decay axial-vector form factor F_A via

$$\left.\frac{d(q^2\Pi_{\bar{u}d,V-A}(q^2))}{dq^2}\right|_{q^2=0} = \int\limits_0^\infty \frac{ds}{s} \,\mathrm{Im}\left[\Pi^{(1)}_{\bar{u}d,V}(s) - \Pi^{(1)}_{\bar{u}d,A}(s)\right] = f_\pi^2 \frac{\langle r_\pi^2 \rangle}{3} - F_A . \qquad (2.39)$$

This relation will be used in Section 10.1.1 in order to perform a finite energy determination of F_A and the polarisability of the pion.

The electromagnetic mass difference has been calculated using current algebra techniques in chiral symmetry by Das *et al.* [83]. They obtained the sum rule

$$m^2_{\pi^\pm} - m^2_{\pi^0} = \frac{12\pi\alpha}{i f_\pi^2} \int \frac{d^4q}{(2\pi)^4} \frac{1}{q^2} \int\limits_0^\infty ds\, s \,\frac{\mathrm{Im}\left[\Pi^{(1)}_{\bar{u}d,V}(s) - \Pi^{(1)}_{\bar{u}d,A}(s)\right]}{q^2 + s - i\epsilon} \qquad (2.40)$$

and, making use of the KSFR relation [84] and lowest resonance saturation, related from it

$$m^2_{\pi^\pm} - m^2_{\pi^0} = \frac{3\alpha M_\rho^2 \ln 2}{4\pi m_\pi} = 5.1 \text{ MeV}/c^2 , \qquad (2.41)$$

in astonishing agreement with the experimental value of 4.59 MeV/c^2 [17].

Useful relations between the OPE terms and the spectral functions are obtained from projective sum rules [85]: conservation of currents in the chiral limit implies ($Q^2 = -q^2$) $Q^2\left[\Pi^{(1)}_{\bar{u}d,V}(-Q^2) - \Pi^{(1)}_{\bar{u}d,A}(-Q^2)\right] = 0$ in momentum space. For large space-like momenta Q^2 one can expand the dispersion relation of the $V - A$ correlator. By virtue of the first and the second WSR one obtains

$$\frac{1}{\pi}\int\limits_0^\infty ds \,\mathrm{Im}\left[\Pi^{(1)}_{\bar{u}d,V}(s) - \Pi^{(1)}_{\bar{u}d,A}(s)\right]\left[\frac{1}{s+Q^2} - \left(\frac{s^2}{Q^6} - \frac{s^3}{Q^8} + \ldots\right)\right] \simeq 0 . \qquad (2.42)$$

On the other hand, non-perturbative effects violate the current conservation giving rise to non-perturbative OPE contributions

$$\Pi^{(1)}_{\bar{u}d,V}(-Q^2) - \Pi^{(1)}_{\bar{u}d,A}(-Q^2) \;=\; \sum_{D=2,4,\ldots} C_D(\mu)\frac{\langle \mathcal{O}_D(\mu)\rangle}{Q^D} \;. \tag{2.43}$$

Comparing the coefficients of the corresponding powers between Eqs. (2.42) and (2.43) yields the sum rules

$$\begin{aligned}
C_6(\mu)\langle \mathcal{O}_6(\mu)\rangle &= \frac{1}{\pi}\int\limits_0^\infty ds\, s^2\,\mathrm{Im}\left(\Pi^{(1)}_{\bar{u}d,V}(q) - \Pi^{(1)}_{\bar{u}d,A}(s)\right)\\
C_8(\mu)\langle \mathcal{O}_8(\mu)\rangle &= -\frac{1}{\pi}\int\limits_0^\infty ds\, s^3\,\mathrm{Im}\left(\Pi^{(1)}_{\bar{u}d,V}(q) - \Pi^{(1)}_{\bar{u}d,A}(s)\right) \;.
\end{aligned} \tag{2.44}$$

2.5 QCD and τ Decays

Tests of Quantum Chromodynamics and the precise measurement of the strong coupling constant α_s at the τ mass scale carried out for the first time by the ALEPH [8, 10] and CLEO [9] Collaborations have been the subject of vivid discussions about theoretical and experimental implications, accompanied by a considerable number of interesting publications (see, *e.g.*, [13, 86, 51, 87, 88, 89]). Following the line traced by the pioneering work of Braaten, Narison and Pich [12], the theoretical framework of the QCD analysis used to measure α_s and to get information about the behaviour of non-perturbative power corrections at M_τ is presented in this section.

It is the inclusive character of hadronic τ decays which opens them for a wide range of interesting studies. Inclusive observables, primarily the total hadronic τ decay rate

$$R_\tau \;=\; \frac{\Gamma(\tau^- \to \text{hadrons}\,\nu_\tau(\gamma))}{\Gamma(\tau^- \to e^-\bar{\nu}_e\nu_\tau(\gamma))} \tag{2.45}$$

are accurately predictable as functions of $\alpha_s(M_\tau)$ using perturbative QCD and the OPE in order to take into account non-perturbative corrections. In fact, one can even say that R_τ is a doubly inclusive observable as it is integrated over all hadronic final states at a given invariant mass and integrated over all masses between m_π and M_τ. In addition, due to its vector and axial-vector decay modes with equal coupling constants, R_τ is even more inclusive than e^+e^- inclusive $I = 0, 1$ final states. It will be learned from this analysis that M_τ lies in a compromise region where $\alpha_s(M_\tau)$ is large enough that R_τ is sensitive to its value, yet still small enough that the perturbative expansions in powers of $\alpha_s(M_\tau)$ converges safely and, in particular, non-perturbative power terms are either small or, when in cases where it is not negligible, the OPE is well behaved.

Experimentally, the most precise value of R_τ is obtained by measuring the leptonic branching ratios, additionally constrained via universality (see Section 1.2.4), using the ingredient that electronic (B_e), muonic and hadronic branching ratios saturate τ decays.

That gives

$$R_\tau = \frac{1}{B_e} - 1 - 0.97257 \ , \tag{2.46}$$

and $\Delta R_\tau = \Delta B_e / B_e^2$. With (1.13) one obtains

$$R_\tau = 3.649 \pm 0.014 \ . \tag{2.47}$$

If strong and electroweak radiative corrections are neglected, the theoretical parton level prediction for $SU_C(N_C)$, $N_C = 3$ reads

$$R_\tau = N_C \left(|V_{ud}|^2 + |V_{us}|^2 \right) \simeq 3 \ , \tag{2.48}$$

from which the contribution to the experimental value of R_τ (2.47) from strong perturbative corrections in Eq. (2.47) is estimated to be about 21%, assuming other sources to be small. One realizes the important increase of sensitivity to α_s compared to the Z hadronic width where due essentially to the three times smaller $\alpha_s(M_Z)$ the perturbative QCD correction reaches only about 4% (see Eq. (2.90) in Section 2.6).

The inclusive observable R_τ can theoretically be separated into contributions from specific quark currents, namely vector (V) and axial vector (A) $\bar{u}d$- and $\bar{u}s$-quark currents. It will not be attempted in the framework of this analysis to separate strange (S) final states into vector and axial-vector components. Some effort in this direction has nevertheless already been undertaken in Ref. [90]. It is therefore appropriate to decompose:

$$R_\tau = R_{\tau,V} + R_{\tau,A} + R_{\tau,S} \ . \tag{2.49}$$

As seen in Section 2.3, parton level and perturbative prediction do not distinguish vector and axial-vector currents. Thus the corresponding naive predictions become $R_{\tau,V/A} = (N_C/2)|V_{ud}|^2$ and $R_{\tau,S} = N_C|V_{us}|^2$, which add up to Eq. (2.48).

A crucial issue of the QCD analysis at the τ mass scale concerns the reliability of the theoretical description, *i.e.*, the OPE ansatz, and the stability against unknown contributions. A reasonable test can be achieved by continuously varying M_τ to lower values $\sqrt{s_0} \le M_\tau$ for both theoretical prediction and measurement. The kinematical factor which describes the τ phase space suppression at masses near to M_τ is correspondingly modified in order that $\sqrt{s_0}$ represents the new mass of the τ. All formulae of the following theoretical sections are consequently expressed as functions of s_0.

2.5.1 Theoretical Prediction of R_τ

According to Eq. (1.27) the imaginary part of the vector and axial-vector two-point correlators (1.26), where the subscripts $i(j)$ denote light quark flavours $u(d, s)$, are proportional to the τ hadronic spectral functions with corresponding quantum numbers. The hadronic τ decay rate can be written as an integral of these spectral functions over the invariant mass-squared s of the final state hadrons [12][3]:

$$R_\tau(s_0) \;=\; 12\pi S_{\rm EW} \int\limits_0^{s_0} \frac{ds}{s_0}\left(1-\frac{s}{s_0}\right)^2 \left[\left(1+2\frac{s}{s_0}\right){\rm Im}\Pi^{(1)}(s+i\epsilon) \;+\; {\rm Im}\Pi^{(0)}(s+i\epsilon)\right] \,, \tag{2.50}$$

with the electroweak radiative correction factor $S_{\rm EW}$ (see Section 1.3.2) and the correlator combinations according to the decomposition (2.49)

$$\Pi^{(J)} \;=\; |V_{ud}|^2\left(\Pi^{(J)}_{ud,V}+\Pi^{(J)}_{ud,A}\right) \;+\; |V_{us}|^2\Pi^{(J)}_{us,V+A}\,. \tag{2.51}$$

Unfortunately, the above integral involves large non-perturbative (resonance) effects at very low energies that certainly will invalidate the OPE approach used here. None the less, the analyticity property of the correlator $\Pi^{(J)}$ allows the evaluation of the integral (2.50). The dispersion relation (1.28) elucidates that indeed $\Pi^{(J)}$ is analytic in the complex s plane everywhere except on the positive real axis where singularities exist. According to Cauchy's integral formula, an integral over s along the closed contour of the product of $\Pi^{(J)}$ with a non-singular function $g(s)$ vanishes. On the other hand, the imaginary part of the correlator is proportional to the discontinuity across the positive real axis. So the following relation holds

$$\frac{1}{\pi}\int\limits_0^{s_0} ds\, g(s){\rm Im}\Pi(s) \;=\; -\frac{1}{2\pi i}\oint\limits_{|s|=s_0} ds\, g(s)\Pi(s)\,, \tag{2.52}$$

where the contour integral runs counter-clockwise around the circle from $s=s_0-i\epsilon$ to $s=s_0+i\epsilon$ as indicated in Fig. 2.5. The integral (2.50) then reads

$$R_\tau(s_0) \;=\; 6\pi i\, S_{\rm EW}\oint\limits_{|s|=s_0}\frac{ds}{s_0}\left(1-\frac{s}{s_0}\right)^2\left[\left(1+2\frac{s}{s_0}\right)\Pi^{(1)}(s) \;+\; \Pi^{(0)}(s)\right]\,. \tag{2.53}$$

The energy scale s_0 of the contour in Eq. (2.53) for $s_0 \simeq M_\tau^2$ is large enough to expect small contributions from non-perturbative effects. One can therefore use the OPE introduced in Section 2.3.1 to disentangle perturbative and non-perturbative contributions to $R_\tau(s_0)$. Note that the factor $(1-s/s_0)^2$ suppresses the contribution from the region near the positive real axis where $\Pi(s)$ has a branch cut and OPE validity is restricted [91]. In order to avoid large logarithms of the form $\ln(-s/\mu^2)$, where μ is the separation scale for short- and long-distance contributions expressed in the Wilson coefficients $C(s,\mu)^{(J)}$ and the operators $\langle\mathcal{O}(\mu)\rangle$, one chooses appropriately $\mu^2=s_0$.

The theoretical prediction of the vector and axial-vector as well as the strange hadronic

---

[3] The parametrisation of the s_0 dependence used here differs from the one introduced in Ref. [13]. While in that work the actual τ mass remains unchanged and only the integration range is varied for $\sqrt{s_0}\le M_\tau$, here the mass of the τ is indeed redefined to be $\sqrt{s_0}$. Leaving the τ mass unchanged keeps the $1/M_\tau^D$ power in the OPE while, in the definition adopted in this work, it becomes $1/s_0^{D/2}$ and therefore more important when evolving s_0 to lower values.

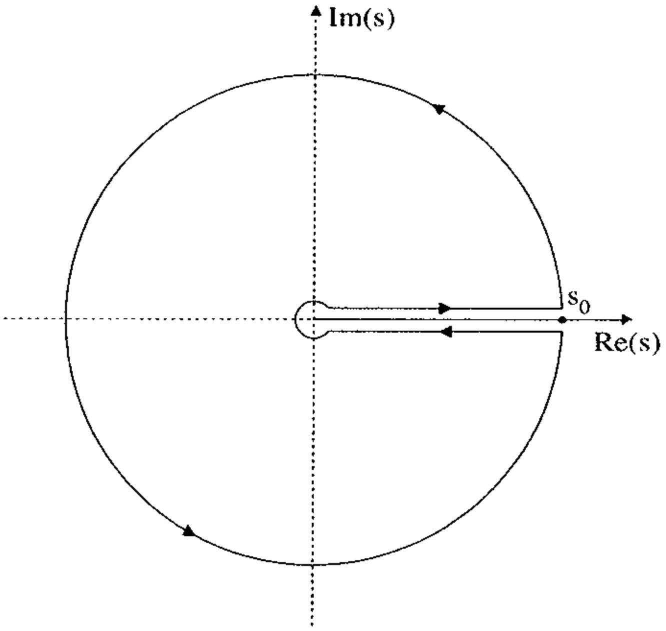

Figure 2.5: *Integration contour followed when performing the integrations of Eqs.* (2.52) *and* (2.53).

widths can now be written as:

$$R_{\tau,V/A} = \frac{3}{2}|V_{ud}|^2 S_{\mathrm{EW}} \left(1 + \delta^{(0)} + \delta'_{\mathrm{EW}} + \delta^{(2-\mathrm{mass})}_{ud,V/A} + \sum_{D=4,6,\ldots} \delta^{(D)}_{ud,V/A}\right) , \qquad (2.54)$$

$$R_{\tau,S} = 3|V_{us}|^2 S_{\mathrm{EW}} \left(1 + \delta^{(0)} + \delta'_{\mathrm{EW}} + +\delta^{(2-\mathrm{mass})}_{us,V+A} \sum_{D=4,6,\ldots} \delta^{(D)}_{us,V+A}\right) , \qquad (2.55)$$

with the residual non-logarithmic electroweak correction $\delta'_{\mathrm{EW}} = 0.0010$ [45] introduced in Section 1.3.2 and the only $D = 2$ contribution $\delta^{(2-\mathrm{mass})}_{ij,V/A}$ from quark masses which is tiny for u, d quarks ($< 0.2\%$). The term $\delta^{(0)}$ is the purely perturbative contribution, while the $\delta^{(D)}$ are the OPE terms in powers of ${s_0}^{-D/2}$. Insertion of the OPE (2.22) in Eq. (2.53) leads to

$$\delta^{(D)}_{ij,V/A} = \sum_{\dim\mathcal{O}=D} \langle\mathcal{O}(\mu)\rangle \, 4\pi i \oint_{|s|=s_0} \frac{ds}{s_0} (-s)^{-D/2} \left(1 - \frac{s}{s_0}\right)^2$$
$$\times \left[\left(1 + 2\frac{s}{s_0}\right) C^{(1)}_{D,ij,V/A}(s,\mu) + C^{(0)}_{D,ij,V/A}(s,\mu)\right] . \qquad (2.56)$$

Setting $\mu^2 = s_0$ expresses the above contour integral as purely a function of the running α_s. Taking now the chiral limit, and neglecting higher order powers in $\alpha_s^{n\geq 2}$ and the logarithmic s dependence of the Wilson coefficients (through the running $\alpha_s(s)$), only dimensions $D = 2, 6, 8$ non-perturbative operators contribute to $R_\tau(s_0)$:

$$\delta^{(D)}_{ij,V/A} = \left[\sum_{\dim\mathcal{O}=\mathrm{D}} \frac{C^{(0+1)}_{V/A}\langle\mathcal{O}\rangle}{s_0^{D/2}}\right] 4\pi \int\limits_{-\pi}^{\pi} d\varphi \left(e^{i(1-D/2)\varphi} - 3e^{i(3-D/2)\varphi} - 2e^{i(4-D/2)\varphi}\right) , \quad (2.57)$$

which is non-zero for $D = 2, 6, 8$. The $D = 2$ quark mass term vanishes in the chiral limit. Nevertheless, anomalous $D = 2$ contributions, not foreseen in the SVZ approach, are not excluded here. The conservation of vector and axial-vector currents in the chiral limit implies $s\Pi^{(0)}_{ij,V}(s) = s\Pi^{(0)}_{ij,A}(s) = 0$ in momentum space. Thus only the $\Pi^{(0+1)}$ term in Eq. (2.57) remains.

2.5.2 Perturbative Prediction

The description of the perturbative prediction follows essentially Ref. [86]. It will be shown that perturbative QCD which appears as a power series in $(\alpha_s(s_0)/\pi)^n$ up to three loops ($n = 3$) provides by far the numerically dominant contribution to $R_\tau(s_0)$. The perturbative contribution is given in the chiral limit. Quark mass effects have been calculated in Ref. [92] and are found to be well below 1%. Thus the contributions from vector and axial-vector currents coincide to any given order of perturbation theory and the results are flavour independent.

For the evaluation of the perturbative series, it is convenient to introduce the Adler function [93] ($Q^2 = -q^2$)

$$D(Q^2) \equiv -Q^2\frac{d\Pi(Q^2)}{dQ^2} = Q^2\int\limits_0^\infty ds\,\frac{\mathrm{Im}\Pi(s)}{(s+Q^2)^2} , \quad (2.58)$$

where the second identity follows from the dispersion relation (1.28). Here, the derivative avoids annoying extra subtractions (renormalisation) on the r.h.s. of Eq. (2.58) which are unrelated to QCD dynamics. The function $D(Q^2)$ calculated in perturbative QCD within the $\overline{\mathrm{MS}}$ renormalisation scheme depends on the non-physical parameter μ occurring as $\ln(\mu^2/Q^2)$. Furthermore it appears as a function of α_s. On the other hand, since $D(Q^2)$ is connected to a physical quantity — the spectral function $\mathrm{Im}\Pi(s)$ —, it cannot depend on the subjective choice of μ. This can be achieved if α_s becomes a function of μ providing independence of $D(Q^2)$ of the choice of μ. Nevertheless, in a truncated series (as it is the case here), the μ dependence remains. $D(Q^2)$ is then a function of $D(\mu^2/Q^2, \alpha_s)$ and obeys the RGE. Choosing $\mu^2 = Q^2$, its solution is expressed in the form

$$D(\alpha_s(Q)) = \sum_{n=0}^{\infty} R_n \left(\frac{\alpha_s(Q)}{\pi}\right)^n . \quad (2.59)$$

with renormalisation scheme dependent coefficients R_n.

To introduce the Adler function in Eq. (2.53) one uses the identity

$$\oint\limits_{|s|=s_0} ds\, g(s)\Pi(s) = -\oint\limits_{|s|=s_0} \frac{ds}{s}\left(G(s) - G(s_0)\right) s\frac{d\Pi(s)}{ds} , \quad (2.60)$$

with the kernel $g(s) = (1 - s/s_0)^2(1 + 2s/s_0)/s_0$ and $G(s) = \int_0^s ds'\, g(s')$. With (2.60) the perturbative contribution from Expression (2.53) and (2.54) becomes [86]

$$1 + \delta^{(0)} = -2\pi i \oint\limits_{|s|=s_0} \frac{ds}{s} \left[1 - 2\frac{s}{s_0} + 2\left(\frac{s}{s_0}\right)^3 - \left(\frac{s}{s_0}\right)^4\right] D(s) . \tag{2.61}$$

The perturbative expansion of the Adler function can be inferred from the three loop calculation of the e^+e^- inclusive cross section ratio $R_{e^+e^-}(s) = \sigma(e^+e^- \to \text{hadrons}\,(\gamma))/\sigma(e^+e^- \to \mu^+\mu^-\,(\gamma))$ performed in Ref. [94] (two-loop) and Ref. [95] (three-loop). One then obtains [86]

$$D(s) = \frac{1}{4\pi^2} \sum_{n=0}^{\infty} \tilde{K}_n(\xi) \left(\frac{\alpha_s(-\xi^2 s)}{\pi}\right)^n , \tag{2.62}$$

with the $\tilde{K}_n(\xi)$ functions

$$\begin{aligned} \tilde{K}_0(\xi) &= K_0 , \\ \tilde{K}_1(\xi) &= K_1 , \\ \tilde{K}_2(\xi) &= K_2 + \frac{1}{2} K_1 \beta_0 \ln\xi , \\ \tilde{K}_3(\xi) &= K_3 + K_2\beta_0 \ln\xi + \frac{1}{4} K_1 \left(\beta_0^2 \ln^2\xi + \beta_1 \ln\xi\right) , \end{aligned} \tag{2.63}$$

and the first elements of the β-function defined in Eq. (2.11). The factor ξ in Eq (2.62) represents the renormalisation scale ambiguity and is therefore arbitrary to some extent. The coefficients K_n are known up to three-loop order α_s^3. For $n \geq 2$ they depend on the renormalisation scheme used:

$$\begin{aligned} K_0 &= 1 , \\ K_1 &= 1 , \\ K_2(\overline{\text{MS}}) &= F_3(\overline{\text{MS}}) , \\ K_3(\overline{\text{MS}}) &= F_4(\overline{\text{MS}}) + \frac{1}{48}\pi^2\beta_0^2 , \end{aligned} \tag{2.64}$$

with

$$\begin{aligned} F_3(\overline{\text{MS}}) &= 1.9857 - 0.1153\, n_f , \\ F_4(\overline{\text{MS}}) &= -6.6368 - 1.2001\, n_f - 0.0052\, n_f^2 , \end{aligned} \tag{2.65}$$

being the coefficients of the perturbative series of $R_{e^+e^-}$. The expansion (2.62) inserted in the r.h.s of Eq. (2.61) yields for the known orders in α_s

$$\delta^{(0)} = \sum_{n=1}^{3} \tilde{K}_n(\xi) A^{(n)}(\alpha_s) , \tag{2.66}$$

where the functions

$$A^{(n)}(\alpha_s) = \frac{1}{2\pi i} \oint\limits_{|s|=s_0} \frac{ds}{s} \left[1 - 2\frac{s}{s_0} + 2\left(\frac{s}{s_0}\right)^3 - \left(\frac{s}{s_0}\right)^4\right] \left(\frac{\alpha_s(-\xi^2 s)}{\pi}\right)^n \tag{2.67}$$

are integrals in the complex s-plane with an integration contour according to Fig. 2.5. The strong coupling constant in the vicinity of s_0 can be expanded in powers of $\alpha_s(s_0)$, with coefficients that are polynomials in $\ln(s/s_0)$ [12]

$$\begin{aligned}\frac{\alpha_s(s)}{\pi} &= \frac{\alpha_s(s_0)}{\pi} - \frac{1}{4}\beta_0 \ln\frac{s}{s_0}\left(\frac{\alpha_s(s)}{\pi}\right)^2 - \left(\frac{1}{8}\beta_1 \ln\frac{s}{s_0} - \frac{1}{16}\beta_0^2 \ln^2\frac{s}{s_0}\right)\left(\frac{\alpha_s(s)}{\pi}\right)^3 \\ &\quad - \left(\frac{1}{128}\beta_2 \ln\frac{s}{s_0} - \frac{5}{64}\beta_0\beta_1 \ln^2\frac{s}{s_0} + \frac{1}{64}\beta_0^3 \ln^3\frac{s}{s_0}\right)\left(\frac{\alpha_s(s)}{\pi}\right)^4 + \ldots \qquad (2.68)\end{aligned}$$

Inserting the series in Eq (2.66) leads to the expression

$$\delta_{\mathrm{E}}^{(0)} = \sum_{n=1}^{4}\left[\tilde{K}_n(\xi) + g_n(\xi)\right]\left(\frac{\alpha_s(\xi^2 s_0)}{\pi}\right)^n , \qquad (2.69)$$

where the g_n are functions of $\tilde{K}_{m<n}$ and of elementary integrals with logarithms of power $m < n$ in the integrand. Setting $\xi = 1$, Eq. (2.69) reads

$$\begin{aligned}\delta_{\mathrm{E}}^{(0)} &= \frac{\alpha_s(s_0)}{\pi} + (1.6398 + 3.5625)\left(\frac{\alpha_s(s_0)}{\pi}\right)^2 + (6.371 + 19.995)\left(\frac{\alpha_s(s_0)}{\pi}\right)^3 \\ &\quad +(K_4 + 78.00)\left(\frac{\alpha_s(s_0)}{\pi}\right)^4 , \qquad (2.70)\end{aligned}$$

with a truncation of the power series at order $\alpha_s^3(s_0)$ since the coefficient K_4 is unknown. The first numbers in the parentheses give the $\tilde{K}_n(1)$, while the second ones are the $g_n(1)$. The truncation is performed despite the fact that parts of the higher coefficients $g_{n>4}(\xi)$ are known to all orders and could be resummed. These known parts are the higher (up to infinite) order terms of the Taylor expansion (2.68) which are functions of $\beta_{n\leq 3}$ only. A rough estimation of the associated error can be performed using the bold guess $\Delta\tilde{K}_4(1) \approx K_3(K_3/K_2) \simeq 25$ which contributes to $\delta^{(0)}(K_4) \approx 1.6\%$ for $\alpha_s(M_\tau) = 0.35$ (see Section 10.2.2 for further discussions). The contributions to $\delta_{\mathrm{E}}^{(0)}$ from the terms of order $n = 1, \ldots, 4$ according to Eq (2.70) are given in the first line of Table 2.1.

Another more promising approach to the solution of the contour integral (2.61) is the direct numerical evaluation of the $A^{(n)}$ integrals (2.67) using the approximative analytical three-loop RGE solution (2.13) or a numerical solution of the RGE (Runge-Kutta [72]) as input for the running $\alpha_s(-\xi^2 s)$. The complex integrals have then the form

$$A^{(n)}(\alpha_s) = \frac{1}{2\pi}\int_{-\pi}^{\pi} d\varphi \left[1 + 2e^{i\varphi} - 2e^{i3\varphi} - e^{i4\varphi}\right]\left(\frac{\alpha_s(\xi^2 s_0 e^{i\varphi})}{\pi}\right)^n . \qquad (2.71)$$

The numerically evaluated perturbative prediction (2.67) at different orders n for the settings $\alpha_s(M_\tau) = 0.35$, $\xi = 1$ and $K_4 = 25$ are shown in Table 2.1. The results are given for the various types of techniques used to evolve $\alpha_s(s_0 e^{i\varphi})$: the truncated Taylor expansion (2.68), the RGE analytical solution and the Runge-Kutta type solution of the RGE which is actually expected to be next to the exact solution. The Runge-Kutta

Integration	$\delta^{(0)}(n=1)$	$\delta^{(0)}(n=2)$	$\delta^{(0)}(n=3)$	$\delta^{(0)}(n=4)$	$\delta^{(0)}(\text{tot})$
Expansion $\delta_{\rm E}^{(0)}$ (Taylor)	0.1114	0.0645	0.0365	0.0159	0.2283
Num. (Taylor)	0.1639	0.0342	0.0138	0.0045	0.2165
Num. (RGE-analyt.)	0.1523	0.0313	0.0130	0.0047	0.2013
Num. (RGE-num., β_2)	0.1531	0.0316	0.0133	0.0048	0.2028
Num. (RGE-num., β_3)	0.1527	0.0313	0.0130	0.0047	0.2017

Table 2.1: *Perturbative contribution to* $R_\tau(M_\tau)$ *at orders* n *with* $\alpha_s(M_\tau) = 0.35$. *The value of* K_4 *is set to* 25. *The first line gives the results of the* α_s *expansion according to Eq.* (2.70), *while the second and third lines give the results of the numerical evaluation of the integrals* (2.67) *using the Taylor expansion* (2.68) *and directly the RGE solution* (2.13), *respectively. The last two lines are obtained from numerical (Runge-Kutta) integration and for the three- and four-loop* β*-functions, respectively.*

results are additionally given at four-loop level. The difference between three- and four-loops is far beyond the experimental and theoretical accuracy of R_τ. Compared to the expansion (2.70), faster convergence is observed for the numerical solutions yielding a significantly smaller error associated with the unknown K_4 of 0.5%. The difference of about 7% between the numerical solutions using the Taylor expansion (2.68) of the RGE (second line in Table 2.1) and the complete RGE solutions (3. - 5. line) for the α_s evolution invalidates the Taylor series as not providing a stable approximation along the integration contour. The same conclusion should then strike the expansion (2.69) based on the same series.

An important difference between the two evaluations of the integral (2.67), fixed order expansion and numerical solution, grounds in the fact that the g_n coefficients in Expression (2.69) stem from a truncated series of fourth-order α_s^4 (2.68) which is not resummed. This resummation is automatically contained in the numerical evaluation using the complete known RGE solution. In addition, the Taylor expansion inserted in the $A^{(n)}$ integral provides imaginary logarithms, $\ln(-s/s_0) = i(\varphi - \pi)$, giving rise to large contributions in some parts of the integration contour [86]. This generates uncomfortably large g_n coefficients at higher orders in α_s which reinforces the importance of resummation.

2.5.3 Renormalons

There has been some excitement on the theoretical side [96, 97, 89] concerning the perturbative expansion of the Adler function $D(s)$ which behaves divergent when considering a gluon propagator chain carrying multiple fermion insertions in a vacuum polarisation loop as depicted in Fig. 2.6. The resummation of this chain with a large number of n bubbles deals with the assumption of a dominating contribution from the $(\beta_0\alpha_s(-s))^n$ term. Higher order terms of the β-function are then neglected. This assumption is supported empirically by the observation that the β_0-term dominates second order radiative corrections for many observables in the $\overline{\rm MS}$ scheme [96]. This procedure provides a *naive*

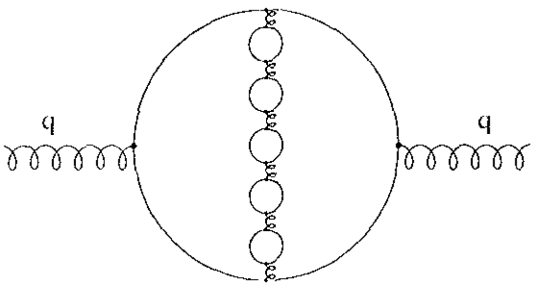

Figure 2.6: *Multi-fermion loop insertion (renormalons) into a fermion anti-fermion vacuum polarisation diagram.*

non-abelianisation of the theory since lowest order radiative corrections apparently do not include gluon self-coupling. The Adler function obeys then the perturbative expansion

$$D(\alpha_s) \;=\; \sum_{n=0}^{N} r_n \alpha_s^{n+1} \;, \tag{2.72}$$

where the coefficients r_n are polynomials in the number of active flavours n_f. Unfortunately, at sufficiently large orders of n vacuum polarisation bubbles, the coefficients diverge as

$$r_n \;\sim\; C_k n!\, n^{\gamma_k} (\beta_0/k)^n \tag{2.73}$$

A convenient way to handle this divergence is to consider the Borel transform of the Adler function

$$B[D](u) \;\equiv\; \sum_{n=0} \frac{r_n}{n!} u^n \;, \tag{2.74}$$

which is believed to have a finite radius of convergence in the u-plane [98]. The nth fixed order perturbation coefficient is then generated by the nth derivative

$$r_n \;=\; \left.\frac{d^n B[D](u)}{du^n}\right|_{u=0} \;. \tag{2.75}$$

The explicit factor $n!$ in $B[D](u)$ makes the Borel transformed series much better behaved. Summing up all orders leads to the integral representation

$$D(\alpha_s) - D(0) \;=\; \int\limits_0^\infty du\, e^{-u/\alpha_s} B[D](u) \;. \tag{2.76}$$

What is needed to perform the integration (2.76) is that $B[D](u)$ has no singularities in the integration range. However, the large n expansion leads to singularities on the real axis which can be distinguished in *infrared* singularities (IR renormalons) — for small virtuality — and *ultraviolet* singularities (UV renormalons) — for high virtuality of the exchanged gluon. At large n, the Borel transform behaves essentially as a geometric series [97]

$$B[D](u) \;\sim\; C_k \sum_n n^{\gamma_k} \left(\frac{\beta_0 u}{k}\right)^n \;\sim\; C_k \Gamma(\gamma_k + 1) \left(1 - \frac{\beta_0 u}{k}\right)^{-(\gamma_k+1)} \;, \tag{2.77}$$

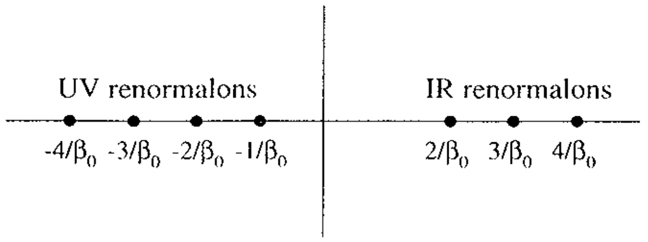

Figure 2.7: *Ultraviolet (UV) and infrared (IR) renormalons in the u-plane.*

which is singular for $u = k/\beta_0$. They are associated with the IR renormalons $k = +2, +3, \ldots$ (the $k = +1$ singularity is assumed to be absent in perturbation theory [99]) on the positive real axis and the UV renormalons $k = -1, -2, \ldots$ on the negative side (see Fig. 2.7).

The IR poles give rise to ambiguities when one uses the generators (2.75) to reconstruct $D(\alpha_s)$ from its Borel transform. Using in first order for space-like $s < 0$

$$\alpha_s(-s) \simeq \frac{4\pi\alpha_s(\mu^2)}{1 + \alpha_s(\mu^2)\beta_0 \ln(-s/\mu^2)} = 4\pi\left[\beta_0 \ln(-s/\Lambda^2)\right]^{-1} , \tag{2.78}$$

one obtains for the associated ambiguity for $k = 2, 3, \ldots$ [97]

$$\begin{aligned} \Delta D(\alpha_s) &= \int\limits_{1/\beta^0}^{\infty} du\, e^{-u/\alpha_s} B[D](u) \\ &\sim \alpha_s B[D](k/\beta_0) e^{-k/\beta_0\alpha_s} \\ &\sim \alpha_s B[D](k/\beta_0)\left(\frac{\Lambda^2}{s}\right)^k . \end{aligned} \tag{2.79}$$

These IR renormalons $\sim (\Lambda^2/s)^k$ are reabsorbed into the non-perturbative terms of the OPE. The absence of a $k = 1$ IR renormalon is thereby related to the impossibility to build a gauge invariant operator of dimension $D = 2$.

Due to asymptotic freedom, the UV renormalons arise on the negative real axis (on the contrary to QED where they occur on the positive side) so that they are outside the integration range of (2.76) and in so far harmless which means Borel-summable [98]. For large n, the factorial growth of the perturbation series is dominated by the contribution of the leading UV renormalon $k = -1$ with alternating coefficients $r_n \sim n^\gamma n!\,(-\beta_0)^n$. The individual contributions $r_n\alpha_s^{n+1}$ to the expansion (2.72) for reasonably small α_s decrease first then pass through a minimun and will finally diverge. This point of minimal sensitivity is the optimal n to truncate the intrinsically divergent expansion. A guess at which order N minimal sensitivity is achieved can be obtained from the argument that the series is convergent,*i.e.*, reliable at order $n+1$ if $\alpha_s r_{n+1}/r_n < 1$. Considering leading IR and UV renormalons one finds from the asymptotic behaviour (2.73) $r_{n+1}/r_n \sim (\beta_0/8\pi)n$ (IR) and $r_{n+1}/r_n \sim -(\beta_0/4\pi)_0 n$ (UV). The break down of convergence is then first caused by the UV renormalon at order $N \approx 4\pi/\beta_0\alpha_s \simeq 4$. However, a series truncated at finite order N brings an intrinsic limitation of accuracy along with it. The associated error is reasonably estimated with the magnitude of the order N term of the perturbative series. That gives using Eqs. (2.73) and (2.78) for the first UV renormalon $k = -1$

$$\begin{aligned}
|r_N|\alpha_s^N &\sim N^\gamma N!\,(\beta_0\alpha_s)^N \\
&\simeq N^\gamma N!\,N^N e^{-N}\sqrt{2\pi N}(\beta_0\alpha_s)^N \qquad \text{(Stirling formula)} \\
&\sim (4\pi/\beta_0\alpha_s)^\gamma e^{-4\pi/\beta_0\alpha_s}\sqrt{8\pi^2/\beta_0\alpha_s} \\
&\sim \frac{\Lambda^2}{s}\ln^{\gamma+\frac{1}{2}}\frac{s}{\Lambda^2}\,. \qquad (2.80)
\end{aligned}$$

Thus, the truncation of the perturbative series is accompanied by an uncertainty which scales like $1/s$, *i.e.*, with apparent dimension $D = 2$. The authors of Ref. [99] (first ref.) showed that the truncation uncertainty at N scales actually with $A\alpha_s^{1/2}\Lambda^2 s/\mu^4$ when the renormalisation scheme dependence of Λ is taken into account. The interpretation of the above uncertainties and its impact on the theoretical error of the $\alpha_s(M_\tau)$ determination will be discussed in Section 10.2.2.

2.5.4 Non-Perturbative Contributions

Following SVZ [11], the first contribution to $R_\tau(s_0)$ beyond the $D = 0$ perturbative expansion is the non-dynamical quark mass correction of dimension $D = 2$, *i.e.*, corrections in powers of $1/s_0$. They have been calculated up to next-to-leading order α_s [100]. Inserting the formulae in Eq. (2.53) and evaluating the contour integral leads to [12]

$$\begin{aligned}
\delta_{ij,V/A}^{(2-\text{mass})} &= -8\left(1+\frac{16}{3}\frac{\alpha_s(s_0)}{\pi}\right)\frac{m_i^2(s_0)+m_j^2(s_0)}{s_0} \\
&\quad \pm 4\left(1+\frac{25}{3}\frac{\alpha_s(s_0)}{\pi}\right)\frac{m_i(s_0)m_j(s_0)}{s_0}\,, \qquad (2.81)
\end{aligned}$$

where $m_i(s_0)$ are the running quark masses evaluated at the scale s_0 using the RGE γ-function (2.15).

The dimension $D = 4$ operators have dynamical contributions from the gluon condensate $\langle(\alpha_s/\pi)GG\rangle$ and quark condensates $\langle m_i q_i q_j\rangle$ which are the matrix elements of the gluon field strength-squared and the scalar quark densities, respectively. Remaining $D = 4$ operators are running quark masses to the fourth power. Inserting the Wilson coefficients of these operators [100, 101] in the integral (2.53) one obtains [12]

$$\begin{aligned}
\delta_{ij,V/A}^{(4)} &= \frac{11}{4}\pi^2\left(\frac{\alpha_s(s_0)}{\pi}\right)^2\frac{\langle(\alpha_s/\pi)GG\rangle}{s_0^2} \\
&\quad + 16\pi^2\left[1+\frac{9}{2}\left(\frac{\alpha_s(s_0)}{\pi}\right)^2\right]\frac{\langle(m_i \mp m_j)\,(\bar{q}_i q_i \mp \bar{q}_j q_j)\rangle}{s_0^2} \\
&\quad - 18\pi^2\left(\frac{\alpha_s(s_0)}{\pi}\right)^2\left[\frac{\langle m_i\bar{q}_i q_i + m_j\bar{q}_j q_j\rangle}{s_0^2} + \frac{4}{9}\sum_k\frac{\langle m_k\bar{q}_k q_k\rangle}{s_0^2}\right]
\end{aligned}$$

$$
-\left[\frac{48}{7}\left(\frac{\alpha_s(s_0)}{\pi}\right)^{-1}-\frac{22}{7}\right]\frac{\left(m_i(s_0)\mp m_j(s_0)\right)\left(m_i^3(s_0)\mp m_j^3(s_0)\right)}{s_0^2}
$$

$$
\pm 6\frac{m_i(s_0)m_j(s_0)\left(m_i(s_0)\mp m_j(s_0)\right)^2}{s_0^2}+36\frac{m_i^2(s_0)m_j^2(s_0)}{s_0^2}\ . \qquad (2.82)
$$

As already seen in Expression (2.57), the gluon condensate vanishes in first order $\alpha_s(s_0)$. However, there appear second order terms in the Wilson coefficients due to the s dependence of α_s which after integration becomes α_s^2.

The contributions from dimension $D = 6$ operators are rather complex. As already mentioned, the most important operators arise from four-quark dynamical effects of the form $\bar{q}_i\Gamma_1 q_j\bar{q}_k\Gamma_2 q_l$. Other operators, such as the triple gluon condensate whose Wilson coefficient vanishes to order α_s, or those which are suppressed by powers of quark masses, are neglected in the evaluation of the contour integrals performed in Ref. [12]. The large number of independent operators of the four-quark type occurring in the $D = 6$ term can be reduced by means of the vacuum saturation assumption [11] to leading order α_s. The operators are then expressed as products of scale dependent two-quark condensates $\alpha_s(\mu)\langle\bar{q}_i q_i(\mu)\rangle\langle\bar{q}_j q_j(\mu)\rangle$. To take into account possible deviations from the vacuum saturation assumption, one can introduce an effective scale independent operator $\rho\alpha_s\langle\bar{q}q\rangle^2$ that replaces the above product. The effective $D = 6$ term obtained in this way reads [12]

$$
\delta^{(6)}_{ij,V/A} \simeq \begin{pmatrix} 7 \\ -11 \end{pmatrix}\frac{256\pi^4}{27}\frac{\rho\alpha_s\langle\bar{q}q\rangle^2}{s_0^3}\ , \qquad (2.83)
$$

providing a large cancellation between the axial and vector contributions.

The basis of the dimension $D = 8$ contribution has a structure of non-trivial quark-quark, quark-gluon and four-gluon condensates which explicit form is given in Ref. [102]. For the theoretical prediction of $R_\tau(s_0)$ used here, the complete long and short distance part is absorbed into the scale invariant phenomenological $D = 8$ operator $\langle\mathcal{O}_8\rangle$ which will be fitted simultaneously with α_s.

Higher order contributions from $D \geq 10$ operators are expected to be small as, equivalent to the gluon condensate, constant terms and terms in leading order α_s vanish after integrating over the contour.

2.5.5 Spectral Moments

It was the idea of the authors of Ref. [13] to benefit from the information provided by the explicit shape of the spectral functions in order to obtain additional constraints on $\alpha_s(s_0)$ and — more importantly — on the non-perturbative condensates to detach the α_s measurement from additional theoretical assumptions. They defined the following spectral moments at M_τ:

$$
R^{kl}_{\tau,V/A} \equiv \int\limits_0^{M_\tau^2} ds \left(1-\frac{s}{M_\tau^2}\right)^k \left(\frac{s}{M_\tau^2}\right)^l \frac{dR_{\tau,V/A}}{ds}\ , \qquad (2.84)
$$

where the factor $(1-s/M_\tau^2)^k$ weights the low energy spectrum and squeezes the integrand at the crossing of the positive real axis where the validity of the OPE is questioned [91] and experimental accuracy is statistically limited. Its counterpart $(s/M_\tau^2)^l$ projects on higher energies. Note that $R_\tau^{00} = R_\tau$. The new spectral information is used to fit simultaneously $\alpha_s(M_\tau)$ and the phenomenological operators $\langle(\alpha_s/\pi)GG\rangle_{D=4}$, $\rho\alpha_s\langle\bar{q}q\rangle^2_{D=6}$ and $\langle\mathcal{O}\rangle_{D=8}$, a procedure which requires at least 4 – better 5 – input variables considering the intrinsic strong correlations between the moments which are reinforced by experimental correlations.

In complete analogy to the τ hadronic width one can separate the respective contributions from perturbative and non-perturbative QCD as

$$R^{kl}_{\tau,V/A} \;=\; \frac{3}{2}|V_{ud}|^2 S_{\rm EW}\left(1+\delta^{(0,kl)}+\delta'_{\rm EW}+\delta^{(2-{\rm mass},kl)}_{ud,V/A}+\sum_{D=4,6,\ldots}\delta^{(D,kl)}_{ud,V/A}\right) . \qquad (2.85)$$

The prediction of the perturbative contribution takes the form

$$\delta^{(0,kl)} \;=\; \sum_{n=1}^{3}\tilde{K}_n(\xi)A^{(n,kl)}(\alpha_s) , \qquad (2.86)$$

with the contour integrals

$$\begin{aligned} A^{(n,kl)}(\alpha_s) \;&=\; \frac{1}{2\pi i}\oint\limits_{|s|=M_\tau^2}\frac{ds}{s}\left[1-2\frac{s}{M_\tau^2}+2\left(\frac{s}{M_\tau^2}\right)^3-\left(\frac{s}{M_\tau^2}\right)^4\right] \\ &\qquad\times\left(1-\frac{s}{M_\tau^2}\right)^k\left(\frac{s}{M_\tau^2}\right)^l\left(\frac{\alpha_s(-\xi^2 s)}{\pi}\right)^n , \end{aligned} \qquad (2.87)$$

which are numerically resolved for the running $\alpha_s(-\xi^2 s)$ obtained from the RGE (2.11) using the numerical solution (Runge-Kutta).

In the chiral limit and neglecting the small logarithmic dependence of the Wilson coefficients on s the dimension D non-perturbative contributions in Expression (2.85) reads [13]

$$\delta^{(D,kl)}_{ud,V/A} \;=\; 8\pi^2\left(\begin{array}{ccccc} (D=2) & (D=4) & (D=6) & (D=8) & (k,l) \\ 1 & 0 & -3 & -2 & (0,0) \\ 1 & 1 & -3 & 5 & (1,0) \\ 0 & -1 & -1 & 3 & (1,1) \\ 0 & 0 & 1 & 1 & (1,2) \\ 0 & 0 & 0 & -1 & (1,3) \end{array}\right)\sum_{{\rm dim}\mathcal{O}=D} C^{(J)}(\mu)\frac{\langle\mathcal{O}(\mu)\rangle}{M_\tau^D} , \qquad (2.88)$$

where the matrix is defined by the choice of the coefficients for the moments $k=1$, $l=0,1,2,3$ and the corresponding dimension D. One notes that with increasing weight l contributions from low dimension operators are cut. For example, the only non-perturbative contribution to the moment $R^{13}_{\tau,V/A}$ stems from the dimension $D=8$ operator. Hence, in a fit using spectral moments, $D=8$ will strongly be constrained from $R^{13}_{\tau,V/A}$. This observation is in some sense a "paradox", as higher moments project higher masses on the contrary to $R_\tau(s_0)$ and the spirit of the OPE, where the higher dimension terms blow up at small s_0.

For practical purpose it is more convenient to define moments that are normalised to the respective value of $R_{\tau,V/A}$ in order to uncorrelate normalisation and shape of the τ spectral functions:

$$D^{kl}_{\tau,V/A} = \frac{R^{kl}_{\tau,V/A}}{R_{\tau,V/A}} . \qquad (2.89)$$

For the use of integrals over experimental data one then directly integrates the normalised invariant mass-squared spectrum. The corresponding theoretical prediction can easily be modified. There now exist two sets of experimentally almost uncorrelated observables — hadronic widths and spectral moments — which provide independent constraints on $\alpha_s(s_0)$and important tests of consistency. It is therefore necessary to obtain from the measurement a precise normalisation (R_τ) as well as an excellent knowledge of the shape of the spectral functions (D^{kl}_τ) .

2.6 Measurements of α_s

The measurement of the genuinely only free parameter of QCD, the coupling constant α_s at various energy scales represents the key issue for a wide range of questions in modern particle physics, *e.g.*. consistency tests of QCD at different energy scales, important quantity for constraints on new physics (electroweak global parameter fit, partial Z decay width into b quarks R_b) and tests of grand unified theories (GUT). The first quantitative measurement of α_s on the basis of event shape variables has become possible through the observation of gluon radiation from quarks in three-jet events [61]. The discovery of the energy dependence of three-jet event production rates [103] gave a first evidence of the running of α_s [104].

Table 2.2 and Fig 2.10 compile published results of α_s measurements which are briefly described in the following paragraphs. One can see that the diversity of the approaches which all lead to compatible results is rather impressive. Already included is the result from τ decays presented in Section 10.2 of this work.

α_s from Deep Inelastic Scattering

Deep inelastic lepton-nucleon scattering (DIS) permits the measurement of α_s over a broad range of lepton-parton squared space-like momentum transfers Q^2. Both experiments at the e-p collider HERA at DESY, H1 and ZEUS, determined $\alpha_s(Q^2)$ from jet rates for $3.3\ \text{GeV} < \sqrt{Q^2} < 63$ GeV. The theoretical prediction in perturbative QCD is known to next-to-leading order (NLO), *i.e.*, including two-loop QCD corrections. The coefficients of α_s in the e-p jet-rate prediction depend, in contrast to e^+e^- annihilation, themselves on Q^2. Thus running of α_s is therefore an explicit input into the theoretical prediction.

The proton structure function $F_2^p(x, Q^2)$ for small parton momentum fraction x and $\sqrt{Q^2} < 10$ GeV can be computed to NLO perturbative QCD including a summation over leading and subleading logarithms. A double-logarithmic scaling of $F_2^p(x, Q^2)$ in x and Q^2 provided an direct evidence of running of $\alpha_s(Q^2)$.

The authors of Ref. [105, 106] used the Bjorken sum rule (BSR) and the Gross-Llewellyn-Smith sum rule (GLSSR) with data on polarised $e-p$ and $\mu-p$ scattering for a first measurement of α_s with this technique. The respective theoretical predictions are known to NNLO perturbative QCD, which reduces clearly the theoretical systematic error.

α_s from Scaling Violations

The study of scaling violation in structure functions in DIS played a fundamental role in establishing QCD as the theory of strong interactions. Scaling violations are observed in the structure function of the nucleon in DIS processes and in the parton fragmentation function in $e^+e^- \rightarrow$ hadrons annihilations. For the nucleon structure function one observes with increasing momentum Q^2 a process of "softening", described by perturbative QCD. Softening means here that at higher momentum transfers more partons are resolved from virtual vacuum fluctuations in the nucleon [107]. Softening in fragmentation functions describes the enhancement of the particle multiplicity in the jets. Theoretical predictions exist to NLO where perturbative and non-perturbative contributions are considered in the framework of the OPE.

Measurements of α_s using scaling violations of structure functions were performed in DIS with neutrino or lepton beams on nuclei targets. Tab. 2.2 cites the averaged value evaluated in Ref. [107].

QCD predicts similar scaling violations in the fragmentation functions of quarks and gluons. In an e^+e^- collider this translates into the fact that the distributions of the scaled-energy $x \equiv 2E/\sqrt{s}$ of the final state particles depend on the c.m. energy $\sqrt{s}$. The measurement the x distributions at different $\sqrt{s}$ compared to the QCD prediction allows the determination of α_s.

α_s from e^+e^- Annihilation

The topology of hadronic events in e^+e^- annihilation is modified by effects from gluon radiation giving rise to events which differ from the collimated two-jet topology coming from the fragmentation of pure $e^+e^- \rightarrow q\bar{q}$ events. Since the amount of gluon radiation is directly proportional to the strong coupling constant, studying the topology of hadronic final states provides a measurement of α_s. Such topological variables, called *event shape variables*, have been used by experiments at energies from 30 GeV to up to 133 GeV (LEP-2). In order to justify the perturbative approach to connect the event shape variables with QCD, one has to make sure that they are insensitive to QCD singularities from soft gluon radiation (infrared divergence) and collinear hadronization (ultraviolet divergence). All global event shape variables used by the experiments are known to NLO α_s^2, where the theoretical predictions are based on numerical integration of the contributing matrix elements.

The definition of multi-jets is arbitrary to some extent so that the absolute number of reconstructed multi-jets depends on the metric ("jet algorithm") used. Commonly used algorithms as measures for the distance between two jets ij are the Durham-metric [108] $y_{ij} = 2\times\min(E_i^2, E_j^2)(1-cos\,\theta_{ij})/2$ and the Jade-metric [109] $y_{ij} = 2(E_i, E_j)(1-cos\,\theta_{ij})/2$.

with the opening angle between the two jets θ_{ij} and the total invariant mass of the final state s.

Theoretical predictions of event shape variables depend strongly on the underlying phenomenology to describe the non-perturbative transition from initial quarks to final state hadrons (hadronization). The systematic uncertainties associated with the hadronization modelling limit the precision of α_s determinations.

α_s from the Z Hadronic Width

The theoretical prediction of the Z hadronic width Γ_{had}, measured at LEP and SLD from the sum of the leptonic widths $\mathrm{Z} \to \ell^+\ell^-$, is known to NNLO perturbative QCD [110]:

$$\Gamma(Z \to q\bar{q}) \simeq \frac{G_{\mathrm{F}} M_{\mathrm{Z}}^3}{6\sqrt{2}} \cdot 3 \left[1 + 1.060 \frac{\alpha_s(M_{\mathrm{Z}})}{\pi} + 0.90 \left(\frac{\alpha_s(M_{\mathrm{Z}})}{\pi}\right)^2 - 15 \left(\frac{\alpha_s(M_{\mathrm{Z}})}{\pi}\right)^3\right] . \tag{2.90}$$

The total QCD correction above amounts unfortunately only to about 4% for $\alpha_s(M_{\mathrm{Z}}) \simeq 0.12$. This limits considerably the sensitivity of the α_s determination. On the other hand, the measurement is safe from the asymptoticness point of view: non-perturbative effects are negligible. The theoretical systematic error in the fit of the Z lineshape gets a non-negligible contribution from the unknown mass of the Higgs boson [111]. The $\alpha_s(M_{\mathrm{Z}})$ value given in Tab. 2.2 is obtained from the combined experimental result for the hadronic width from all four LEP experiments better expressed as the ratio [111] $R_\ell(s) = \Gamma_{\mathrm{Z}\to\mathrm{had}}/\Gamma_{\mathrm{Z}\to e^+e^-} = (\Gamma_{\mathrm{Z}} - \Gamma_{\mathrm{Z}\to e^+e^-})/\Gamma_{\mathrm{Z}\to e^+e^-} = 20.778 \pm 0.029$, using the top quark mass $M_{\mathrm{top}} = 180$ GeV/c^2 and a Higgs mass of $M_{\mathrm{Higgs}} = 300$ GeV/c^2. The measurement is still statistically limited.

α_s from a Combined Electroweak Fit

Not only the hadronic width but also the Z production cross section receive contributions from QCD loops. One can combine this information by means of a global SM electroweak fit using all available data from LEP, SLC, $p\bar{p}$ collisions (CDF, DØ at TEVATRON), $b\bar{b}$ production (CLEO at CESR) and DIS. The input variables are then obtained from

electroweak data:

M_{Z}, Γ_{Z}, σ^0_{had}, R_ℓ, A^ℓ_{FB},
A_τ, A_e ,
$\langle Q_{\mathrm{FB}} \rangle$,
A_{LR} , (SLC) ,
M_{W}, $1 - \frac{M_{\mathrm{W}}^2}{M_{\mathrm{Z}}^2}$, M_{top} ,

where A^ℓ_{FB} is the forward-backward asymmetry measured in leptonic Z decays, A_τ, A_e are the polarisation asymmetries, $\langle Q_{\mathrm{FB}} \rangle$ is the quark-antiquark charge asymmetry (sensitive to $\sin^2\theta_{\mathrm{W}}$), M_{W} is measured at $p\bar{p}$ colliders and $1 - M_{\mathrm{W}}^2/M_{\mathrm{Z}}^2$ is measured in deep-inelastic neutrino-nucleon scattering.

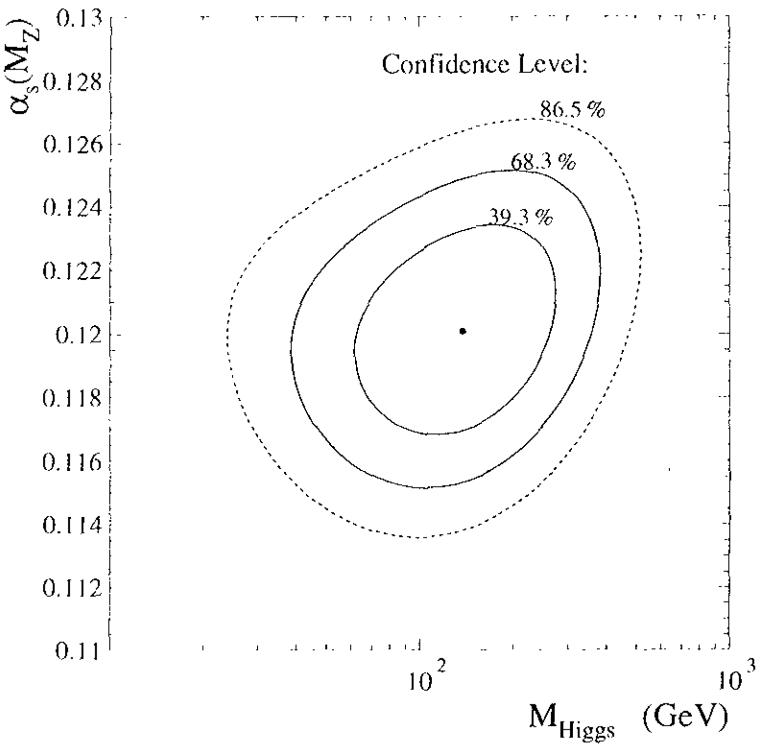

Figure 2.8: *Correlation between* $\alpha_s(M_Z)$ *and the Higgs mass* M_{Higgs} *simultaneously obtained from the global electroweak fit. The contours denote the respective confidence regimes.*

- heavy flavour data ($Z \to b\bar{b}$, $Z \to c\bar{c}$):

$$R_b,\ R_c,\ A^b_{\text{FB}},\ A^c_{\text{FB}}\ , \quad (\text{LEP})\ ,$$
$$R_b,\ A_b,\ A_c\ , \quad (\text{SLC})\ .$$

A careful analysis of the theoretical and experimental correlations between these input variables has to be performed.

The above information allows the simultaneous determination of top and Higgs mass, $\alpha_s(M_Z)$ and the weak mixing angle yielding [112]

$$\begin{aligned}\alpha_s(M_Z) &= 0.1202 \pm 0.0033\ ,\\ M_{\text{top}} &= 172 \pm 5.8\ \text{GeV}/c^2\ ,\\ M_{\text{Higgs}} &= 149\ ^{+148}_{-82}\ ,\\ \sin^2\theta_W &= 0.2316 \pm 0.0004\ .\end{aligned}$$

using $\alpha^{-1}(M_Z^2) = 128.90 \pm 0.090$. Fig. 2.8 plots the results for $\alpha_s(M_Z)$ and M_{Higgs} with their $1\,\sigma$ and $2\,\sigma$ contours.

α_s from Hadron Collision

Similarly as in DIS, hadron colliders simultaneously probe QCD in a wide range of

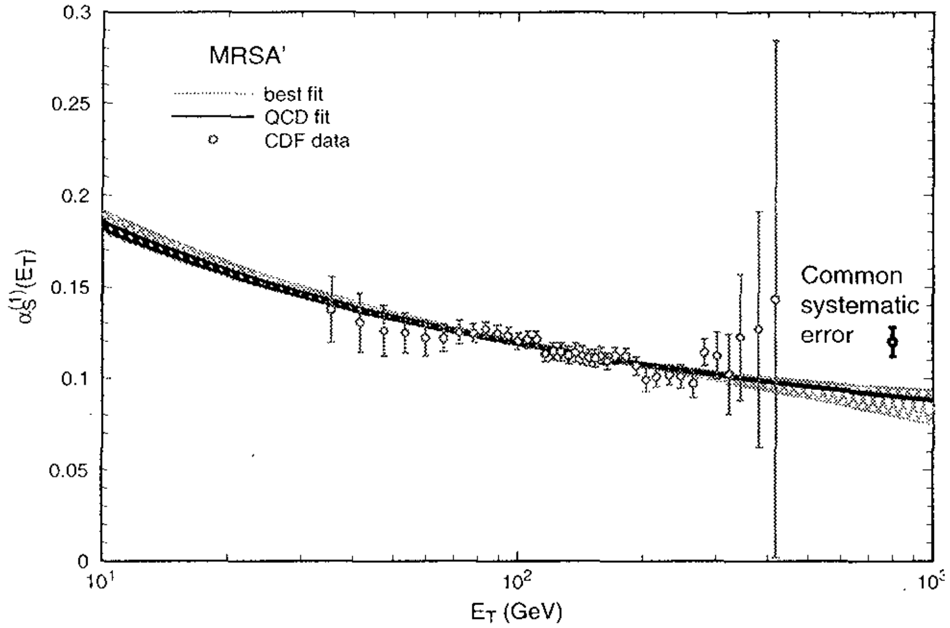

Figure 2.9: *Values of* $\alpha_s(E_T)$ *determined from CDF data* [113] *using one-jets of transverse energies* 30 *GeV* $< E_T <$ 500 *GeV. The plot is taken from Ref.* [114].

momentum transfers Q^2. Theoretical prediction of inclusive processes are commonly known in NLO QCD. Direct photon production in hard parton-parton scattering is a Compton-like process scaling with $\alpha \cdot \alpha_s$. In the inclusive cross section difference $\sigma(p\bar{p} \to \gamma + X) - \sigma(pp \to \gamma + X)$, sea quark and gluon structure functions of the proton cancel (no explicit dependence on the sign of the electromagnetic charge) so that only the well known valence quark distribution contributes as theoretical input for the α_s determination.

Using the α_s dependence of the inclusive transversal energy (E_T) distribution of one-jets, values of $\alpha_s(E_T^2)$ for energies $E_T = 30$ GeV to 500 GeV could be measured [114] using CDF data recorded in 1988-89 [113]. Neglecting non-perturbative contributions, the inclusive differential cross section $d\sigma/dE_T$ is then directly related to the perturbative prediction governed by the running coupling $\alpha_s(E_T)$ at the characteristic scale E_T. The large accessible energy range in which the dynamics of parton-parton scattering is probed can be illustrated by expressing E_T in terms of the impact parameter b, *i.e.*, the "distance scale" given by $b = \hbar c/E_T$. The above energy range corresponds then to extremely small distances from b = 0.07 fm to 0.0004 fm compared to the proton dimension of about 0.8 fm. In order to obtain a value for $\alpha_s(M_Z)$ the results of different energies have been averaged over the statistical errors while keeping the systematic uncertainties as being of common origin. Consequently, the final error reflects the systematic uncertainty while statistical errors are negligible. The α_s measurements versus E_T are shown in Fig. 2.9.

Another, however less sensitive, approach is the measurement of the inclusive $pp \to bb$ cross section [115]. In hadron collisions heavy quarks are produced by quark-antiquark annihilation or gluon-gluon fusion processes which to leading order are quadratic in α_s. Experimentally b-quarks are tagged using decay characteristics (*e.g.*, lifetime).

α_s from the Υ System

The $b\bar{b}$ quarkonium resonances of the Υ family are used in a new analysis [116] in order to extract values for the bottom quark mass M_b and $\alpha_s(M_b)$. It is a reconsideration of a previous work where the extremely precise value of $\alpha_s(M_Z) = 0.109 \pm 0.001$ was claimed using a perturbative expansion in first order α_s [117]. The result turned out to be in sharp disagreement with the current world average $\alpha_s(M_Z) = 0.118 \pm 0.003$ [107]. This gave rise to some speculations relating the "difference" found between α_s evaluations from low and high energy data to the possible appearance of new physics [118]. The new analysis readjusts this picture: the authors of Ref. [116] employed moments of order $n = 1, \ldots, 20$ obtained according to Eq. (2.23) from the nth derivative of the heavy quark vacuum polarisation correlator $\Pi_{b\bar{b}}(q^2)$ whose imaginary part is proportional to the rate $R_b(s) = \sigma(e^+e^- \to b\bar{b})/\sigma(e^+e^- \to \mu^+\mu^-)$. High n moments give a weight on low resonance states, while the moment $n \to \infty$ projects on the Υ ground state (see Section 2.3.2). To avoid systematic errors due to unmeasured higher resonances, only the $n = 8, \ldots, 20$ moments were used. The correlator and its derivatives can be predicted by NLO α_s^2 perturbative QCD (where some unknown α_s^2 terms were estimated using the technique of Padé approximants[4]. Although correlated, the simultaneous fit of all moments used provides a precise measurement of the bottom quark mass $M_b = 4.60 \pm 0.02$ GeV/c^2 and $\alpha_s(M_Z) = 0.119 \pm 0.008$, in now perfect agreement with the world average. The error includes a careful analysis of the systematic uncertainties from theoretical origin.

α_s from Lattice QCD

Additionally shown in Table 2.2 is the average over recent α_s results from lattice QCD calculations [119], using measurements of level splittings between S and P heavy quarkonia states in the Υ system. Lattice calculations are based on a discretization of a finite space-time volume where the latter is generally chosen of order 2 fm in each dimension to be large enough that hadrons fit comfortably into it. The discretized volume allows then the calculation of multi-dimensional, quantum field theory path integrals using Monte Carlo methods. The lattice spacing a is chosen according to the machine and time resources available. Currently they are chosen between 0.05–0.2 fm [119] corresponding to an energy scale of 1–4 GeV, which is at 4 GeV large enough to escape from low energy QCD dynamics. In principle, the QCD action can be calculated using quark propagators with gluon background. However, such calculations are extremely demanding so that, in practice, gluon background is often set to its average value ("quenching") which means that internal quark loops are neglected. This is compensated by a renormalisation of the lattice coupling constant which is input.

---

[4] The Padé approximant "[M,N]" of a function f is given by the ratio of two polynomials of order M and N which to order $M+N$ has the same Taylor series as f. This ratio opens a systematic way to guess how a perturbative series resums, by explicitly rewriting the latter as a ratio of polynomials. Compared to the f, the ratio "[M,N]" $= P_M/P_N$ introduces poles on the real axis in the s-plane similar to the renormalons when performing a Borel transformed resummation of the perturbative series (see Section 2.5.3).

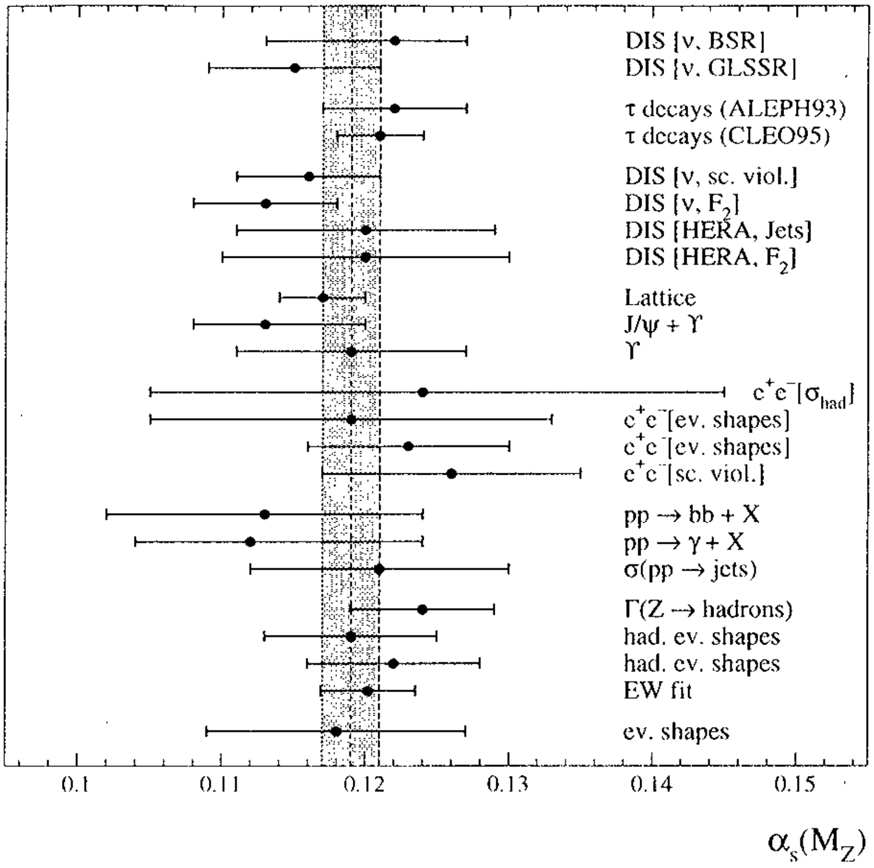

Figure 2.10: *Compilation of α_s measurements evolved to M_Z. The corresponding values are found in Table* 2.2. *The shaded band depicts the combined value of $\langle\alpha_s(M_Z)\rangle$ =* 0.1201 ± 0.0012.

Calculations of α_s exist with $n_f = 0$ and $n_f = 2$ dynamic fermions which give only marginally different results and thus allow a safe extrapolation to the physical $n_f = 3$ flavours. The determination follows a three step procedure: (*i*), the definition and measurement of a coupling $\alpha_{\rm latt}$, (*ii*), determination of the spacing a which fixes the energy scale at which $\alpha_{\rm latt}$ has its measured value and finally, (*iii*), compute $\alpha_s(\overline{\rm MS})$ from $\alpha_{\rm latt}$. Major sources of uncertainties are the resolution loss from discretization and the conversion of the bare lattice coupling constant to $\alpha_s(\overline{\rm MS})$ of a continuum scheme. Two new results are available both using $1S$-$1P$ and $1S$-$2S$ quarkonium level splittings in the Υ system to fix the lattice spacing. Two values of different collaborations which obtained $\alpha_s(M_Z) = 0.118 \pm 0.003$ (NRQCD [131]) and $\alpha_s(M_Z) = 0.116 \pm 0.003$ (Fermilab/SCRI [131]) which are dominated by theoretical uncertainties whose largest contribution stems from the matching $\alpha_{\rm latt}$ – $\alpha_s(\overline{\rm MS})$. Tab. 2.2 quotes the average of both values keeping the systematic errors unchanged.

Process	Q [GeV]	$\alpha_s(Q)$	$\alpha_s(M_Z)$	$\Delta\alpha_s(M_Z)$ exp.	theo.	Theory	Ref.	Fit
DIS [ν; BSR]	1.58	$0.375^{+0.062}_{-0.081}$	$0.122^{+0.005}_{-0.009}$	—		NNLO	[105]	yes
DIS [ν; GLSSR]	1.73	0.32 ± 0.05	0.115 ± 0.006	0.005	0.003	NNLO	[106]	yes
τ decays	1.777	0.361 ± 0.046	0.122 ± 0.005	—		NNLO	[8]	
τ decays	1.777	0.349 ± 0.024	0.121 ± 0.003	0.002	0.002	NNLO	[9]	yes
DIS [ν, ℓ; sc. viol.]	5.4	0.200 ± 0.016	0.116 ± 0.005	·	—	NLO	[120]	yes
DIS [ν; F_2]	7.1	0.180 ± 0.014	0.113 ± 0.005	0.003	0.004	NLO	[121]	yes
DIS [HERA; Jets]	10 60		0.120 ± 0.009	0.005	0.007	NLO	[122]	yes
DIS [HERA; F_2]	2 10		0.120 ± 0.010	0.005	0.009	NLO	[104]	yes
$q\bar{q}$ states	5.0	0.203 ± 0.007	0.117 ± 0.003	0.000	0.003	Lattice	[119]	yes
J/ψ + Υ	10.0	$0.167^{+0.015}_{-0.011}$	$0.113^{+0.007}_{-0.005}$	0.001	$^{+0.007}_{-0.005}$	NLO	[123]	
Υ	4.1	$0.233^{+0.045}_{-0.030}$	0.119 ± 0.008	0.002	0.008	NLO	[116]	yes
e^+e^- [σ_{had}]	34.0	$0.146^{+0.031}_{-0.026}$	$0.124^{+0.021}_{-0.019}$	$^{+0.021}_{-0.019}$	–	NLO	[124]	
e^+e^- [ev. shapes]	35.0	0.14 ± 0.02	0.119 ± 0.014	–	—	NLO	[125]	yes
e^+e^- [ev. shapes]	58.0	0.132 ± 0.008	0.123 ± 0.007	0.003	0.007	resum.	[126]	yes
e^+e^- [sc. viol.]	22 91.2	0.126 ± 0.009	0.126 ± 0.009	0.007	0.006	resum.	[127]	yes
$p\bar{p} \rightarrow b\bar{b} + X$	20.0	$0.145^{+0.018}_{-0.019}$	0.113 ± 0.011	$^{+0.007}_{-0.006}$	$^{+0.008}_{-0.009}$	NLO	[115]	yes
$p\bar{p}\, pp \rightarrow \gamma + X$	24.2	$0.137^{+0.017}_{-0.014}$	$0.112^{+0.012}_{-0.008}$	0.006	$^{+0.010}_{-0.005}$	NLO	[128]	yes
$\sigma(p\bar{p} \rightarrow \text{jets})$	30 500		0.121 ± 0.009	0.001	0.009	NLO	[114]	yes
$e^+e^- \rightarrow$ Z:								
[Γ(Z $\rightarrow$ had.)]	91.2	0.124 ± 0.005	0.124 ± 0.005	0.004	0.002	NNLO	[111]	
[ev. shapes]	91.2	0.119 ± 0.006	0.119 ± 0.006	0.001	0.006	NLO	[129]	
[ev. shapes]	91.2	0.122 ± 0.006	0.122 ± 0.006	0.001	0.006	resum.	[129]	yes
[EW fit]	91.2	0.1202 ± 0.0033	0.1202 ± 0.0033	·	·	NNLO	[112]	yes
e^+e^- [ev. shapes]	133.0	0.112 ± 0.009	0.118 ± 0.009	0.003	0.009	resum.	[130]	yes
Average	91.2		0.1190 ± 0.0020	0.0001	0.0020			

Table 2.2: Summary of α_s measurements at various energy scales Q evolved to M_Z.

2.6.1 Combined Value for $\alpha_s(M_Z)$

The mean value of the measurements presented in Table 2.2 is calculated via χ^2 minimizations over $N_{\rm meas}$ measurements $\alpha_s^{(i)}$, $i = 1, \ldots, N_{\rm meas}$ as explained below. The measurements entering into the average are denoted in the last column of Tab. 2.2. They are chosen in order to minimize the correlated experimental input, *i.e.*, only the best (or most recent) measurement for a given data set and method is used.

Defining

$$\chi^2 = \sum_{i,j=1}^{N_{\rm meas}} (\alpha_s^{(i)} - \langle\alpha_s\rangle) C_{ij}^{-1} (\alpha_s^{(j)} - \langle\alpha_s\rangle) , \tag{2.91}$$

with the mean value $\langle\alpha_s\rangle$ to be determined and the covariance matrix C_{ij} defined as

$$C_{ij} = \begin{cases} (\Delta_{\rm stat}\alpha_s^{(i)})^2 + (\Delta_{\rm sys}\alpha_s^{(i)})^2 & \text{for } i = j \\ \rho^2\, \Delta_{\rm sys}\alpha_s^{(i)} \Delta_{\rm sys}\alpha_s^{(j)} & \text{for } i \neq j \end{cases} , \quad i,j = 1, \ldots, N_{\rm meas} , \tag{2.92}$$

where the correlation coefficient between the theoretical (and in some cases experimental) errors of the measurements is estimated from the expectation $\chi^2/\text{d.o.f.} = 1$ (this is not true if the correlations are too large since then the "real" degree of freedom ia smaller than the naive one). The vanishing first derivative and the second derivative of Eq. (2.91) lead to

$$\langle\alpha_s\rangle = \sum_{i,j=1}^{N_{\rm meas}} C_{ij}^{-1}\alpha_s^{(i)} \Big/ \sum_{i,j=1}^{N_{\rm meas}} C_{ij}^{-1} , \tag{2.93}$$

$$\Delta\langle\alpha_s\rangle = \left(\sum_{i,j=1}^{N_{\rm meas}} C_{ij}^{-1} \right)^{-1/2} , \tag{2.94}$$

yielding the well known weighted mean formula if correlations are absent.

First, in order to estimate the correlations consistently, several subgroups are attributed to the measurements. These subgroups are (the averages of the measurements of each subgroup and the estimated correlations, obtained using Eqs. (2.93) and (2.94), are given in parentheses): the DIS measurements ($\alpha_s(M_Z) = 0.1154 \pm 0.0038$, $\rho = 60\%$), the measurements using event shape variables ($\alpha_s(M_Z) = 0.1228 \pm 0.0058$, $\rho = 80\%$) and the measurements from $p\bar{p}$ collisions ($\alpha_s(M_Z) = 0.1173 \pm 0.0083$, $\rho = 80\%$). The results are averaged with the remaining measurements which are individually more characteristic: α_s from τ decays taken from Refs. [8, 9][5] α_s from Lattice calculations, α_s from Υ quarkonia states and α_s from the combined electroweak fit.

Averaging the results of the subgroups with the above measurements and assuming them to be still 30% correlated yields the combined α_s value at M_Z

$$\langle\alpha_s(M_Z)\rangle = 0.1190 \pm 0.0020 , \tag{2.95}$$

---

[5] The results given in these references were obtained using massless leptonic branching ratios (universality improved) which changed quite a lot since then: $B_\ell = 0.1809 \pm 0.0064$ [8] and $B_\ell = 0.1817 \pm 0.0019$ [9] compared to $B_\ell = 0.1779 \pm 0.004$ from Eq. (1.13). The published values for $\alpha_s(M_\tau)$ are therefore renormalised to the present B_ℓ value using the relation (10.23): $\Delta\alpha_s \simeq 0.44\Delta R_\tau$.

with a χ^2/d.o.f. = 3.3/6. The value of $\langle\alpha_s(M_Z)\rangle$ and its error is depicted as shaded band in Fig. 2.10.

Part II

Experiment and Data Analysis

Chapter 3

The Experimental Conditions

This analysis is based on data accumulated during 1991–1994 with the ALEPH detector, installed, as the experiments DELPHI, L3 and OPAL, at one of the four collision points of the Large Electron-Positron Collider (LEP) at CERN. The LEP is a storage ring of 26.66 km in circumference and some 100 meters underground which is is situated on the French-Swiss border near Geneva, Switzerland. The scientific aim of the first phase of LEP (LEP I) was the performance of high precision tests of the electroweak Standard Model with the preference on high statistics obtained on the Z peak at 91.2 GeV center-of-mass (c.m.) energy ("Z-factory"). In addition, energy scans were carried out in the years 1991, 1993 and parts of 1995 in order to measure the Z lineshape. The second phase (LEP II) started in 1996 with an c.m. energy of about 133 GeV and terminated its first year with 172 GeV. It is dedicated to a precise measurement of the cross section of $e^+e^- \rightarrow \mathrm{W}^+\mathrm{W}^-$ events and the $\mathrm{W}^\pm$ mass as well as to searches for new particles and phenomena (Higgs, supersymmetry, etc.). The integrated luminosity seen by the experiments between 1993 and 1996 as a function of the time is shown in Fig. 3.2. The total integrated luminosity used in this analysis (1991–94) amounts to 134.1 pb^{-1} produced with an average luminosity of the order 10^{31} $\mathrm{cm}^{-2}\mathrm{s}^{-1}$.

The CERN accelerator complex is shown in Fig. 3.1. To accelerate the electron and positron beams to Z peak energies of each 45.6 GeV, electrons are preaccelerated after being produced to 200 MeV in the LINAC Injector of LEP (LIL). Positrons are then produced from converting electrons passing a tungsten target. In a second part of LIL electrons and positrons are accelerated to 600 MeV, before being injected into the Electron-Positron Accumulator (EPA), where they are collected separately in bunches and cooled by synchrotron radiation. These bunches are sent to the Proton Synchrotron (PS) and after being accelerated to 3.5 GeV they pass to the Super Proton Synchrotron (SPS), where they are accelerated to 20 GeV, before being injected into LEP and reaching their nominal energy of 45.6 GeV.

The energy loss ΔE_{sync} of an electron per LEP turn (radius $\rho_{\mathrm{LEP}} \simeq 4.2$ km) due to synchrotron radiation is given by

$$\Delta E_{\mathrm{sync}} = \left(8.85 \times 10^{-5}\ \mathrm{m\,GeV}^{-3}\right) \frac{E_e^4}{\rho_{\mathrm{LEP}}} \simeq 90\ \mathrm{MeV}\ .$$

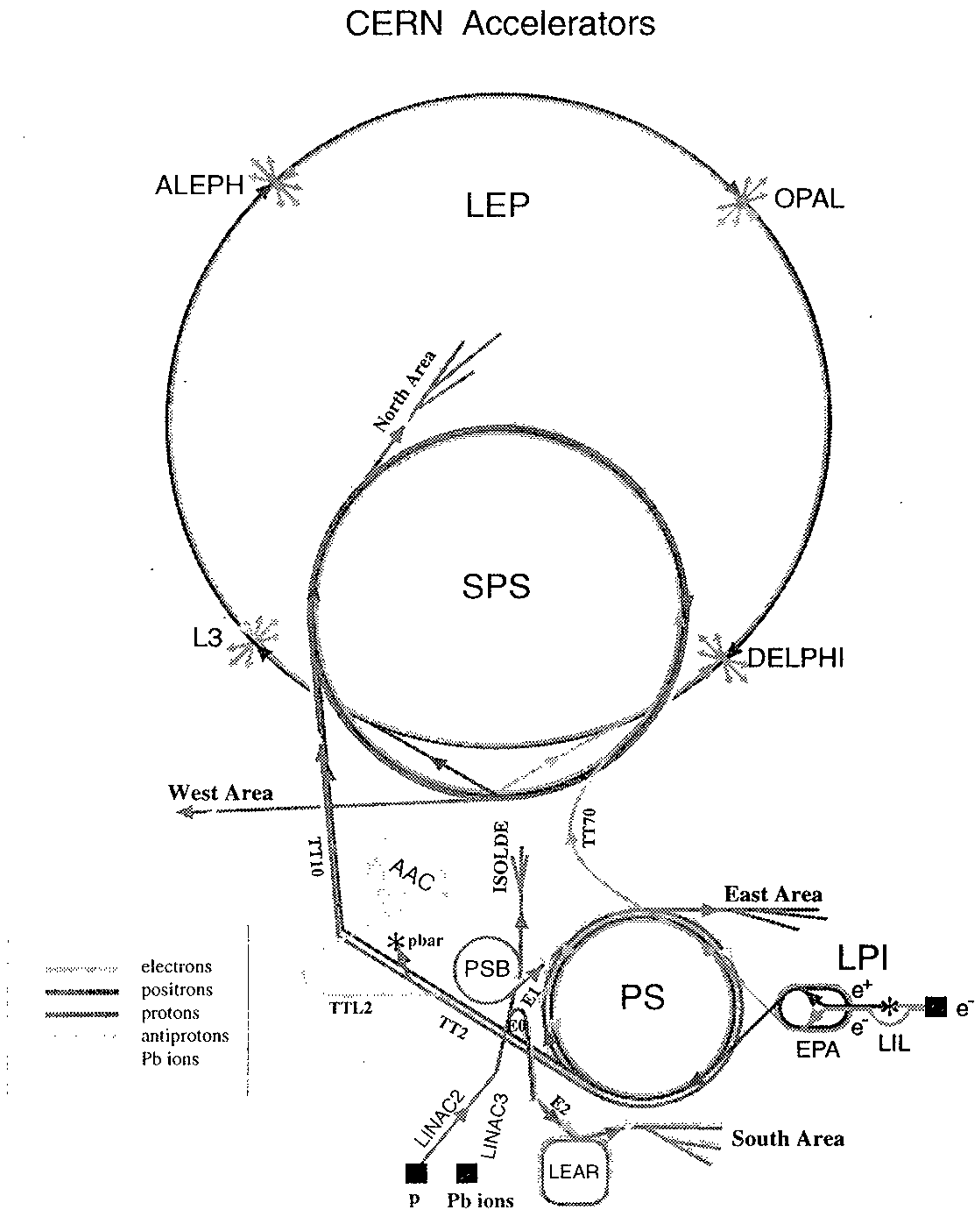

LEP: Large Electron Positron collider
SPS: Super Proton Synchrotron
AAC: Antiproton Accumulator Complex
ISOLDE: Isotope Separator OnLine DEvice
PSB: Proton Synchrotron Booster
PS: Proton Synchrotron

LPI: Lep Pre-Injector
EPA: Electron Positron Accumulator
LIL: Lep Injector Linac
LINAC: LINear ACcelerator
LEAR: Low Energy Antiproton Ring

Rudolf LEY, PS Division, CERN, 02.09.96

Figure 3.1: *CERN accelerator complex.*

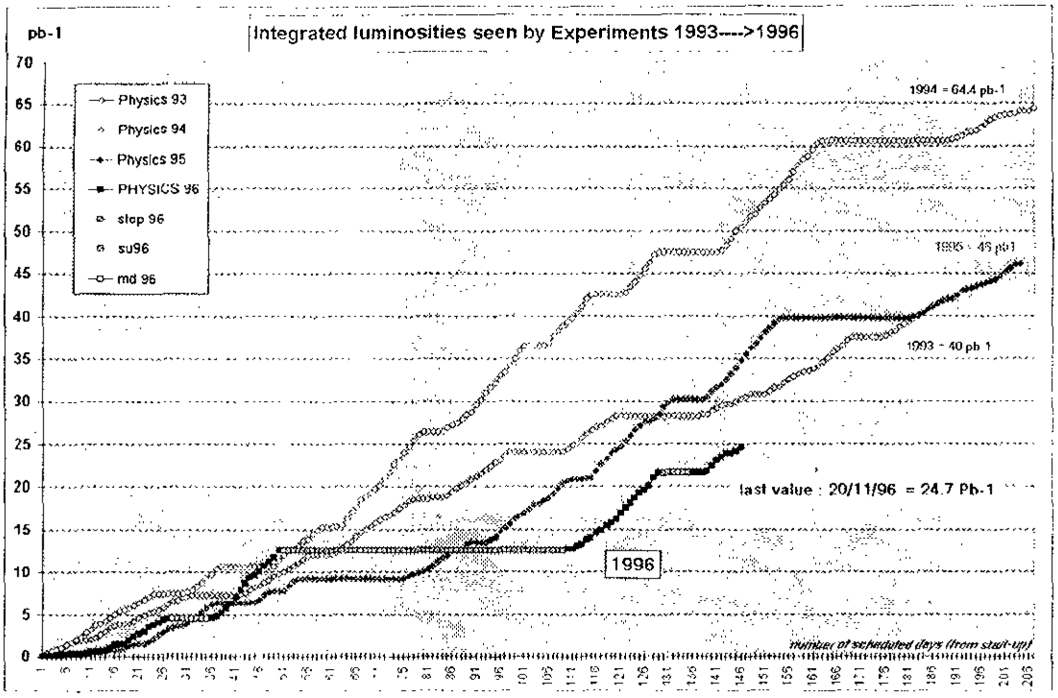

Figure 3.2: *LEP integrated luminosity between* 1993 *and* 1996.

with the energy E_e of the electron. This energy loss has to be recovered every turnaround in the LEP storage ring by continuous acceleration in RF cavities.

3.1 The ALEPH Detector

ALEPH is a particle detector consisting of several subdetectors designed for an optimal reconstruction and identification of particles produced in high energy e^+e^- collisions. The features relevant for this analysis are briefly described here, while a detailed description of its components and performance can be found in Refs. [132, 133, 134]. Typical events are complex, having many particles distributed in jets over the entire sphere, while typical event rates (of interesting events) at the Z peak are lower than 1 Hz. Thus, as much information as possible should be collected over a wide ranged solid angle. The large geometrical acceptance has been achieved by a cylindrical arrangement around the beam pipe, with the interaction point in the centre (see Figs. 3.3 and 3.4). The following elements represent the main components of ALEPH:

- A **magnetic field** of 1.5 Tesla parallel to the beam axis (z-axis) is created by a superconducting coil, 6.4 m long and 5.3 m in diameter. The magnet has an axial symmetry in order to avoid azimuthal field components. The coil consists of a main solenoid and two compensating coils at both ends of the main solenoid to provide the field uniformity. The helium cooled niobium-titanium superconductor conducts a 5000 A current. In order to perform a precise track momentum calibration, radial field components ($B_r/B_z < 0.4\%$) as well as azimuthal field components ($B_\phi/B_z < 0.04\%$) and field inhomogeneity ($\Delta B_z/B_z < 0.2\%$) are minimized.

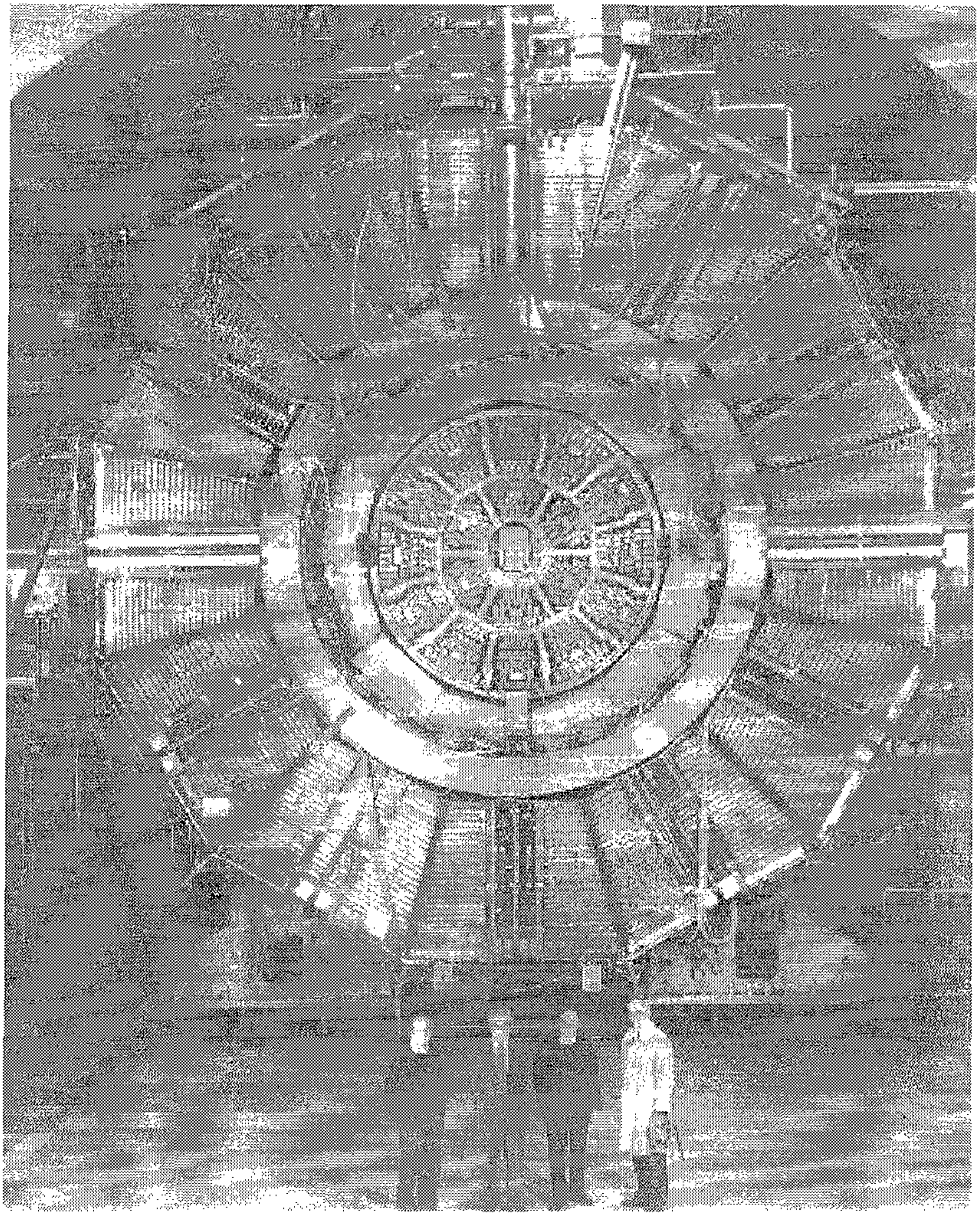

Figure 3.3: *Photo of the open ALEPH detector. Shown are from the centre to outside: the TPC readout end-plate with sectors, the 12 ECAL modules, the superconducting coil of the magnet and the 24 HCAL modules with each 23 layers.*

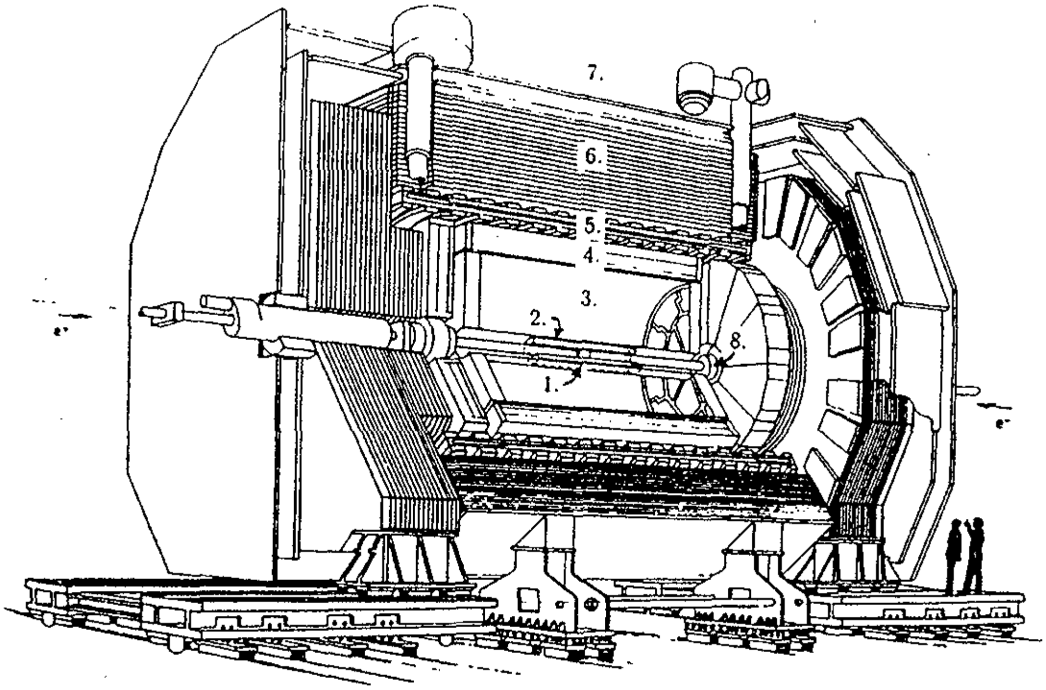

Figure 3.4: *The ALEPH detector: (1) VDET, (2) ITC, (3) TPC, (4) ECAL, (5) superconducting coil, (6) HCAL, (7) muon chambers and (8)luminosity calorimeters LCAL and SICAL.*

The iron return yoke is instrumented by limited-streamer tubes so that it serves as an active **hadron calorimeter (HCAL)**.

Outside the last iron slab of the calorimeter are two double layers (inner and outer **muon chambers**) of limited-streamer chambers (wire counters) separated by 50 cm. They serve to record the position and angle of muons that have penetrated the iron. The two sets of coordinates of one double-layer are combined to yield a space point. A track is defined to have a hit in the muon chambers if at least one of the two double-layers yields a space point whose distance from the extrapolated track is less than four times the estimated standard deviation from multiple scattering.

Inside the coil is found the **electromagnetic calorimeter (ECAL)** designed for the highest possible angular resolution (granularity) for the photon reconstruction and electron identification. It consists of alternating layers of lead and proportional tubes read out in projective towers, each subdivided into three segments in depth.

The central detector for charged particles is a **time-projection chamber (TPC)**, 4.4 m long and 3.6 m in diameter, providing up to 21 three-dimensional space-points of each track helix and up to 340 ionization measurements (dE/dx) for a track, which is useful, in particular, for particle identification in τ decays.

The TPC surrounds the **inner tracking chamber (ITC)**, which is a conventional axial-wire drift chamber with inner and outer diameters of 13 cm and 29 cm, respectively, and a length of 2 m. The ITC has 960 cells distributed over 8 concentric layers parallel to the beam axis. Each cell consists of one sense wire at a positive potential between 1.8 kV and 2,5 kV surrounded by six field wires at earth potential. It thus provides 8 track coordinates with an accuracy of 150 μm in $r - \phi$, which is the plane transverse to the beam axis, and a trigger signal for charged particles that come from the interaction point. A measurement of the z-coordinate of 7 cm accuracy is provided by the time difference for the pulse to reach the two end-points of the wire.

Closest to the beam pipe there is a double-sided silicon microstrip **vertex detector (VDET)** measuring for each track two pairs of coordinates 6.3 cm and 10.7 cm away from the beam axis, with an accuracy of typically 12 μm in ϕ and 12 to 22 μm in z. Points are reconstructed through the average position of the extrapolated ITC and TPC tracks, weighted by the deposited charge in the VDET. The track helix is then refitted taking into account the new coordinates. The improvement of the momentum and impact parameter resolution by virtue of the additional VDET information is shown in Tab. 3.2. For the high energy use at LEP II the VDET has been replaced by a larger model to improve the geometrical acceptance and also the radiation sensitivity was reduced to cope with the higher radiation level at LEP II.

The LEP luminosity is measured by means of a sampling **luminosity calorimeter (LCAL)**, consisting of lead sheets and wire chambers grouped in 3 stacks. It provides an energy (angular) resolution of about $15\%/\sqrt{E/\text{GeV}}$ ($2.5\text{mrad}/\sqrt{E/\text{GeV}}$). In addition, a cylindrical silicon tungsten luminosity calorimeter (**SICAL**) was installed in 1992 on each side of the interaction region enclosing the beam pipe. These devices permit the determination of the absolute luminosity to a systematic précision of 0.12% (experimental) and 0.16% (theoretical) (1994 results) [135].

The central part of the **beam pipe** is a cylinder with an outer radius of 5.4 cm made of beryllium in order to reduce the radiation length[1] ($0.00312X_0$ at normal incidence). Then outgoing in the beam direction, after some connecting parts, the material becomes aluminium with $0.29X_0$.

The geometrical characteristics and the thickness of the ALEPH subdetectors are given in Tab 3.1:

3.1.1 The Trigger

Understanding the efficiency of the trigger is crucial in many analyses at LEP which demand precise measurements of the cross sections. The ALEPH trigger is a three-level

---

[1] In dealing with electrons and photons at high energies, it is convenient to measuré the thickness of the material in units of the radiation length X_0. This is the average distance over which a high-energy electron loses on average all but $1/e$ of its energy by bremsstrahlung, and is the appropriate scale length for describing high energy electromagnetic cascades.

	VDET	ITC	TPC	ECAL	Magnet	HCAL
Length of cylinder (cm)	21	200	470	477	700	700
Inner radius (cm)	6.3	12.8	31	185	248	300
Outer radius (cm)	10.8	28.8	180	225	292	468
X_0 for $\|cos\,\theta\| = 0$	0.041	0.014	0.071	21.5	1.6	
Acceptance ($\|cos\,\theta\|$)	0.85	0.97	0.95	0.97		0.92 .

Table 3.1: *Geometrical dimension and acceptance of the subdetectors.*

system which is sensitive to single particles or single jets. At first and second level the trigger consists of specially built hardware to look for signals in coarse segments of the subdetectors.

The **Level-one trigger** decides within 5 μs (compared to about 11μs between two beam crossings). It requires a minimal ECAL energy of 6 GeV in the barrel, 3 GeV in one end-cap or 1.5 GeV in both end-caps. To trigger for electrons, an ITC track is roughly extrapolated to an ECAL module with a deposited energy larger than 200 MeV. Muon tracks are triggered by the extrapolation of an ITC track to the HCAL. Furthermore, an event is triggered when two tracks are back-to-back in the ITC or if energy is deposited in the two luminosity calorimeters.

The **Level-two trigger** has a deadtime of 50 μs (the time needed for the electron drift in the TPC). It refines the Level-one trigger in searching for tracks pointing to the interaction zone. If the Level-one decision cannot be confirmed, the readout is stopped and cleared.

The **Level-three trigger** is applied only after readout. All detector components are used and software analysis can be performed in order to separate genuine e^+e^- interactions from background. The maximum allowed rate out of the Level-three trigger is 1 Hz.

The trigger efficiency for hadronic and leptonic Z decays is better than 99.99%, with an uncertainty of less than 0.01%. Bhabha events are triggered with an efficiency of $(99.7 \pm 0.2)\%$.

3.1.2 The Time-Projection Chamber

The TPC is the heart piece of the ALEPH tracking system. It consists of a cylindrical drift volume with a central electrode and planar wire chambers at the two ends as schematically depicted in Fig. 3.5. The axis of the TPC is parallel to the magnetic field. The electric field extends from each end-plate towards the central membrane that divides the chamber into two halves. The electrons produced by ionization of the argon (91%) and methane (9%) gas mixture (at atmospheric pressure) by traversing charged particles drift towards one end-plate, where they are collected. Their arrival position and time are measured by a system of proportional wire chambers (sectors) which are capacitively coupled to cathode readout pads. There are 6 inner and 12 outer sectors on each end-plate.

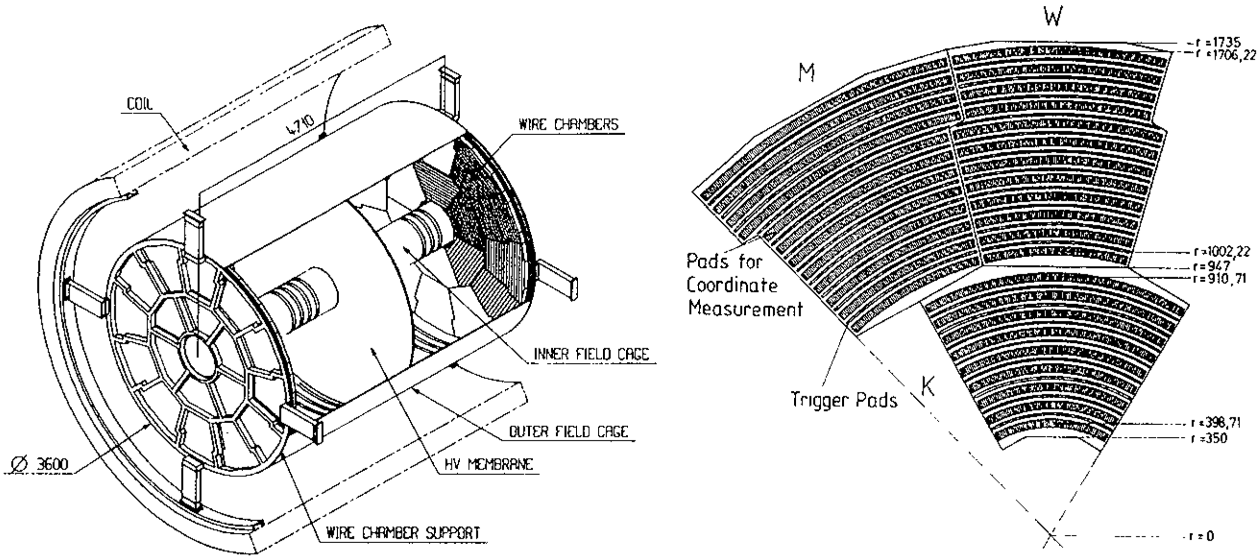

Figure 3.5: *A schematic view on the TPC devices (left figure) and on the pad distribution on an end-plate (right figure).*

The sectors have concentrical rows of pads in order to provide a 3-dimensional coordinate measurement. The angular acceptance is limited to $|\cos\theta| < 0.96$. It is important to assure a good relative alignment of both end-plates since misalignment would give rise to wrongly physically interpreted effects, *e.g.*, a violation of CP symmetry in τ decays due to a non-vanishing average value $\langle \phi^- - \phi^+ \rangle$ of positive and negative tracks [136]. The alignment is tested with $Z \to \mu^+\mu^-$ events (see Section 3.1.3).

The quality of the track reconstruction depends critically on the precise knowledge of systematic distortions of the tracks during the drift of the ionization showers towards the end-plates. Distortions due to inhomogeneities of the magnetic and electric fields are determined from a magnetic field map and from laser-induced tracks. The z-coordinate is obtained from the drift time the electrons need to arrive at the end-plate and the known drift velocity[2], The $r - \phi$-coordinates are obtained from the interpolation of the signals induced on cathode pads which are located precisely on the sectors. The TPC measures 21 tridimensional space points on each track traversing the inner and the outer field cage yielding a best $r - \phi$ spatial resolution of 180 μm and about 1 mm in z.

The procedure for the charged track reconstruction consists of several stages. During the first stage, the coordinates of hits and their errors (obtained from preliminary track parameters) are determined for each tracking device VDET, ITC and TPC. Then, these coordinates are fitted to a helix, using a filtering procedure which takes into account multiple scattering between the measurements, starting from the TPC, where the maximum space information is provided, to the ITC and then to the VDET. The TPC track reconstruction inefficiency due to track overlap and cracks has been measured from hadronic Z

---

[2] The drift velocity is measured using a laser calibration system and a comparison of the track polar angle reconstructed in the TPC to the one observed in the vertex detector.

	Transverse Momentum	Impact parameter	
Tracking device used	$\Delta p_T/p_T^2$ (GeV/c)$^{-1}$	$r-\phi$ (μm)	z (μm)
TPC	1.2×10^{-3}	310	808
TPC + ITC	0.8×10^{-3}	107	808
TPC + ITC + VDET	0.6×10^{-3}	23	28

Table 3.2: *Track momentum and impact parameter resolution using the TPC only, using the TPC and the inner tracking chamber and using all available tracking information.*

decays to be 1.4%, which is well reproduced by the ALEPH detector simulation. Tab. 3.2 shows the momentum and impact parameter resolution of the ALEPH tracking system. The measurement resolution is studied with low radiating $Z \to \mu^+\mu^-$ events, where the nominal muon momentum is the beam energy. Low energy information on the impact parameter resolution is obtained from hadronic Z decays.

The TPC is supplied with sense wires across the sectors on each end-plate which serve to measure the specific energy loss by ionization (dE/dx) of a particle travelling through the TPC. The ionization of each charged particle is sampled with a sense-wire spacing of 4 mm, giving a total of 340 possible measurements for one track. The dE/dx measurement is an important tool for the identification of charged particles originating from τ decays. The value of dE/dx versus the particle momentum and the separation power using dE/dx in units of 1σ between electrons, pions, kaons and protons are shown in Fig. 3.6.

An important point in the hadronic τ spectral function analysis is a good knowledge of the reconstruction efficiency of multi-prong τ decays which are in general highly collimated due to the large $M_Z^2/4M_\tau^2$ and thus the strong boost of the produced τ's. The pattern recognition in the $\tau^- \to 2\pi^-\pi^+\nu_\tau$ events has been studied in Ref. [137], where it was found that in about 10% of τ three-prong decays, only two good tracks are reconstructed. These details are well reproduced by the detector simulation as shown in Section 7.2.

3.1.3 Alignment of the Tracking Devices

The alignment of the ALEPH tracking devices uses kinematically well measured tracks with maximal compatibility between the reconstructed hits and the helix of a trajectory in the axial magnetic field. The procedure is, first, to align the three detectors in a global manner, then the TPC sectors are aligned with respect to each other and the VDET silicon wafers are aligned among them. In an iterative procedure global and subdetector alignments are repeated until an overall convergence is found. The tracks used for the alignment originate from: cosmic rays, μ pairs and hadronic Z decays.

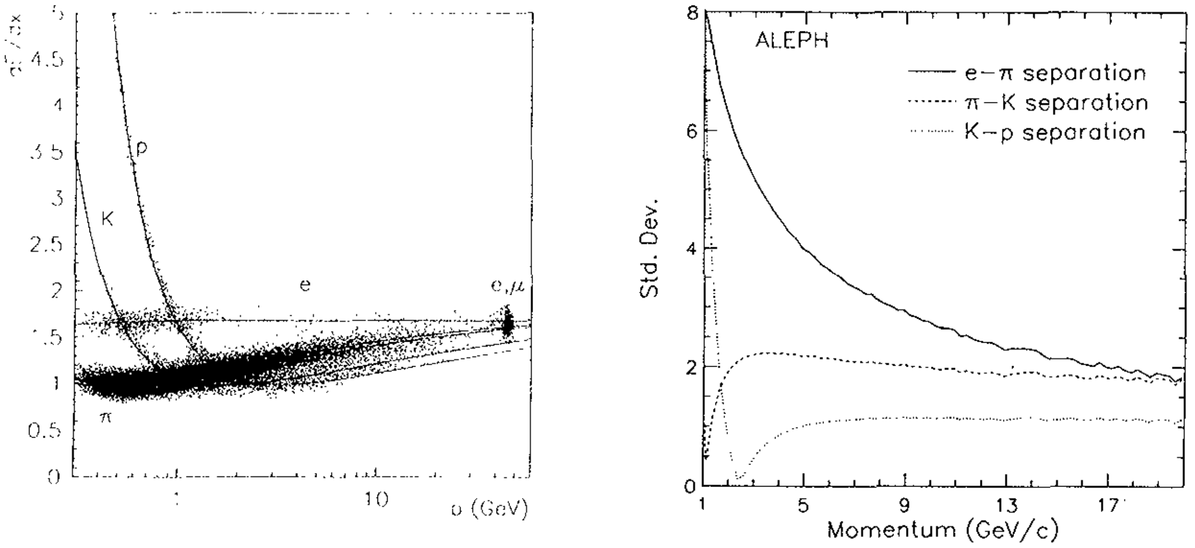

Figure 3.6: *Performance of dE/dx in the ALEPH TPC. The left hand plot is the measured ionization loss as a function of momentum, showing the dE/dx for different particles. The right hand plot depicts the dE/dx separation for pairs of particle types in units of 1σ.*

3.1.4 The Electromagnetic Calorimeter

The ALEPH electromagnetic calorimeter is a lead/wire-chamber sampling device with a nominal thickness of $22X_0$. It is arranged as a barrel surrounding the TPC inside the magnetic coil, closed at both ends with end-caps as shown in Fig. 3.7. The two types of subdetector elements — barrel and end-caps — are divided into modules, each covering 30° in azimuthal angle, the endcap modules having a 15° rotation with respect to the barrel modules. The inactive zones ("cracks") between the ECAL modules represent 2% of the total solid angle in the barrel and 6% in the endcaps. Fig. 3.8 shows the number of reconstructed photons in the barrel versus ϕ. The minima indicate the position of the ECAL cracks.

An electromagnetic shower develops, for an incident of a particle, in the lead sheets (see Fig. 3.7); the processes that govern the shower development are the energy loss of electrons emitting bremsstrahlung and photon conversion into an e^+e^- pair. The shower deposits in the active volume only a fraction of its energy by ionizing the gas, which is a mixture of 80% xenon and 20% carbon dioxyde, in the proportional wire chambers. The ionization is then amplified in avalanches around the wires and the energy is measured via capacitive coupling to cathode pads with dimensions of 30×30 mm^2. Signals obtained with cathode pads are also used to measure the position of the electromagnetic shower, while signals from the wire planes provide a complementary measurement of deposited energy, a low-noise trigger timing and the energy calibration. More details concerning the ECAL energy calibration is found in Section 7.1.2.

The cathode pads are connected internally to form "towers" pointing to the interaction

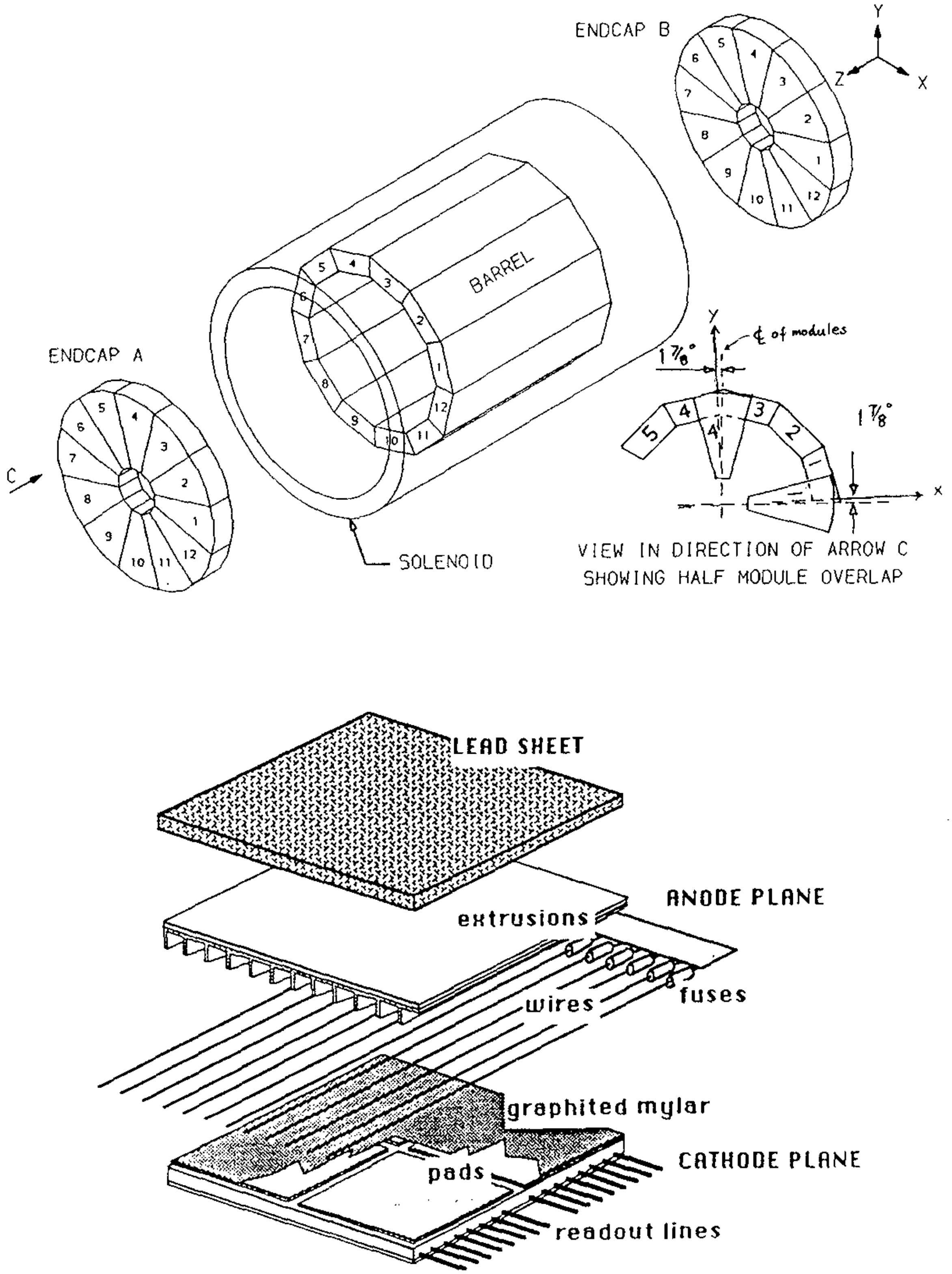

Figure 3.7: *The ECAL: schematic overall view (upper figure) and electromagnetic stack layer (lower figure).*

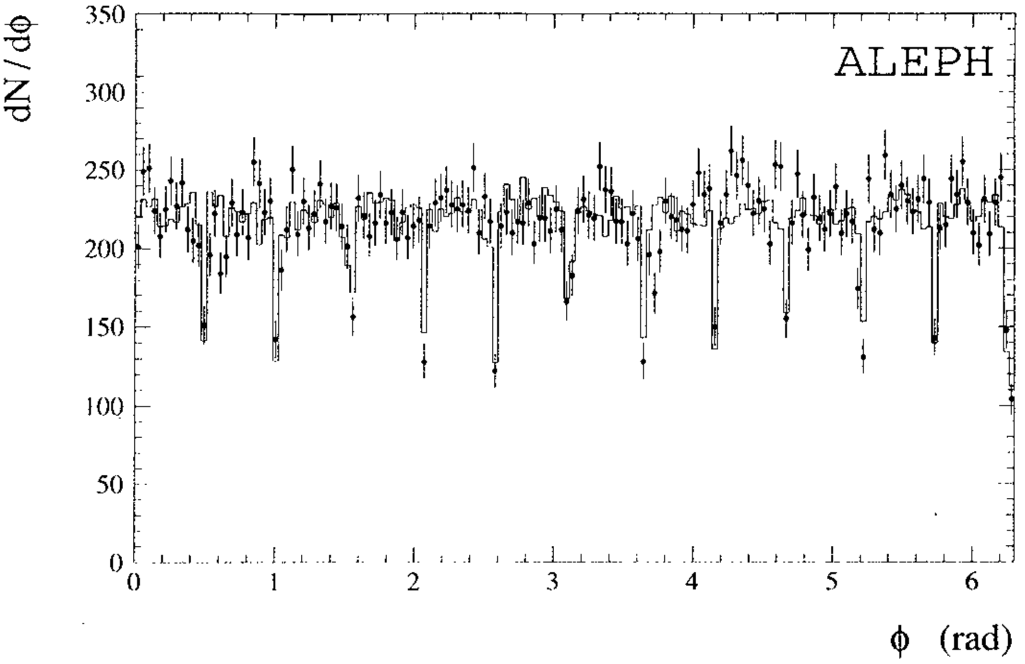

Figure 3.8: *Number of reconstructed photons with* $E_\gamma > 5$ *GeV in the barrel as a function of the azimuthal angle* ϕ *for data (points with error bars) and Monte Carlo simulation. The minima indicate the position of the* 12 *ECAL cracks.*

zone. Each tower is read out in three stacks in depth ("storeys") of 10, 23 and 12 layers, corresponding to 4, 9 and 9 radiation lengths, respectively. There are 74 000 such towers, each covering a solid angle of 0.92° × 0.92°. This high granularity is crucial for the identification of electrons, photons and π^0's which are highly collimated in τ decays. The energy and angular resolution of the ECAL, measured with electrons from Bhabha events, two photon events and from τ decays, read

$$\begin{aligned} \frac{\Delta E}{E} &= 1\% \oplus \frac{18\%}{\sqrt{E/\mathrm{GeV}}} \\ \Delta\phi = \frac{\Delta\theta}{\sin\theta} &= 0.32 \oplus \frac{2.7}{\sqrt{E/\mathrm{GeV}}}\ \mathrm{mrad}\ . \end{aligned}$$

The efficient photon finder and good angular resolution of the ECAL due to the fine granularity compensate the middling energy resolution. For example, the energy resolution of low energy photons originating from a π^0 decay can be improved by a factor of two by means of a constrained fit to the known π^0 mass. Many details about the photon and π^0 reconstruction are found in the following Chapter 4.

3.1.5 The Hadron Calorimeter

The large iron structure that constitutes the main support of ALEPH and collects the return flux of the magnetic field also acts as the absorber for hadrons produced in the final states. The iron is split into self-supporting slabs spaced by air gaps in which layers of plastic streamer tubes are inserted. The main structure is subdivided into a central barrel and two end-caps.

The hadron calorimeter serves two purposes: it is used, together with the ECAL, to measure hadronic energy deposits, and it is part of the muon identification system since strong interacting hadrons are filtered from minimal-ionizing muons that are afterwards detected by the streamer tubes of the muon chambers. It consists of 23 layers of streamer tubes separated by the iron slabs. The total iron thickness is 120 cm at $\theta = 90°$ with an interaction length[3] of $7.16\lambda_{\rm int}$ at $\theta = 90°$. The calorimeter is constructed from 36 modules, 24 in the barrel and 6 in each end-cap, and is read out capacitatively in 4788 projective towers each covering a solid angle of typically $3.7° \times 3.7°$, which is 16 times larger than the ECAL towers. When hadrons interact with matter, they produce either π^0's which create electromagnetic showers, charged hadrons (mainly $\pi^\pm$'s) interacting with surrounding nuclei but also neutrons which are undetected and give rise to an energy leakage.

A digital (*yes* or *no*) signal is recorded for each of the 1 cm wide tubes, providing a two-dimensional projection of the energy deposition. This is used for the identification of muons, and, together with the towers, in the energy-flow algorithm for the reconstruction of the total energy and multiplicity of an event (Section 4.1). In addition, trigger signals are derived from the wires of the tubes.

The energy calibration is done using $Z \to \mu^+\mu^-$ events, to fix the overall energy scale, and hadronic Z decays to intercalibrate the calorimeter modules. The calibration must correct for dead zones (cracks) and the angular dependence of the signal. The tower information is clusterized similarly to the ECAL yielding a mean of 9 clusters per hadronic event. The HCAL energy resolution measured with pions is

$$\frac{\Delta E}{E} = \frac{85\%}{\sqrt{E/\mathrm{GeV}}} \; .$$

3.2 Analysis Tools

A huge package of analysis tools is provided by the ALEPH Collaboration to translate the raw detector response into proper analysis variables and to simulate the physical processes and the measurement procedure.

3.2.1 Event Reconstruction

The event reconstruction builds friendly objects and variables out of the raw data acquisition, *e.g.*, tracks, impact parameters, secondary vertices and calorimeter clusters. The

---

[3] One interaction length $\lambda_{\rm int}$, defined as

$$\lambda_{\rm int} = 35\ \mathrm{g\,cm}^{-2} A^{-1/3} \; ,$$

where A is the atomic weight of the penetrated medium, is the mean distance between two nuclear interactions. In a given medium, one has $\lambda_{\rm int} > X_0$.

reconstruction is performed by the program JULIA:

> Tracks are reconstructed by fitting trajectories of charged particles to the measurement points provided by TPC, ITC and VDET. The TPC wires are analysed in order to extract the dE/dx information. The combined fit of the measurements in the tracking devices provides also the track's impact parameters d_0 and z_0, defined as the minimal distance in the $r-\phi$ plane between the primary vertex and the track helix (point of closest approach (p.c.a.)) and the z coordinate of the p.c.a., respectively.
>
> Secondary vertices are formed for particles with opposite charges.
>
> Energetic storeys of the ECAL are combined to clusters and corrected for calibration and geometrical effects. In addition, effects from the minimum energy threshold and leakage (lost energy) are taken into account. The electromagnetic calorimeter suffers from a non-linear response signal due to saturation of the charge collection in an avalanche. The effect increases with the cluster energy and can be parameterized by the approximative formula
>
> $$E_{\text{true}} \simeq E_{\text{meas}}(1 + aE_{\text{meas}}) \ ,$$
>
> with the saturation constant $a = (8.0 \pm 0.6) \times 10^{-5}$ [138] measured using the ratio of energy over momentum for electrons in data to the Monte Carlo simulation.
>
> In a similar way to electromagnetic clusters, HCAL clusters are formed by combining energetic tubes. In addition, near ECAL and HCAL clusters are associated and both are associated to near extrapolated tracks.
>
> For an easy access to the detector information, JULIA converts the raw detector response into "physical variables" like energies, momenta or geometrical distances and provides error matrices for the fitted tracks. These variables are retrievable via the routine ALPHA. The visualization of the detector response and reconstructed (data and Monte Carlo) events is performed by the program package DALI.

3.2.2 Monte Carlo Simulation

Important for the analysis, in order to extract physical phenomena, distributions and constants from the measurement, is the possibility to compare measured data to a simulation which contains both physical input of known processes and the detector response. Using such a simulation it is even possible to directly extract physical distributions from measured ones by means of unfolding (Chapter 5). It is clear that the quality of the analysis then crucially depends on the exactness of the simulation. The stages of the simulation of $e^+e^- \to Z \to \tau^+\tau^-$ processes are the physical event generation using the program KORALZ followed by the simulation of the measurement procedure realized by GALEPH which is based on GEANT [139].

The Event Generation — `KORALZ`

The physical event generator **KORALZ** [140, 141, 142] provides the simulation of all stages of the τ pair production at c.m. energies around the Z peak and of the successive τ decays based on phenomenological models obeying the known dynamics. Included in the τ pair production are initial and final state radiation as well as the $\gamma - \mathrm{Z}$ interference and electroweak theory which produces, *e.g.*, a τ polarization of about 15% due to the parity violation in weak interactions.

The generation of τ decays uses the program library **TAUOLA**. It takes into account radiative corrections (bremsstrahlung) of the final state leptons, pions and kaons. In addition it contains known decay dynamics, *e.g.*, the $\pi^-\pi^0$ decay via a $\rho^-(770)$ intermediate resonance, $2\pi^-\pi^+$, $\pi^-2\pi^0$ final states via the $a_1^-(1260)$ or the $2\pi^-\pi^+\pi^0$ decay product coming partly from a $\omega\pi^-$ intermediate state. **TAUOLA** simulates explicitly the following τ decays (not all dynamical details are given): $\tau^- \rightarrow \nu_\tau + \ldots$

$e^-\bar{\nu}_e$
$a_1^- \rightarrow 2\pi^-\pi^+$
$2\pi^-\pi^+\pi^0$ (incl. $\omega\pi^-$)
$3\pi^-2\pi^+\pi^0$
$\mathrm{K}^-\pi\pi$

$\mu^-\bar{\nu}_\mu$
$a_1^- \rightarrow \pi^-2\pi^0$
$\pi^-3\pi^0$
$2\pi^-\pi^+3\pi^0$
$\mathrm{K}^0\pi^-\pi^0$

π^-
K
$3\pi^-2\pi^+$
$\mathrm{K}^-\mathrm{K}^0$
$\eta\pi^-\pi^0$

$\rho^- \rightarrow \pi^-\pi^0$
K^*
$\omega\pi^-\pi^0 \rightarrow 2\pi^-\pi^+2\pi^0$
$\mathrm{K}\bar{\mathrm{K}}\pi$
$\omega\pi^- \rightarrow \pi^-\pi^0\gamma$

The Detector Simulation — `GALEPH`

The simulation of the detector response, *i.e.*, the measurement procedure, is performed by the program **GALEPH** which is based on the library **GEANT**. After being fed with the specific geometry of ALEPH, it simulates the creation of new particles and showers during the penetration of matter of an incident charged or neutral particle. For practical reasons (calculation time), the shower simulation in the ECAL is performed using an energy and angular dependent parametrization.

The detector simulation provides in principle all event variables used for an analysis, generates secondary interactions as well as fake photons, etc., and keeps the true, *i.e.*, physical information retrievable so that the distortion due to the finite detector resolution and acceptance can be explicitly drawn after.

Chapter 4

Analysis of τ Pair Events

The topology of τ pairs produced at the Z mass scale is characterised by back-to-back, narrow jets with an average multiplicity much lower than for hadronic Z decays. Thus, candidates are selected by retaining low multiplicity events coming mainly from lepton pair decays of the Z. A detailed description of the τ pair preselection can be found in Ref. [143]. Additional cuts are applied in order to suppress Bhabha (e^+e^-) and dimuon ($\mu^+\mu^-$) background as well as background coming from two-photon processes and cosmic ray events [23]. Details about the cuts to remove hadronic Z decays from the τ pair sample are given in Ref. [24]. The analysis presented here is based on a sample of data recorded by the ALEPH detector at LEP during the years 1991 to 1994. In total 124 358 τ pairs are selected with an overall detection efficiency of $(78.8 \pm 0.1)\%$. This corresponds to an integrated luminosity of 158 pb^{-1}. The following section gives a survey of the selection cuts and algorithms used.

4.1 Selection of τ Pairs

The selection of τ pairs is based on the routine `TSLT` version `02`. An event is subdivided into two hemispheres given by the plane perpendicular to the thrust axis which defines the direction of maximum longitudinal momentum in both jets. The reconstruction of neutral and charged objects in a jet, needed in to calculate the thrust axis, is provided by the energy-flow algorithm (EFLW). The EFLW permits to calculate the visible energy recorded in the track devices and calorimeters by correcting for redundant information. Tracks for example deposit charged and neutral energy, while neutral objects are only reconstructed in the calorimeters. ECAL objects, declared as independent neutral objects, are therefore energetic clusters without associated track. To be finally assigned as neutral object, their energy is required to be larger than 1 GeV (ECAL) and 1.5 GeV (HCAL) in order to reduce the dependence on shower fluctuations which are difficult to simulate and give rise to systematic uncertainties. The number of reconstructed charged and neutral objects represents an important constraint to eliminate $Z \to q\bar{q}$ events owing to the high multiplicity of their final states. Fig. 4.1 (taken from Ref. [144]) shows the average charged multiplicity as a function of the c.m. energy. Low energy experiments, *e.g.*, a τ/charm factory, are limited in precision due to irreducible $q\bar{q}$ background from charm decays. The distribution of the total reconstructed final state invariant mass versus the particle

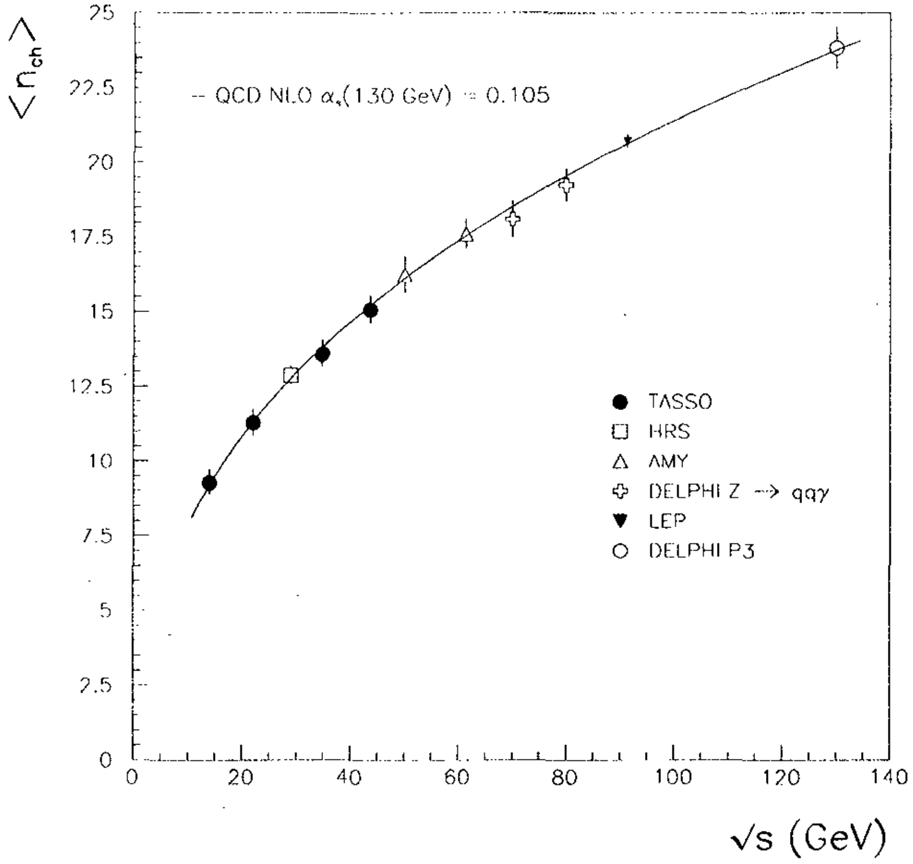

Figure 4.1: *Average charged multiplicity of* $e^+e^- \rightarrow q\bar{q}$ *events. The average multiplicity of* $e^+e^- \rightarrow \tau^+\tau^-$ *decays is* $\langle n_{\rm ch} \rangle_{\tau^+\tau^-} \simeq 2B^2_{1-\rm prong} + 4 \times 2B_{1-\rm prong}B_{3-\rm prong} + 6B^2_{3-\rm prong} \simeq 2.6$.

multiplicity is shown in Fig. 4.2.

Both reconstructed hemispheres are required to have at least one *good* charged track, where a good track fulfills the following quality criteria:

at least 4 coordinates (measurement points) in the TPC,

$|d_0| \leq 2$ cm,

$|z_0| \leq 10$ cm,

a polar angle $|\cos\theta| \leq 0.95$.

In addition, the polar angle $|\cos\theta^*|$ of the τ pair, calculated from the polar angles of the positive and negative hemispheres

$$\cos\theta^* \;=\; \sin\frac{\frac{1}{2}(\theta_+ - \theta_-)}{\frac{1}{2}(\theta_+ + \theta_-)} \;,$$

must obey the condition

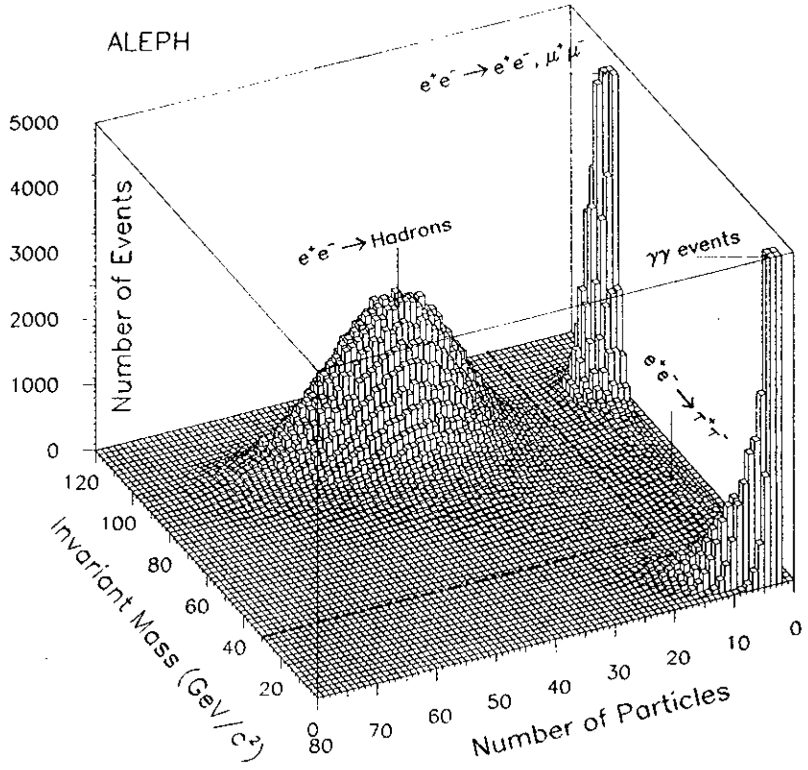

Figure 4.2: *Invariant mass versus the number of particles for all events with at least two tracks, from part of the 1992 data. The two low multiplicity peaks have been truncated.*

$$|\cos\theta^*| < 0.9 \, ,$$

in order to guarantee that the event is reconstructed inside the geometrical acceptance of the detector.

The sources of background after the above preselection are e and μ pairs, $Z \rightarrow q\bar{q}$ and $e^+e^- \rightarrow \gamma\gamma$ events as well as triggered showers from cosmic radiation. Several cuts applied to suppress a background signal from one specific mode aid nevertheless in some cases also for the rejection of other modes with similar signals.

Rejection of $Z \rightarrow q\bar{q}$ Events

Hadronic Z decays are characterised by a high charged and neutral multiplicity of their final states (on the average 20.91 ± 0.22 [127] tracks per event) and a larger opening angle of the tracks compared to $\tau^+\tau^-$ events due to the smaller average boost energy carried by each track.

The most efficient cut concerns the number of reconstructed charged and neutral objects. To pass the selection, an event is required to have

$$2 \leq N_{\mathrm{tracks}} \leq 8 \ ,$$

where $\tau^+\tau^-$ events with more than 8 tracks occur only in less than 0.01% of the cases. In order to maintain a high efficient τ pair selection, the following cuts are exclusively applied if an event is flagged as being non-τ-like, *i.e.*, both hemispheres have at least two good tracks or the invariant mass of the one-track hemisphere exceeds 0.8 GeV/c^2:

The product of neutral and charged EFLW objects of both hemispheres must not be larger than 40.

The charged tracks of both events are required to form narrow jet cones. The sum of the maximum angle θ^i_{op} between two tracks of a hemisphere i is required to be $\theta^1_{\mathrm{op}} + \theta^2_{\mathrm{op}} < 14.3°$.

Rejection of $e^+e^- \rightarrow \gamma\gamma$ Events

Two-photon events stem from the collision of photons radiated by the initial electron-positron pair which itself escapes detection due to the small scattering angles $|\cos\theta$-$\cdot\cdot$. The reconstructed $\gamma\gamma$ event consists therefore of a large acollinearity angle η between the thrust axes of both hemispheres, caused by the, in general, unequal photon energies and the associated boost along the beam axis, and of an amount of missing visible energy. In addition, the transversal momenta p_T of both hemispheres are balanced. The rejection cuts are:

Maximum acollinearity of $\eta < 40°$.

The total visible energy in each hemisphere must exceed 35% of the beam energy.

The transversal momenta are required to be unbalanced (due to the recoil of the two invisible τ neutrinos): $|p^1_T - p^2_T| > 3$ GeV/c .

Z Decays into e and μ Pairs

As this analysis is concerned with hadronic τ decays only, the non-τ background from electronic or muonic Z decays is of minor importance as it is to a large amount reconstructed in the corresponding τ decay channels. Z decays into an e or μ pair have no energy loss from decays into neutrinos. There EFLW energy shows therefore a sharp peak at 45 GeV as can already be seen for the track momenta in Fig. 4.3.

$Z \rightarrow e^+e^-$ events are produced via the interfering s-channel annihilation and t-channel scattering. s-channel events have an angular distribution which is essentially given by $\sim (1 + \cos^2\theta)$ whereas a t-channel electron is sharply peaked in forward, *i.e.*, initial electron direction. Photons originating from radiative t-channel events vanish therefore frequently in the beam pipe. To consider this, the total energy of an hemisphere is calculated by adding the reconstructed energy E_{rec} to the energy of eventually radiated photons E_{rad}, calculated via the deviation of both thrust axes from collinearity. For τ pairs, this total energy is then required to be

$$E_{\mathrm{tot}} = E_{\mathrm{rec}} + E_{\mathrm{rad}} < 1.6 \times E_{\mathrm{beam}} \ .$$

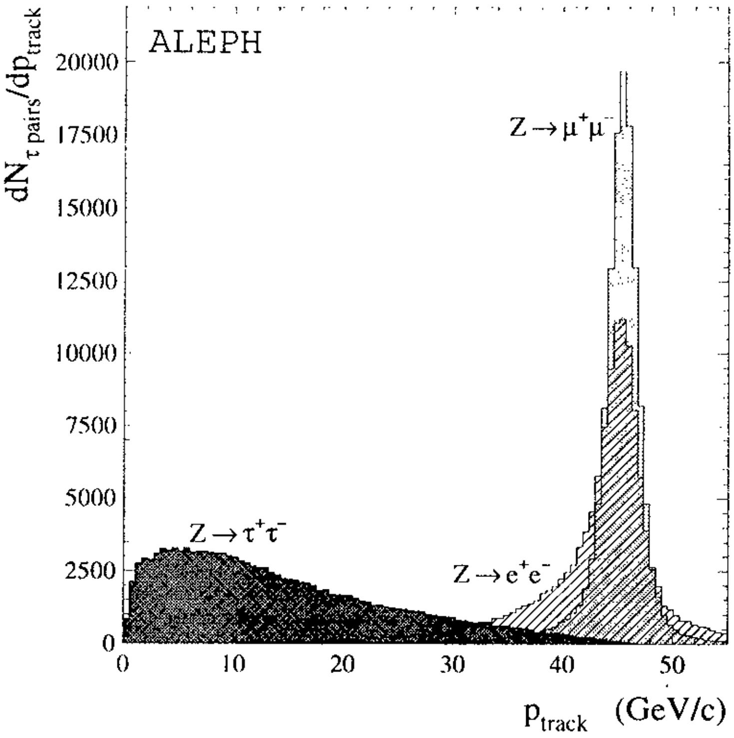

Figure 4.3: *Track momenta distributions of selected e, μ and τ pairs (track with highest momentum in case of multi-prong τ final states). The electron peak is asymmetric due to the more frequent energy loss by bremsstrahlung. In addition, one observes a worse TPC resolution for electrons compared to muons which is due to the t-channel electrons scattered at small angles where less TPC coordinates are measured.*

The above cut is reinforced to $E_{\rm tot} < 1.4 \times E_{\rm beam}$ if the distance between extrapolated track and ECAL crack is smaller than 6 cm, *i.e.*, the ECAL energy measurement is incomplete.

Z → $\mu^+\mu^-$ events have a much lower radiation probability in the final state (see Fig 4.3. They are rejected by requiring

$$E_{\rm track,1} + E_{\rm track,2} < 1.6 \times E_{\rm beam} \ .$$

The following cuts are only applied if the event has a dimuon character (*muon-like*), namely, either if the most energetic track in each hemisphere is identified as muon, or if in one hemisphere the most energetic track is identified as muon and the track momentum on the recoil side exceeds $0.9 \times E_{\rm beam}$. In order to reject these events, one requires

$$E_{\rm track,1} + E_{\rm track,2} < 1.8 \times E_{\rm beam} \ .$$

Additional cuts to reduce persisting background from e and μ cuts have been applied in order to optimize the selection purity of crucial importance for a measurement of the τ leptonic branching fractions. This is comprehensively presented in Ref. [145].

Process	Background (%)
$Z \to e^+e^-$	0.15 ± 0.03
$Z \to \mu^+\mu^-$	0.07 ± 0.02
$\gamma\gamma \to e^+e^-$	0.07 ± 0.02
$\gamma\gamma \to \mu^+\mu^-$	0.08 ± 0.02
four fermion	0.14 ± 0.02
$Z \to q\bar{q}$	0.31 ± 0.09
Cosmics	0.02 ± 0.01
Total	0.84 ± 0.10

Table 4.1: *Non-τ background contamination of the selected τ pair sample on the Z peak. The values are essentially obtained from data studies.*

Rejection of Cosmics

Events originating from cosmic showers in the atmosphere (to a large amount muons) are efficiently rejected by the requirement to pass near to the interaction point:

$|d_0| \leq 1$ cm ,

$|z_0| \leq 5$ cm .

Selection Results

The precise knowledge of the selection efficiency has been of extreme importance for the recent ALEPH branching ratio measurements [23, 24]: in order to obtain the absolute branching ratio of a given exclusive τ decay mode, the number of selected events is divided by the efficiency of the respective channel. Associated errors scale therefore linearily. To reduce possible biases from the Monte Carlo simulation, the efficiency has been tested as far as possible using *tagged* τ-like hemispheres both in data and simulated events and calculating the efficiency of the recoil side. A tagged hemisphere is distinguished thanks to a particularly characteristic τ signal. It is clear that such a method depends strongly on the correlations between both hemispheres. In order to study the effect of these correlations, the recoil hemispheres of the tagged τ-like sample are randomly paired to reform a "complete" τ event. In this way correlations between the two hemispheres are suppressed. This *break-mix* procedure is applied simultaneously to data and Monte Carlo events and the distributions of the cut variables are compared afterwords. The efficiency of cut variables where the correlation between the τ hemispheres is not explicitly used can now directly be measured using the break-mixed data sample. Strongly correlated variables are checked by comparison to the simulation and corrections of the Monte Carlo efficiencies can be deduced.

The final overall τ pair selection efficiency is found to be

$$\epsilon_{\tau^+\tau^-} = (78.83 \pm 0.13)\,\% ,$$

with a non-τ background of $(0.84 \pm 0.10)\%$, while the non-τ background in the purely

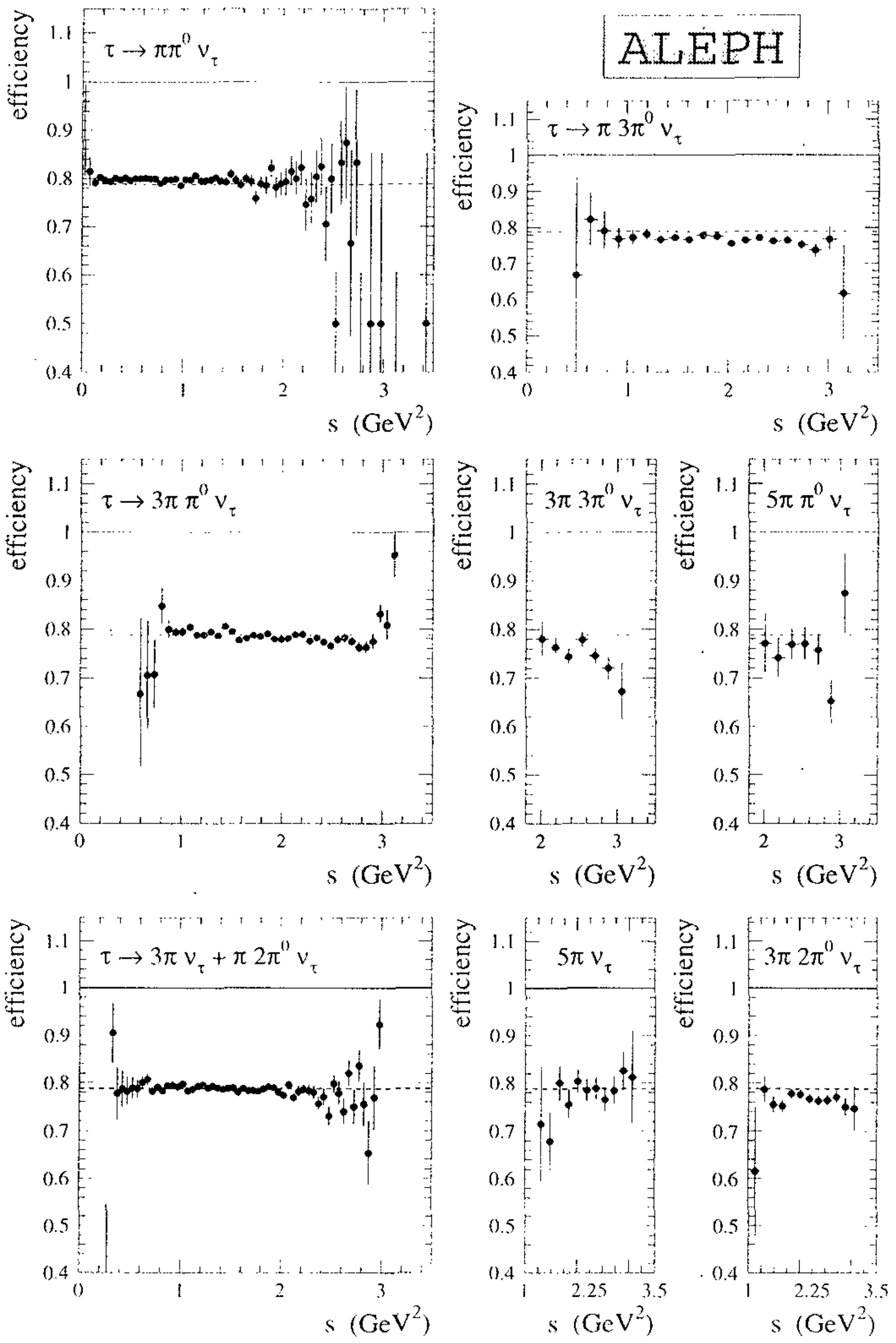

Figure 4.4: *Efficiency of the τ pair selection in τ hadronic final states as a function of the true invariant mass-squared. The distributions are taken from the Monte Carlo simulation. The dashed lines depict the overall τ pair selection efficiency.*

hadronic τ decay modes is measured to be $(0.6 \pm 0.2)\%$. Table 4.1 shows the background contamination from the respective non-τ sources [27]. Fig. 4.4 depicts the efficiency of the τ pair selection as a function of the generated invariant mass-squared taken from the Monte Carlo simulation.

4.2 Charged Particle Identification

To identify charged particles coming from τ decays, a maximum likelihood method is employed, combining different and essentially uncorrelated information measured for each individual track. This procedure is originally described in Ref. [146] and additionally improved in Ref. [23]. The implementation as a FORTRAN program, called `TAUPIDX`, was performed by Z. Zhang, H.J. Park and M. Davier at Orsay.

The global identification facility used is based on a maximum likelihood method which combines the probability densities $f_i^j(x_i)$ of a set of discriminating variables x_i and a particle type $j = e, \mu$, hadron to a normalised global estimator P_j

$$P_j = \frac{\prod_i f_i^j(x_i)}{\sum_j \prod_i f_i^j(x_i)} .$$

The normalised reference distributions $f_i^j(x_i)$ are obtained from the Monte Carlo simulation. The questioned τ hemisphere (*i.e.*, track) is then assigned to the particle type with the largest global estimator P_j .

Nevertheless: Cuts

In general one can state that selections based on a likelihood procedure (*fuzzy-logic*) are clearly superior in cases where the discriminating variables have large overlaps between the channels to be selected. Cuts are here very inefficient. However, quality cuts should be applied first in order to purify the sample from ill-reconstructed decays:

> Charged particles are not accepted (reconstructed) when their momenta are below 150 MeV/c.
>
> A minimum momentum of 2 GeV/c is required for muon and hadron candidates since lower energy muons cannot reliably be identified in the HCAL. The corresponding efficiency loss amounts to 5.7%. No minimum momentum is imposed on electrons which, below 2 GeV/c, are well distinguished from muons/hadrons by using the dE/dx information.
>
> Cuts are applied for electrons and hadrons in the vicinity of ECAL cracks. This causes an efficiency loss of 4.7%.

Discriminating Variables

A number of eight discriminating variables x_i, $i = 1, \ldots, 8$ is used in the likelihood:

The ionization loss dE/dx provided by the TPC where at least 40 samplings are required. dE/dx discriminates electrons from muons/hadrons, while in the case of muons and hadrons the information is almost degenerated.

Two ECAL shower profile variables for the transverse shape and energy deposition, and the longitudinal shape. Both profiles of a cluster use the four storeys in each stack that are closest to the extrapolated track. The ECAL variables are used to separate electrons from hadrons.

Three HCAL variables: the average shower width measured on the HCAL tubes in the fired planes, the number of fired planes among the last ten, the HCAL pad energy associated to the track (only used if more than 8 HCAL planes have fired). All HCAL and muon chamber variables serve to separating muons from hadrons.

The average shower width is obtained defining a road of 60 cm around the extrapolated track. In each fired HCAL plane one now determines the maximum separation between the responding tubes. The average separation of all fired planes determines the shower width. Contrary to ECAL cracks, dead zones in the HCAL (empty spaces between the modules in the central detector and the edges) are taken into account by the use of three individual reference distributions depending on the geometric position of the response in the detector.

Two variables provided by the muon chambers: the number of hits within a road of $\pm 4\sigma$ around the extrapolated track, where σ is the standard deviation expected from multiple scattering. Finally, the average distance in units of σ of the hits from the extrapolated track position is used.

The correlation between the variables are expected to be very small. Correlations exist between the average HCAL shower width and the HCAL energy measured on the pads. Nevertheless the use of the HCAL energy improves slightly the muon–hadron separation as observed in the simulation.

Identification Procedure

The global likelihood method is applied on one-prong hemispheres. Three prong hemispheres with a possible converted electron-positron pair from photon radiation or π^0 decays go in for a preidentification in order to reconstruct electrons. Only dE/dx and the ECAL shower profile variables are used.

The reference distributions are obtained from simulated events. Checks are performed using tagging routines both for data and Monte Carlo simulation and comparing the variable distributions. Fig 4.5 depicts the probability distributions P_j of identified electrons, muons and hadrons for data and Monte Carlo simulation. Reasonable agreement is observed. Additionally depicted is the expected τ background taken from the simulation.

Identification Efficiencies and Results

The performance of this identification is studied in detail using samples from electron

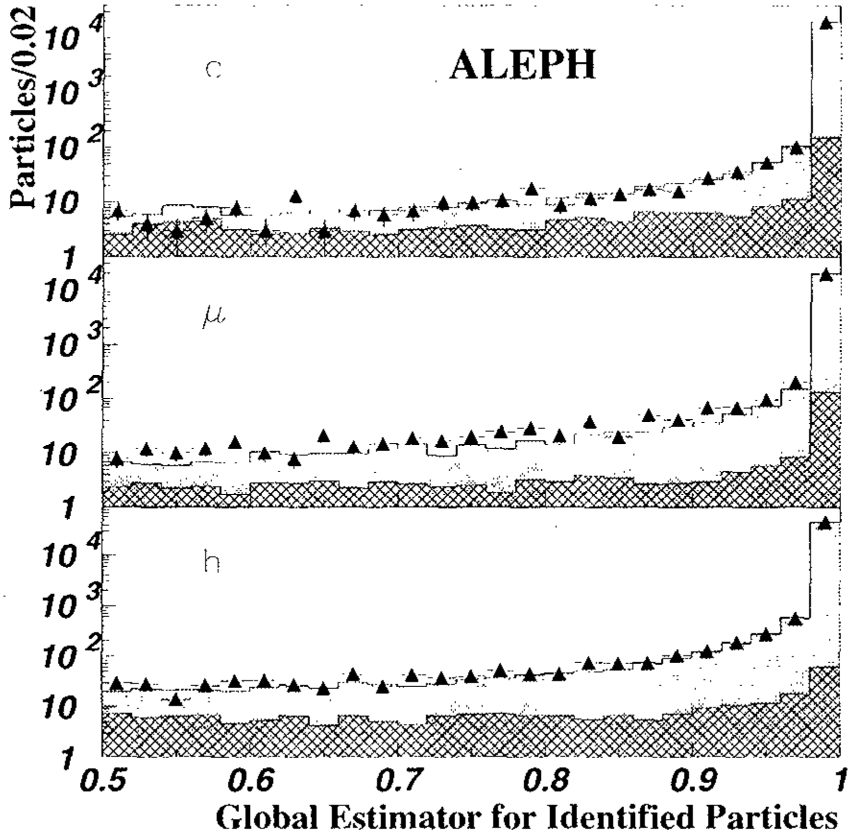

Figure 4.5: *Distributions of the electron, muon and hadron estimators in data (points) and Monte Carlo simulation (histograms). Wrong identified tracks are indicated by the hatched areas.*

pairs, muon pairs and two-photon decays into lepton pairs [23]. Z $\to e^+e^-$ events provide a high energy electron sample (> 8 GeV) and, complementarily, $\gamma\gamma \to e^+e^-$ events provide low energy electrons. Similarly, a wide-ranged muon sample is obtained from the corresponding processes Z $\to \mu^+\mu^-$ and $\gamma\gamma \to \mu^+\mu^-$. In practice, lepton samples are obtained by tagging in every event the opposite particle with severe identification and momentum cuts. In all cases a small contamination from τ pairs has to be subtracted out (using the Monte Carlo simulation) in order to get the correct misidentification rates of leptons into hadrons.

In addition, two complementary data samples from τ decays are used in order to test the hadron misidentification probability distribution. The first sample is obtained using dE/dx discrimination for an electron vetoing against hadrons while muons are rejected using HCAL and muon chamber estimators. The second sample is tagged by requiring the presence of at least one reconstructed π^0 which vetos hadrons originating dominantly from $\tau^- \to \pi^-\pi^0\nu_\tau$ and $\tau^- \to \pi^- 2\pi^0\nu_\tau$ decays. Both samples indicate a higher probability for the misidentification of hadrons as electrons in data $(0.79 \pm 0.06)\%$ with respect to the expectation from Monte Carlo simulation $(0.59 \pm 0.02)\%$ [24]. Corrections according to

Id.: ↓ True: →	e	μ	hadron
e	94.79 ± 0.10	≤ 0.01	0.79 ± 0.06
μ	≤ 0.01	93.62 ± 0.10	0.90 ± 0.06
hadron	0.51 ± 0.10	0.68 ± 0.10	87.91 ± 0.10

Table 4.2: *Particle identification efficiencies and misidentification probabilities (in percent) as measured from data in one-prong τ decays. The efficiencies given include the precuts of the likelihood identification.*

these values are applied. Table 4.2 shows the efficiency (including precuts) and misidentification matrix for one-prong τ decays.

The electron identification is independently tested using three-prong τ hemispheres with two tracks being identified as $\gamma \to e^+e^-$ conversion.

The momentum dependence of the electron and muon efficiency is very weak while the hadron efficiency increases by 1% (over the full momentum range) with increasing momentum due to the parallel increase of hadron-to-electron and decrease of hadron-to-muon misidentification. The angular dependence of the efficiencies is small. A 1% loss is observed in the overlap region between barrel and end-caps. A similar efficiency loss is seen in the azimuthal distribution of muons due to dead HCAL zones.

4.3 Photons and Neutral Pion Reconstruction

This is a decisive point of the analysis: about 44% of the τ decays and 67% of the hadronic τ decays are accompanied by at least one neutral pion (π^0). These are reconstructed in the electromagnetic calorimeter through their decays $\pi^0 \to \gamma\gamma$ (branching fraction 98.8%) which challenges the energy and angular resolution of the ECAL as well as the separation power between adjacent clusters from high collimated τ decays. By virtue of the high ECAL granularity it has been shown [24] that even τ decays with $4\pi^0$'s can in principle be resolved. In the case of two reconstructed photons originating from a π^0, the known π^0 mass helps to improve the middling energy resolution of the ALEPH ECAL via the, at not too high energies, well measured photon directions. In order to maintain a good efficiency of the π^0 reconstruction, the minimum photon energy is set to 300 MeV. This low choice is vulnerable to low energy fake photons produced by fluctuations from hadronic and electromagnetic showers.

The following sections give a detailed description of the ALEPH photon finder and the π^0 reconstruction algorithms used.

4.3.1 Converted Photons

A special case of photons are those which have converted inside the tracking volume into an e^+e^- pair and are therefore reconstructed as TPC tracks and not in the calorimeter.

Photon conversion diagrams need the presence of an external field as provided by matter so that it becomes possible to visualize the elements of the ALEPH tracking devices by the measurement of the conversion radius (distance vertex - point-of-conversion) as seen in Fig. 4.6.

Conversion candidates are required to have an invariant mass smaller than 30 MeV/c^2 and the minimal distance between the two helices in the x-y plane must be at least 0.5 cm. Remaining charged tracks which are identified as electrons in a multi-prong environment originating from a hadronic τ decay are thought to be single track conversions assuming that due to too low momentum ($P \leq 150$ MeV/c) or secondary scattering effects the other track got lost. Fig. 4.6 shows that the conversion rate when passing material such as ITC and TPC walls is fairly well modelled in the simulation. Additionally plotted is the invariant mass distribution of converted photons for data and Monte Carlo simulation. The respective fractions of converted photons among a sample of "genuine" photons is measured to be [24] $(9.8 \pm 0.2)\%$ in data and $(9.4 \pm 0.1)\%$ in the simulation with a small excess in data with respect to the simulation. The fraction of single track conversions is found to be well reproduced by the simulation.

4.3.2 Photon Reconstruction

To understand the photon reconstruction algorithm one should recall the basic construction elements of the ALEPH ECAL: it consists of 45 layers of a total thickness of 22 radiation lengths. The energy and position of a shower is read out using cathode pads with dimensions 3×3 cm^2, arranged to form towers pointing to the interaction zone; each tower is read out in three segments in depth, so-called *storeys*, corresponding to 4, 9, and 9 radiation lengths, respectively. The characteristic longitudinal segmentation and the fine granularity (which compares to the average width of an electromagnetic shower) of the calorimeter play an important role in the photon and neutral pion reconstruction, and in the identification of fake photons.

`GAMPEX` Algorithm

The practical work of photon reconstruction is performed using the program package `GAMPEX` [147, 148] that first detects energy maxima in the lowest storeys since electromagnetic showering starts almost immediately (~ one radiation length) after the photon's entrance into matter. Adjacent energetic storeys (those which share a face) are then associated to the maximum energetic storey in order to form a cluster. The same clustering is afterwards applied to the storeys of the second and third level of depth and the clusters found are associated to the primary one. This procedure is applied to all isolated ECAL energy maxima. An important source of background are hadronic interactions with the calorimetric matter producing as well photons and π^0's. In order to distinguish them from genuine τ final state photons one uses the characteristic form of the shower in combination with a cut requiring a minimal distance between the barycentre of the energy deposition (photon) and the extrapolated track of 2 cm. In addition, reconstructed photons are required to exceed a minimal energy of 300 MeV. After the clustering, the number of fake photons in data reaches about 26% in the photon sample of hadronic τ decay modes.

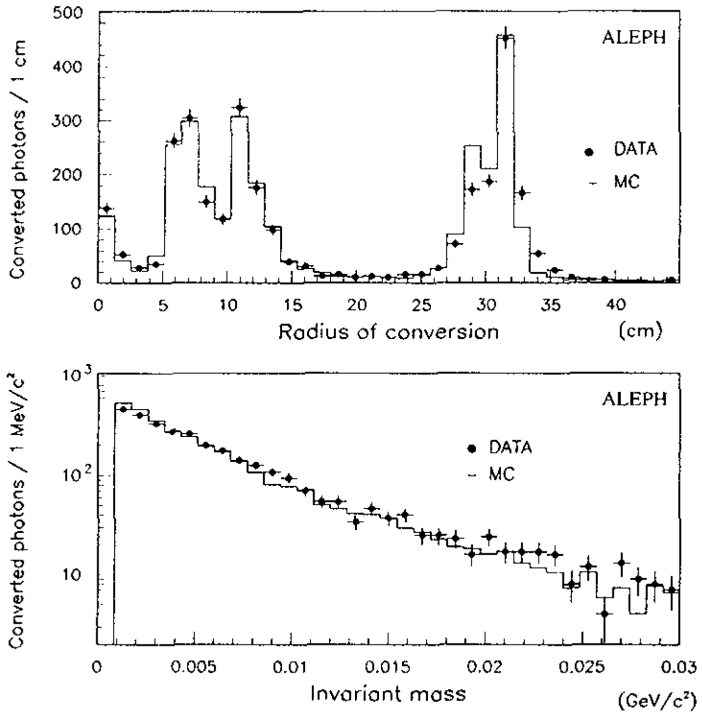

Figure 4.6: *The upper plot depicts the radial distance of a photon conversion vertex (materialization point) to the beam spot for data (points with error bars) and Monte Carlo simulation. Accumulations occur when photons penetrate matter: the beam pipe at* 5.4 *cm, the silicon strip vertex detector (VDET) at* 6 11 *cm, the outer walls of the ITC* 13 *cm and* 29 *cm, and the inner TPC wall at* 31 *cm. The lower plot shows the invariant mass distribution for observed and simulated converted photons. The* e^+e^- *enhancement at the primary vertex is due to so-called "Dalitz decays"* $\pi^0 \to e^+e^-\gamma$ *occurring with a branching ratio of* 1.2% *[17].*

The fractions of fake photons originating from hadronic interactions and electromagnetic showers are approximately 60% and 40%, respectively.

The photon energy is calculated taking the deposited energy in the four central towers in order to reduce the sensitivity of the energy measurement to hadronic background and clusterization effects. Several corrections are applied concerning energy loss in the case of transversally or longitudinally outbreaking showers or amplification saturation effects. A new ECAL energy calibration with respect to the Monte Carlo simulation is performed in the framework of this analysis. It is described in Section 7.1.2. In cases where the measured energy is not compatible with the one photon expectation, the energy is calculated on the basis of all associated energetic towers. Finally, the polar and azimuthal angles, *i.e.*, the photon direction are measured from the barycentre of the cluster in assuming the photons to be produced in the primary vertex (e^+e^- interaction point).

PEGASUS Algorithm

Photons that are reconstructed by the above clusterization algorithm have to be subjected to a certain number of tests in order to be able to classify them according to their origin: genuine photons (also called photons) from π^0 decays, photons from bremsstrahlung or radiation and fake photons issuing from hadronic or electromagnetic shower fluctuations.

The routine PEGASUS [24] uses a maximum likelihood method which combines the information from different variables in order to discriminating between the above mentioned photon origin: consider a discriminating variable y_i with its probability density $p_i^{\text{genuine}}(y_i)$ ($p_i^{\text{fake}}(y_i)$) to be a genuine (fake) photon. The (genuine) photon estimator is then given by

$$P_\gamma = \frac{\prod_i p_i^{\text{genuine}}(y_i)}{\prod_i p_i^{\text{genuine}}(y_i) + \prod_i p_i^{\text{fake}}(y_i)} \ . \tag{4.1}$$

The following discriminating ECAL variables are used:

fractions of energy in the first and the second ECAL stack ($E^{1./2.\text{ stack}}$),

fraction of energy outside the four central ECAL towers,

transverse size of the photon shower,

angular distance of the photon's barycentre to a nearest second photon shower ($d_{\gamma\gamma}$),

distance from the photon's barycentre to an extrapolated track. A sign is computed depending on the position of the photon shower with respect to the curvature of the track in the r-ϕ projection, and

the photon energy (E_{total}).

Reference distributions of the above variables are produced from the Monte Carlo simulation where the origin of the photons can be inquired (which is not always clear). The distributions additionally distinguish the number of tracks measured in the given hemisphere. They have been confronted with data in order to check their reliability. For this purpose, a tagged sample enriched with photons and fake photons, respectively, is established for data as well as for the simulation on the basis of the estimator P_γ and the fact whether or not they belong to a reconstructed π^0 (see next section). Fig. 4.7 shows some of the variables used for the respective genuine (called "good") and fake photon sample for data and Monte Carlo simulation. They agree fairly well. Disagreements lead to systematic errors which are discussed in Chapter 7. In general one can say that, not surprisingly, genuine photons (from physics origin) are much better modelled than fake photons whose origins are diverse and difficult to simulate. An iterative procedure is performed to derive from the data the corrections to be applied to the simulated reference distributions [24]. One thus obtains individual references for the use on data and Monte Carlo simulation. Additional studies concerning corrections of the hadronic invariant mass spectra due to biases from fake photons are presented in the following section. Until this point, the energy of the photons is not used as discrimination variable in the likelihood to avoid biases on the invariant mass reconstruction. The energy is included

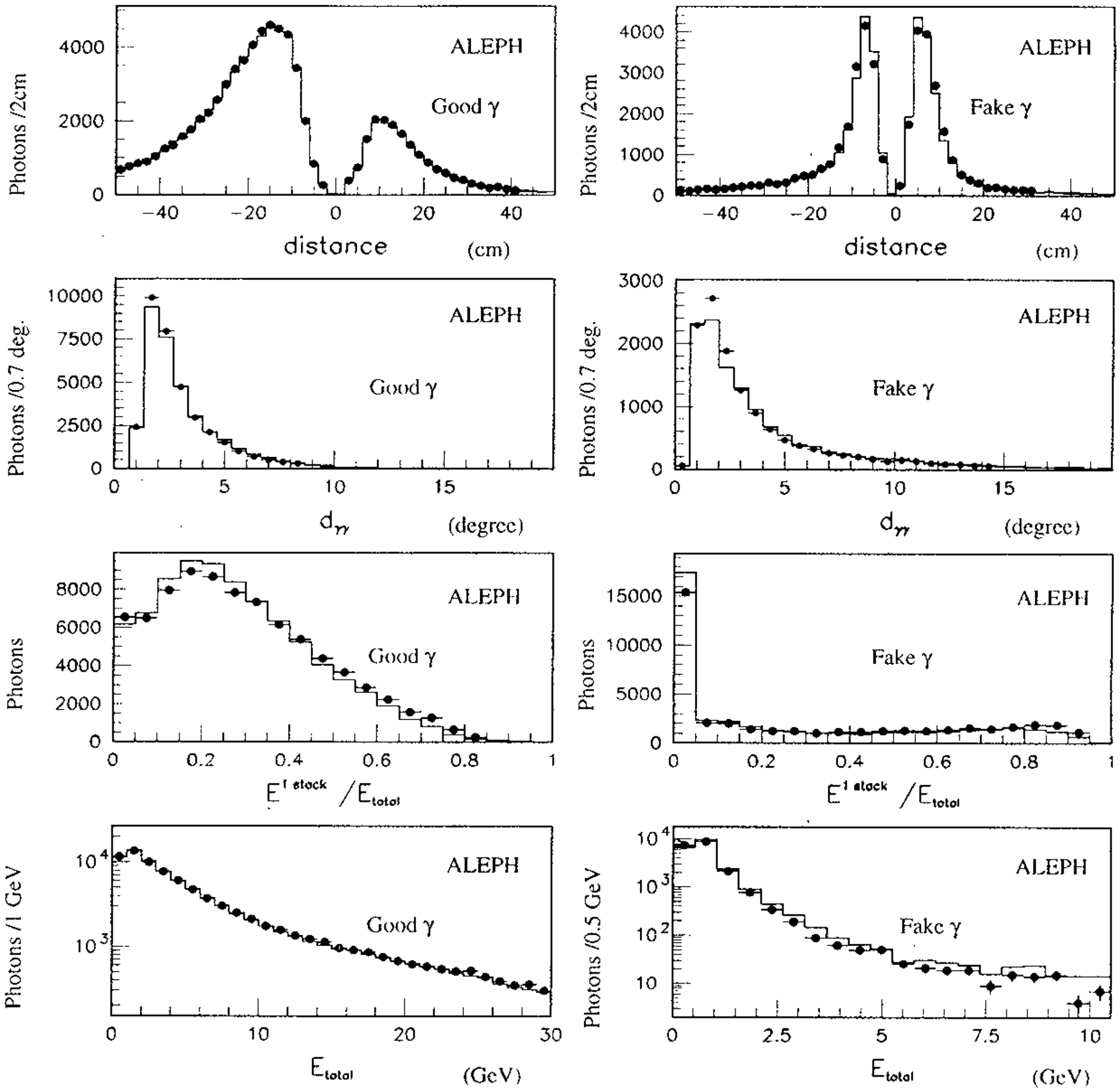

Figure 4.7: *Distributions used in the likelihood to separate genuine photons (left hand plots) from fake photons (right hand plots) for data (points) and Monte Carlo simulation (histograms).*

into the procedure after the pairing of photons to π^0's has been performed in order to obtain stronger constraints on residual photons (remaining photons without a partner). Note, that up to this moment no cut has been applied, *i.e.*, all `GAMPEX` photons are still present equipped with their individual genuine photon estimators.

4.3.3 Reconstruction of π^0's

The π^0 reconstruction procedures is primarily designed with the aim of achieving the highest possible reconstruction efficiency. Three types of π^0's are distinguished:

resolved π^0's are paired from two photons,

unresolved π^0's are reconstructed from a high-energetic cluster where two photons are merged together, and

residual photons are remaining photons supposed to originate from a π^0 while the second photon has been lost.

The procedure leads to an overall π^0 reconstruction efficiency of about 84%.

Resolved π^0's

In order to produce π^0 candidates, all photons reconstructed inside a 45° cone around the thrust axis are paired to π^0's. Then for each photon pair one calculates a π^0 estimator D_{ij} defined as

$$D_{ij} \; = \; P_{\gamma_i} \times P_{\pi^0,ij} \times P_{\gamma_j} \; , \tag{4.2}$$

where the P_{γ_i} are the genuine photon estimators from Eq. (4.1) and $P_{\pi^0,ij}$ represents the probability obtained from a compatibility test between the measured two-photon mass and the expected one in units of one standard deviation of the apparent mass using Gaussian probability density. It turns out that the apparent mass depends sensitively on the two-photon energy (*i.e.*, π^0 energy), as observed in Fig. 4.8. This effect issues from overlapping high energetic photon showers for which the reconstruction algorithm tends to overestimate the two-photon opening angle and thus the π^0 mass. As also seen in Fig. 4.8, the functional form of this behavior depends on the geometrical region of the ALEPH detector. It is obviously not well reproduced by the simulation. At low and high energies, the simulated average π^0 mass lies systematically above the data. This effect ensues from an overestimation of the two photon opening angle caused by clusterization effects, which are not sufficiently well modelled in the simulation. Another contribution originates from calibration shifts which are mainly located at low energies. In order to come up to the above deviations, the apparent π^0 mass is individually obtained for data and Monte Carlo simulation from an energy-dependent reference distribution (according to Fig. 4.8) which distinguishes barrel and end-caps as well as the years 1991–93 and 1994 of data taking, respectively. In the case where one of the paired photons has converted to e^+e^-, corresponding parametrisations for the π^0 mass and its resolution are derived from data to obtain the $P_{\pi^0,ij}$ probability.

Fig. 4.9 depicts the estimator D_{ij} for hadronic τ decays (corrected for an excess of

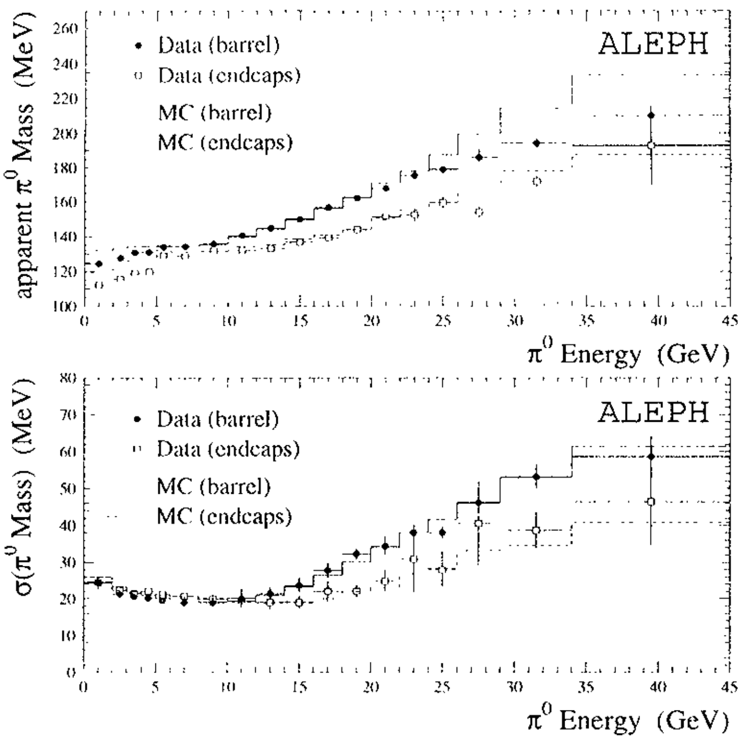

Figure 4.8: *Observed mean values for the* π^0 *mass (upper plot) and its experimental width (lower plot) as a function of the* π^0*energy for* 1991 – 93 *data (points) and the simulation (histograms) before the final energy calibration. The simulated distributions are corrected for fake photons.*

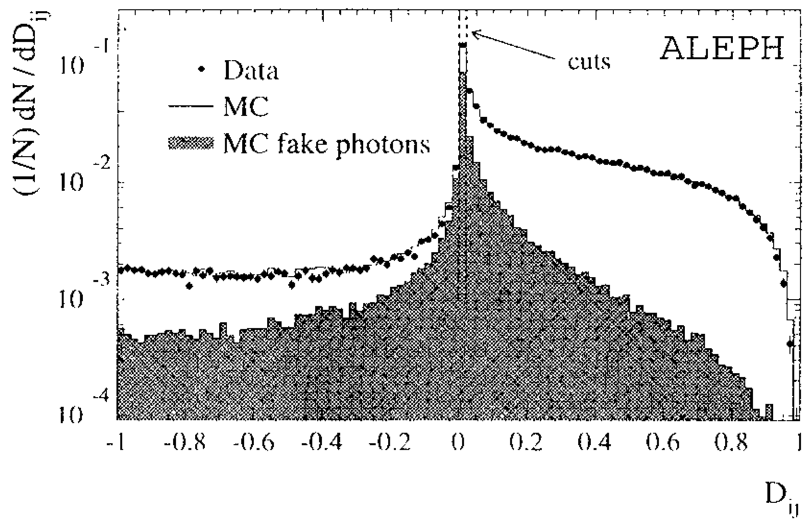

Figure 4.9: *Estimator* D_{ij} *from Eq.* (4.2) *for data, Monte Carlo simulation and fake photons taken from simulated events. Negative probabilities signify that one of the photons has converted to an* e^+e^- *pair for which the photon probability is defined* $P_{\gamma\to e^+e^-} \equiv -1$. *The Monte Carlo is corrected for fake photons.*

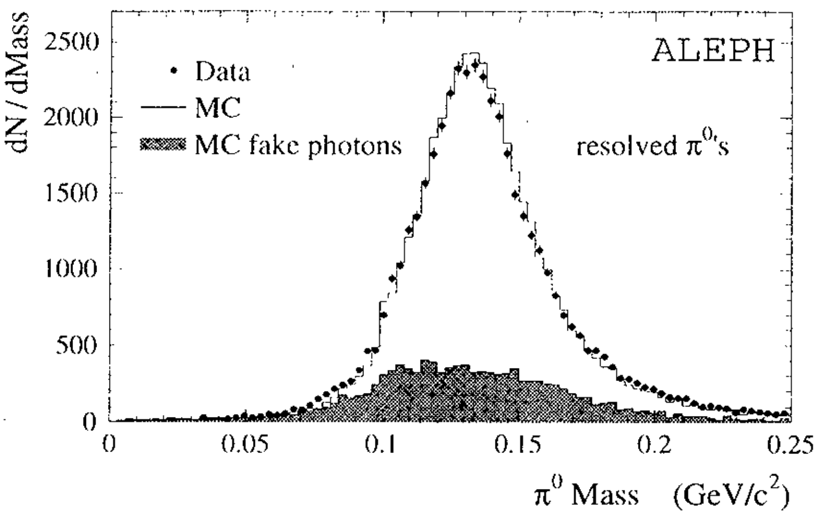

Figure 4.10: *Invariant mass of resolved π^0's. The simulated (MC) distribution is shifted by 2% to smaller masses in order to correct for the deviation observed in Fig. 4.8. The shaded region are resolved π^0's with at least one fake photon according to the simulation. The simulated distribution is corrected for fake photons.*

fake photons in data see Section 4.3.4). A pair ij of photons is accepted as π^0 candidate if

$$D_{ij} > 0.0009 ,$$

which corresponds for given average values $\langle P_{\gamma_i}, P_{\gamma_j} \rangle$ of genuine photons to a $P_{\pi^0,ij}$ threshold probability for an invariant mass three standard deviations away from the expected value [24].

In a τ hemisphere with more than two photons the following criterion defines the hierarchy of π^0 pairing within all candidate pairs ij: Among all possible combinations the one is chosen which maximizes the product $\prod_{i \neq j} D_{ij}$. The comparison of the invariant mass distribution for resolved π^0's, after correcting the mass shift established in Fig. 4.8 and an excess of fake photons in data, is depicted in Fig. 4.10. Reasonable agreement between the shapes is observed.

Once the resolved π^0's are reconstructed, a kinematic fit is performed in order to constrain the measured π^0 mass to the nominal mass $m_{\pi^0} = 0.13498$ GeV/c^2 [17]. The expected energy and angular resolutions are used to adjust both values according to the relation $m_{\pi^0} = (2E_{\gamma_1}E_{\gamma_2}(1 - \cos\theta_{\gamma_1\gamma_2}))^2$. The constraint imposes primarily on the photon energies E_{γ_i} at low π^0 energies, where due to the wide two-photon opening angle $\cos\theta_{\gamma_1\gamma_2}$ the photon directions are well measured. At higher π^0 energies the critical resolution comes from the opening angle whose reconstruction becomes more difficult owing to the overlapping photon showers. Fig. 4.11 shows the gain on energy resolution according to the Monte Carlo simulation which, as expected, is situated at lower π^0 energies.

Unresolved π^0's

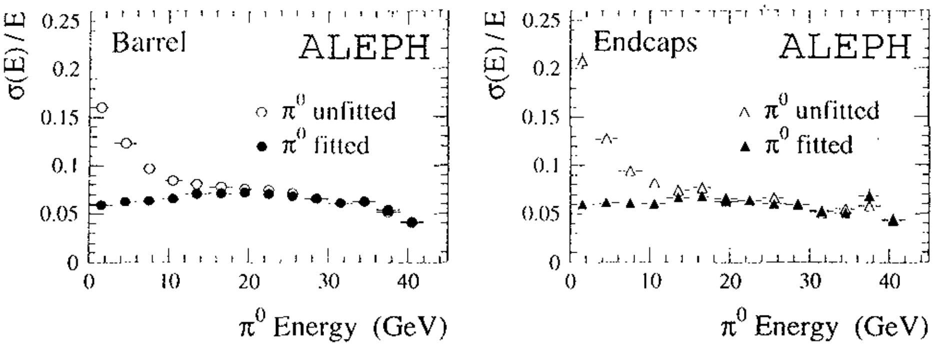

Figure 4.11: *Energy resolution of resolved and unresolved* π^0 *in the simulation as a function of the* π^0 *energy before and after the* π^0 *mass constrained fit in the barrel* ($|\cos\theta| \leq 0.774$) *and end-caps* ($0.774 < |\cos\theta| \leq 0.95$), *respectively.*

Once the π^0 energy increases the two photon showers tend to overlap and to be reconstructed as one energetic cluster. However, assuming the presence of two photons with identical shower shapes in the cluster, one can calculate energy weighted moments from the measured two-dimensional energy distribution in the plane transverse to the shower direction. After a rotation of the ALEPH coordinate system in the two-dimensional system (X, Y) where the barycentres of the two photon showers lie on the same axis $(X_1, 0)$ and $(X_2, 0)$, the moments obey the relations

$$\begin{aligned} \langle X^n \rangle &= \frac{E_1 X_1^n + E_2 X_2^n}{E} , \\ \langle Y^n \rangle &= 0 , \end{aligned} \tag{4.3}$$

with the total measured cluster energy $E = E_1 + E_2$. By definition $\langle X^1 \rangle = 0$ holds in the new system. Eq. (4.3) is calculated up to the second moment $n = 2$ in order to get sufficient information (four equations: $\langle X^1 \rangle, \langle Y^1 \rangle, \langle X^2 \rangle, \langle Y^2 \rangle$) to solve the system (four unknowns: X_1, X_2, E_1, E_2). The consideration of an error on the common axis for the second moments, which then reads $\langle X^2 \rangle = (E_1 X_1^2 + E_2 X_2^2)/E + \sigma^2$ and $\langle Y^n \rangle = \sigma^2$, requires as additional information the third moment $\langle X^3 \rangle$ defined according to Eq (4.3). Having reduced the five equations, the coordinates of the two barycentres are reexpressed by ALEPH coordinates and the invariant mass of the two-photon system is calculated.

All two-photon systems with an invariant mass larger than 0.1 GeV/c^2 are thought and accepted to be unresolved π^0's. Fig. 4.12 depicts the reconstructed mass for data and Monte Carlo simulation. Fake photons in high energy unresolved π^0's stem from shower split-offs, *i.e.*, electromagnetic shower fluctuations. This π^0 reconstruction procedure does intrinsically not distinguish between high energetic radiative photons and overlapping two-photon configurations originating from π^0's. However, high energetic photon radiation is extremely rare in hadronic τ decays.

Residual Photons

Photons inside a 30° degree cone around the thrust axis which are neither paired to

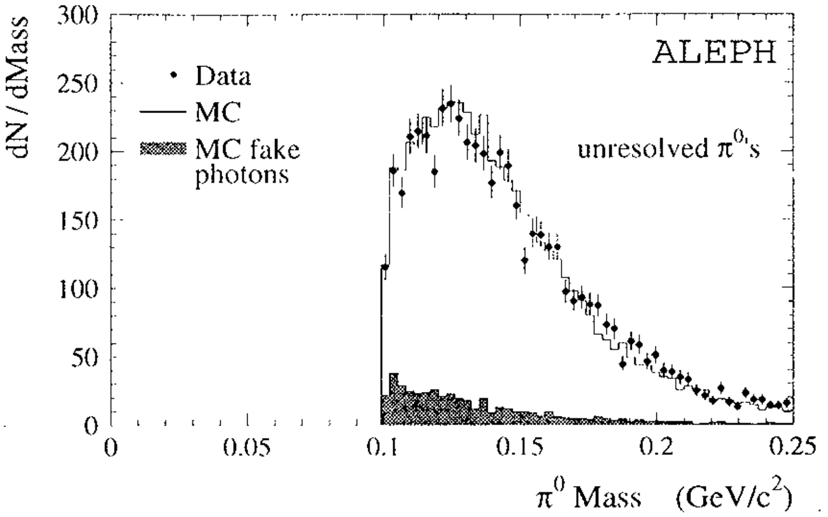

Figure 4.12: *Invariant mass of accepted unresolved π^0's ($m_{\pi^0} > 0.1$ GeV/c^2). The data distribution is corrected for an excess of fake photons.*

resolved π^0's nor found to have sufficient unresolved invariant mass may issue from

- π^0 decays where the partner photon got lost in an ECAL crack, or did not pass the minimal energy or track distance requirements, or was overlapped by another photon shower,
- final state (or initial state) radiation and bremsstrahlung,
- from $\omega \to \pi^0\gamma$ and $\eta \to 2\gamma$ τ final states,
- shower fluctuations (*i.e.*, fake photons).

The most important sources of residual photons are π^0's and low energy shower fluctuations. The fraction of fake photons in the total sample of residual photons in hadronic τ hemispheres is $(50 \pm 1.4)\%$ in data compared to $(41 \pm 0.1)\%$ in the Monte Carlo simulation.

In order to remove this large quantity of fake photons the discrimination power of the genuine photon estimator P_γ obtained from the likelihood (4.1) is reinforced by including the photon energy E_γ (plotted in Fig. 4.7) as additional variable. It is a strong constraint disfavouring low energy photons. Residual photon with an estimator $P_{\gamma-\mathrm{res}} < 0.5$ are declared to be fake and are rejected. Fig. 4.13 shows the estimator $P_{\gamma-\mathrm{res}}$ for the reaction $\tau^- \to h^- \nu_\tau$.

To distinguish among the different physical sources feeding the sample of remaining residual photons (thought to be genuine), new estimators P_{brems}, P_{rad} and $P_{``\pi^0 \to \gamma"}$ are calculated [24]. As additional discriminating variable, the angle between photon and nearest track is introduced in the likelihood (4.1). The reference distributions for the new estimators are obtained from Monte Carlo simulation tested with tagged data samples. The overall agreement is found to be satisfactory [24].

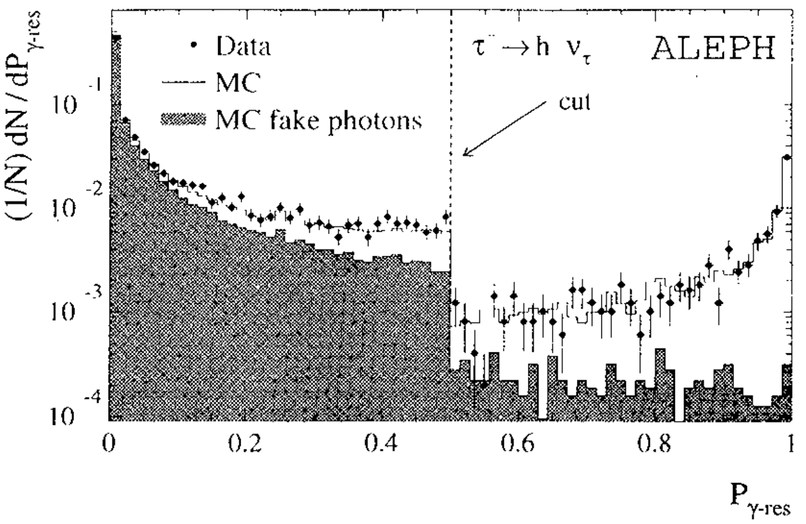

Figure 4.13: *Single Photon estimator $P_{\gamma-\mathrm{res}}$ for data, Monte Carlo simulation and fake photons taken from simulated events. Genuine photons declared fake, i.e., $P_{\gamma-\mathrm{res}} < 0.5$ issue mainly from $\tau^- \rightarrow \pi^- \pi^0 \nu_\tau$ background. The simulation is corrected for fake photons.*

Fig. 4.14 show the respective fraction of resolved, unresolved and single (residual) photon π^0's as a function of the π^0 energy. The fractions are not corrected for the excess of fake photons in data (see following section). The data excess of resolved π^0's at high energy is caused by electromagnetic split-offs from shower fluctuations faking an additional low energy photon nearby the main cluster which is then reconstructed as resolved, *i.e.*, two-photon π^0. Accordingly one recognizes the lack of unresolved π^0's in data at corresponding energies.

Crucial points concerning the simulation of π^0's in the detector are the origin and amount of low energy fake photons as well as high energy shower split-offs, energy and angular resolution of the reconstructed photons and the energy calibration. These details, apart from fake photons which are treated in the following section, are part of the systematic studies which are discussed in Chapter 7.

4.3.4 Fake Photons

The data suffer from an excess of fake photons compared to the simulation. The amount of this excess is derived by fitting the simulated distributions of the π^0 probabilities D_{ij} for resolved π^0's and the single photon probabilities $P_{\gamma-\mathrm{res}}$ for residual photons originating from fake and genuine photons to the corresponding data distributions. The excess of fake photons, *e.g.*, in the residual π^0 sample of the $h^- \pi^0 \nu_\tau$ final state is thereby determined in fitting the probability distributions of residual photons in the $h^- \nu_\tau$ channel as the main background source due to fake photons (see Figs. 4.9 and 4.13).

In the case of resolved π^0's the fit is very sensitive to the shape of the distribution at low probabilities, *i.e.*, to π^0 reconstruction problems and non-Gaussian tails. The obtained fit results are therefore independently tested by fitting simulated distributions

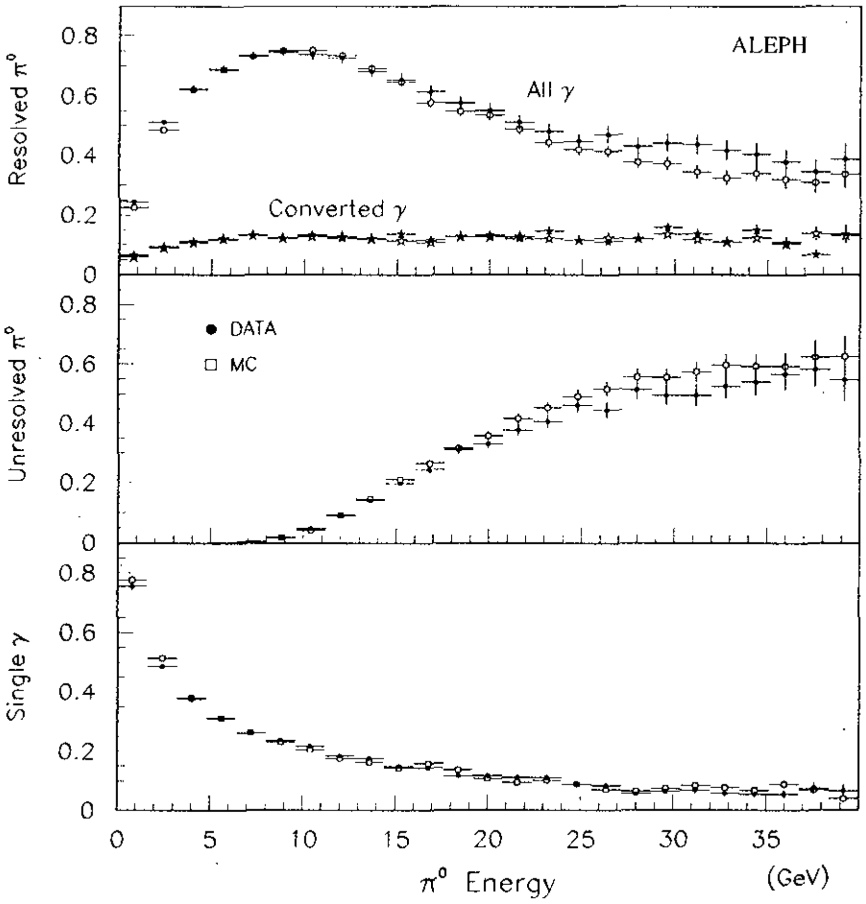

Figure 4.14: *Fraction of resolved, unresolved and single (residual) photon π^0's as a function of the π^0 energy (Not corrected for fake photons). The points are data and the open squares represent the simulation. Additionally shown is the fraction of converted photons in the resolved π^0 sample.*

of the asymmetry in the photon energies $x_{\rm asym} = (E_{\gamma_1} - E_{\gamma_2})/(E_{\gamma_1} + E_{\gamma_2})$ at π^0 energies lower than ~15 GeV to data (see upper right plot of Fig 7.2). In addition, the variable $P_{\gamma_1 \ \rm res} \times P_{\gamma_2 \ \rm res}$ which is the product of the residual probabilities (*i.e.*, using the photon energies) of both photons forming the resolved π^0 is fitted. The disagreements in the excess of fake photons between these fits is considered as systematic uncertainty (see Chapter 7). Fig. 4.15 depicts the fitted fractions of fake photons in the total hadronic sample of resolved π^0's (upper plot) and single photon π^0's (lower plot) as a function of the π^0 energy for 1991 93 and 1994 data respectively. Unresolved π^0's occur predominantly at high energy. They have a negligible contamination of fake photons. The enhancement of the fraction of fake photons in this energy region in the resolved π^0 sample (see Fig. 4.14)

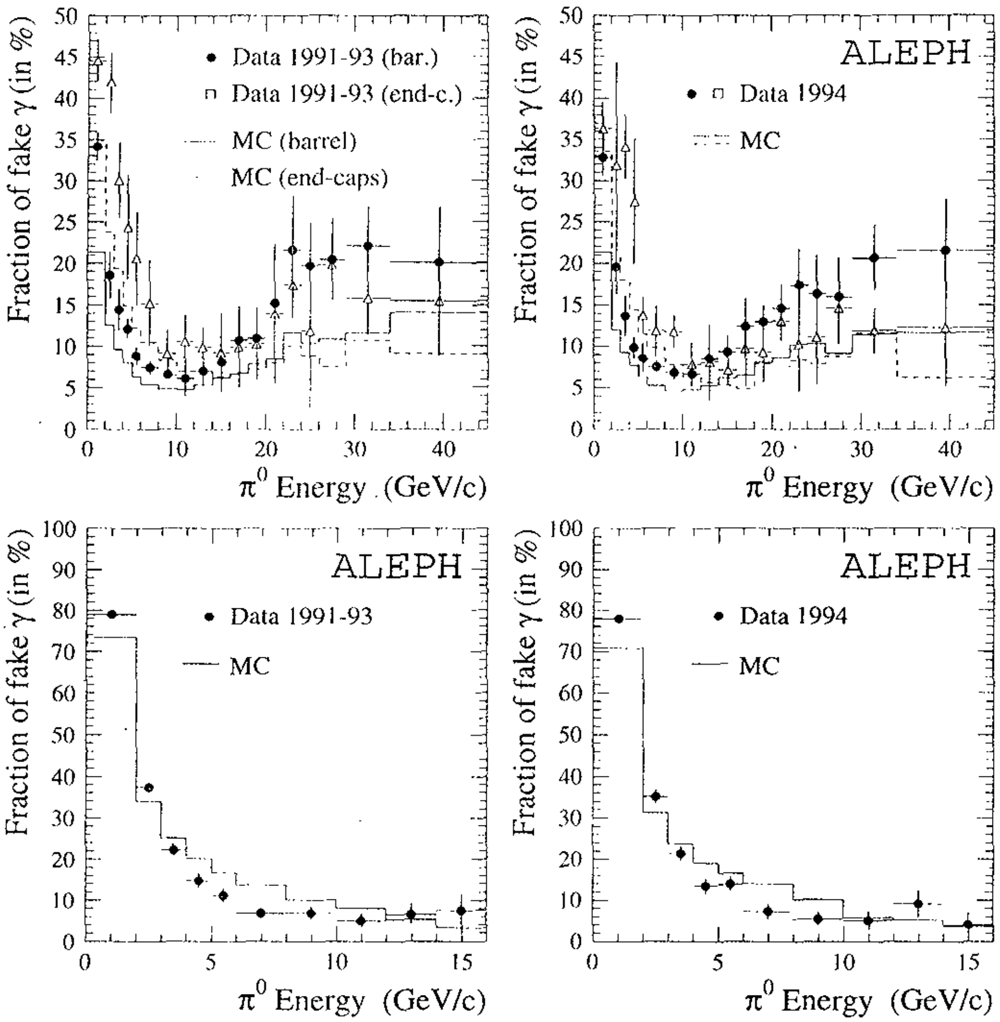

Figure 4.15: *Fraction of fake photons in resolved π^0's (upper plots) and single photon π^0's (lower plots) in the whole sample of hadronic τ decay channels as a function of the π^0 energy.*

stems from split-off effects of two photons, merged together, where energy fluctuations produced a low energy deposition misidentified as a photon near by the unresolved cluster.

The measured invariant mass-squared distributions have to be corrected due to their excess of fake photons. As already mentioned, excesses of residual fake photons increase, *e.g.*, the pion background in the $\pi^-\pi^0$ decay channel as well as the $\pi^- 2\pi^0$ contamination in the $\pi^- 3\pi^0$ channel etc. This background enhances the corresponding invariant mass distributions at the low energy side as observed in Fig. 4.16. Generally one can say that an excess of fake photons in the sample of resolved π^0's does not induce an alteration to the event topology. An excess means that more π^0's have been reconstructed by two photons instead of being a single photon π^0 formed by a single photon. As an example, the correction distributions for the vector τ decay channels are shown in Fig. 4.16. The invariant mass-squared correction distributions showed are taken from the simulation

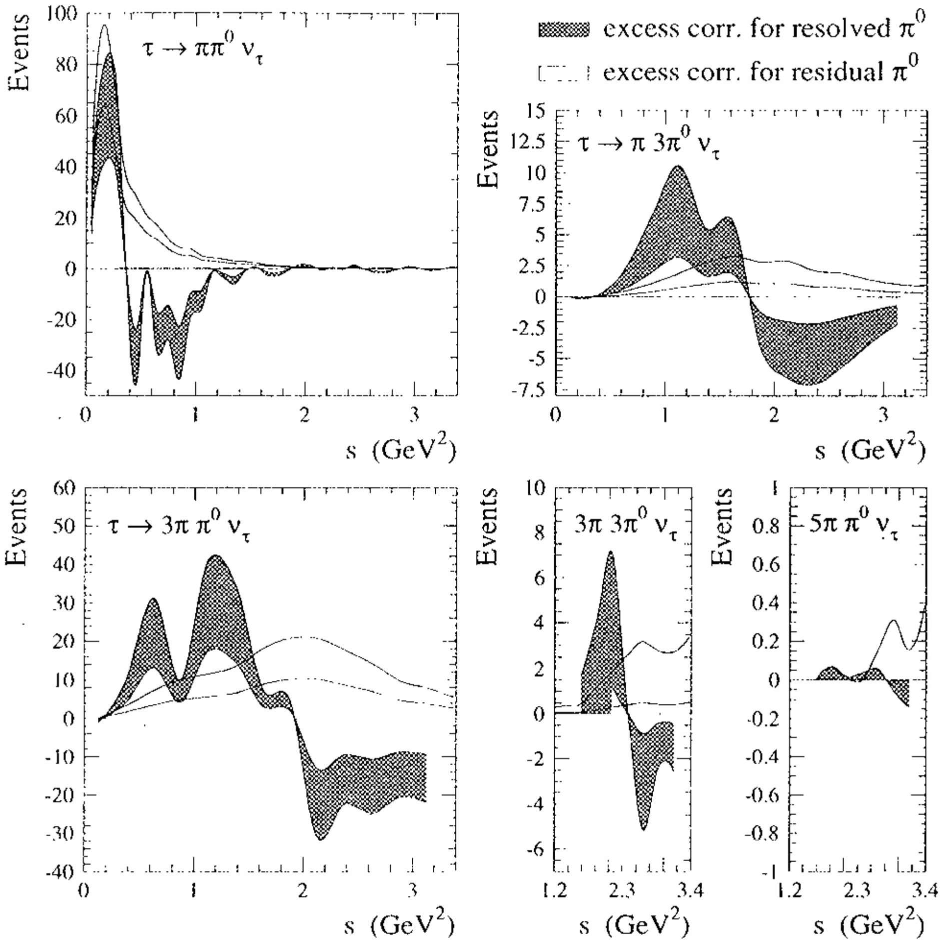

Figure 4.16: *Correction of the invariant mass-squared distribution for some τ decay channels due to fake photon excesses in resolved π^0 (hatched areas) and single photon π^0 (empty areas) samples. The normalisation of the curves is proportional to the respective excesses of fake photons in the data. The bands depict the statistical and systematic uncertainties of the corrections.*

corrected by data.

Fake photons may originate from hadronic and electromagnetic interaction in the ECAL. The decay $\tau^- \to h^- \nu_\tau$ provides an almost pure sample of fake photons (up to a small fraction of bremsstrahlung photons) issued from hadronic interactions, whereas in $\tau^- \to e^- \bar{\nu}_e \nu_\tau$ decays fake photons originate from electromagnetic shower fluctuations. Fig. 4.17 shows the distribution of the distance photon track and the photon energy in enriched samples of fake and genuine photons occurring in $\tau^- \to h^- \nu_\tau$ and $\tau^- \to e^- \bar{\nu}_e \nu_\tau$ decays, respectively. The distributions of the energy and the distance track - photon for fake photons disagree between data and Monte Carlo simulation. Measured fake photons tend to higher photon - track distances and to lower photon energies than simulated ones (see left hand plots of Fig 4.17). These effects partly cancel out in the invariant mass

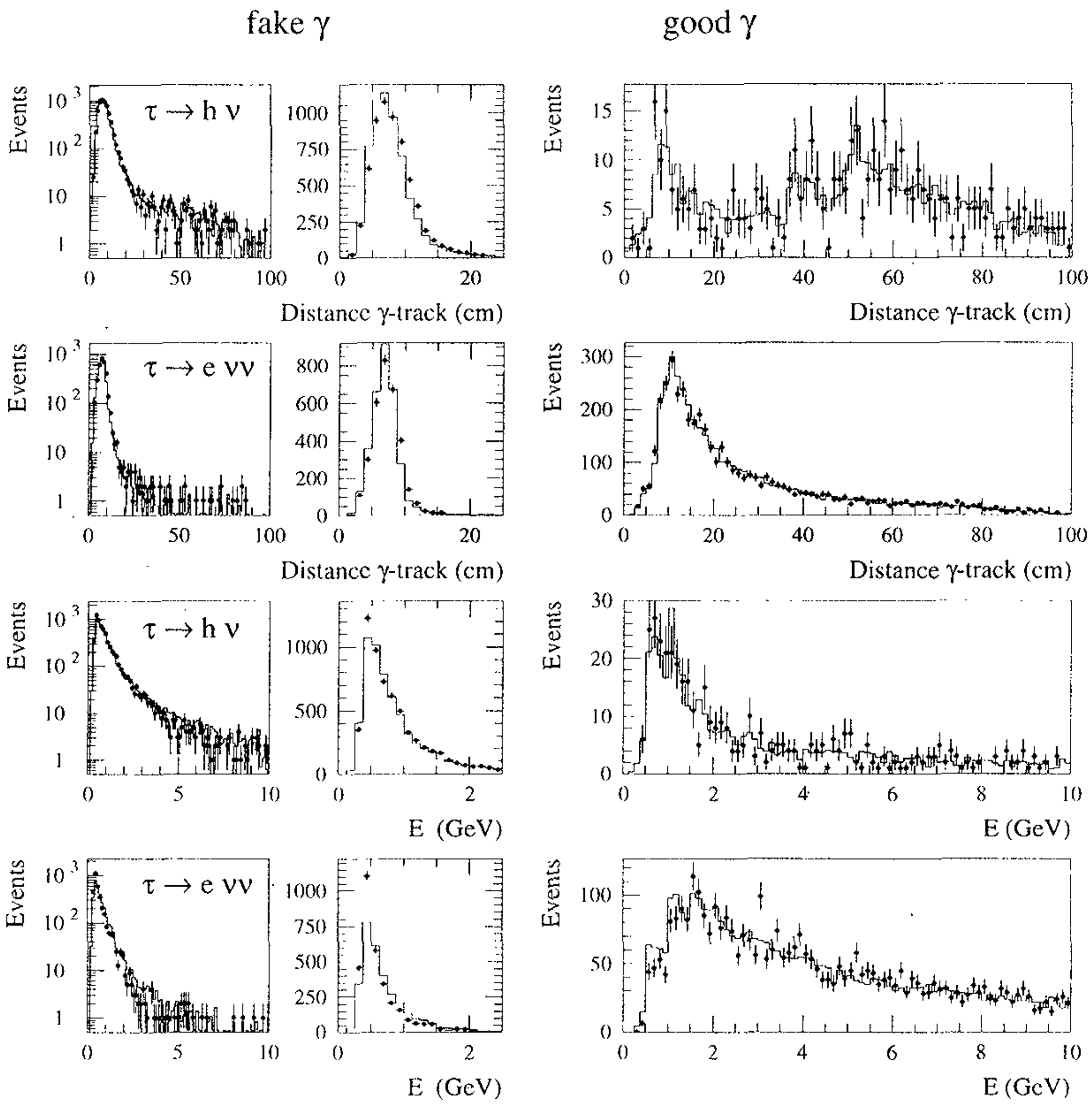

Figure 4.17: *Distributions of the distance photon to track and the photon energy for enriched samples of fake (left hand plots) and genuine ("good") photons (right hand plots) in* $\tau^- \to h^- \nu_\tau$ *(purities fake: 91% and good: 97%) and* $\tau^- \to e^- \bar{\nu}_e \nu_\tau$ *(purities fake: 57% and good: 98%). In these decays good photons originate from radiation. The points show the data and the histograms the corresponding simulated events. The second column of the left hand plots show the peak parts of the first column plots with linear scale. Fake photons in* $\tau^- \to h^- \nu_\tau$ *decays originate from hadronic interaction in the electromagnetic calorimeter, whereas fake photons in* $\tau^- \to e^- \bar{\nu}_e \nu_\tau$ *are due to electromagnetic shower fluctuations.*

correction distributions of the excesses of fake photons in samples with single photon π^0's. The distributions of samples with hadrons and electrons in the final states enriched with genuine photons (right hand plots of Figure 4.17) show a fairly good agreement between data and the simulation.

Chapter 5

The Unfolding Method

The spectral functions defined in Eq. (1.22) use the invariant mass-squared distributions dN/ds as direct experimental input. Unfortunately, the measured "raw" mass distributions are distorted by various detector effects, such as the finite energy, momentum and angular resolution as well as kinematical and geometrical acceptance. The unfolding from these detector effects requires good knowledge of all sources biasing the measurement. In particular, one has to make sure that calibration and resolution of the detector are well described by the detector simulation. Unfolding means the deconvolution of measurement artifacts modelled by the Monte Carlo simulation. The resulting distribution then ideally contains pure physics information. Again ideally, the result of the unfolding process does not depend on the physical dynamics put in the Monte Carlo. The generally known practical problems of unfolding come from the numerical singularity of the problem: the matrix which describes the detector response, *i.e.*, the convolution of a physical distribution with non-diagonal detector effects (measurement distortion) has not full "rank" which means in this case that it is numerically singular, *i.e.*, unstable against small variations in the initial system. The inversion of the detector response matrix (unfolding) is hence restricted. The problem appears even worse: because of inevitable statistical errors in the measured distribution, the exact solution (even if it exists) is in most cases wildly oscillating and therefore useless (see Ref. [149]).

The method introduced in the following regularizes the problem of insignificance in reducing the detector response matrix to its informative part which then can be inverted using standard techniques. It is based upon an idea of V. Kartvelishvili; practical problems and implementation have been solved in collaboration. The description given here follows in main parts the original work published in Ref. [150]. An unfolding procedure based on considerations which are similar to those presented here has been described more than a decade ago in [149], and is still widely used in experimental analyses. While there are no significant differences between the foundations of the two procedures, the authors believe that the formulation presented here allows one to obtain more reliable and precise results, being at the same time much simpler and easier to implement.

The approach is based on the extensive use of the *Singular Value Decomposition* (SVD) of the detector response matrix, and results in a linear unfolding algorithm which is applicable to a wide range of problems. Also derived is a number of recommendations about the proper normalisation of the response matrix and choice of the variables. Complete error propagation is implemented, and a reliable procedure for determining the optimal value of the regularisation parameter is proposed.

The problem of unfolding has been studied in various forms, giving rise to a number of independent methods described in the literature. For instance, a method based on Bayes' theorem was proposed in [8, 151]. The authors manage to avoid partly the inversion difficulties by using a non-linear iterative procedure, leading asymptotically to the unfolded distribution.

5.1 Notation

The following notation conventions are used throughout this chapter:

All one-dimensional histograms/vectors are denoted by small letters (e.g. b, z etc.).

All two-dimensional histograms/matrices are denoted by capital letters (e.g. A, X etc.).

The covariance matrix associated with a one-dimensional variable is denoted by the same letter in capital (i.e. the matrix W_{ij} denotes the covariance matrix of the vector w_j).

No implicit summation is assumed over repeated indices; i.e. no repeated index is summed unless the summation is explicitly shown.

Upper index T stands for the transposed matrix, $A^T_{ik} = A_{ki}$, so that the euclidean norm of a vector z equals $\sqrt{z^T z}$.

Upper index -1 denotes the inverse matrix, $A^{-1}A = AA^{-1} = I$, where I stands for the unit matrix, $I_{ik} = \delta_{ik}$.

All scalar variables are denoted by small greek letters (e.g. ϵ, ξ etc.).

5.2 The Problem

Let the distribution of a *measured* observable be stored in a vector b of dimension n_b, where the ith coordinate of the vector contains the number of entries in the corresponding bin of the histogram. The measurement is affected by the finite experimental resolution and/or the limited acceptance of the detector, so that each event from the true distribution may find itself in a range of (not necessarily) adjacent bins, or nowhere at all. Using Monte Carlo simulation, the distribution x^{ini} of dimension n_x is generated, according to some idea of the underlying physical process, and the detector simulation is performed. At this stage, every entry in a measured bin (*i.e.*, every *event*) can be directly traced to its origin. This gives a well defined system of linear relations between the simulated *true* and *measured* distributions:

$$\hat{A}\, x^{\text{ini}} = b^{\text{ini}} . \qquad (5.1)$$

The $n_b \times n_x$ matrix $\hat{A}$ is a probability matrix, which actually performs the simulated folding procedure. Now, with $\hat{A}$ and x^{ini} given, for any vector b obtained by a real measurement using the detector described by its response matrix $\hat{A}$, one can attempt to find a corresponding unfolded true distribution x. Trying to solve the linear system of equations

$$\hat{A}x = b \tag{5.2}$$

against x directly, using the exact inversion of the matrix, usually leads to completely unacceptable rapidly oscillating solutions.

To be more general one can express the discrete distributions x, b and the response matrix $\hat{A}$ in terms of the underlying continuous probability density functions: let y^{true} be the continuous true variable under consideration, whose variation range $\{y_0^{\text{true}} \div y_{n_x}^{\text{true}}\}$ is divided into n_x bins with boundaries $y_j^{\text{true}}, j = 1, \ldots, n_x - 1$. Each component of the vector x is then calculated as an integral over the true distribution function $\mathcal{X}(y^{\text{true}})$ in the appropriate range:

$$x_j = \int_{y_{j-1}^{\text{true}}}^{y_j^{\text{true}}} dy^{\text{true}}\, \mathcal{X}(y^{\text{true}}) \,, \qquad j = 1, \ldots, n_x \,. \tag{5.3}$$

Analogously, let $\{y_0 \div y_{n_b}\}$ be the variation range of the measured variable y, with bin boundaries $y_i, i = 1, \ldots, n_b - 1$. Then the components of the vector b are appropriate integrals over the continuous distribution function $\mathcal{B}(y)$:

$$b_i = \int_{y_{i-1}}^{y_i} dy\, \mathcal{B}(y) \,, \qquad i = 1, \ldots, n_b \,. \tag{5.4}$$

Let $\hat{\mathcal{A}}(y, y^{\text{true}})$ be the detector response function, which maps the true distribution to the observed one, according to the convolution integral:

$$\mathcal{B}(y) = \int_{y_0^{\text{true}}}^{y_{n_x}^{\text{true}}} dy^{\text{true}}\, \hat{\mathcal{A}}(y, y^{\text{true}})\, \mathcal{X}(y^{\text{true}}) \,. \tag{5.5}$$

After this, the response matrix $\hat{A}$ can be defined as the ratio of two integrals:

$$\hat{A}_{ij} = \frac{\int_{y_{i-1}}^{y_i} dy \int_{y_{j-1}^{\text{true}}}^{y_j^{\text{true}}} dy^{\text{true}}\, \hat{\mathcal{A}}(y, y^{\text{true}})\, \mathcal{X}(y^{\text{true}})}{\int_{y_{j-1}^{\text{true}}}^{y_j^{\text{true}}} dy^{\text{true}}\, \mathcal{X}(y^{\text{true}})} \,. \tag{5.6}$$

Each element $\hat{A}_{ij}$ is equal to the probability for an event generated in the *true* bin j to be found in *measured* bin i.

5.3 Singular Value Decomposition

5.3.1 Definitions

A singular value decomposition (SVD) of a real $m \times n$ matrix A is its factorization of the form

$$A = U S V^T \,. \tag{5.7}$$

where U is an $m \times m$ orthogonal matrix, V is an $n \times n$ orthogonal matrix, while S is an $m \times n$ diagonal matrix with non-negative diagonal elements:

$$UU^T = U^TU = I, \quad VV^T = V^TV = I \ , \tag{5.8}$$

$$S_{ij} = 0 \ \text{ for } \ i \neq j, \quad S_{ii} \equiv s_i \geq 0 \ . \tag{5.9}$$

The quantities s_i are called *singular values* of the matrix A, and columns of U and V are called the left and right *singular vectors.* The singular values contain very valuable information about the properties of the matrix. If, for example, A is itself orthogonal, all its singular values are equal to 1. On the contrary, a degenerate matrix will have at least one zero among its singular values. In fact, the rank of a matrix is the number of its non-zero singular values. If the matrix and/or the r.h.s. of a linear system is known with some level of uncertainty, and some singular values of the matrix are significantly smaller than others, the system may be difficult to solve even if formally the matrix has full rank. In many aspects such matrices behave like degenerate ones, and SVD suggests a method of treating such problems, which is common for small and exactly zero singular values. It will be assumed that the singular values s_i form a decreasing sequence, *i.e.*, $s_1 \geq s_2 \geq \ldots \geq s_n$. This is easily achieved by swapping pairs of singular values, swapping simultaneously corresponding columns of U and V. It will further be assumed also that $m \geq n$, which means that the number of bins in the measured histogram b should not be smaller than the number of bins in the unfolded histogram x. If necessary, one can just add rows of zeroes to the initial matrix.

Comprehensive descriptions of SVD with many technical details and examples can be found in the literature (see, e.g., [152, 153]). In practice, SVD is performed by the FORTRAN routine `SVD` which is present in the CERN program library `CERNLIB`. Some earlier implementations can be found in refs. [152, 153] as well.

Once the matrix is decomposed into the form (5.7), its properties can be readily analyzed and it becomes easy to manipulate, as illustrated in following subsections. This kind of analysis is useful for ill-defined linear systems with almost (or even exactly) degenerate matrices, as it not only locates the difficulty, but can also suggest ways of overcoming it.

5.3.2 A Simple Example

Let the response matrix $\hat{A}$ have the form

$$\hat{A} = \frac{1}{2}\begin{pmatrix} 1+\epsilon & 1-\epsilon \\ 1-\epsilon & 1+\epsilon \end{pmatrix} \ , \tag{5.10}$$

with $0 \leq \epsilon \leq 1$ determining the "quality" of the detector: $\epsilon = 1$ means an ideal detector with the response matrix equal to unity, while small $\epsilon \ll 1$ corresponds to a poor detector, almost unable to distinguish the two bins. Note however, that the overall efficiency is 100%, so that no event escapes detection (sum of elements in each column equals 1). The measurement process now is simulated by multiplying the matrix $\hat{A}$ over the true distribution x, resulting in the measured histogram b:

$$\hat{A}\,x = b\,. \tag{5.11}$$

With vector b measured and the response matrix (5.10) given, one can try to unfold the true distribution. Singular value decomposition of 2×2 matrices is simple, involving a single rotation from left and another from right. As the matrix (5.10) is symmetric, the orthogonal matrices U and V should coincide. One obtains:

$$\hat{A} = U\,S\,V^T\,, \tag{5.12}$$

with

$$U = V = \frac{1}{\sqrt{2}}\begin{pmatrix} 1 & 1 \\ 1 & -1 \end{pmatrix}, \qquad S = \begin{pmatrix} 1 & 0 \\ 0 & \epsilon \end{pmatrix}. \tag{5.13}$$

The two singular values of the matrix (5.10) are $s_1 = 1,\ s_2 = \epsilon$.

Suppose now that the apparatus described by the matrix (5.10) has been used to measure numbers of events in a two-bin histogram

$$b = \begin{pmatrix} b_1 \\ b_2 \end{pmatrix}. \tag{5.14}$$

Let B be the corresponding covariance matrix, which is diagonal with entries b_1, b_2 in the case of purely statistical errors. In order to solve the system, one uses U, S and V from (5.13) to rotate both the unknown vector x and the r.h.s. of the system b,

$$z = V^T x = \frac{1}{\sqrt{2}}\begin{pmatrix} x_1 + x_2 \\ x_1 - x_2 \end{pmatrix}, \qquad d = U^T b = \frac{1}{\sqrt{2}}\begin{pmatrix} b_1 + b_2 \\ b_1 - b_2 \end{pmatrix}, \tag{5.15}$$

in order to form a *diagonal* system of equations

$$S\,z = d, \qquad z = S^{-1} d, \tag{5.16}$$

where

$$S^{-1} = \begin{pmatrix} 1 & 0 \\ 0 & \frac{1}{\epsilon} \end{pmatrix}. \tag{5.17}$$

The unknown vector x can now be easily obtained by rotating z back:

$$x = Vz = VS^{-1}d = VS^{-1}U^Tb = \hat{A}^{-1}b = \frac{b_1 - b_2}{2\epsilon}\begin{pmatrix} 1 \\ -1 \end{pmatrix} + \frac{b_1 + b_2}{2}\begin{pmatrix} 1 \\ 1 \end{pmatrix}. \tag{5.18}$$

Expression (5.18) gives the exact solution of the system (5.11) for whatever small but finite ϵ.

Formally, SVD of the matrix $\hat{A}$ means a decomposition of the r.h.s. b into a series of orthogonal and normalized functions of the discrete variable $i = 1, \ldots, n_b$. The basis is given by the columns of the matrix U, and the components of the vector d form the coefficients of this decomposition. Similarly, the vector of unknowns x is also decomposed into a series of ortho-normalized functions of the discrete variable $j = 1, \ldots, n_x$, given by the columns of the matrix V, while the coefficients stored in the vector z are new unknowns. After performing these transformations, the initial system of equations (5.11) is reduced to the diagonal system (5.16) which can be readily solved: the matrix S in Eq. (5.13) is diagonal and can be inverted by just inverting the singular values.

The inverse matrix $\hat{A}^{-1}$ exists for any $\epsilon \neq 0$:

$$\hat{A}^{-1} = V\, S^{-1} U^T = \frac{1}{2\epsilon} \begin{pmatrix} 1+\epsilon & -1+\epsilon \\ -1+\epsilon & 1+\epsilon \end{pmatrix} = \frac{1}{2} \begin{pmatrix} 1 & 1 \\ 1 & 1 \end{pmatrix} + \frac{1}{2\epsilon} \begin{pmatrix} 1 & -1 \\ -1 & 1 \end{pmatrix}. \tag{5.19}$$

Note that the expressions (5.18) and (5.19) are exact, so that SVD and the subsequent analysis can be considered as just another method of solving well determined full rank linear systems, maybe a bit too complicated but quite capable. If all components of the rotated r.h.s. d are statistically significant *and* if neither of the singular values s_i of the matrix $\hat{A}$ is too small, the system (5.11) can be solved without any problem using any other method like Gaussian elimination. But if ϵ is small the problem becomes ill-determined, and when in addition the r.h.s. is affected by measurement errors, the exact solution usually does not make any sense. In this case it is not the exact solution one is interested in, and conventional methods of solving linear systems do not work. Usually they cannot even detect the problem. To illustrate this, one may assume that the measured event numbers b_1 and b_2 satisfy the following relation:

$$\begin{aligned} b_1 - b_2 &\leq \Delta(b_1 - b_2) \\ \Rightarrow (b_1 - b_2)^2 &\leq b_1 + b_2. \end{aligned} \tag{5.20}$$

This means that the difference $b_1 - b_2$ is not statistically significant, so that the first term in the exact solution (5.18) is in fact a random number. But if ϵ is small enough (in this case - smaller than $1/\sqrt{b_1 + b_2}$), this first term in both x_1 and x_2 dominates over the well-behaved and statistically significant second term, leading to almost arbitrary results. This phenomenon can be understood by recalling the detector response matrix (5.10) of the example: for very small ϵ the apparatus is almost "blind", and one can hardly expect to determine x_1 and x_2 separately, unless the errors in b are sufficiently small.

5.4 Rescaling Equations and Normalizing Unknowns

Going back to the full-scale problem defined in Section 5.2 one can look at the initial linear system (5.2) from another viewpoint. It represents the solution of the following least square problem:

$$\sum_{i=1}^{n_b} \left(\sum_{j=1}^{n_x} \hat{A}_{ij} x_j - b_i\right)^2 = \min\ , \tag{5.21}$$

and is adequate if the equations are exact, or if the errors in b_i are identical. This is not generally the case, as measurement errors in the vector b vary from bin to bin, and hence, different equations have different significance. In fact, one should consider a weighted least squares problem, where the following expression is being minimized:

$$\sum_{i=1}^{n_b} \left(\frac{\sum_{j=1}^{n_x} \hat{A}_{ij} x_j - b_i}{\Delta b_i}\right)^2 = \min , \tag{5.22}$$

where Δb_i is the error in b_i. The general case of (5.22) reads

$$(\hat{A}x - b)^T B^{-1} (\hat{A}x - b) = \min , \tag{5.23}$$

where B is the covariance matrix of the measured vector b.

5.4.1 Normalisation of the Unknowns

The exact solution of a well-determined linear system remains unchanged, if either the equations, or the unknowns, or both are rescaled. However, in the cases under consideration (where $n_x \leq n_b$ and some singular values are small) the minimization of Eq. (5.23) leads to an overdetermined system which should be solved in the least-squares sense. In this case any rescaling of equations and/or unknowns changes the singular values of the system and hence the solution as well. One can suggest various ways of rescaling, and some of them may lead to a serious improvement in the system behavior. The task is then to optimize the system by rescaling it so that significant information is not suppressed while the non-significant one is at least not enhanced.

One can, for instance, divide an unknown x_k everywhere in the system by a number λ, multiplying simultaneously all corresponding coefficients $A_{ik}, i = 1, \ldots, n_b$ by λ. Choosing various λ's for different k's, one can obtain substantially different matrices. Thus one may argue that one particular choice of rescaling coefficients is the most suitable for our purposes, provided the probability matrix $\hat{A}$ is obtained using a Monte Carlo simulation procedure (see Section 5.2).

Consider a new unknown vector $w_j = x_j / x_j^{\text{ini}}$, which measures the *deviation* of x from the initial Monte Carlo input vector x^{ini}. If one now multiplies each column of the probability matrix $\hat{A}_{ij}$ by the corresponding number of events generated in this bin x_j^{ini}, the system becomes

$$\sum_{j=1}^{n_x} A_{ij} w_j = b_i , \tag{5.24}$$

where A_{ij} is no longer the *probability*, but rather the *actual number of events,* which were generated in bin j and ended up in bin i[1]. Now, $x = x^{\text{ini}}$ corresponds to all components of the vector w being equal to 1, so that $b_i^{\text{ini}} = \sum_{j=1}^{n_x} A_{ij}$. At the end of the unfolding procedure, in order to obtain the correctly normalized unfolded solution x_j, one has to multiply the unfolded vector w by x^{ini}:

$$x_j = w_j x_j^{\text{ini}}, \qquad j = 1, \ldots, n_x . \tag{5.25}$$

---

[1] If defined through continuous probability distributions, this new matrix is equal to the *numerator* of Eq. (5.6).

Of course, if the number of generated events is the same for each bin, $x^{\text{ini}} = \text{const}$, then the probability matrix $\hat{A}$ and the number-of-events matrix A coincide up to an overall constant factor which is irrelevant for the analysis.

The systems (5.2) and (5.24) are equivalent for any shape of x^{ini}, if the exact solution is required, but there are two reasons why, for the class of problems considered here, the system (5.24) is much better suited.

If the initial Monte Carlo distribution x^{ini} is physically motivated and is reasonably close to the one being unfolded, the unknown vector w should be smooth and should have small bin-to-bin variation, thus requiring less terms in the decomposition into orthogonal functions. This in turn means that more accurate unfolding should be possible, as fewer unknowns are required in order to obtain the unfolded solution.

The second reason is more technical and is connected to the singular value analysis. Whatever high statistics is generated in order to obtain the matrix A, some of its columns and/or rows may contain very few events, and some elements A_{ij} may have just a single entry. In the probability matrix, these elements will contain the probability one, unjustifiably giving a high weight to that particular equation and unknown, and the fact that this element has a 100 % error is completely ignored. At the same time, highly populated columns with statistically well-determined elements usually contain values significantly smaller than 1, due to finite resolution and limited acceptance. This makes the probability matrix $\hat{A}$ a bad choice. On the contrary, the elements of the number-of-event matrix A are large if the generated statistics is large, and vice versa, thus giving a larger weight to better determined equations and unknowns.

5.4.2 Rescaling Equations

The very form of Eq. (5.22) suggests the way of rescaling the equations: after dividing each equation by the corresponding error Δb_i one obtains a balanced system, where all the equations have equal weights. If B is not diagonal, the equation rescaling becomes slightly more complicated but still straightforward. Being a covariance matrix, B should be symmetric and positive-definite. Its SVD yields:

$$B = QRQ^T, \qquad R_{ii} \equiv r_i^2 \neq 0, \qquad R_{ij} = 0 \text{ for } i \neq j, \qquad B^{-1} = QR^{-1}Q^T \,. \tag{5.26}$$

Substituting B^{-1} into Eq. (5.23) one sees that after the rotation and rescaling of both the r.h.s. b and the matrix A,

$$\tilde{A}_{ij} = \frac{1}{r_i}\sum_m Q_{im}A_{mj}, \quad \tilde{b}_i = \frac{1}{r_i}\sum_m Q_{im}b_m \,. \tag{5.27}$$

the expression being minimized looks very simple again,

$$(\tilde{A}w - \tilde{b})^T(\tilde{A}w - \tilde{b}) = \min \,. \tag{5.28}$$

and the minimization leads to the system

$$\sum_j \tilde{A}_{ij}w_j = \tilde{b}_i \,. \tag{5.29}$$

The covariance matrix of the rescaled r.h.s., $\tilde{B}$, is now explicitly made equal to the unit matrix I, and all the equations have equal importance.

5.5 Regularisation and Unfolding

The transition from Eq. (5.21) to (5.28) changes the appearance of the system from (5.2) to (5.29). The singular values of the matrix are also changed, but the main problem with small singular values still remains. The exact solution of Eq. (5.29) will again most certainly lead to a rapidly oscillating distribution, which may have a smaller amplitude but is still useless. This spurious oscillatory component should be suppressed, using some *a priori* knowledge about the solution. Technically this can be achieved by adding a *regularisation* or *stabilization* term to the expression to be minimized (see Refs. [153, 149, 154] and references therein):

$$(\tilde{A}\,w - \tilde{b})^T\,(\tilde{A}\,w - \tilde{b}) + \xi \cdot (C\,w)^T C\,w \;=\; \min\,. \tag{5.30}$$

Here C is a matrix which defines the *a priori* condition on the solution, while the value of the regularisation parameter ξ determines the relative weight of this condition. For example, the choice $C_{ik} = \delta_{ik}$ would minimize the euclidean norm of the vector w, and if ξ is set to be infinitely large, this would result in a vector $w_j = 0$ for any $\tilde{A}$ and $\tilde{b}$. While the optimal value of ξ is very much problem-dependent and its determination is an important part of our procedure, the explicit form of the matrix C should be chosen from general considerations. The common belief is that the solution histogram w should be smooth, with small bin-to-bin variation.

One appropriately defines the "curvature" of the discrete distribution w_j as the sum of the squares of its second derivatives [149]:

$$\sum_i [(w_{i+1} - w_i) - (w_i - w_{i-1})]^2\,. \tag{5.31}$$

Then the choice

$$C \;=\; \begin{pmatrix} -1 & 1 & 0 & 0 & \dots & & \\ 1 & -2 & 1 & 0 & \dots & & \\ 0 & 1 & -2 & 1 & \dots & & \\ & \dots & & & \dots & & \\ & \dots & & & 1 & -2 & 1 \\ & \dots & & & & 1 & -1 \end{pmatrix} \tag{5.32}$$

will suppress solutions w having large curvatures. Minimization of Eq. (5.30) leads to a new linear system, which has n_x additional equations:

$$\begin{bmatrix} \tilde{A} \\ \sqrt{\xi}\cdot C \end{bmatrix} w \;=\; \begin{bmatrix} \tilde{b} \\ 0 \end{bmatrix}\,. \tag{5.33}$$

This system is over-determined and one can apply SVD to the $(n_b + n_x) \times n_x$ matrix in the l.h.s. in order to solve it. This is possible, but would require calling SVD for each value of ξ. Fortunately, a more efficient method (called sometimes *damped least squares* [153]) can be suggested, which allows to express the solution of Eq. (5.33) for any ξ through the solution of the initial non-regularized problem corresponding to $\xi = 0$. The first step is to make the regularisation term proportional to the unit matrix I:

$$\begin{bmatrix} \tilde{A}\, C^{-1} \\ \sqrt{\xi} \cdot I \end{bmatrix} C w \;=\; \begin{bmatrix} \tilde{b} \\ 0 \end{bmatrix} . \tag{5.34}$$

For $\xi = 0$ the system (5.34) is equivalent to (5.29) if the inverse C^{-1} exists and can be safely calculated. The "second derivative" matrix (5.32), however, is apparently degenerate (every column and every row sums up to zero) so some measures should be taken to make the exact inversion possible. The most simple thing to do is to add a small diagonal component, $C_{ik} \Rightarrow C_{ik} + \kappa \cdot \delta_{ik}$, with κ large enough to make the inversion possible, but small enough not to change significantly the condition of minimum curvature. In most cases, $\kappa = 10^{-3}$ or 10^{-4} is a good choice. C now is a symmetric non-singular matrix,

$$C \;=\; \begin{pmatrix} -1+\kappa & 1 & 0 & 0 & \dots & & \\ 1 & -2+\kappa & 1 & 0 & \dots & & \\ 0 & 1 & -2+\kappa & 1 & \dots & & \\ & \dots & & & \dots & & \\ & \dots & & 1 & -2+\kappa & 1 \\ & \dots & & & 1 & -1+\kappa \end{pmatrix} . \tag{5.35}$$

which can be inverted using standard techniques[2].

In order to solve the system (5.34) with $\xi = 0$. first, one needs SVD to decompose the product of matrices $\tilde{A}\, C^{-1}$:

$$\tilde{A}\, C^{-1} \;=\; U\, S\, V^{T} . \tag{5.36}$$

Here, once again, U and V are orthogonal and S is diagonal, with non-increasing positive diagonal elements s_i. Rotating both $\tilde{b}$ and Cw one obtains the diagonal system:

$$d \equiv U^{T} \tilde{b} \,, \qquad z \equiv V^{T} C\, w \, . \tag{5.37}$$

The system now looks (and actually is) very simple:

$$s_i \cdot z_i \;=\; d_i \,, \qquad i = 1, \dots, n_x \, . \tag{5.38}$$

Note that because the covariance matrix of the r.h.s. $\tilde{b}$ was made equal to the unit matrix, the orthogonality of U guarantees that the new rotated r.h.s. d also has a unit covariance matrix, *i.e.*, the equations (5.38) are completely independent and have identical unit errors in their r.h.s.

Solving (5.38) yields the exact solution of the non-regularized system:

$$z_i^{(0)} \;=\; \frac{d_i}{s_i}, \qquad w^{(0)} = C^{-1} V z^{(0)} \,, \tag{5.39}$$

---

[2] One has, however, to be careful, as the matrix is very close to a singular one, and some of the standard routines may not work for small κ (even in double numerical precision). For example RFIN, RSINV and RSFINV fail for $\kappa = 10^{-4}$, while RINV is successful. It is convenient to use SVD once again for this purpose: decompose $C = U_C S_C V_C^T$ and then calculate $C^{-1} = V_C S_C^{-1} U_C^T$.

and the true distribution x can be obtained by multiplying each w_i by the corresponding $x_i^{\rm ini}$. With $\xi = 0$ there is no regularisation, so this solution is as useless as it used to be. But the solution of the system (5.33) with non-zero ξ can now be found easily using the procedure explained in detail in Ref. [153] (Chapter 25, Sect.4). In short, introducing a non-zero ξ is effectively equivalent to changing d_i by a regularized distribution:

$$d_i^{(\xi)} = d_i \frac{s_i^2}{s_i^2 + \xi} , \tag{5.40}$$

so that the solution of the rotated system becomes

$$z_i^{(\xi)} = \frac{d_i \, s_i}{s_i^2 + \xi}, \qquad w^{(\xi)} = C^{-1} V \, z^{(\xi)} . \tag{5.41}$$

One can now see how a non-zero ξ regularizes the singularities due to small s_i's, effectively working as a low-pass filter in the language of Fourier-transform. By definition, s_i is small when the index i is large, which in general corresponds to quickly oscillating singular vectors (*i.e.*, columns of U and V) defining the new basis in the rotated space. Continuing the analogy with Fourier analysis, one can mention that the cutoff provided by the above regularisation procedure happens to be quite smooth, thus avoiding specific quasi-periodic fluctuations of the solution known as the Gibbs phenomenon.

The covariance matrices Z and W of the solutions (5.41) now read:

$$\begin{aligned} Z_{ik}^{(\xi)} &= \frac{s_i^2}{(s_i^2 + \xi)^2} \cdot \delta_{ik} , \\ W^{(\xi)} &= C^{-1} V \, Z^{(\xi)} V^T C^{T \, -1} . \end{aligned} \tag{5.42}$$

In order to obtain the true unfolded distribution x and its covariance matrix X one multiplies w and W by the initial Monte Carlo distribution $x^{\rm ini}$:

$$x_i^{(\xi)} = x_i^{\rm ini} \, w_i^{(\xi)} , \tag{5.43}$$

$$X_{ik}^{(\xi)} = x_i^{\rm ini} \, W_{ik}^{(\xi)} x_k^{\rm ini} . \tag{5.44}$$

It is important to note that while Eqs. (5.43) and (5.44) are regularized and as such depend on the value of ξ, the inverse of the covariance matrix X^{-1} (which should be used for any χ^2 calculation involving the unfolded distribution (5.43)), is regular and readily calculable:

$$X_{jk}^{-1} = \frac{1}{x_j^{\rm ini} x_k^{\rm ini}} \sum_i \tilde{A}_{ij} \tilde{A}_{ik} . \tag{5.45}$$

In fact, $X^{(\xi)}$ defined by Eq. (5.44) is the *effective pseudoinverse* of the matrix (5.45). This means that while the equation

$$X^{(\xi)} X^{-1} X^{(\xi)} = X^{(\xi)} \tag{5.46}$$

is valid as if $X^{(\xi)}$ were the true inverse of X^{-1}, for a different ordering one has (see [152, 153]):

$$\| X^{-1} X^{(\xi)} X^{-1} - X^{-1} \| < \xi . \tag{5.47}$$

5.6 Error Analysis and Choice of ξ

Important and interesting information about the whole problem can be disclosed by plotting d_i, or, better, $\log|d_i|$ versus i. The i-th component of the vector d is the coefficient in the decomposition of the measured (and rescaled) histogram $\tilde{b}$ in front of a basis function defined by the i-th column of the rotation matrix U. For reasonably smooth measured distributions, only the first few (say, k) terms of the decomposition are expected to be significant, while the contribution of quickly oscillating basis vectors corresponding to large values of $i > k$ should be compatible with zero, well within the statistical errors in d_i (which are equal to 1 for all i). So, on the plot one should see two separate patterns (see Section 5.8 for a few illustrations): for small i, d_i should be statistically significant, $|d_i| \gg 1$, falling gradually (usually exponentially) towards a gaussian-distributed random value for large i with the standard deviation equal to 1 and the mean close to zero (the absolute values of non-significant components $|d_i|, i > k$ should have the average close to $\sqrt{2/\pi} \approx 0.8$). The critical value $i = k$, after which d_i's are non-significant, determines the effective rank of the obtained system of equations. Usually it is clearly seen on the plot of $\log|d_i|$ versus i, as the value of i where the behavior of d_i changes from exponentially falling to a constant.

The standard statistical tests can be used to check whether the last $n_x - k$ components of d, are compatible with the expected normal distribution with zero mean and unit variance. If this is not the case, then the errors in the measured data (or maybe the response matrix itself) seem not to be estimated correctly. If, for example,the actual measurement errors in b are under(over)estimated, then the variance of d_i for $i > k$ will be smaller (larger) than 1. Moreover, if some additional correlations exist in the measured data which are not accounted for in the covariance matrix B, then $\log|d_i|$ may steadily decrease for all i, though probably for $i > k$ the slope will be different. All this shows that the analysis of the plot of $\log|d_i|$ versus i is of great interest by itself, being able to reveal the actual level of understanding the measurement errors in the experiment described by the simulated matrix A.

If the number of statistically significant equations is determined to be equal to k, the regularisation parameter ξ is appropriately put equal to the square of the kth singular value $s_k \equiv S_{kk}$ of the matrix $\tilde{A}C^{-1}$, determined in Eq. (5.36):

$$\xi = s_k^2 \, . \tag{5.48}$$

With ξ given by (5.48), the unfolded vector x, its covariance matrix X and the inverse of the latter X^{-1} are completely defined by the corresponding Eqs. (5.43), (5.44) and (5.45), forming the solution of the unfolding problem.

Yet another (and maybe more convincing) way of determining ξ is to generate a test distribution which is close to the expected true one, but still significantly different from the initial Monte Carlo distribution x^{ini}. Then one should simulate the measurement process by applying the response matrix to it, and add corresponding random statistical errors to the thus obtained "measured" distribution. The described unfolding procedure should be applied to the latter, and the best choice for ξ is the one giving the smallest

χ^2 between the test and the unfolded distributions (see our second example in Sect. 5.8). This approach is followed in the τ spectral functions analysis analysis.

5.7 The Algorithm

In this section the concise description of the complete unfolding algorithm is presented. The algorithm is linear (*i.e.*, contains no loops) and can be divided into three distinct parts: initialization, rescaling/rotation and actual unfolding. Each step includes references to relevant subsections and equations.

- Initialization:
  1. Define the number of bins n_b and bin boundaries of the measured histogram b.
  2. Define the number of bins n_x and bin boundaries, common for the initial Monte Carlo x^{ini} and the unfolded distribution x.
  3. Build the "second derivative" matrix C, according to Eq. (5.35).
  4. Calculate the inverse C^{-1} (see Section 5.5).
  5. Generate the initial Monte Carlo histogram x^{ini}, and simulate the detector response in terms of the two-dimensional $n_b \times n_x$ histogram A. The elements of A should contain actual numbers of events rather than probabilities.
  6. Read and fill the measured distribution b and its covariance matrix B.
- Rescaling and rotation:
  1. Perform SVD of the covariance matrix B, according to Eq. (5.26).
  2. Rotate and rescale both the r.h.s. b and the matrix A, in order to make the covariance matrix of the r.h.s. equal to the unit matrix, according to Eqs. (5.27).
  3. Calculate the inverse of the covariance matrix, X^{-1}, of the unfolded vector x, according to Eq. (5.45).
  4. Multiply matrices $\tilde{A}$ and C^{-1} and perform SVD of the product, according to Eq. (5.36).
  5. Calculate the rotated r.h.s. d, according to Eq. (5.37).
- Unfolding:
  1. Plot $\log|d_i|$ vs i and determine the effective rank k of the system (see Section 5.6).
  2. Put $\xi = s_k^2$.
  3. Alternatively, put $\xi = s_k^2$ and determine the the appropriate k by means of a simulated *test* distribution where the true distribution is known.
  4. Calculate $z^{(\xi)}; w^{(\xi)}, Z^{(\xi)}, W^{(\xi)}$, according to Eqs. (5.41-5.42).

5. Calculate the unfolded distribution $x^{(\xi)}$ and its covariance matrix $X^{(\xi)}$, according to Eqs. (5.43-5.44).

The vector $x^{(\xi)}$ and matrices $X^{(\xi)}$ and X^{-1} form the complete solution of the unfolding problem defined by the matrix A, simulated initial distribution $x^{\rm ini}$, the measured vector b and its covariance matrix B.

5.8 Examples

The use of the unfolding procedure described above is now illustrated with two examples.

The first one is rather academic, and it is included because it was already used in Refs. [149] and [154]. The response function $\hat{\mathcal{A}}(y, y^{\rm true})$ is given by

$$\hat{\mathcal{A}}(y, y^{\rm true}) = \left[1 - 0.5(1 - y^{\rm true\,2})\right]\left\{4\exp[-50(y - y^{\rm true} + 0.05y^{\rm true\,2})^2]\right\} . \tag{5.49}$$

Then the probability response matrix was built according to Eq. (5.6) for 40 equidistant bins in the interval (0,2) for both $y^{\rm true}$ and y. The matrix is presented in Fig. 5.1a. The true continuous distribution is taken to be

$$\mathcal{X}(y^{\rm true}) = \frac{4}{4 + (y^{\rm true} - 0.4)^2} + \frac{0.4}{0.04 + (y^{\rm true} - 0.8)^2} + \frac{0.2}{0.04 + (y^{\rm true} - 1.5)^2} . \tag{5.50}$$

After the convolution (5.5), the distribution $\mathcal{B}(y)$ is discretized according to Eq. (5.4). Simulating a counting experiment, a random normally distributed error is then added to each entry, assuming the overall initial statistics of 5000 events. The resulting "measured" distribution b is plotted in Fig. 5.1b by a dotted line. The distortions caused by the measurement process can be seen by comparing the latter to the true distribution (5.50), shown by the solid curve in Fig. 5.1b.

The unfolding algorithm described above is then applied to the distribution b. Fig. 5.1c shows the plot of the rescaled and rotated r.h.s. vector d. The solid line corresponds to the actual measured histogram, and the horizontal dashed line shows the one standard deviation statistical error in d_i, which is equal to one for each i. One can see that after $i = 10$ the components d_i are clearly non-significant. The flatness of this distribution for $i > 10$ and its apparent compatibility with the expected gaussian distribution with zero mean and unit variance, is in fact a test of the gaussian random number generator used to generate the errors in the measured histogram b. Restricting oneself to less than 10 equations, one loses significant information. Namely, the choice $k = 1$ leaves effectively only one equation, and the obtained "unfolded" distribution $x^{(1)}$ will be nothing else but a constant. On the contrary, by taking more than 10 equations one includes rapidly oscillating components with non-significant (and large) coefficients d_i/s_i. In this particular example taking $k = 40$ would result in a distribution x wildly oscillating with the amplitude of about 5000 (see Fig. 5.2 for $\xi = s_6^2$ and $\xi = s_{15}^2$).

The shape of the distribution d suggests that the effective rank k should be put equal to 10. The dashed line on Fig. 5.1c shows the regularized distribution $d^{(\xi)}$ calculated using

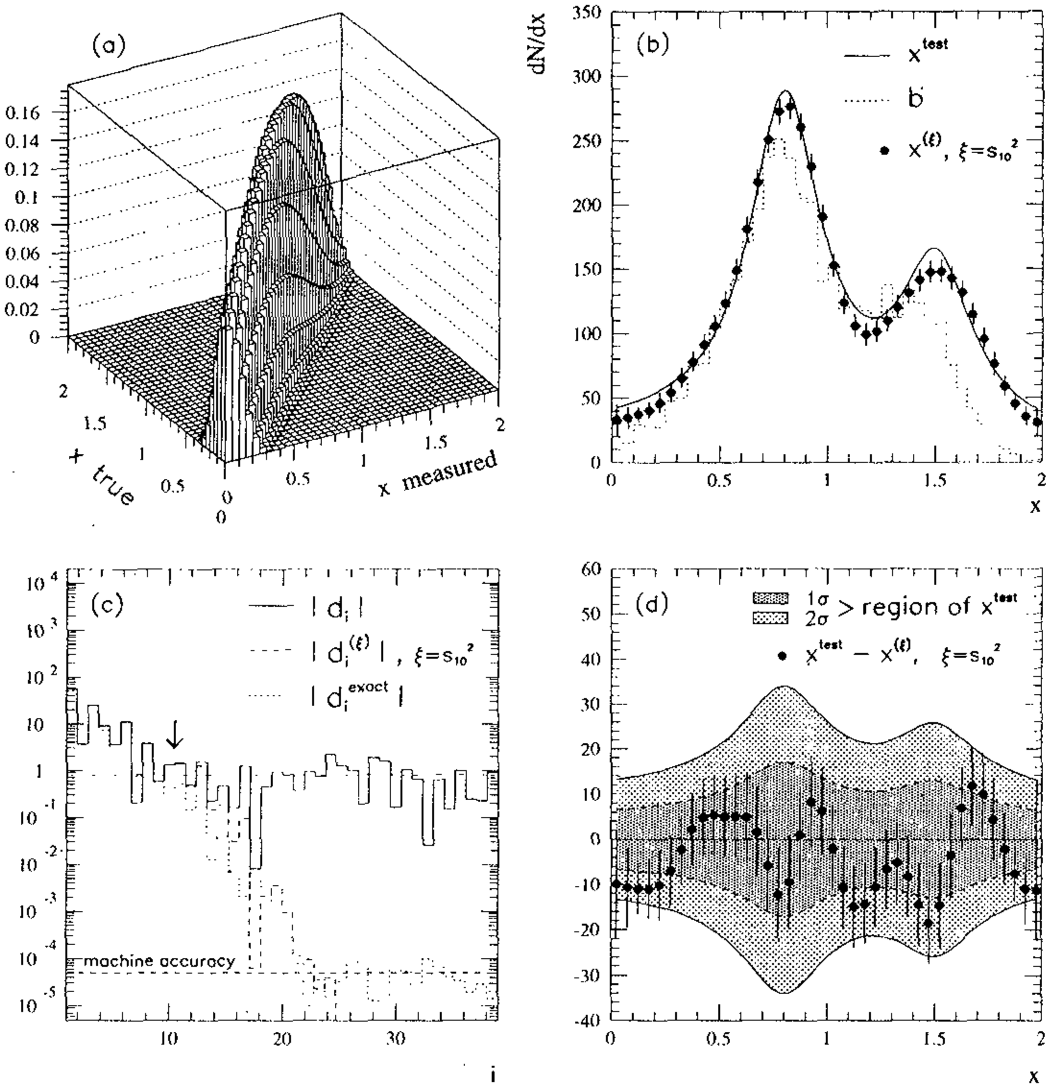

Figure 5.1: **a** *The probability matrix $\hat{A}$ corresponding to the response function (5.49).* **b).** *The true distribution (5.50) (solid curve) compared to the measured histogram b and the unfolded distribution $x^{(\xi)}$ for $\xi = s_{10}^2$.* **c).** *The absolute values of d_i (solid line) compared to the regularized r.h.s. (dashed line) and the one unaffected by the statistical fluctuations (dotted line). The horizontal line shows statistical errors in d_i, while the arrow indicates the boundary between the significant and non-significant equations.* **d).** *The deviation of the unfolded distribution from the true exact one (see text for details).*

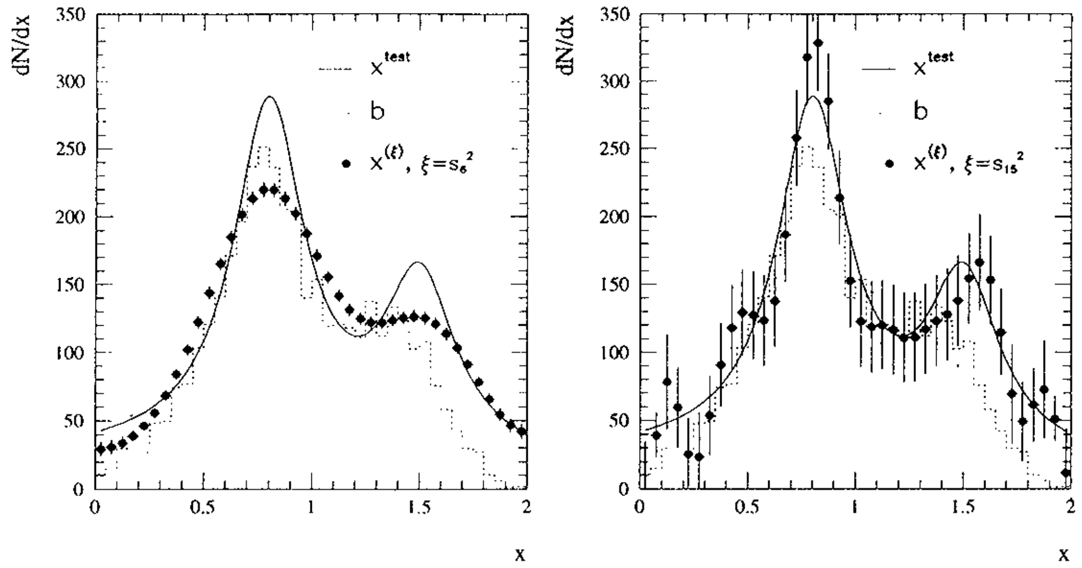

Figure 5.2: *Example of Fig. 5.1 with* $\xi = s_6^2$ *(left hand plot) and* $\xi = s_{15}^2$ *(right hand plot). Too large cutoffs* ξ *lead to a loss of structure (too smoothed) whereas too small* ξ*'s do not cut artificial oscillations. Since not only the measured distribution b but also its errors are unfolded, insignificant information blows also the errors up. Contrarily, the suppression of significant information (left hand plot) reduces the sensibility to small statistical fluctuations and thus the statistical errors.*

(5.40), with $\xi = s_{10}^2$. It is interesting to compare this distribution with the similar one calculated for the exact true distribution (5.50) by the same procedure of rescaling and rotation, but *without* adding the random error (the dotted histogram in Fig. 5.1c). One can see that the regularized distribution is quite close to the true exact one.

The obtained distribution $d^{(\xi)}$ is then used to calculate the unfolded histogram $x^{(\xi)}$, plotted in Fig. 5.1b (data points). It should be compared to the true distribution (5.50), shown by the smooth solid curve. Note that the error bars in $x^{(\xi)}$ account only for the diagonal elements of the covariance matrix X, and thus underestimate the actual errors. The correlations between adjacent bins $x_j^{(\xi)}$ are quite significant, so one should use the exact inverse of the covariance matrix X^{-1} for any kind of χ^2 calculation involving the unfolded vector, and the regularized covariance matrix $X^{(\xi)}$ for the further error propagation.

Fig. 5.1d presents the difference between the exact distribution and the unfolded one, together with the bands showing one and two standard deviation statistical fluctuations in the true exact distribution. At this scale, one still observes some oscillations of the unfolded solution, but they are well balanced, distributed almost uniformly, and are confined inside the two standard deviation band of the true solution, thus indicating that the genuine error is about twice as large as the true statistical one would be, if the measurements were exact. The average χ^2 over the 40 bins is equal to 0.9, meaning that the unfolded distribution is quite satisfactory.

In the second example a simulated spectrum of the invariant mass of two pions is unfolded, corresponding to the $\rho(770)$-meson mass region. An artificial two-dimensional histogram reflecting a possible detector behavior is generated as the detector response matrix A, and is shown in Fig. 5.3a. This time it is a number-of-event matrix resulting from Monte Carlo simulation, as opposed to the probability matrix obtained by the integration of some analytical response function used in the previous example. The matrix is far from being diagonal, and the initial simulated distribution x^{ini}, shown by a dotted line in Fig. 5.3b, varies by about four orders of magnitude.

The "measured" distribution b was obtained in a way similar to the first example: a distribution x^{test} was generated (solid line in Fig. 5.3b), which has a behavior distinctly different from x^{ini}. The measurement process was then simulated by the matrix multiplication:

$$\sum_j A_{ij} \frac{x_j^{\text{test}}}{x_j^{\text{ini}}} = b_i \ , \tag{5.51}$$

and finally a random gaussian error was added to each entry b_i, simulating statistical fluctuations.

Rescaling and rotation results in a distribution d_i plotted in Fig. 5.3c. One sees that the effective rank of the system k is close to 9, so the parameter ξ should be set to the square of the 9th singular value of the matrix AC^{-1}. The components d_i with $i > 9$ are clearly compatible with zero and have standard deviation close to one, thus confirming that the errors in the measured data are estimated correctly.

As in the first example, the choice $k = 1$ would leave us effectively with only one equation, and the obtained "unfolded" distribution $x^{(1)}$ will be nothing else but the initial Monte Carlo distribution x^{ini}, shown by the dotted line in Fig. 5.3b. As for the solution of the non-regularized system with $\xi = 0$, it would include all non-significant components and would oscillate rapidly within the range $\pm(2 \div 3) \cdot 10^4$. This solution depends on the machine accuracy and obviously does not make sense.

The regularized distribution $d_i^{(\xi)}$ is shown by a dashed line in Fig. 5.3c. It is to be compared with the exact distribution d^{test} corresponding to the vector (5.51) after the same procedure of rescaling and rotation, but *without* the random error added. One can see that the regularized vector is much closer to the true exact one for large $i > 9$. The resulting unfolded histogram $x_i^{(\xi)}$ is shown by the data points in Fig. 5.3b. The difference of the unfolded and the exact test distributions is presented in Fig. 5.3d, together with one and two standard deviation bands describing the statistical errors in the test vector. Here, too, the error bars show just the diagonal elements of the error matrix, which in fact contains quite strong bin-to-bin correlations. The agreement is very good indeed, especially if one considers the four orders of magnitude variation range of the test distribution.

5.9 Conclusion

The data unfolding method developed above can be used in a wide range of applications, but is especially well-suited for high energy physics, where the response matrix is usually

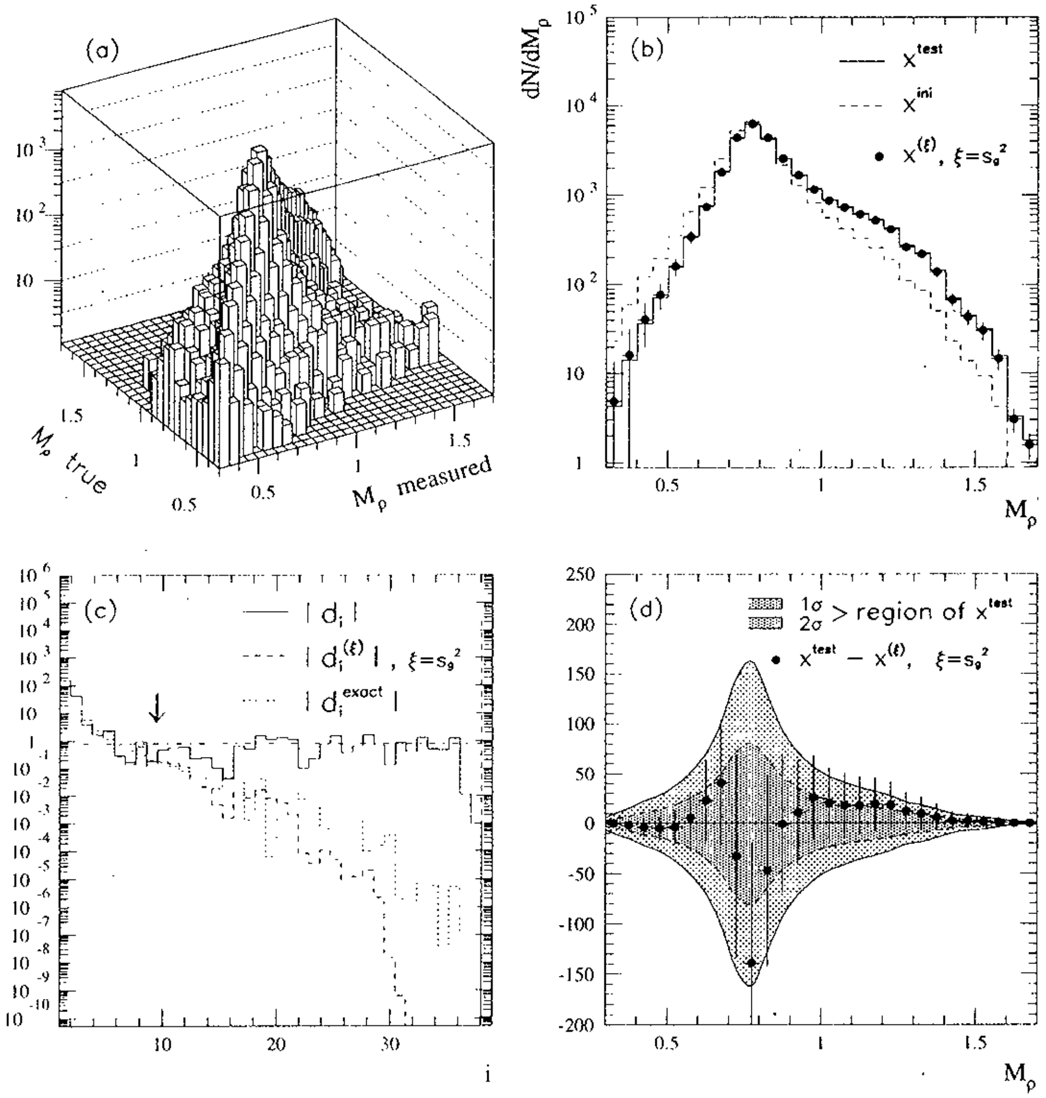

Figure 5.3: **a).** *The simulated number-of-events response matrix A.* **b).** *The true test distribution* x^{test} *(solid line) compared to the unfolded one (data points). The dashed histogram corresponds to the initial distribution* x^{ini} *according to which the response matrix was generated.* **c).** *The absolute values of* d_i *(solid line) compared to the regularized r.h.s. (dashed line) and the one unaffected by the statistical fluctuations (dotted line). The horizontal line shows statistical errors in* d_i*, while the arrow indicates the boundary between the significant and non-significant equations.* **d).** *The deviation of the unfolded distribution from the true exact one (see text for details).*

estimated by a Monte Carlo simulation of the measurement process, using some physically motivated initial distribution of the quantity under consideration.

The use of a very versatile and flexible tool — the Singular Value Decomposition of a matrix — allowed to derive a concise loop-free algorithm for data unfolding.

Obviously, curvature minimization as regularisation criterion introduces some systematic bias into the unfolded distribution. Thus, if the probability response matrix is used, the method will lead to acceptable results only if the true solution is indeed smooth. However, when one uses the number-of-events response matrix, the condition of minimum curvature means that the *deviation* of the expected distribution from the initial Monte Carlo one should be smooth enough. This allows one to use the procedure in cases when the measured distribution has some structure and/or a wide variation range, provided the initial Monte Carlo has a similar behaviour. If this is the case, then even for the small effective rank of the system, when the unfolded distribution happens to be quite close to the initial Monte Carlo, the former (in conjunction with the error matrix and its inverse) is still expected to give a useful solution of the problem.

For the measurement of exclusive spectral functions, individual unfolding procedures with specific detector response matrices A_X and cut parameters ξ_X are applied for each τ decay channel X considered.

Chapter 6

Spectral Functions for Exclusive τ Decay Modes

The spectral function analysis distinguishes between vector and axial-vector modes. The dominant vector contributions are supplied by the decay channels $\tau^- \to \pi^-\pi^0\,\nu_\tau$ (dominated by $\rho^- \to \pi^-\pi^0$) and $\tau^- \to 2\pi^-\pi^+\pi^0\,\nu_\tau$. The axial-vector spectral function is mainly obtained from the $\tau^- \to (3\pi)^-\,\nu_\tau$ (dominated by $a_1^- \to (3\pi)^-$) decay.

6.1 Vector Spectral Functions

The following vector τ decay modes are exclusively reconstructed: $\pi^-\pi^0\,\nu_\tau$, $\pi^-3\pi^0\,\nu_\tau$, $2\pi^-\pi^+\pi^0\,\nu_\tau$, $2\pi^-\pi^+3\pi^0\,\nu_\tau$and $3\pi^-2\pi^+\pi^0\,\nu_\tau$. The measured mass-squared spectra corresponding to these channels are shown in Fig. 6.1 and 6.2. Before unfolding them, the τ and non-τ background and the strange contributions are subtracted out using the Monte Carlo simulation[1] which is based on models of resonance production implemented in `KORALZ3.8` with `TAUOLA1.5` as τ decay library [140, 141, 142]. Remaining hadrons are thought to be pions only.

The spectral functions of the dominant two- and four-pion modes are shown in Fig. 6.3. The errors shown are the diagonal elements of the covariance matrix. They include both statistical and systematic uncertainties. The $2\pi^-\pi^+\pi^0\,\nu_\tau$ decay mode is compared to data of the ARGUS Collaboration [3].

The Inclusive τ Vector Spectral Function

The total inclusive vector current spectral function is obtained by summing up the exclusive spectral functions with the addition of small contributions from unmeasured modes, as discussed below. Table 6.1 gives a survey of the exclusive decay modes considered, their classification and the corresponding branching ratios. If not otherwise specified, the latter were taken from ALEPH publications [24, 5] complemented by CLEO measurements [155, 156, 157, 158] and new results about branching fractions of τ decay

---

[1] No strange contribution is assumed in the $2h^-h^+3\pi^0\,\nu_\tau$ channel.

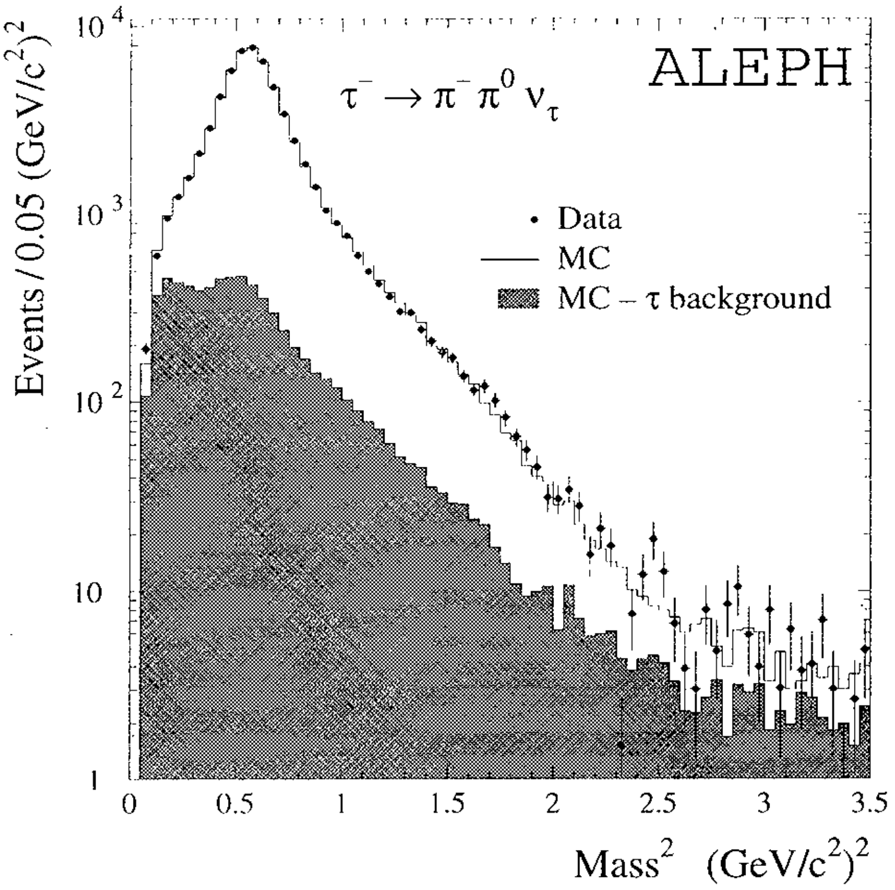

Figure 6.1: *Invariant mass-squared distribution of the $\tau^- \to \pi^-\pi^0\,\nu_\tau$ decay. The PDG* [17] *values $m_{\pi^\pm}$ (m_{π^0}) are assumed for the masses of charged (neutral) particles.*

modes involving kaons presented in Refs. [159, 47]. The individual fractions have been refitted so that the sum of all branching ratios adds up to 100%. The branching ratios of the subsequent meson decays are taken from [17]. The small contributions labeled "MC" are taken from the Monte Carlo simulation. The two-, four- and six-pion modes are exclusively reconstructed as explained in Section 6.1. Special care is taken with isospin-violating ω and η decays, and with final state Kaon production, as explained in the following:

> The decay channel $\tau^- \to \omega\pi^-\,\nu_\tau$ is partly reconstructed in the $2\pi^-\pi^+\pi^0\,\nu_\tau$ class ($\omega \to \pi^+\pi^-\pi^0$), in the $\mathrm{h}^- 2\pi^0\,\nu_\tau$ class ($\omega \to \pi^0\gamma$) and in the $2\pi^-\pi^+\,\nu_\tau$ class. ($\omega \to \pi^+\pi^-$). Corrections to the inclusive τ vector spectral function are applied for the latter two cases using invariant mass-squared distributions predicted by the Monte Carlo simulation. The systematic error due to the uncertainties in the Monte Carlo predictions is estimated to be 20% in every simulated mass bin. For all the following channels where the Monte Carlo simulation is used to complete the inclusive τ vector current spectral function, the uncertainty is assumed to be 50% in every simulated mass bin in order to take into account the poorer knowledge of the spectrum.

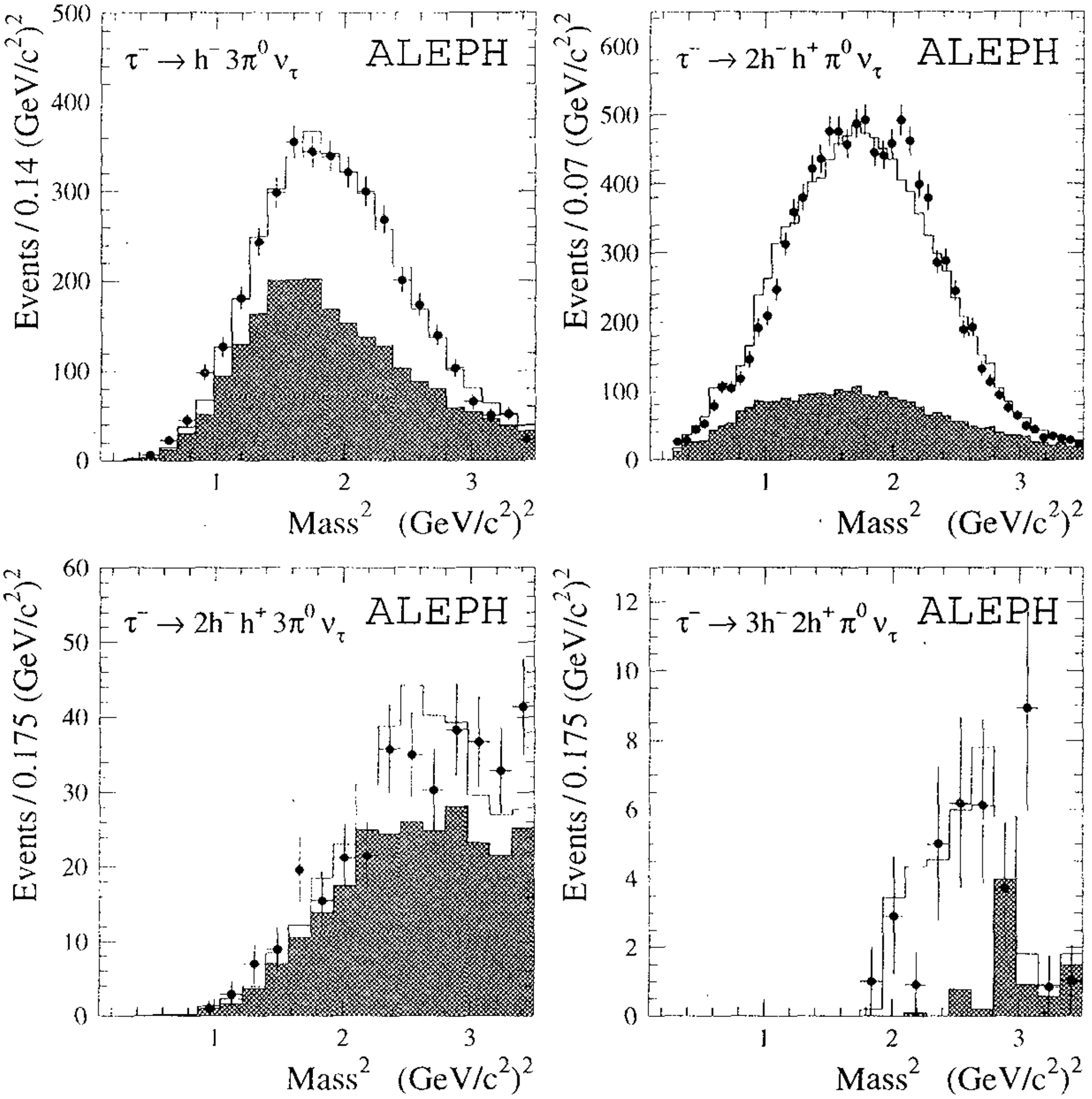

Figure 6.2: *Invariant mass-squared distributions of the τ decay channels $\pi^- 3\pi^0 \nu_\tau$, $2\pi^- \pi^+ \pi^0 \nu_\tau$, $2\pi^- \pi^+ 3\pi^0 \nu_\tau$ and $3\pi^- 2\pi^+ \pi^0 \nu_\tau$. The points are the measured data, the histograms represent the simulation and the hatched areas are the expected τ background distributions according to the simulation.*

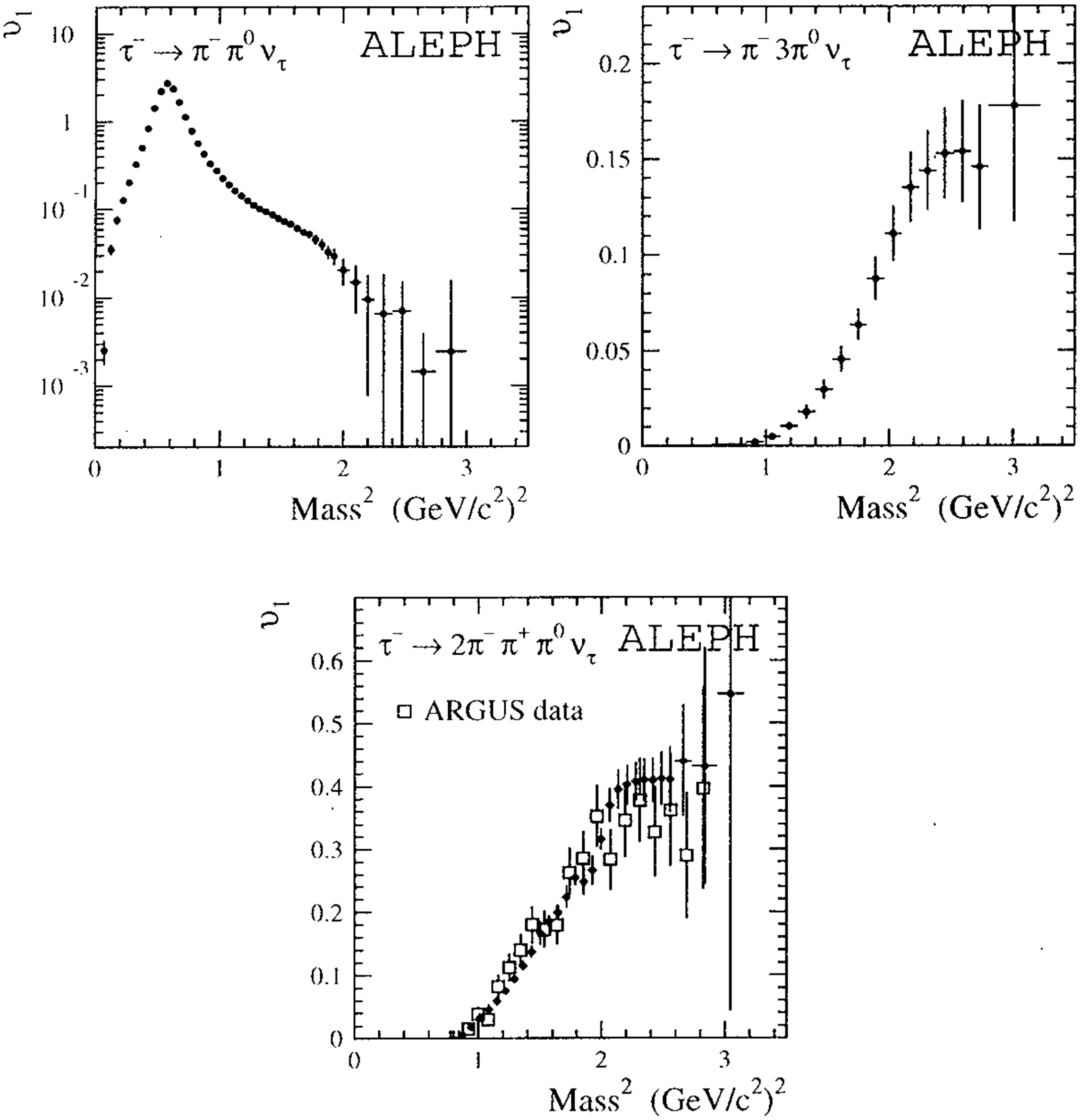

Figure 6.3: *Spectral functions of the τ decay channels $\pi^-\pi^0\,\nu_\tau$, $\pi^-3\pi^0\,\nu_\tau$ and $2\pi^-\pi^+\pi^0\,\nu_\tau$. The error bars are the diagonal elements of the covariance matrices. They contain both statistical and systematic contributions. The ARGUS data [3] in the $\tau^- \to 2\pi^-\pi^+\pi^0\,\nu_\tau$ channels contain statistical errors only.*

original τ^- vector mode	final state	input data	τ branching ratio (in%)
$\pi^-\pi^0\nu_\tau$			25.35 ± 0.19
$\pi^-3\pi^0\nu_\tau$			1.17 ± 0.14
$2\pi^-\pi^+\pi^0\nu_\tau$			2.54 ± 0.09
$2\pi^-\pi^+3\pi^0\nu_\tau$ $3\pi^-2\pi^+\pi^0\nu_\tau$ $\pi^-5\pi^0\nu_\tau$		$2\pi^-\pi^+3\pi^0$ $3\pi^-2\pi^+\pi^0$	$0.037 \pm 0.022^{(1)}$
$\omega\pi^-\nu_\tau$	$2\pi^-\pi^+\pi^0\nu_\tau$	$2\pi^-\pi^+\pi^0$	1.63 ± 0.08
	$\pi^-\pi^0\gamma\nu_\tau$	MC	0.155 ± 0.010
	$2\pi^-\pi^+\nu_\tau$	MC	0.038 ± 0.005
$\eta\pi^-\pi^0\nu_\tau$	$\pi^-\pi^0 2\gamma\nu_\tau$	$\pi^-3\pi^0$	0.068 ± 0.011
	$\pi^-4\pi^0\nu_\tau$	MC	0.055 ± 0.009
	$2\pi^-\pi^+2\pi^0\nu_\tau$	MC	0.039 ± 0.007
	$2\pi^-\pi^+\pi^0\gamma\nu_\tau$	MC	0.008 ± 0.001
$\mathrm{K}^-\mathrm{K}^0\nu_\tau$		MC	0.194 ± 0.042
$\mathrm{K}^-\mathrm{K}^0\pi^0\nu_\tau$ (V)		MC	$0.078 \pm 0.036 \pm 0.025$
$\mathrm{K}^-\mathrm{K}^+\pi^-\nu_\tau$ [160, 161] (V)		MC	$0.131 \pm 0.023 \pm 0.042$
$\mathrm{K}^0\bar{\mathrm{K}}^0\pi^-\nu_\tau$ (V)		MC	$0.131 \pm 0.023 \pm 0.042^{(1)}$
$\mathrm{K}\bar{\mathrm{K}}\pi\pi$ (V)		MC	0.08 ± 0.08
Total Vector			31.71 ± 0.31

---

[1] The branching ratio is obtained using isospin invariance as explained in the text.

Table 6.1: *Tau decays contributing to the total inclusive vector current spectral function. The first and second columns contain the physical decay modes and the corresponding final states. The third column shows the topology as reconstructed in the detector. Contributions from the "MC" labeled modes, are taken from the Monte Carlo simulation. The right-hand column gives the corresponding final state branching ratios. The vector part (V) of the* $\mathrm{K}\bar{\mathrm{K}}\pi\,\nu_\tau$ *modes is estimated to be* $(78^{+22}_{-28})\%$ [90]. *The last line gives the total branching fraction of vector hadronic* τ *decays.*

The decay channel $\mathrm{K}^-\mathrm{K}^0\nu_\tau$ consists of 50% K^0_L and 50% K^0_S. The long-lived K^0_L does not decay within the reach of the ALEPH tracking system. Its characteristic signature in the detector is a large energy deposition in the HCAL, exceeding the expected amount from the charged kaon alone. The decay rate for $\tau^- \to \mathrm{K}^-\mathrm{K}^0_\mathrm{L}\nu_\tau$ was measured by ALEPH [162, 145]. The $\mathrm{K}^-\mathrm{K}^0_\mathrm{L}\nu_\tau$ decay is included in the inclusive $\tau^- \to \mathrm{h}^-\nu_\tau$ selection sample. The $\mathrm{K}^-\mathrm{K}^0_\mathrm{S}\nu_\tau$ decay is reconstructed in the $2\pi^-\pi^+\nu_\tau$ and $\pi^-2\pi^0\nu_\tau$ samples which are dominated by axial-vector decays. Thus both $\mathrm{K}^-\mathrm{K}^0\nu_\tau$ contributions are taken from the simulation and added to the vector spectral functions.

The τ decay channel $\eta\pi^-\pi^0\nu_\tau$ is reconstructed in the inclusive channels $\pi^-3\pi^0\nu_\tau$, $\pi^-4\pi^0\nu_\tau$ and $2\pi^-\pi^+2\pi^0\nu_\tau$. The last two contributions to the τ vector spectral functions are taken from the simulation, whereas in the $\pi^-3\pi^0\nu_\tau$ channel, the mea-

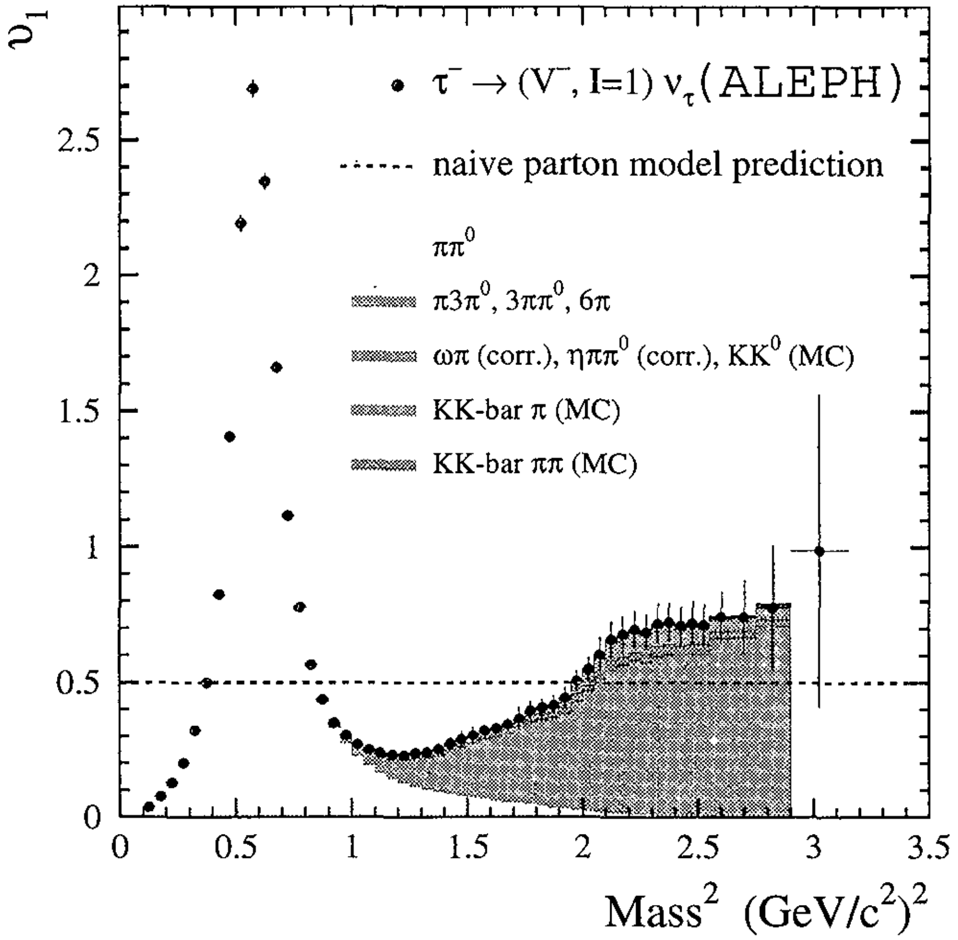

Figure 6.4: *Total vector spectral function. The colors indicate the respective contributions from the τ vector channels.*

surement includes the contribution from the $\eta\,\pi^-\pi^0\,\nu_\tau$ mode.

- By virtue of isospin constraints it was deduced in Ref. [90] that the τ decay modes $K^-K^0\pi^0\,\nu_\tau$, $K^-K^+\pi^-\,\nu_\tau$ and $K^0\bar{K}^0\pi^-\,\nu_\tau$ are originating to $(78^{+22}_{-28})\%$ from vector currents. Their contributions to the τ vector spectral functions are taken from the simulation. Neglecting so-called *second class currents*, the branching ratios of both $K\bar{K}\pi^-$ states are equal using isospin symmetry ([54] and references therein).

- The τ decay into $K\bar{K}\pi\pi$ is poorly known. According to their respective final states, about 40% of the $K\bar{K}\pi\pi$ decays are reconstructed in vector channels while about 30% (30%) are selected in the axial-vector (strange) channels. The vector part of the total $K\bar{K}\pi\pi$ branching ratio is estimated to be $(0.08 \pm 0.08)\%$.

- For the six-pion final states, one can deduce most restrictive upper bounds for unknown or unprecisely measured channels utilizing isospin invariance in conjunction with the method developed by Pais [52] (see Section 1.4) in which the τ partial width

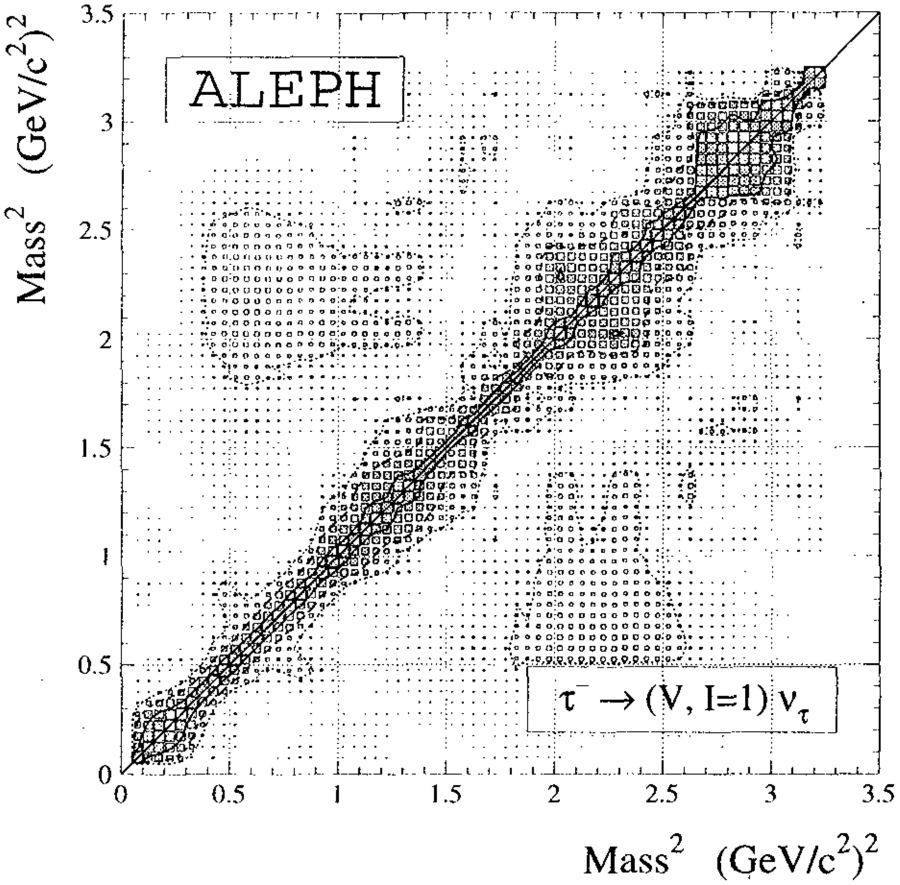

Figure 6.5: *Correlations between the data points of the total inclusive τ vector spectral function shown in Figure 6.4. The shaded (empty) boxes are proportional to the positive (negative) correlation in the interval* $[0, 1]$ ($[0, |-1|]$). *The contour lines illustrate the* 75% *(solid line),* 50% *(dashed line) and* 25% *(dotted line) correlations, respectively, for positive and negative correlations.*

is decomposed into a set of orthogonal classes $\{ijk\}$. As values for the corresponding branching ratios one may take half the bounds with 100% uncertainty. Using advantageously only the $3\pi^-2\pi^+\pi^0\,\nu_\tau$ data [24, 17, 155] and subtracting from it the contribution from the isospin violating, axial-vector $\eta\,2\pi^-\pi^+$ final state [163], one obtains a total *vector* six-pion branching ratio of $B(\tau^-\to(6\pi)^-_V\,\nu_\tau) = (0.030\pm0.030)\%$ from an upper (lower) limit when choosing the class $\{330\}$ ($\{411\}$) to be dominant.

The complete inclusive τ vector spectral function is shown in the lower right hand plot of Fig. 6.4. The dashed line depicts the naive parton model prediction[2], while the QCD

---

[2] The low energy $I = 1 + 0$ inclusive naive parton model prediction for $R^{(1+0)}(s)$ is obtained from the sum over the quark charges squared

$$R^{(1+0)}(s) = N_C \times \sum_{q=u,d,s} Q_q^2 = 2 \,,$$

with three colours $N_C = 3$. Only the isovector part $R^{(1)}(s)$ is CVC related to the τ vector spectral prediction lies roughly 14% higher. One observes that at $s \sim M_\tau^2$ the inclusive τ vector spectral function is larger than the QCD prediction, *i.e.*, the asymptotic region is still not reached. Fig. 6.5 depicts the corresponding correlation matrix.

6.2 Axial-Vector Spectral Functions

Exclusively measured axial-vector channels are the three-pion spectral functions, occurring in both final states $2\pi^-\pi^+\,\nu_\tau$ and $\pi^-2\pi^0\,\nu_\tau$, and the five-pion modes $3\pi^-2\pi^+\,\nu_\tau$ and $2\pi^-\pi^+2\pi^0\,\nu_\tau$. The corresponding invariant mass-squared spectra before unfolding are depicted for data and Monte Carlo simulation in Figs. 6.6 and 6.7. The small shoulder seen in the measured $2\pi^-\pi^+\,\nu_\tau$ spectrum at low mass-squared (upper plot in Fig. 6.6) stems from decays where only two tracks are reconstructed and the invariant mass as a result is underestimated. Due to incomplete ECAL energy collection, the measured $\pi^-2\pi^0\,\nu_\tau$ distribution is slightly shifted to lower masses. These details are well reproduced by the detector simulation.

The τ decay library `TAUOLA1.5` employs for both three-pion decay modes the identical Kühn-Santamaria parametrisation (KS) [164] based on a dominant large $a_1^-(1260)$ resonance, $\Gamma_{a_1(1260)} = 0.4\ \mathrm{GeV}/c^2$, which decays into $\rho^-(770)\pi^0 \to \pi^-2\pi^0$ or $\rho^0(770)\pi^- \to 2\pi^-\pi^+$ where in the Dalitz plane of one given final state the two possible two $\rho\pi$ combinations interfere. Scalar contributions to the three pion decay, *e.g.*, $\pi(1300) \to \rho\pi$, suppressed by the PCAC theorem and by helicity considerations, are neglected in the model. Recently, the DELPHI Collaboration claimed some evidence for an additional a_1' resonance contribution at high invariant masses [42] yielding a slight excess at the phase space suppressed end of the measured mass spectrum compared to the pure KS $a_1(1260)$ model. The questioned mass region is zoomed in Fig. 6.6. No excess, neither in the three charged pion nor in the $\pi^-2\pi^0$ mass-squared spectra is observed in ALEPH data with respect to the Monte Carlo simulation.

Fig. 6.8 shows the unfolded $2\pi^-\pi^+\,\nu_\tau$ and $\pi^-2\pi^0\,\nu_\tau$ mass spectra with reasonable agreement in form and normalization ($\chi^2 = 41.4$ per 59 (correlated) degrees of freedom). In the following both channels are assumed to have identical spectra so that it is appropriate to use the weighted average of the distributions for the inclusive axial-vector spectral

---

functions. The quark model yields for the isovector triplet $|1,1\rangle = -u\bar{d}$, $|1,0\rangle = (u\bar{u} - d\bar{d})/\sqrt{2}$, $|1,-1\rangle = d\bar{u}$, and for the isoscalar singlets $|0,0\rangle = (u\bar{u} + d\bar{d})/\sqrt{2}$ and $|0,0\rangle = s\bar{s}$. Only the $|1,0\rangle$ and $|0,0\rangle$ states are allowed. Thus, the total cross sections read $R^{(1)}(s) = 3 \times (2/3 + 1/3)^2/2 = 3/2$ and $R^{(0)}(s) = 3 \times ((2/3 - 1/3)^2/2 + 1/9) = 1/2$, respectively. The CVC parton model prediction for the total $I = 1$ vector spectral function is then $v_1(s) = 1/2$. Perturbative QCD does not distinguish between vector and axial-vector currents so that one correspondingly has $a_1(s) = 1/2$.

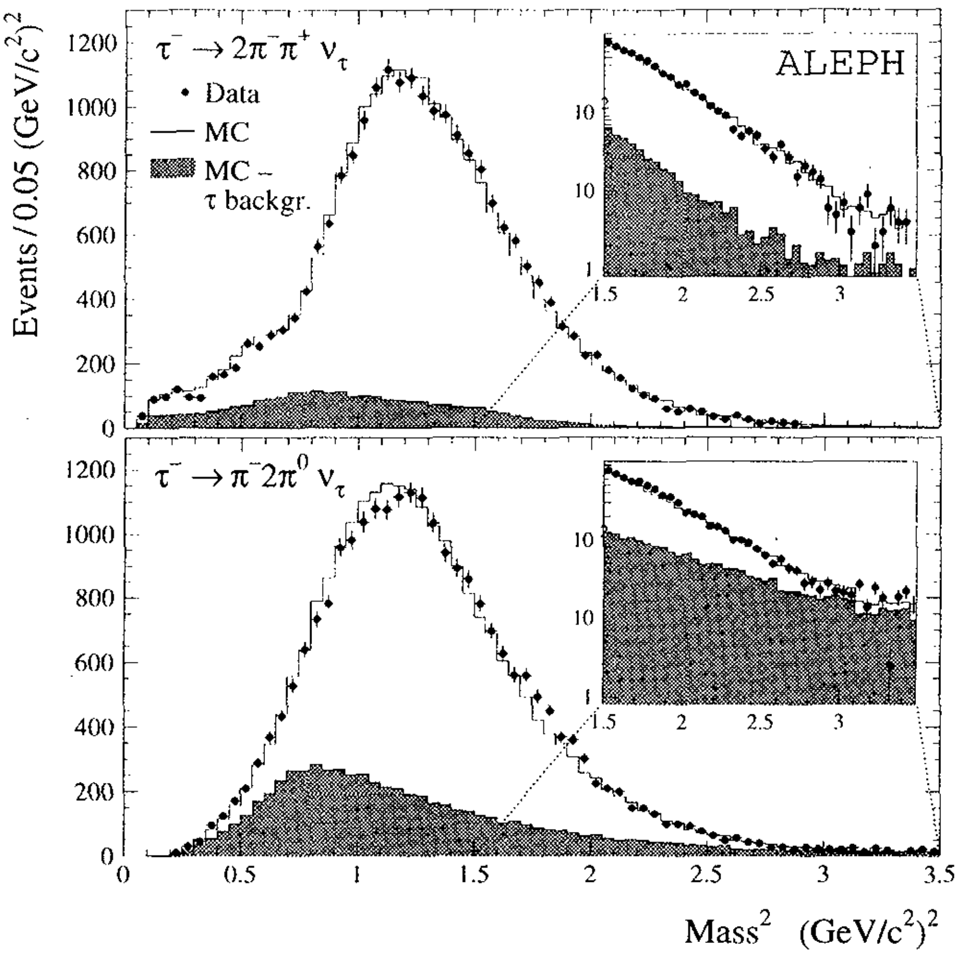

Figure 6.6: *Invariant mass-squared distributions of the decays* $\tau^- \to 2\pi^-\pi^+\,\nu_\tau$ *and* $\tau^- \to \pi^-2\pi^0\,\nu_\tau$.

function[3].

The Inclusive τ Axial-Vector Spectral Function

In complete analogy to the vector spectral function the inclusive axial-vector spectral function is obtained by summing up the exclusive axial-vector spectral functions with the addition of small unmeasured modes taken from the Monte Carlo simulation. Table 6.2

---

[3] Note that the weighted average is calculated between two intrinsically correlated distributions. The averaged distribution k with bin entries k_i, $i = 1, \ldots N_{\rm bin}$ is defined to minimize the χ^2

$$\chi^2 \;=\; (x_{(--+)} - k)C^{-1}_{(--+)}(x_{(--+)} - k) + (x_{(-00)} - k)C^{-1}_{(-00)}(x_{(-00)} - k)\;,$$

where the indices denote the charges of the respective τ final states, x are the mass-squared distributions and C^{-1} the corresponding inverted covariance matrices. The weighted average is then the solution of the system of linear equations $x_{(--+)}C^{-1}_{(--+)} + x_{(-00)}C^{-1}_{(-00)} = k(C^{-1}_{(--+)} + C^{-1}_{(-00)})$, and the covariance matrix of the average becomes $C_k^{-1} = C^{-1}_{(--+)} + C^{-1}_{(-00)}$. See also Section 9.2 in Chapter 9.

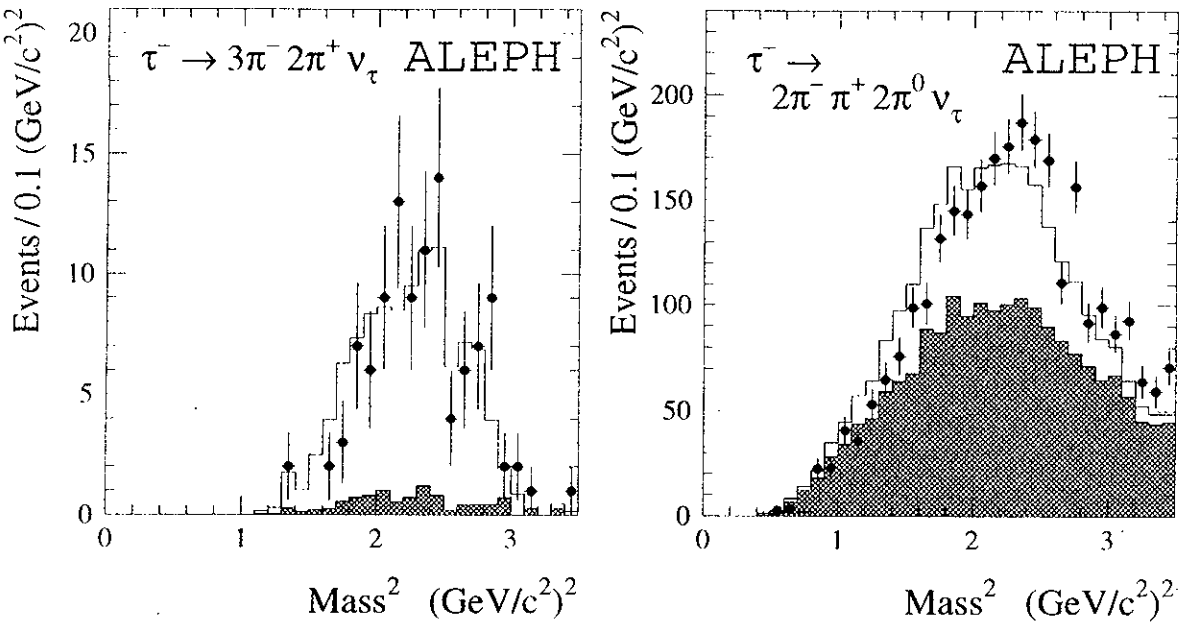

Figure 6.7: *Invariant mass-squared distributions of the decays* $\tau^- \to 3\pi^- 2\pi^+ \nu_\tau$ *and* $\tau^- \to 2\pi^- \pi^+ 2\pi^0 \nu_\tau$. *The points are the ALEPH data, the histograms represent the simulation and the hatched areas are the expected* τ *background distributions according to the simulation.*

gives a compilation of the exclusive axial-vector branching ratios used.

The five-pion spectral functions are exclusively measured in the $2\pi^-\pi^+2\pi^0\,\nu_\tau$ and $3\pi^-2\pi^+\,\nu_\tau$ final states. Using Pais' isospin classes [52] (see Tab. 1.1 in Section 1.4), the branching fraction of $\pi^-4\pi^0\,\nu_\tau$ can be bounded entirely using the $3\pi^-2\pi^+\pi^0\,\nu_\tau$ branching fraction. It is found to be smaller than 0.055%. Half of this upper limit is taken with an error of 100%.

Corresponding to the vector case, the small fraction of the $\omega\,\pi^-\pi^0\,\nu_\tau$ decay channel that is not accumulated in the $2\pi^-\pi^+2\pi^0\,\nu_\tau$ final state is added from the simulation.

Also considered are the axial-vector $\eta\,(3\pi)^-\,\nu_\tau$ final states [163]. CLEO observed that the dominant part of it issues from the $\tau^- \to \mathrm{f}_1(1285)\pi^-$ intermediate state ($B(\tau^- \to \mathrm{f}_1\pi^-\,\nu_\tau) = 0.068 \pm 0.030\%$, measured from the $\mathrm{f}_1 \to \eta\,\pi^+\pi^-$ and $\mathrm{f}_1 \to \eta\,\pi^0\pi^0$ decay modes [163], see Fig. 6.10), which means that owing to the isoscalarness of the f_1 meson the respective branching ratios relate as $B(\tau^- \to \eta\,2\pi^-\pi^+\,\nu_\tau) = 2 \times B(\tau^- \to \eta\,\pi^-2\pi^0\,\nu_\tau)$. The distributions are taken from ordinary six-pion phase space simulation accompanied by large systematic errors.

The $\mathrm{K}\mathrm{K}\pi$ and $\mathrm{K}\bar{\mathrm{K}}\pi\pi$ final states contribute with $(22^{-22}_{+28})\%$ and $(50 \pm 50)\%$, respectively, to the inclusive axial-vector spectral function, with full anticorrelation to the inclusive vector spectral function. Both spectral functions are taken from the simulation accompanied by comfortable systematic errors due to the uncertainty of the respective invariant mass distributions.

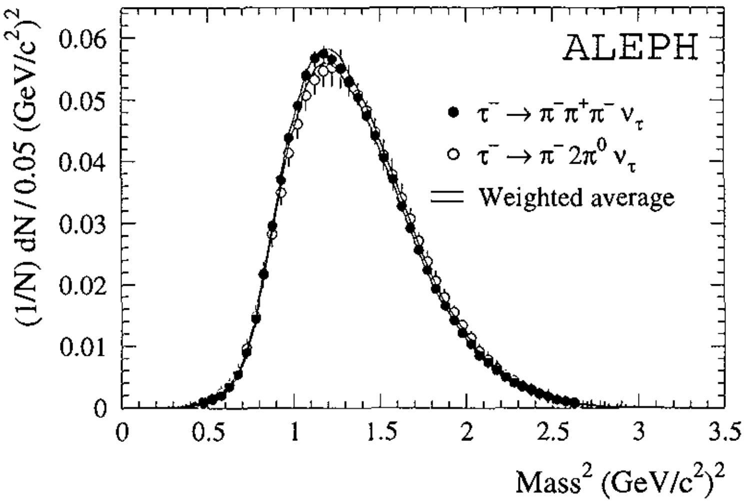

Figure 6.8: Unfolded (physical) invariant mass-squared spectra of the τ final states $2\pi^-\pi^+\nu_\tau$ and $\pi^-2\pi^0\nu_\tau$.

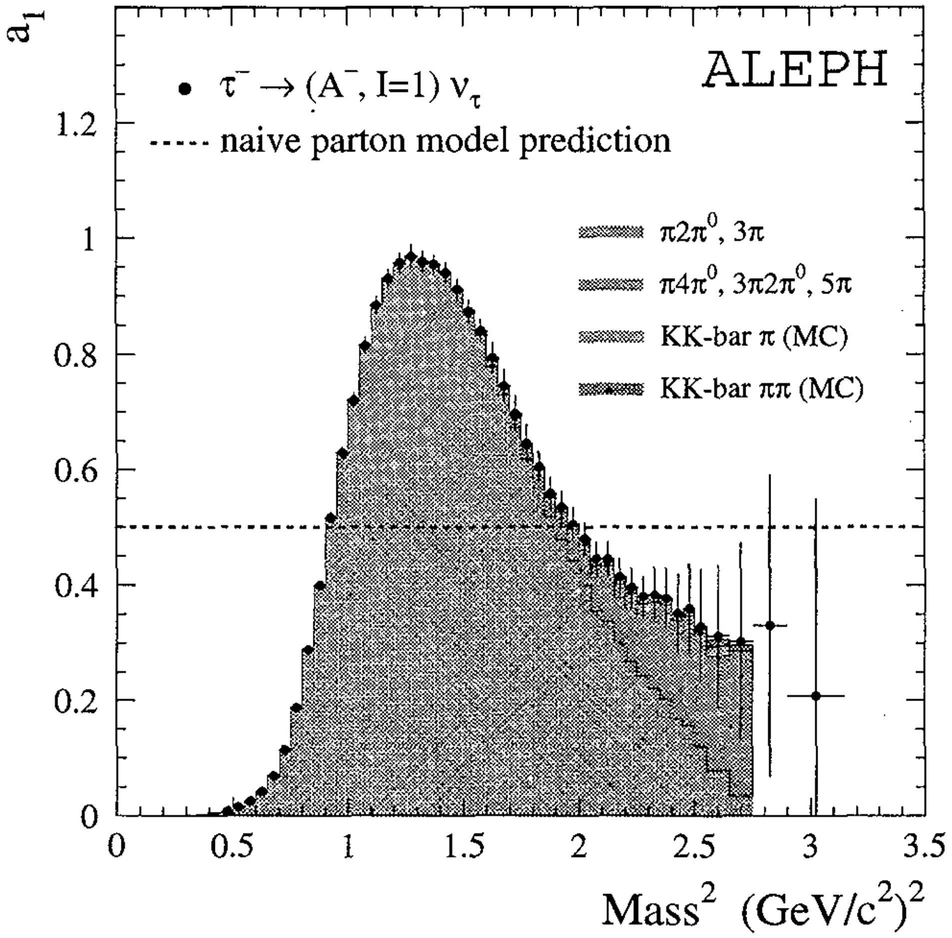

Figure 6.9: Total inclusive τ axial-vector current spectral function (without the pion pole). The dashed line represents the naive parton model prediction.

original τ^- vector mode	final state	input data	τ branching ratio (in%)
$\pi^-\,\nu_\tau$			$11.23\ \pm 0.16$
$\pi^-2\pi^0\,\nu_\tau$			$9.23\ \pm 0.17$
$2\pi^-\pi^+\,\nu_\tau$			$9.13\ \pm 0.15$
$\pi^-4\pi^0\,\nu_\tau$			$0.03\ \pm 0.03$
$2\pi^-\pi^+2\pi^0\,\nu_\tau$			$0.09\ \pm 0.02$
$3\pi^-2\pi^+\,\nu_\tau$			$0.066\ \pm 0.008$
$\omega\,\pi^-\pi^0\,\nu_\tau$	$2\pi^-\pi^+2\pi^0\,\nu_\tau$	$2\pi^-\pi^+2\pi^0$	$0.34\ \pm 0.10$
	$\pi^-2\pi^0\gamma\,\nu_\tau$	MC	$0.032\ \pm 0.009$
	$2\pi^-\,\pi^+\pi^0\,\nu_\tau$	MC	$0.009\ \pm 0.002$
$\eta\,2\pi^-\pi^+\,\nu_\tau$		MC	$0.04\ \pm 0.01$
$\eta\,\pi^-2\pi^0\,\nu_\tau$		MC	$0.02\ \pm 0.01$
$\mathrm{K^-K^0}\pi^0\,\nu_\tau$ (A)		MC	$0.022\ \pm 0.010\ \pm 0.022$
$\mathrm{K^-K^+}\,\pi^-\,\nu_\tau$ [160, 161] (A)		MC	$0.037\ \pm 0.007\ \pm 0.037$
$\mathrm{K^0\bar{K}^0}\pi^-\,\nu_\tau$ (A)		MC	$0.037\ \pm 0.007\ \pm 0.037$(1)
$\mathrm{KK}\pi\pi$ Axial-Vector		MC	$0.08\ \pm 0.08$
Total Axial-Vector			$30.41\ \pm 0.32$

[1] The branching ratio is obtained using isospin invariance as explained in the text.

Table 6.2: *Tau decays contributing to the inclusive axial-vector current spectral function. The first and second columns contain the physical decay modes and the corresponding final states. The third column shows the topology as reconstructed in the detector. Contributions from the "MC" labeled modes, are taken from the Monte Carlo simulation. The right-hand column gives the corresponding final state branching ratios. The axial-vector part (A) of the* $\mathrm{K\bar{K}}\pi\,\nu_\tau$ *modes is estimated to be* $(22^{-22}_{+28})\%$ [90]. *The last line gives the total branching fraction of axial-vector hadronic* τ *decays.*

The total inclusive axial-vector spectral function is plotted in Fig. 6.9 together with the naive parton model prediction, One observes that the asymptotic region is apparently not reached at the τ mass scale. One may expect additional oscillations to lift the spectral function to roughly 1.14 times the naive parton model prediction, where 14% is expected asymptotically for low energy e^+e^- annihilation cross sections to be the QCD perturbative correction.

6.3 $(v_1 + a_1)$ Spectral Function

In the favourable case of the vector plus axial-vector spectral function one does not have to distinguish the current properties of the respective non-strange hadronic τ decay channels. Hence the mixture of all contributing non-strange final states is measured as inclusively as possible. The dominating two- and three-pion final states are still measured exclusively, while the remaining contributing topologies are treated inclusively, *i.e.*, without any subtraction of τ-background originating from one of the contributing decay modes.

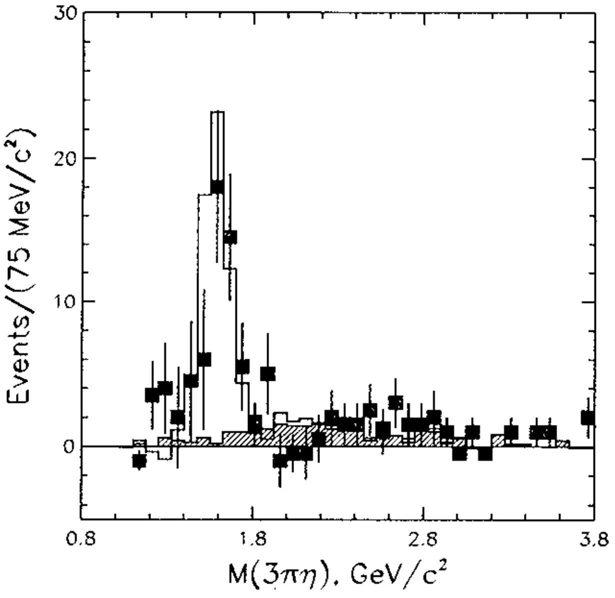

Figure 6.10: *Invariant mass $M_{3\pi\eta}$ measured by the CLEO Collaboration [163]. The shaded area describes $e^+e^- \rightarrow q\bar{q}$ background.*

This improves statistics. Another even more important advantage is, that one does not have to worry about the current properties of the $K\bar{K}\pi$ and $K\bar{K}\pi\pi$ modes or about possible missing, *i.e.*, unmeasured τ decay modes as they are necessarily contained in the inclusive sample.

The $(v_1 + a_1)$ spectral function is depicted in Fig. 6.11. The improvement in precision in comparison to an exclusive sum of Fig. 6.4 and Fig. 6.9 becomes obvious at higher mass-squared. One clearly sees the oscillating behaviour of the spectral function which seems, on the contrary to the exclusive vector/axial-vector spectral functions, to approximately reach the asymptotic limit at $s \rightarrow M_\tau^2$, which is predicted from perturbative QCD to lie about 14% higher than the naive parton model prediction.

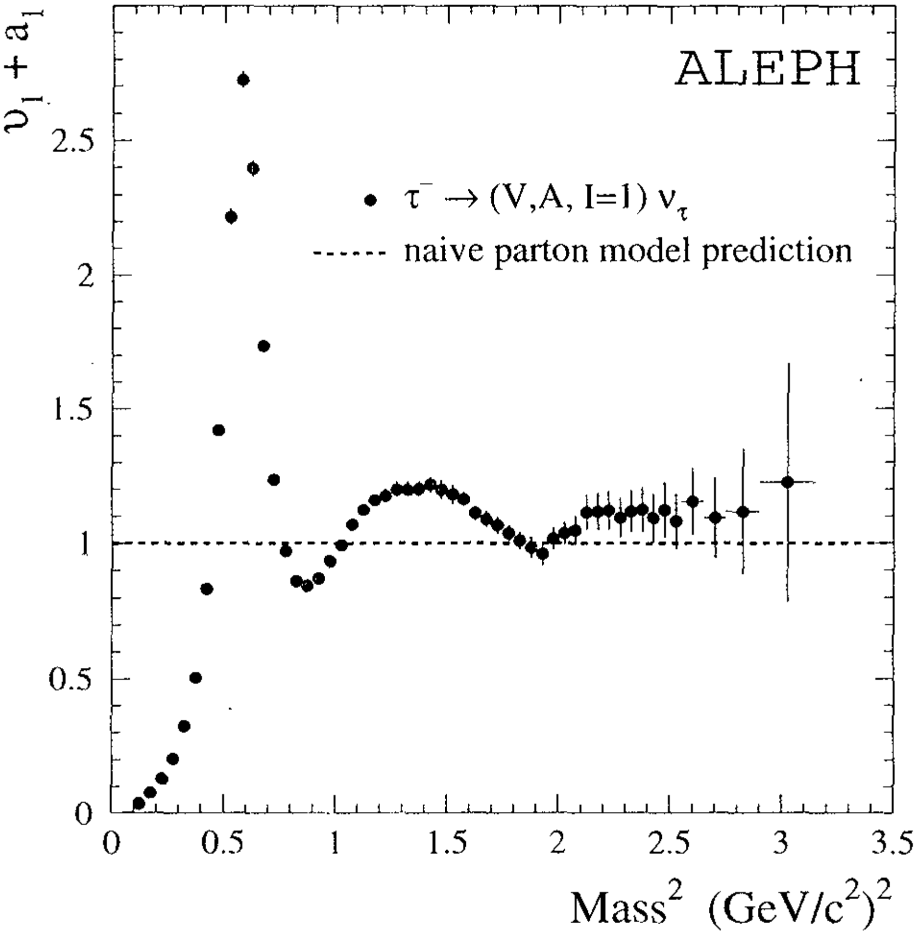

Figure 6.11: Inclusively measured vector plus axial-vector (v_1 + a_1) spectral function (without the pion pole). Again, the dashed line represents the naive parton model prediction.

Chapter 7

Studies of Systematic Uncertainties

The study of systematic errors affecting the measurement is subdivided into several classes according to their origin, *i.e.*, the photon and π^0 reconstruction, the charged track measurement, the unfolding procedure and additional sources. All systematic uncertainties concerning the classification are contained in the errors of the branching ratios measured under equivalent conditions using essentially the same analysis techniques [24]. Only the systematic effects affecting the mass-squared distributions need to be examined here. All systematic effects are studied with respect to the Monte Carlo simulation since the latter is used to unfold detector effects from the measured distributions. For example, concerning the ECAL enrgy calibration it is not necessary to perform an absolute calibration in order to achieve, *e.g.*, an exact reproduction of the beam energy for non-radiating Bhabha events. The point is that any shift from physical to measured energy must be perfectly modelled (within systematic uncertainties) by the simulation.

7.1 Photon and π^0 Reconstruction

The following effects are studied:

7.1.1 Fake Photons

The data suffer from an excess of fake photons compared to the simulation. As described in Section 4.3.4, the measured spectrum of invariant mass of each considered hadronic τ decay channel is corrected according to its energy-dependent excess of fake photons. The statistical errors of the probability fits together with the systematic uncertainty coming from genuine differences in the probability distributions (extracted by switching off the corrections to the respective likelihood variable distributions) are used to estimate the corresponding systematic uncertainties.

7.1.2 ECAL Energy calibration

The photon energy is calibrated by comparing the ratio of the ECAL cluster energy of electrons, reconstructed as if they were photons, to the momentum of the track in data and simulation. The electrons are taken from:

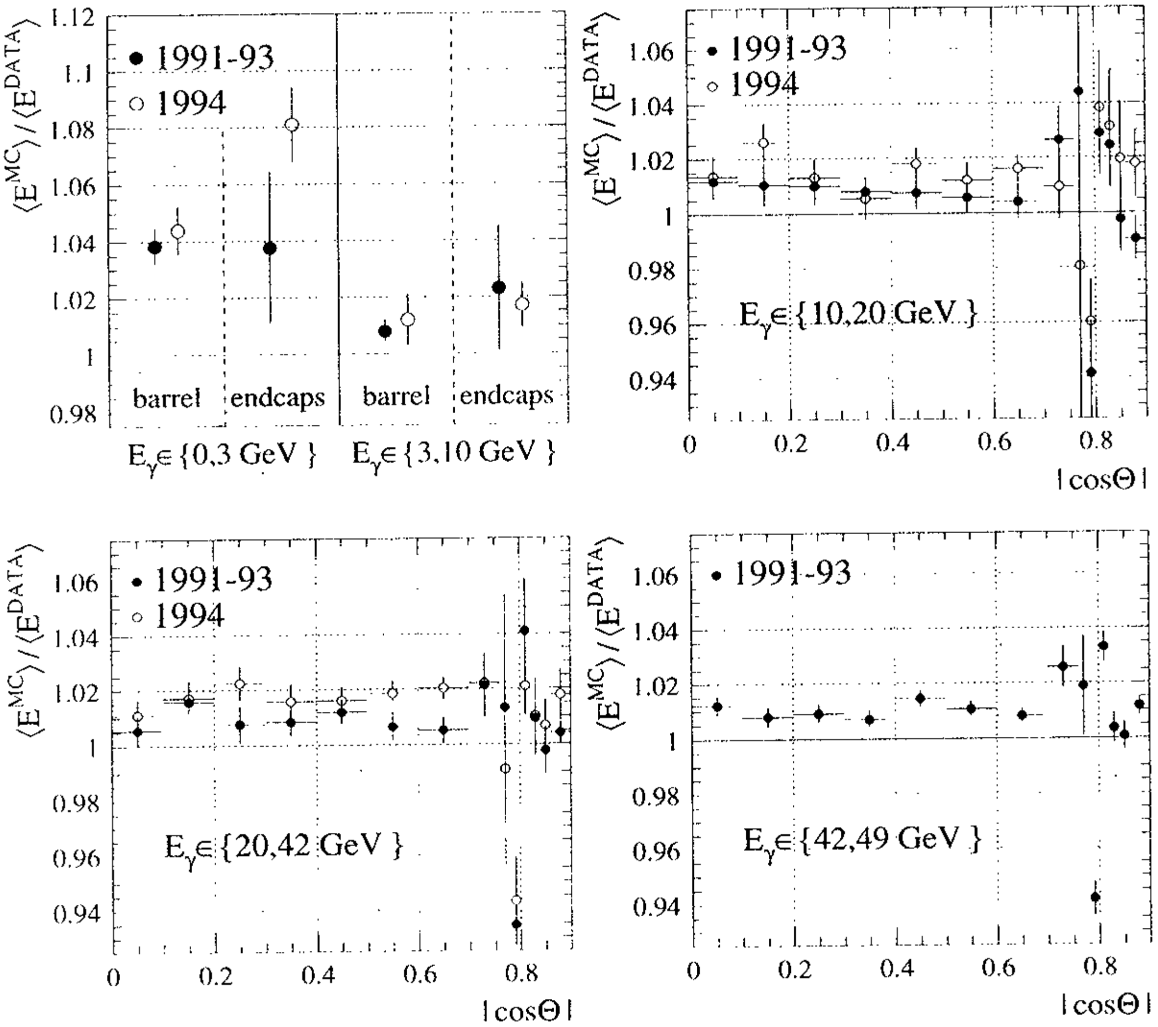

Figure 7.1: *ECAL energy calibration using resolved π^0's at low and electrons at intermediate and high energies as a function of the polar angle. The errors between 0 and 10 GeV are dominated by systematics.*

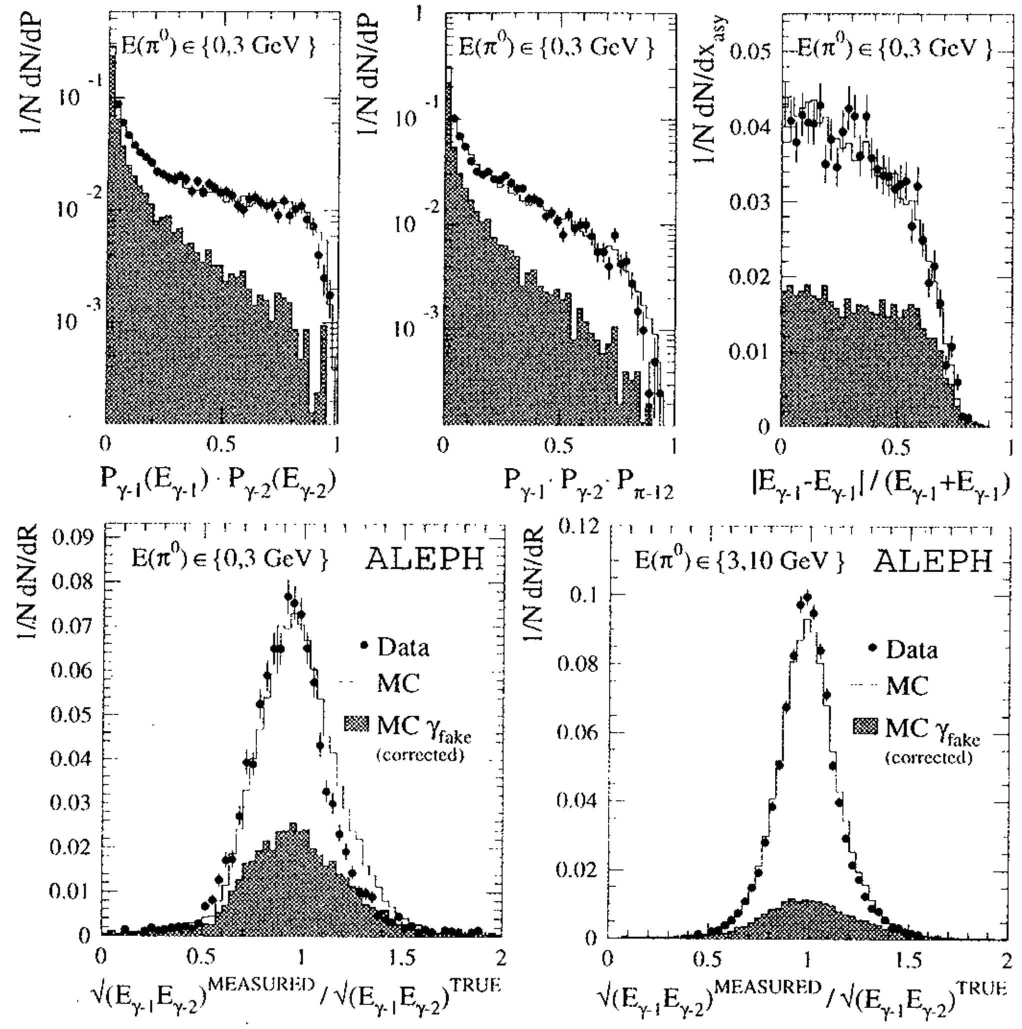

Figure 7.2: *The three upper plots show the fitted distributions of photon and* π^0 *probabilities as well as the two-photon energy asymmetry for data and Monte Carlo simulation. The lower plots depict the distributions of the calibration ratios in both low energy ranges.*

- two-photon processes at intermediate energies,
- $\tau \rightarrow e\,\bar{\nu}_e \nu_\tau$ decays at intermediate and high energies,
- Bhabha events at beam energy.

In total three energy- and fourteen different regions in the polar angle are distinguished. The corresponding plots for the calibration correction of energies between 10 and 49 GeV are shown in Figure 7.1. For low energies ($0 \sim 10$ GeV) it is not appropriate to use electron showers because of the large curvature of their trajectories. To circumvent this, neutral pions with wide opening angles are used for the energy calibration at low energies (0–3 and 3–10 GeV).

Special care was necessary to correct the calibration for energy changing effects, *i.e.*,

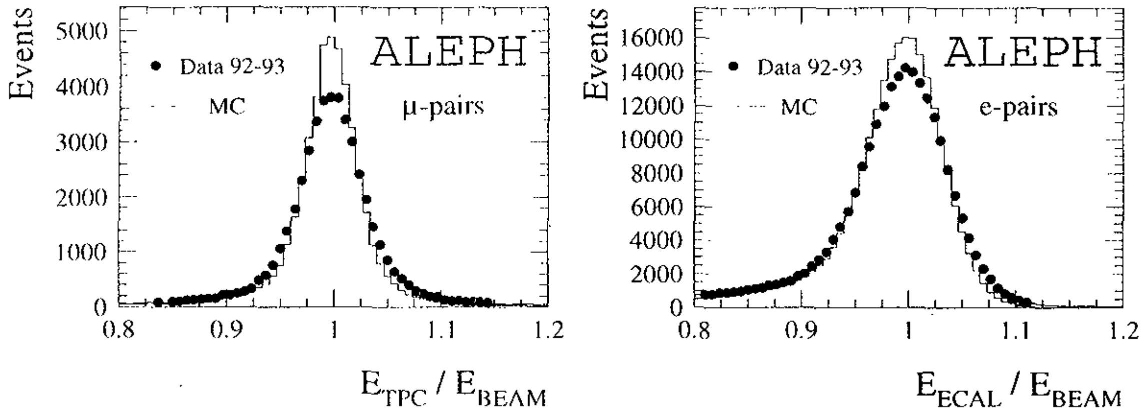

Figure 7.3: *TPC momentum resolution (left figure) and ECAL energy resolution (right figure) measured at beam energy with* $e^+e^- \to \mu^+\mu^-$ *and* $e^+e^- \to e^+e^-$ *events, respectively, in data and Monte Carlo.*

differences in the distribution of the photon opening angle between data and the simulation due to the excess of fake photons in the data. Individually, for both considered energy ranges and geometries (barrel: $|\cos\Theta| \leq 0.774$ and end-caps: $0.774 < |\cos\Theta| \leq 0.95$) the fractions of fake photons in data and the simulation were determined as in the invariant mass correction by fitting the distributions of the overall π^0 probability, the product of the corresponding single photon probabilities and the energy asymmetry. For the higher energy range, an additional systematic error due to uncertainties in the two photon opening angle was included. The corresponding plots are shown in Figure 7.2 together with the distributions of the calibration variable, corrected for the excess of fake photons, defined as

$$\left\langle R^{\mathrm{MC,DATA}} \right\rangle \equiv \left\langle \frac{\sqrt{(E_{\gamma_1} E_{\gamma_2})^{\mathrm{MC,\,DATA}}}}{\sqrt{(E_{\gamma_1} E_{\gamma_2})^{\mathrm{TRUE}}}} \right\rangle = \left\langle \frac{\sqrt{(E_{\gamma_1} E_{\gamma_2})^{\mathrm{MC,\,DATA}}}}{m_{\pi^0}^{\mathrm{TRUE}} / \sqrt{2(1 - \cos\theta_{\gamma_1 \gamma_2}^{\mathrm{MC,\,DATA}})}} \right\rangle ,$$

where the MC ratio is corrected according to

$$\langle R^{\mathrm{MC^{corr.}}} \rangle = x_{\mathrm{fake}}^{\mathrm{DATA}} \langle R_{\mathrm{fake}}^{\mathrm{MC}} \rangle + \frac{(1 - x_{\mathrm{fake}}^{\mathrm{DATA}})}{(1 - x_{\mathrm{fake}}^{\mathrm{MC}})} \left(\langle R^{\mathrm{MC}} \rangle - x_{\mathrm{fake}}^{\mathrm{DATA}} \langle R_{\mathrm{fake}}^{\mathrm{MC}} \rangle \right) .$$

and $x_{\mathrm{fake}}^{\mathrm{MC,\,DATA}}$ denote the fractions of fake photons in the simulation and data, respectively. The ratios $\langle R^{\mathrm{MC^{corr.}}} \rangle / \langle R^{\mathrm{DATA}} \rangle$, *i.e.*, the calibration values are shown in Fig 7.1. In this measurement a total energy calibration for all years was used, which is found by weighting the calibration ratios of Fig. 7.1 by the respective number of events in 1991-1993 and 1994. As systematic errors, always the largest ones in a given energy and polar angle bin are taken.

7.1.3 ECAL Energy resolution

The energy resolution in data and Monte Carlo simulation is studied using Bhabha events with low radiation at high energies ($E_{\mathrm{ECAL}}/E_{\mathrm{TPC}} \simeq 1$, at beam energy). It is found to be

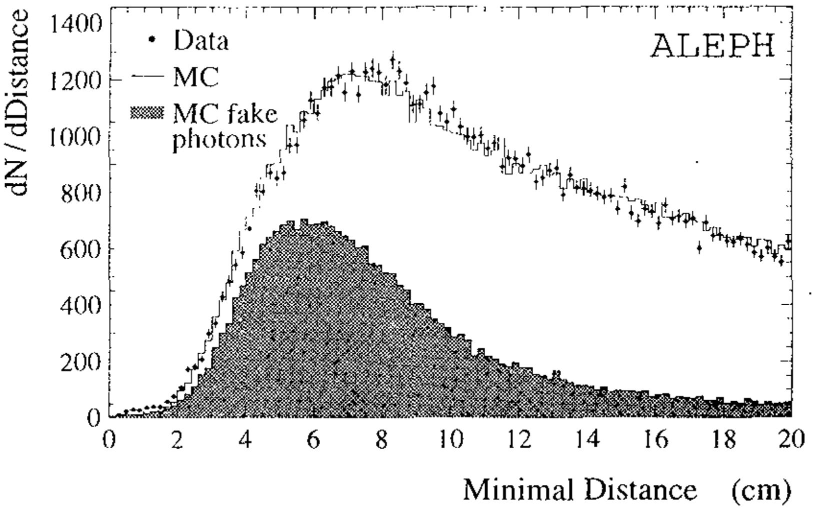

Figure 7.4: *Minimal distance distribution for data and Monte Carlo simulation. The data are corrected for the excess of fake photons.*

overestimated in the simulation by about 14% (see Fig. 7.3. At low energies, the resolution of photon energies is directly tested, using the experimental width of the reconstructed π^0 mass. All detected deviations in the energy resolution are corrected in the simulation, while its uncertainties are taken as systematic errors.

7.1.4 Photon Reference Distributions

The reference distributions used for the likelihood procedure to evaluate the photon probabilities P_γ and $P_{\gamma-\mathrm{res}}$ are obtained from the Monte Carlo simulation. These distributions are slightly corrected after detailed comparisons between data and Monte Carlo simulation. By switching off this correction, a conservative systematic error is determined [24].

7.1.5 Photon Energy Threshold

The threshold for ECAL photon detection is set to 300 MeV. The comparison of low energy photons belonging to resolved π^0's in data and Monte Carlo simulation shows that the inefficiency in data is larger by $(4.4 \pm 3.4)\%$ with respect to the simulation [24]. This excess is corrected in the simulation. A variation of the threshold by ±20 MeV corresponds to a change of the photon reconstruction efficiency near threshold of 3.4%. A variation of the photon energy threshold by ±30 MeV is used to extract a conservative systematic error due to the quoted uncertainty in the determination of the efficiency.

7.1.6 Minimal Distance Photon-Track

A cut on the minimal distance between the barycentre of an electromagnetic cluster and the closest track is applied in order to veto fake photon candidates from hadronic interactions in the ECAL. Thus, a cluster deposited in the ECAL is considered as a

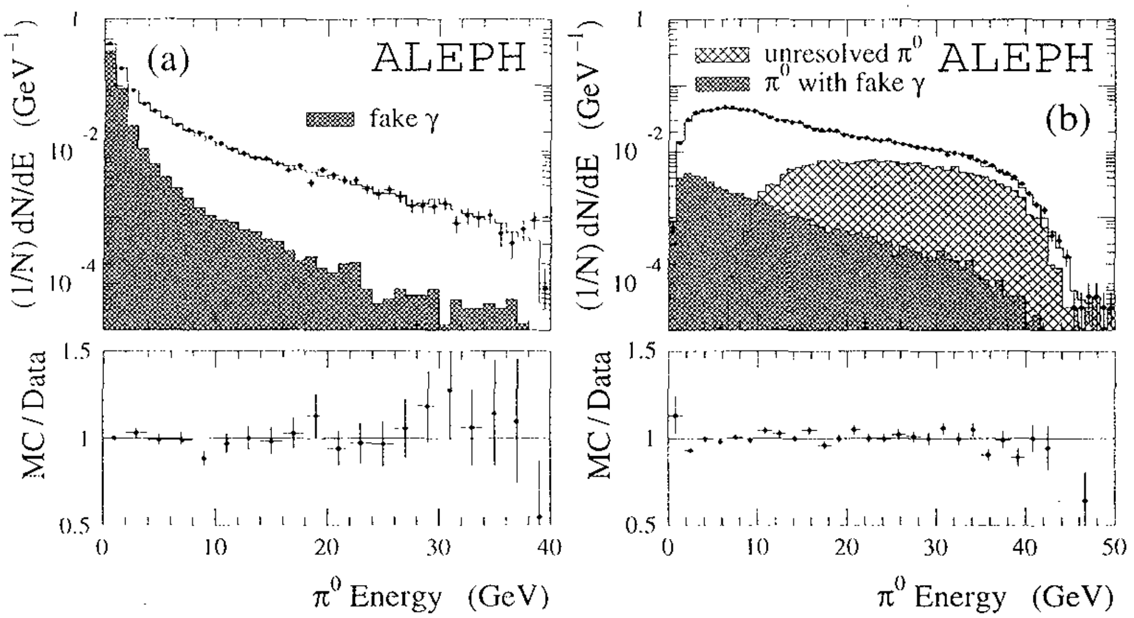

Figure 7.5: *Spectra of π^0 energy for (a) single photon π^0's and (b) reconstructed π^0's in $\tau^- \to h^-\pi^0\nu_\tau$ decays for data (points) and the Monte Carlo simulation (histogram). The shaded areas illustrate the fake photon contamination. The unresolved component of the π^0 sample in (b) is shown by the hatched area. The lower plots show the corresponding Monte Carlo/data ratios.*

photon candidate if its minimal distance to the nearest charged track exceeds 2 cm. The comparison of the distribution of this distance between data and simulation below 8 cm shows good agreement. Similar to the minimal photon energy threshold, a possible discrepancy can be covered by a variation of the minimal distance cut value by ±0.1 cm, which is used to extract the corresponding systematic error [24]. Fig. 7.4 shows the minimal distance distribution for data (corrected for fake photon excess) and Monte Carlo simulation. The shaded area depicts the fitted part of fake photons according to the simulation.

7.1.7 π^0 Mass

The apparent π^0 mass and its resolution depend on the the π^0 energy (see Fig. 4.8). The functional dependence is used as a reference in order to calculate the probability for two photons to belong to a π^0. Varying these dependences within their uncertainties yields the corresponding systematic errors. The measured photon energies and their opening angle are readjusted in a resolved π^0 in order to constrain the apparent energy dependent masses to the nominal π^0 mass.

Fig. 7.5 shows the energy spectrum of residual and reconstructed π^0's after applying the corrections mentioned above. The contamination of the residual sample with fake photons is illustrated by the shaded area (upper left plot).

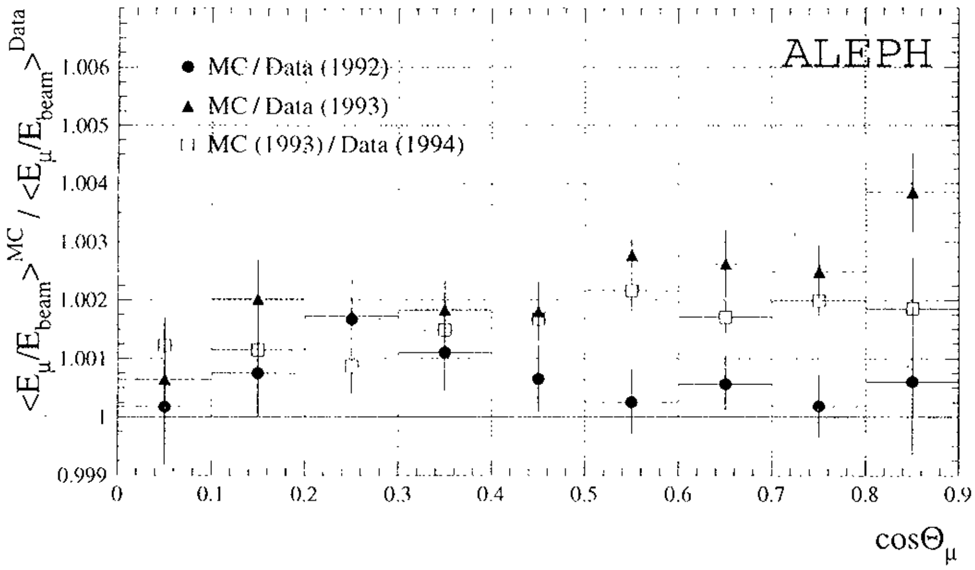

Figure 7.6: *Ratio of the TPC momentum of muons originating from* $e^+e^- \longrightarrow \mu^+\mu^-$ *processes of Monte Carlo simulation and data as a function of the polar angle.*

7.2 Tracking Systematics

The following systematic effects are studied:

7.2.1 Momentum Calibration

The track momentum calibration is performed using the techniques developed in [38] which exploit the known masses of narrow resonances at low energies and muon pairs for the final, polar angle dependent calibration at beam energy. The resulting ratios of the measured mean values $\langle E_\mu/E_{\rm beam}\rangle$ of the Monte Carlo simulation over data for the years 1992, 1993 and 1994 of LEP running are shown in Figure 7.6 (where for the comparison to the 1994 data muon pairs of the 1993 Monte Carlo have been used). These ratios have been used to correct the data momentum calibration.

The calibration includes an angular dependent sagitta correction (done before the above final momentum calibration), scaling with the squared particle momentum, which gives an asymmetry for positive and negative tracks [165]. The effect is expected to be polar (θ) and azimuthal (ϕ) angle dependent where only the polar angle dependence is considered here. Again, the effect is studied with $Z \rightarrow \mu^+\mu^-$ events with a known energy (beam energy). With the central detector (barrel) length of 2.2 m and the end-cap height of 1.8 m, where barrel and end-cap overlap at the polar angle $|\cos\theta| = 0.774$, the sagitta correction (in meters) of a bended trajectory is given by

$$\text{Barrel}: \qquad \Delta f \;=\; \frac{0.3B}{8}\,\frac{1.8^2}{\sin\theta_\mu}\left(\frac{1}{p_\mu - p_{\rm beam}}\right) ,$$

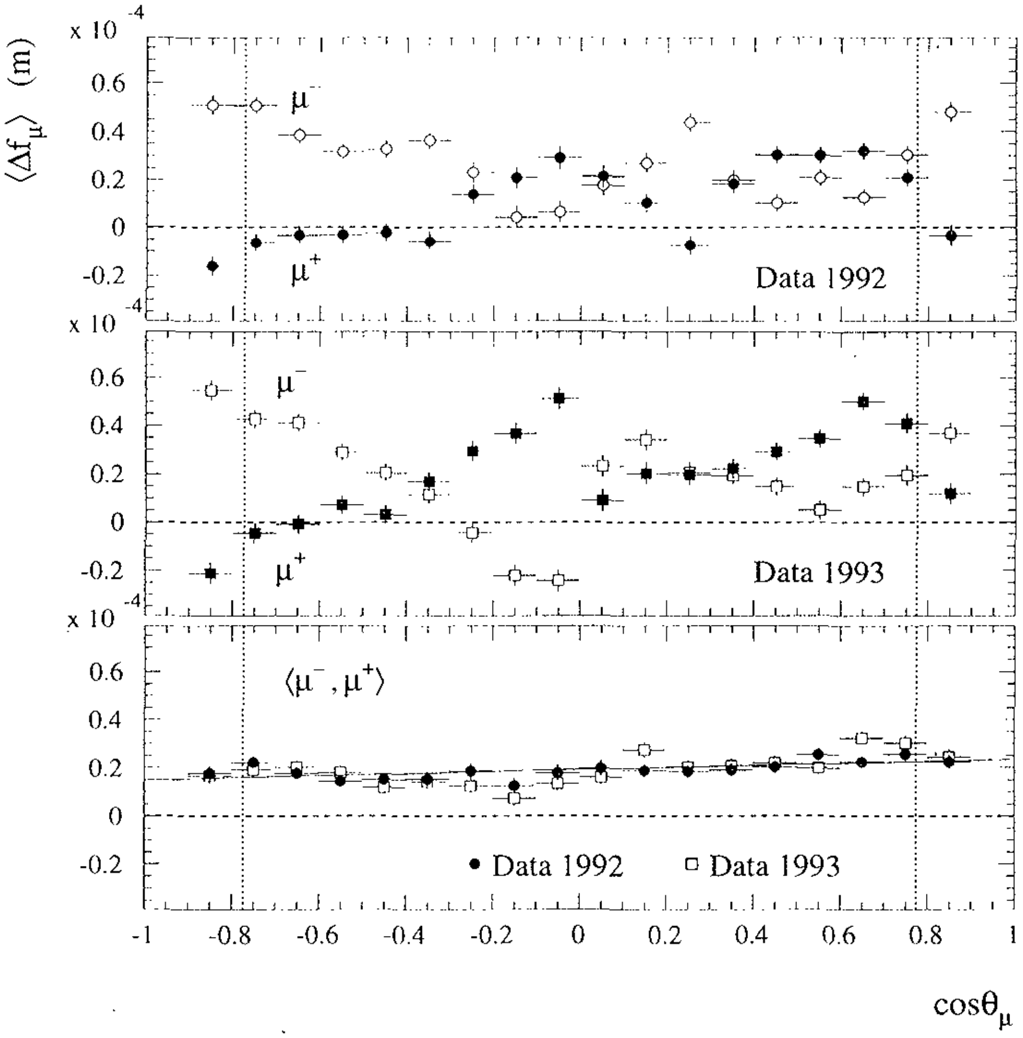

Figure 7.7: *Sagitta asymmetry of positive and negative muons from the decay* $Z \rightarrow \mu^+\mu^-$. *The vertical dotted line depicts the overlap at* $|cos\theta| > 0.774$ *between central detector (barrel) and end-caps.*

$$\text{End-caps}: \qquad \Delta f = \frac{0.3B}{8} \frac{2.2^2 \sin\theta_\mu}{\cos\theta_\mu} \left(\frac{1}{p_\mu - p_{\text{beam}}} \right) . \tag{7.1}$$

The momentum p_{beam} is the nominal muon momentum and $B = 1.5$ Tesla is the ALEPH magnetic field strength. Fig. 7.7 shows Δf for 1992 and 1993 data separately for positive and negative muons. One clearly sees that the shapes for the two muon charges are almost symmetrical around a non-zero central value. The fact that the average muon momentum is not centered at beam energy is mainly due to energy loss from bremsstrahlung which produces an asymmetry in the muon momentum distribution. The lower plot in Fig. 7.7 depicts the average over both charges. The sagitta asymmetry almost cancels. The remaining discrepancies are corrected in a year, polar and azimuthal angle dependent sagitta calibration.

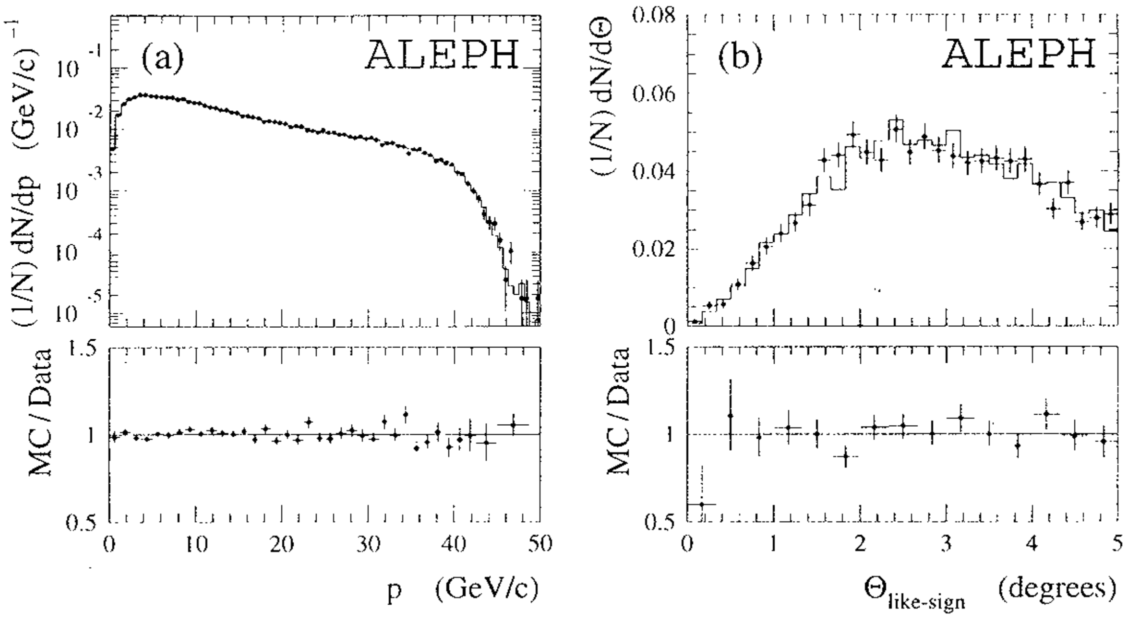

Figure 7.8: *Momentum spectrum of the charged hadron in* $\tau^- \to h^- \pi^0 \nu_\tau$ *decays (a) and distribution of the angle between equal charged tracks in three-prong* τ *decays (b) for data (points) and the Monte Carlo simulation (histogram). The lower plots show the corresponding Monte Carlo/data ratios.*

The systematic errors corresponding to track calibration uncertainties are evaluated by varying the partly correlated errors of the polar angle dependent final calibration (Fig.7.6). These fluctuations are assumed to be sagitta errors and therefore scale with the squared particle momentum ($\Delta f \sim \Delta(1/p) = \Delta p/p^2$). They amount up to an uncertainty of 0.1%. The relative uncertainty on the magnetic field scaling linearily with the momentum is estimated to be lower than 0.03% [132].

7.2.2 Momentum Resolution

The track momentum resolution is studied with μ pair events at beam energy. A correction of about 20% has to be applied to the simulation (see Fig.7.3). The uncertainty on this correction yields a systematic error.

7.2.3 Reconstruction Efficiency

The reconstruction efficiency of highly collimated tracks as they occur in multi-prong events can be tested by comparing the angular distribution between like-sign tracks in the data and the simulation in $\tau^- \to 2h^- h^+ \nu_\tau$ events. They are found to be in good agreement (see Fig. 7.8b). The corresponding systematic uncertainty is negligible.

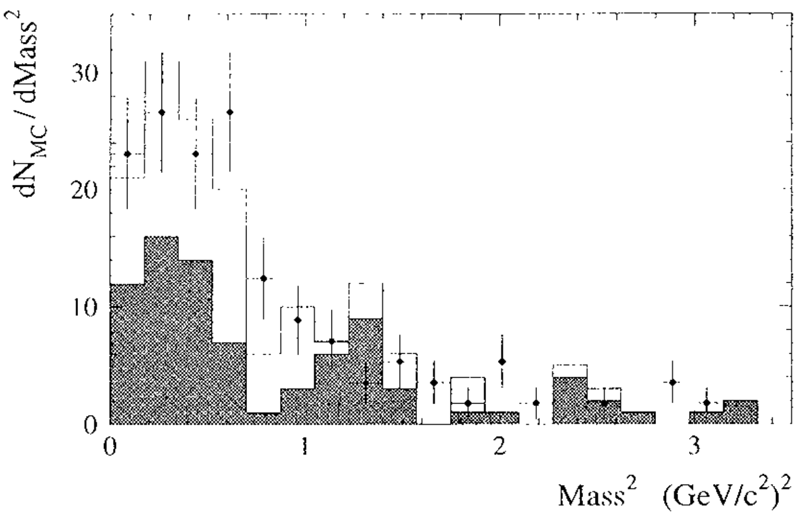

Figure 7.9: *Invariant mass-squared distribution of samples with enriched cases of secondary nuclear interaction. ALEPH data are depicted by the points with error bars, the histogram is the Monte Carlo simulation and the shaded area are those events where, according to the simulation, nuclear interaction occurred.*

7.2.4 Nuclear Interactions

The effect of secondary nuclear interactions is studied by comparing the invariant mass-squared distributions of enriched data samples to the Monte Carlo simulation. An enrichment of about 48% of events containing nuclear interactions is found in the simulation when requiring a minimal distance d_0 between track(s) and interaction point of at least 1 cm [133]. The resulting hadronic invariant mass spectra are found to be in good agreement between data and the simulation. Again, the systematic effect on the shape of the measured distributions is negligible. The consequences of topology-changing effects, *i.e.*, a feed through of events between different τ decay modes, are contained in the branching ratio uncertainty and are described in Ref. [24].

Fig. 7.8a shows the momentum spectrum of the charged hadron in $\tau^- \rightarrow h^- \pi^0 \nu_\tau$ decays for data and the Monte Carlo simulation. Good agreement is found.

7.3 Systematic Errors from the Unfolding Procedure

As seen in Chapter 5, unfolding needs a regularisation procedure for which (in addition to the original least square problem of Eq. (5.23)) the minimisation of the total curvature is found to be suitable. The parameter ξ controls the relative importance of the two terms in Eq. (5.30): if ξ is chosen too small, the solution x contains meaningless fluctuations; on the other hand, if ξ is too big, significant physical information gets lost. The solution of the unfolding problem is now transformed into the optimal choice of ξ. In practice, the best ξ is found by means of the parallel unfolding of a simulated test distribution b_{test}, for which the solution x_{test} is known (see Fig. 7.10). The best choice of ξ yields then the

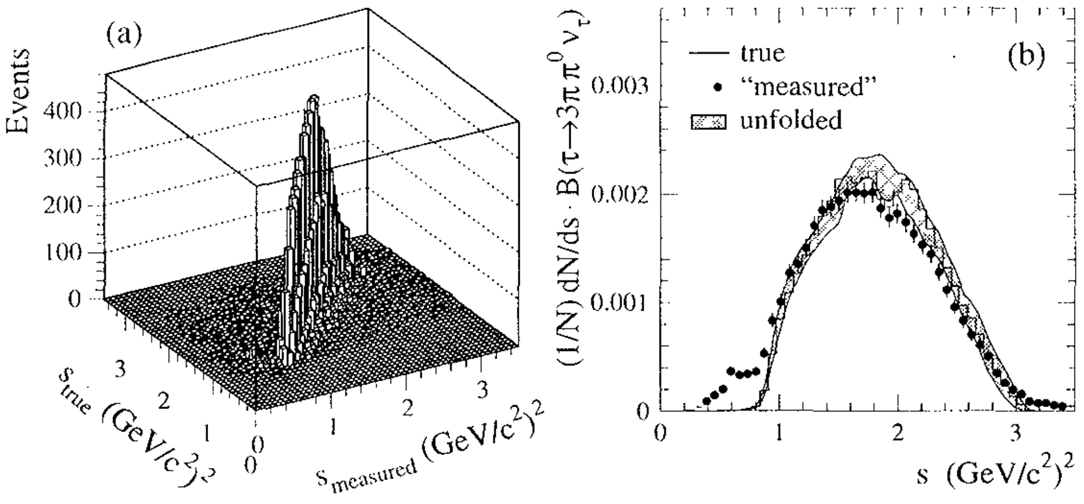

Figure 7.10: *Plot (a) shows the detector response matrix used for the unfolding of the mass-squared (s) spectrum of the decay* $\tau^- \to 2\pi^-\pi^+\pi^0\,\nu_\tau$. *The true, reconstructed ("measured") and unfolded distributions of the corresponding Monte Carlo test spectrum are plotted in (b). The shaded region illustrates the uncertainty after unfolding, taking into account the statistical errors.*

smallest χ^2 between the unfolded test distribution and the original true one. In order to make sure that this procedure applied to a simulated distribution leads to the optimal ξ for data use, a test distribution has to be found, which reproduces the data as well as possible. For example, in the particular case of the $\tau^- \to 2\pi^-\pi^+\pi^0\,\nu_\tau$ channel (see Fig. 6.2), the Monte Carlo simulation disagrees with the data in the peak region. As an appropriate test function, the unfolded data distribution is taken, found by an iterative adjustment of ξ for the data. In this process it is important to distinguish significant information in the raw data distribution from insignificant statistical fluctuations, taking into account the mass resolution. Local statistical fluctuations in the measured distribution are washed out after unfolding.

The following tests are performed in order to evaluate potential systematic biases introduced by the unfolding procedure:

> The cut parameter ξ is varied in the region $\chi^2/\mathrm{dof} \leq 2$ around the minimum, obtained when unfolding the corresponding test distribution under same conditions as the data, *i.e.* using the same detector response matrix. The appropriate test distribution is designed to reproduce well the data (as explained in Chapter 5). The test distribution must not introduce additional statistical fluctuations and should therefore be smoothed as if it were built with infinite statistics. Nevertheless, the corresponding χ^2 is computed within the accuracy of given data statistics.
>
> The total bin-to-bin differences between the unfolded test and its true distribution is considered as an additional systematic uncertainty of the unfolding procedure in

order to be more conservative. It is taken as a diagonal, *i.e.*, uncorrelated, systematic error in the unfolded data distribution (see Fig. 7.10).

7.4 Other Sources of Systematic Errors

In addition, the following sources are examined:

The limited statistics in the simulation causes a systematic error which is determined by making the two-dimensional entries in the detector response matrices fluctuate independently. Although the average ratio of Monte Carlo to data statistics exceeds a factor of five, low populated bins of the response matrix can generate significant uncertainties in the output distribution.

The uncertainties in the hadronic branching ratios introduce the dominant systematic errors in the subtraction of the τ background and kaon channels from data and in the respective normalisation of the spectral functions. They are found by varying the branching ratios, taking into account the correlation matrix given in Ref. [24].

The non-τ background is varied by ±50%.

All mentioned sources of systematic errors other than those originating from uncertainties in the branching ratios, *i.e.*, the absolute normalisation of the respective mass-squared distributions are only considered when they concern the shape of the measured distribution. Their effect on the normalisation is already included in the error of the corresponding branching ratio.

In order to illustrate the respective importance of the mentioned systematic uncertainties, one may perform an integration over the spectral function with some given kernel which depends on the physical problem to be studied. The integration error is then obtained by Gaussian error propagation, taking into account the correlations; using moderate, s-dependent integration kernels, the integration error will clearly be dominated by normalisation uncertainties, *i.e.*, the errors on the respective τ branching ratios. However, the error of an integration with strongly s-dependent weighting kernels enhancing the low energy part of the spectral functions will be dominated by systematics (mainly due to the fake photon rejection and the photon efficiency correction at threshold), while the central energy region (0.6 1.4 GeV/$c^2$2) is statistically limited. When enhancing the higher part of the spectrum, the integration error will be equally dominated by uncertainties due to the unfolding process, and by limited data and Monte Carlo statistics. Numerical results for the respective contributions to the total error obtained from an integration are given in Section 10.2.1 for the case of the spectral moments. Tab. 7.1 gives the relative contributions to the *diagonal* errors of the total vector spectral function in four characteristic energy bins. One should keep in mind that correlations may considerably change the weight of the respective contributions.

Error source	Rel. errors (%) at $s = \ldots$ (GeV^2/c^4)			
	0.2	0.6	2.0	2.6
Statistics error	6.1	0.63	1.8	7.3
ECAL energy calibration	1.1	0.23	1.3	3.7
ECAL energy resolution	3.2	0.16	1.3	1.9
Photon likelihood: ref. distributions	3.7	0.10	1.5	1.8
Photon likelihood: cut on estimator	1.5	0.03	0.5	1.9
Photon min. energy threshold	0.4	0.01	1.3	3.7
Cut on distance: photon–track	1.4	0.06	0.7	1.6
Fake photons	5.1	0.17	1.1	1.8
Energy dependence of reconstr. m_{π^0}	0.9	0.09	0.3	1.2
Momentum calibration	0.1	0.02	0.2	0.2
Momentum resolution	0.1	0.01	0.1	0.2
Unfolding: variation of ξ	1.2	0.10	2.5	4.7
Unfolding: difference test–true	0.5	0.28	2.5	7.0
MC statistics	2.7	0.44	2.7	3.6
Branching ratios	0.8	0.76	3.7	3.8
Non-τ background	0.2	0.05	1.2	4.5
Separation V A	–		2.1	1.8
MC distributions		–	2.7	2.2
Total error	10.2	1.18	7.7	15.0

Table 7.1: *Relative contributions (in %) to the errors of the total vector spectral function in four characteristic mass-squared bins. The line labeled "MC distributions" gives the uncertainty due to use of the Monte Carlo simulation for some unmeasured τ decay modes as explained in Section 6.1.*

Part III

Applications

Introduction

As indicated in the theoretical description of Part I, τ spectral functions open a wide range of phenomenological studies of low energy behaviour of QCD and chiral symmetry. Interesting tests on the basis of the CVC hypothesis can be performed and QCD loop contributions are obtained via dispersion relations from low energy e^+e^- cross sections improved by τ data. The separation of vector and axial-vector spectral functions provide the unique possiblility to study directly the influence of non-perturbative strong effects on inclusive physical observables. This knowledge improves the understanding and quantification of the diverse contributions to the total hadronic width R_τ and elucidates *fortes* as well as *foibles* of the OPE theoretical prediction used at low energy scales. The main result of these tests concerns a stable, reliable and very precise measurement of the strong coupling constant α_s at the τ mass scale.

The measurement procedure described in the preceeding Part II provides after completing the τ pair selection, decay identification and classification, photon and π^0 reconstruction, invariant mass measurement, unfolding and systematic checks, exclusive and inclusive binned spectral functions with, in general, strong bin-to-bin correlations ensueing from the unavoidable unfolding of the measured spectra. Thus, every spectral function is accompanied by an individual covariance matrix of the same bin size containing all relevant errors and correlations. In practice, it is then straightforward to calculate errors of physical observables which use the spectral functions as input by means of simple error propagation.

Chapter 8

Comparison to e^+e^- Results

Two applications of vector spectral functions to e^+e^- data are described in this chapter. In the first one the measured spectral functions of the two- and four-pion final states are compared via isospin rotation to cross sections from e^+e^- annihilation experiments. The second application deals with a fit of the $\pi^-\pi^0$ spectral function and a combined fit of τ and e^+e^- data in terms of vector resonances. The results presented here are published by the ALEPH Collaboration in Ref. [166].

8.1 Comparison to e^+e^- Results

In this section, the most precise spectral function measurements of the τ vector current final states $\pi^-\pi^0$, $\pi^-3\pi^0$ and $2\pi^-\pi^+\pi^0$ are compared to the cross sections of the corresponding e^+e^- annihilation isovector states $\pi^+\pi^-$, $\pi^+\pi^-\pi^+\pi^-$ and $\pi^+\pi^-\pi^0\pi^0$. Using Eq. (1.22) and isospin rotation [167, 168] (see Section 1.4) the following relations hold:

$$\sigma^{I=1,0}_{e^+e^-\to\pi^+\pi^-} - \Delta I_{\rho\omega} = \frac{4\pi\alpha^2}{s} v_{1,\,\pi^-\pi^0\nu_\tau} , \tag{8.1}$$

$$\sigma^{I=1}_{e^+e^-\to\pi^+\pi^-\pi^+\pi^-} = 2\cdot\frac{4\pi\alpha^2}{s} v_{1,\,\pi^-3\pi^0\nu_\tau} , \tag{8.2}$$

$$\sigma^{I=1}_{e^+e^-\to\pi^+\pi^-\pi^0\pi^0} = \frac{4\pi\alpha^2}{s}\left[v_{1,\,2\pi^-\pi^+\pi^0\nu_\tau} - v_{1,\,\pi^-3\pi^0\nu_\tau}\right] . \tag{8.3}$$

In Eq. (8.1) the small isospin-violating electromagnetic contribution $\omega(782) \to \pi^+\pi^-$ is taken into account through its interference with the main isovector contribution yielding the (s-dependent) correction $\Delta I_{\rho\omega}$ obtained from a fit of the total $e^+e^-\to\pi^+\pi^-$ cross section [164]. The mass and the width of the $\omega(782)$ are taken from Ref. [17].

The $e^+e^-\to\pi^+\pi^-$ measurements are taken from OLYA [169, 170], TOF [171], NA7 [172], CMD [169], DM1 [173], DM2 [174], MEA [175] and BCF [176, 177]. The comparison to τ data according to Eq. (8.1) is shown in Fig. 8.1. The two sets of measurements are very precise and in good agreement. Fig. 8.1b shows the square of the isovector pion form factor $F_\pi^{I=1}$ in the threshold region of the two-pion production for τ and e^+e^- data. A second order expansion can be used as a description of $F_\pi^{I=1}$ at very low energies [178, 179]:

$$F_\pi^{\mathrm{ChPT}} \simeq 1 + \frac{1}{6}\langle r^2\rangle_\pi\, s + c_\pi\, s^2 + O(s^3)\ . \tag{8.4}$$

Exploiting precise results from space-like data [180], the pion charge radius-squared $\langle r^2\rangle_\pi = (0.431 \pm 0.026)$ fm^2 and the coefficient $c_\pi = (3.2 \pm 1.0)$ GeV^{-4} from Eq. (8.4) have recently been determined by means of a simultaneous fit [53]. An expanded view of the $\rho(770)$ peak region is given in Fig. 8.1c.

The $e^+e^- \rightarrow \pi^+\pi^-\pi^+\pi^-$ data are taken from OLYA [181], ND [182], MEA [183], CMD [184], DM1 [185, 186], DM2 [187, 188, 189] and M3N [190]. The comparison to the decay channel $\tau^- \rightarrow \pi^- 3\pi^0\, \nu_\tau$ using Eq. (8.2) is shown in Fig. 8.2a. It is found to be in rather good agreement.

The $e^+e^- \rightarrow \pi^+\pi^-\pi^0\pi^0$ data are taken from OLYA [181], ND [182], M2N [191], DM2 [187, 188, 189] and M3N [190]. The measurements originating from different e^+e^- experiments show some inconsistencies (see Fig. 8.2b). On the low mass side, the cross section is dominated by ND and OLYA data from the VEPP-2M storage ring at Novosibirsk. The ND measurement points are significantly higher than the OLYA data. At higher mass, data are dominated by the Orsay experiments DM2 and M3N: the DM2 cross section points are significantly lower than the M3N measurements. Tau data slightly favor the OLYA data on the low mass side; furthermore, they are clearly higher than the DM2 results in the central region between 2 and 2.6 GeV/c^2. The small dots in Fig. 8.2b illustrate the resonant $\omega\pi^0 \rightarrow \pi^+\pi^-\pi^0\pi^0$ contribution taken from ND [182] and DM2 [188].

Finally, the total e^+e^- isovector cross section is compared to the τ vector current spectral function. The following contributions require some discussion:

- The isospin descriptions for the two- and four-pion final states are easily found by inverting Eqs. (8.1), (8.2) and (8.3). The isoscalar $\omega \rightarrow \pi^+\pi^-$ contribution is subtracted from the total $\pi^+\pi^-$ cross section.

- The four-pion final state of the $\omega\pi^0$ mode is already contained in the $\pi^+\pi^-\pi^0\pi^0$ cross section. A 11.2% correction for the other ω decay modes is applied.

- The $e^+e^- \rightarrow \pi^+\pi^-\eta$ data are taken from ND [182] and DM2 [192].

- The cross sections for the six-pion final states $3\pi^+3\pi^-$ and $2\pi^+2\pi^-2\pi^0$ were measured by DM1 [193], M3N [190], CMD [184] and DM2 [194]. Using Pais' classes [52] (see Section 1.4) one can deduce an upper limit for the unknown $\sigma_{\pi^-\pi^+4\pi^0}$ cross section. Assuming conservatively the classes {411} and {510} to be dominant, one obtains $\sigma_{\pi^+\pi^-4\pi^0} \leq (3/2) \times \sigma_{2\pi^-2\pi^+2\pi^0} - (9/24) \times \sigma_{3\pi^-3\pi^+}$.

- To extract the isovector part of the $\mathrm{K}^+\mathrm{K}^-$ and $\mathrm{K}_\mathrm{S}^0\,\mathrm{K}_\mathrm{L}^0$ states, the $SU(3)$ relation between pion and kaon form factors is adopted to infer the relation [177]

$$\sigma_{\mathrm{K}^+\mathrm{K}^-}(s) = \frac{\beta_\mathrm{K}^3}{4\,\beta_\pi^3}\,\sigma_{\pi^+\pi^-}(s)\ , \tag{8.5}$$

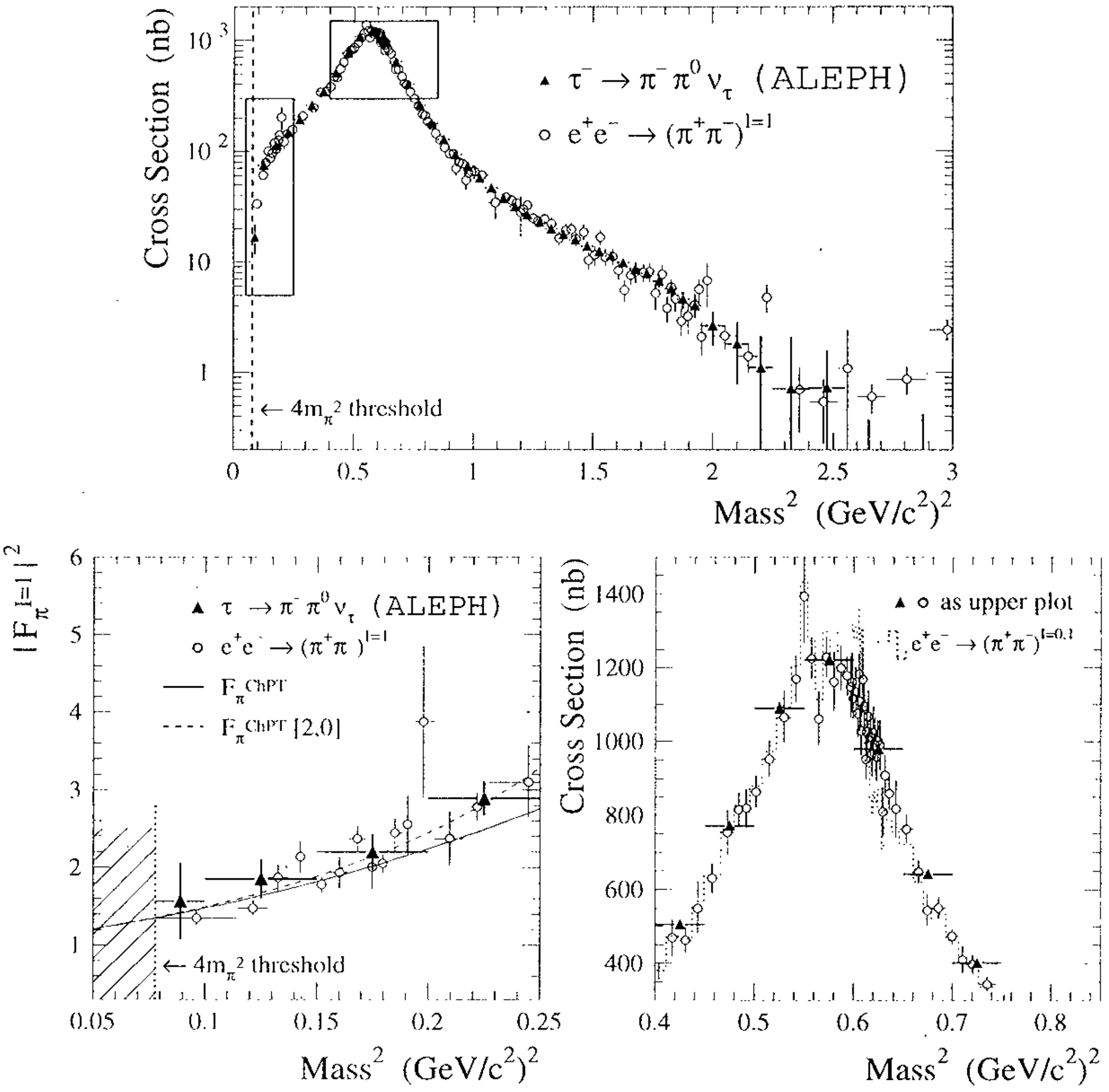

Figure 8.1: *The two-pion data from τ decays compared to the corresponding isovector e^+e^- cross section (data points from different e^+e^- experiments, measured at the same mass have been averaged). Both distributions are shown with statistical and systematic errors. The two rectangles indicate the regions that are expanded in (b) and (c). Figure (b) shows the pion form factor near threshold. The chiral expansion $F_\pi^{\rm ChPT}$ is defined in Eq.* (8.4). *The additional function labeled* "[2, 0]" *(indistinguishable from* "[1, 1]" *in the plotted energy region) denotes different parametrisations (Padé approximants* [195]) *deduced from Chiral Perturbation Theory as discussed in Ref.* [178, 179]. *The dotted line in Figure (c) represents the total (uncorrected) isoscalar and isovector e^+e^- cross section.*

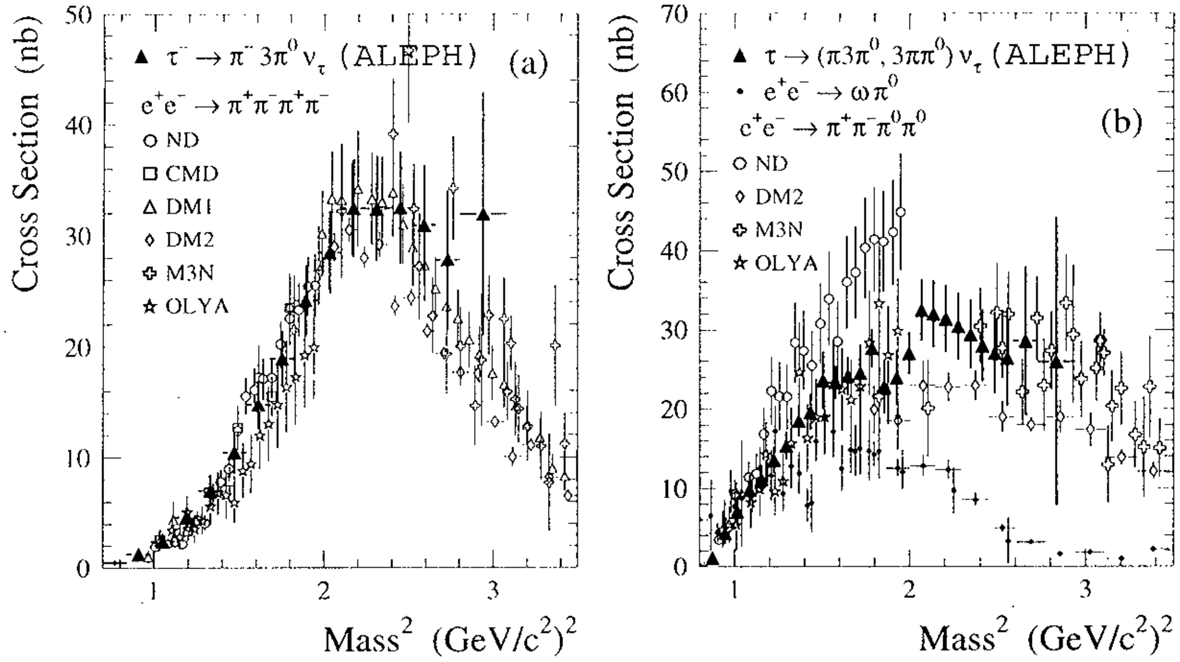

Figure 8.2: *Comparison of the isospin-rotated four-pion τ data with the corresponding e^+e^- cross sections. The error bars shown contain both statistical and systematic errors. An enhancement in the low mass part of the $\pi^+\pi^-\pi^0\pi^0$ channel in (b) is expected from the resonant $\omega\pi$ contribution (small points).*

where $\beta_{K,\pi} = (1 - 4M^2_{K,\pi}/s)^{1/2}$. This can be directly related to the $\tau^- \to K^- K^0 \nu_\tau$ spectral function, for which, due to the uncertainty of the relation (8.5), a total systematic uncertainty of 25% is assumed.

The DM1 and DM2 collaborations [196, 197] made some effort to isolate a small isovector component of the $e^+e^- \to K^\pm K^0_S \pi^\mp$ cross section. This can be scaled up to the full $K\bar{K}\pi$ contribution which can be related to the corresponding τ spectral function using isospin symmetry.

The inclusive reaction $e^+e^- \to K^0_S + X$ was analysed by DM1 [198]. Having subtracted from its cross section the separately measured contributions of the final states $K^0_S K^0_L$, $K^0_S K^+\pi^-$ and $K^0_S K^0_L \pi^0$, it still includes the modes $K^0_S K^0_S \pi^+\pi^-$, $K^0_S K^0_L \pi^+\pi^-$, $K^0_S K^0_L \pi^0\pi^0$, $K^0_S K^+\pi^-\pi^0$ and $K^0_S K^-\pi^+\pi^0$. With the assumption that the cross sections for the processes $e^+e^- \to K^0\bar{K}^0(\pi\pi)^0$ and $e^+e^- \to K^+K^-(\pi\pi)^0$ are equal, one can summarize the total $K\bar{K}\pi\pi$ contribution as twice the above corrected $K^0_S + X$ cross section. A reasonable estimate of the systematic uncertainty, implied by the assumption made, is obtained by taking the cross section for the channel $K^+K^-\pi^+\pi^-$ measured by DM1 [199] and DM2 [187]. Since the $K\bar{K}\pi\pi$ isovector part is unknown it is assumed to be $(50 \pm 50)\%$.

Fig. 8.3 shows both the total τ vector current spectral function and the corresponding spectral function coming from the isovector e^+e^- cross section. Agreement is found at

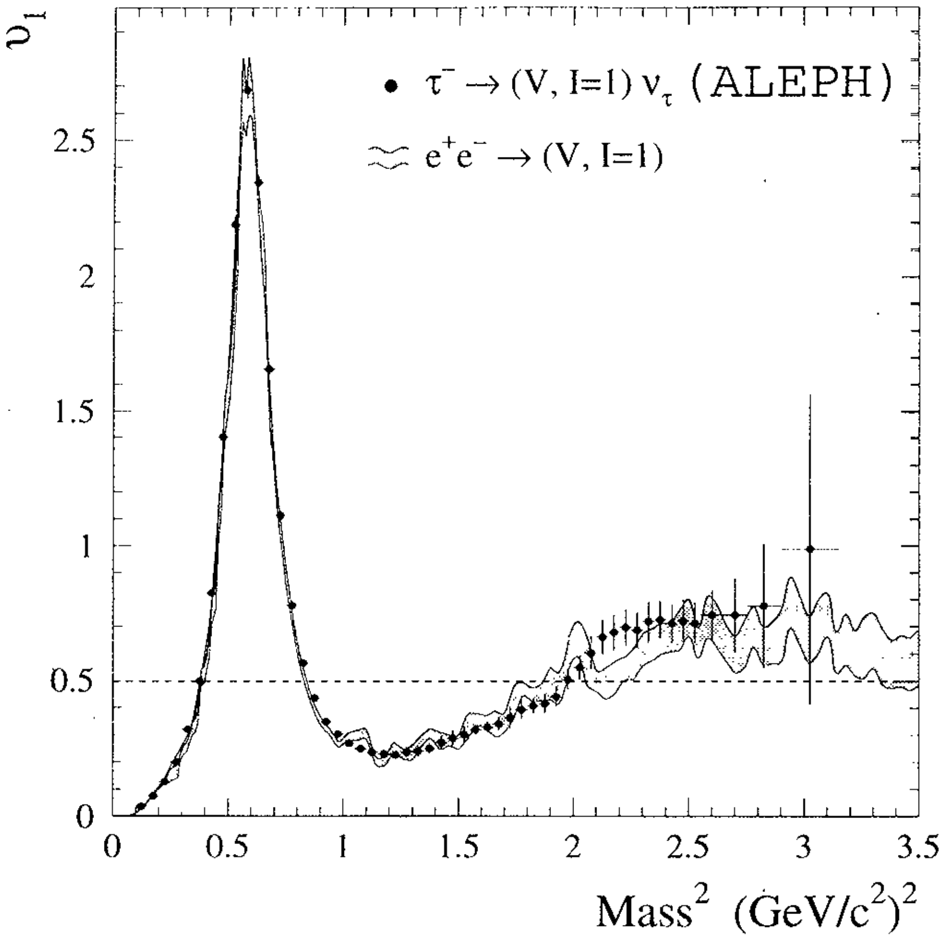

Figure 8.3: *Total hadronic vector current spectral function from τ decays (data points) and the corresponding distribution calculated from e^+e^- isovector states using isospin symmetry. The shaded band includes statistical and systematic errors. The dashed line corresponds to the naive isovector quark-parton prediction.*

low mass-squared. Above 2 GeV/$c^2$2, the τ data are somewhat higher than the e^+e^- measurements (note that the τ data points are highly correlated — see Fig. 6.5). This is essentially due to the observed disagreement between the $\tau^- \to 2\pi^-\pi^+\pi^0\,\nu_\tau$ spectral function and the corresponding e^+e^- cross section.

8.2 τ Branching Ratios from e^+e^- Cross Sections

Following the spirit of the preceeding section it is interesting vice versa to compare τ vector branching ratios to CVC predictions obtained from the integral

$$\frac{B_{\rm CVC}(\tau^- \to X^-\nu_\tau)}{B(\tau^- \to e^-\,\nu_\tau\bar{\nu}_e)} = \frac{3\,|V_{ud}|^2\,S_{\rm EW}}{2\pi\alpha^2 M_\tau^2}\int\limits_{4m_\pi^2}^{M_\tau^2} ds\,s\left(1-\frac{s}{M_\tau^2}\right)^2\left(1+\frac{2s}{M_\tau^2}\right)\sigma^{I=1}_{e^+e^-\to X^0}(s)\ . \quad (8.6)$$

τ vector mode	BR_τ (%)	$\mathrm{BR}_{\mathrm{CVC}}$ (%)	σ
$\pi^-\pi^0\,\nu_\tau$	25.35 ± 0.19	24.31 ± 0.65	1.5
$\pi^-3\pi^0\,\nu_\tau$	1.24 ± 0.14	1.10 ± 0.10	0.8
$2\pi^-\pi^+\pi^0\,\nu_\tau$	4.17 ± 0.12	4.36 ± 0.38	0.5
$(6\pi)^-\,\nu_\tau$	0.037 ± 0.022	0.20 ± 0.09	1.8
$\omega\,\pi^-\,\nu_\tau$	1.83 ± 0.10	1.76 ± 0.17	0.4
$\eta\,\pi^-\pi^0\,\nu_\tau$	0.170 ± 0.028	0.134 ± 0.031	0.9
$\mathrm{K}^-\,\mathrm{K}^0\,\nu_\tau$	0.194 ± 0.042	0.182 ± 0.053	0.2
$(\mathrm{K}\bar{\mathrm{K}}\pi)^-\,\nu_\tau$	0.34 ± 0.13	0.072 ± 0.036	2.0

Table 8.1: *CVC predictions for the branching ratios of the τ vector channels. The reference values of the τ branching ratios are taken from Tab. 6.1. The last column gives the standard deviation between corresponding values in units of 1σ.*

where $B(\tau^- \to e^-\,\nu_\tau\bar{\nu}_e)$ is taken from Eq. (1.13) assuming universality; the electroweak correction factor S_{EW} is defined as in Section 1.3.2 and $\sigma^{I=1}_{e^+e^-\to X^0}(s)$ is the measured cross section of the rotated e^+e^- isovector final state which corresponds to the τ^- hadronic decay channel $X^-\,\nu_\tau$. The integration is performed over correlated data points affected by statistical and systematic uncertainties. The procedure is identical with the one used for the evaluation of the muonic $(g-2)$ and the running $\alpha(s)$ on measured data grounds. It is described in detail in Section 9.2.

For the two- and six-pion channels, the coresponding e^+e^- final states X^0 are deduced by simply inverting Eqs. (8.1), (8.2) and (8.3). The isoscalar $\omega \to \pi^+\pi^-$ contribution is subtracted from the total $\pi^+\pi^-$ cross section. The effect of the interference is small compared to the total error of the integral (8.6): $B_{\mathrm{CVC}}(\pi^-\pi^0\,\nu_\tau)^{\omega-\rho-\mathrm{Int.}} - B_{\mathrm{CVC}}(\pi^-\pi^0\,\nu_\tau) = -0.09\%$. The total six-pion branching ratio is obtained using isospin constraints to bound the missing $\pi^+\pi^-4\pi^0$ cross section as explained in the preceeding section. The total $I=1$ e^+e^- six-pion cross section equates then via CVC the vector part of $B(\tau^- \to (6\pi)^-\,\nu_\tau)$. Eq. (8.5) is used to extract the isovector part of the final states $\mathrm{K}\bar{K}$. An uncertainty of 25% is assumed in this relation. The total $\tau^- \to \mathrm{K}\mathrm{K}^0\,\nu_\tau$ branching ratio is equal to two times the $\mathrm{K}^+\mathrm{K}^-$ contribution. Finally, $B(\tau^- \to (\mathrm{K}\bar{\mathrm{K}}\pi)^-\,\nu_\tau)$ is obtained from the rescaled (factor three) isovector part of the $e^+e^- \to \mathrm{K}^\pm\mathrm{K}^0_S\pi^\mp$ cross section, provided the dynamics to be governed by $\mathrm{K}^*\mathrm{K}$.

The CVC results and the corresponding τ branching ratios are compiled in Tab. 8.1. All channels but the six-pion and the $\mathrm{K}\bar{\mathrm{K}}\pi$ final states show reasonable agreement between the measured τ branching ratios and the CVC predictions. Using three times the total, $I=(0+1)$ $e^+e^- \to \mathrm{K}^\pm\mathrm{K}^0_S\pi^\mp$ cross section and neglecting the difference in shape between the two isospin states, one can estimate the isovector contribution to the integral (8.6) from the inclusive CVC branching ratio $B^{(I=0+1)}_{\mathrm{CVC}}(\tau^- \to (\mathrm{K}\bar{\mathrm{K}}\pi)^-\,\nu_\tau) = (0.24 \pm 0.04)\%$ to be $(100^{+0}_{-13})\%$. In the same way, but using the e^+e^- measurement as reference, one obtains for the vector part of $(\mathrm{K}\bar{\mathrm{K}}\pi)^-$ in τ decays the estimate $(17 \pm 9)\%$.

8.3 A Fit of the Pion Form Factor

Several parametrisations of the pion form factor Eq. (1.31) can be found in the literature. (See, *e.g.*, Refs. [164, 200, 169, 201].) In this section, different fits using the Kühn-Santamaria [164] and the Gounaris-Sakurai parametrisations [200] are presented. In addition, a combined fit to τ and e^+e^- data is performed, where the masses and widths of the $\rho^\pm(770)$ and the $\rho^0(770)$ are separately determined, in order to extract possible isospin violating effects.

As seen in Section 7.3, the unfolding procedure introduces additional systematic uncertainties because of the numerical instability of the problem. Generally, one can state that unfolding is necessary if a theoretical description of an observed distribution is not available, as is the case for the total vector (and axial-vector) hadronic spectral functions in τ decays. Also, unfolding is needed for comparison with e^+e^- results where the mass is experimentally known with very good accuracy. However in the specific case of the $\pi^-\pi^0$ spectral function, phenomenological models based on vector resonances which describe the lineshape exist. One therefore does not need to unfold, as a convolution of the theoretical curve with the detector response matrix A is a well defined and stable problem. The convolved theoretical distribution can subsequently be fitted to the data. This procedure is followed here.

The results of all types of fits are given with errors, including both statistical and systematic uncertainties. The sources of systematic uncertainties correspond in detail to those mentioned in Chapter 7, apart from those introduced by the unfolding procedure. The correlations between the fitted parameters in the combined fit are given as a correlation matrix.

Systematic errors of the e^+e^- annihilation data are caused by uncertainties coming mainly from the determination of the efficiency of the two-pion reconstruction and the luminosity measurement. These errors are given as *normalisation* uncertainties by the experiments, *i.e.*, they scale linearly with the measured cross sections. The usual way of introducing such errors into a least square minimisation is to treat them as being totally correlated. They therefore populate the off-diagonal elements of the corresponding covariance matrix. However, it is known that this procedure introduces a bias into the minimisation, leading systematically to lower values in terms of the normalisation of the fitted parametrisation [202]. This can be demonstrated by means of the following simple example:

Consider two measurements x_1, x_2 with statistical errors σ_1, σ_2. Consider further a common offset error $\sigma_{\rm off}$ of systematic origin (*e.g.*, a calibration uncertainty). The covariance matrix reads then

$$C = \begin{pmatrix} \sigma_1^2 + \sigma_{\rm off}^2 & \sigma_{\rm off}^2 \\ \sigma_{\rm off}^2 & \sigma_2^2 + \sigma_{\rm off}^2 \end{pmatrix} . \tag{8.7}$$

The mean value $\langle k\rangle$ and its error Δk are obtained from the mimization of $\chi^2 = \sum_{i,j=1,2}(x_i - k)C^{-1}_{ij}(x_j - k)$. Using Eqs. (2.93) and (2.94), one has

$$\begin{aligned} \langle k\rangle &= \frac{x_1\sigma_2^2 + x_2\sigma_1^2}{\sigma_1^2+\sigma_2^2} , \\ (\Delta k)^2 &= \frac{\sigma_1^2\sigma_2^2}{\sigma_1^2+\sigma_2^2} + \sigma_{\rm off}^2 . \end{aligned} \tag{8.8}$$

The mean value $\langle k\rangle$ keeps unchanged by the systematic offset error $\sigma_{\rm off}$ while the error Δk increases. Offset errors therefore do not introduce a bias into the χ^2 minimization, *i.e.*, the fit.

Unfortunately, the case becomes annoying when normalisation errors occur. Considering the same two-measurement example but replacing the offset error by a normalisation uncertainty $\sigma_{\rm norm}$, *e.g.*, luminosity or efficiency errors which scale with the measured value, yields the following covariance matrix

$$C = \begin{pmatrix} \sigma_1^2 + x_1^2\sigma_{\rm norm}^2 & x_1x_2\sigma_{\rm norm}^2 \\ x_1x_2\sigma_{\rm norm}^2 & \sigma_2^2 + x_2^2\sigma_{\rm norm}^2 \end{pmatrix} . \tag{8.9}$$

and the minimization leads then to

$$\begin{aligned} \langle k\rangle &= \frac{x_1\sigma_2^2 + x_2\sigma_1^2}{\sigma_1^2+\sigma_2^2+(x_1-x_2)^2\sigma_{\rm norm}^2} , \\ (\Delta k)^2 &= \frac{\sigma_1^2\sigma_2^2 + (x_1^2\sigma_2^2 + x_2^2\sigma_1^2)\sigma_{\rm norm}^2}{\sigma_1^2+\sigma_2^2+(x_1-x_2)^2\sigma_{\rm norm}^2} . \end{aligned} \tag{8.10}$$

One observes a systematic tendency of $\langle k\rangle$ in Eq. (8.10) to lower values governed by the strength of the normalisation uncertainty $\sigma_{\rm norm}$ and the difference between the input measurements. The same bias occurs in the expression for Δk. Citing d'Agostini [202]: "*The advantage for the fit to prefer under these conditions, normalization factors smaller than one finds its deeper reason in the standard formalism of the error propagation, where only first derivatives are considered.*" In order to quantify the importance of the above observations one can imagine two measurements $x_1 = 5 \pm 2$, $x_2 = 5 \pm 1$ and $\sigma_{\rm norm} = 20\%$. That gives $\langle k\rangle = 5.00 \pm 1.80$. Setting now $x_1 = 6 \pm 2$, $x_2 = 4 \pm 1$ with the same $\sigma_{\rm norm} = 20\%$ one would in an unbiased case expect the same mean value and error; instead, Eq. (8.10) yields $\langle k\rangle = 4.26 \pm 1.55$ where both, mean value and error decreased.

To avoid such an effect, the best estimate of the parameters is found when using systematic errors without correlations as for the statistical ones. The corresponding parameter errors, however, are determined by repeating the fit when taking into account the full correlations of the systematic errors among the measurements of one experiment. Measurements between different experiments are assumed to be uncorrelated.

8.3.1 The Kühn-Santamaria (KS) Parametrisation

In the Kühn-Santamaria parametrisation the pion form factor is given by contributions from the known isovector meson resonances $\rho(770)$, $\rho(1450)$ and $\rho(1700)$, taking into account $\rho - \omega$ interference:

$$F_{\pi}^{I=1,0}(s) \;=\; \frac{\mathrm{BW}_{\rho(770)}(s)\,\frac{1+\delta\,\mathrm{BW}_{\omega(783)}(s)}{1+\delta} \;+\; \beta\,\mathrm{BW}_{\rho(1450)}(s) \;+\; \gamma\,\mathrm{BW}_{\rho(1700)}(s)}{1\;+\;\beta\;+\;\gamma}\,, \tag{8.11}$$

with the Breit-Wigner propagators

$$\mathrm{BW}^{\mathrm{KS}}_{\rho(M_\rho)}(s) \;=\; \frac{M_\rho^2}{M_\rho^2 \;-\; s \;-\; i\sqrt{s}\,\Gamma_\rho(s)} \tag{8.12}$$

and the energy dependent width

$$\Gamma_\rho(s) \;=\; \Gamma_\rho(M_\rho^2)\left(\frac{M_\rho^2}{s}\right)^{\lambda}\left(\frac{k(s)}{k(M_\rho^2)}\right)^{3}, \tag{8.13}$$

where $k(s) = \frac{1}{2}\sqrt{s}\,\beta_\pi(s)$ and $k(M_\rho^2)$ is the pion momentum in the ρ rest frame. As in Refs. [164] and [169] the amplitudes β, γ and δ are assumed to be real. Interference with the isospin-violating electromagnetic $\omega \rightarrow \pi^+\pi^-$ decay occurs only in e^+e^- annihilation. Consequently, δ is fixed to zero when fitting τ data. According to Ref. [201] a fit parameter λ is added to take into account possible uncertainties in the p-wave approximation of the s-dependent width.

Parameter	Kühn-Santamaria	Gounaris-Sakurai
$M_{\rho^\pm(770)}$	774.9 ± 0.9	776.4 ± 0.9
$\Gamma_{\rho^\pm(770)}$	144.2 ± 1.5	150.5 ± 1.6
β	-0.094 ± 0.007	-0.077 ± 0.008
$M_{\rho^\pm(1450)}$	1363 ± 15	1400 ± 16
$\Gamma_{\rho(1450)}$	$\equiv 310$	$\equiv 310$
γ	-0.015 ± 0.008	0.001 ± 0.009
$M_{\rho^\pm(1700)}$	$\equiv 1700$	$\equiv 1700$
$\Gamma_{\rho(1700)}$	$\equiv 235$	$\equiv 235$
λ	$\equiv 1.0$	$\equiv 1.0$
χ^2/dof	$81/65$	$54/65$

Table 8.2: *Fit results of the pion form factor in $\tau^- \rightarrow \pi^-\pi^0\,\nu_\tau$ decays using the Kühn-Santamaria (left-hand column) and the Gounaris-Sakurai parametrisation (right-hand column). The values of $\Gamma_{\rho(1450)}$, $M_{\rho^\pm(1700)}$ and $\Gamma_{\rho(1700)}$ are taken from Ref.* [17].

The results of the τ data and the combined fit using the KS parametrisation are listed in the left-hand columns of Tables 8.2 and 8.3.

8.3.2 The Gounaris-Sakurai (GS) Parametrisation

Starting from a more elaborate treatment of the p-wave scattering amplitude for a broad resonance, the following parametrisation was obtained with the additional requirement of the normalisation $F_\pi(0) \equiv 1$, as in the KS parametrisation. The simple Breit-Wigner resonances in (8.11) are replaced (for $s \geq 4m_\pi^2$) by [200]

$$\mathrm{BW}^{\mathrm{GS}}_{\rho(M_\rho)}(s) \; = \; \frac{M_\rho^2(1 + d \cdot \Gamma_\rho/M_\rho)}{M_\rho^2 \; - \; s \; + \; f(s) \; - \; i\sqrt{s}\,\Gamma_\rho(s)} \; , \tag{8.14}$$

where

$$f(s) \; = \; \Gamma_\rho \frac{M_\rho^2}{k^3(M_\rho^2)} \left[k^2(s) \left(h(s) - h(M_\rho^2) \right) \; + \; (\, M_\rho^2 - s)\, k^2(M_\rho^2)\, \frac{dh}{ds}\bigg|_{s=M_\rho^2} \right] . \tag{8.15}$$

The s dependence of $\Gamma_\rho(s)$ and $k(s)$ is the same as in Eq. (8.13). The function $h(s)$ is defined as

$$h(s) \; = \; \frac{2}{\pi}\, \frac{k(s)}{\sqrt{s}} \ln \frac{\sqrt{s} + 2k(s)}{2m_\pi} \; , \tag{8.16}$$

with $dh/ds|_{M_\rho^2} = h(M_\rho^2) \left[(8k^2(M_\rho^2))^{-1} - (2M_\rho^2)^{-1} \right] \; + \; (2\pi M_\rho^2)^{-1}$.

The normalisation $\mathrm{BW}^{\mathrm{GS}}_{\rho(M_\rho)}(0) = 1$ fixes the parameter $d = f(0)/(\Gamma_\rho M_\rho)$. It is found to be [200]

$$d \; = \; \frac{3}{\pi} \frac{m_\pi^2}{k^2(M_\rho^2)} \ln \frac{M_\rho + 2k(M_\rho^2)}{2m_\pi} \; + \; \frac{M_\rho}{2\pi\, k(M_\rho^2)} \; - \; \frac{m_\pi^2 M_\rho}{\pi\, k^3(M_\rho^2)} \; . \tag{8.17}$$

The results of the τ data and the combined fit using the GS parametrisation are listed in the right-hand columns of the Tables 8.2 and 8.3.

Concluding from Table 8.2, the fits establish a need for the $\rho(1450)$ contribution to the weak pion form factor in the KS and GS parametrisations ($\beta = -0.087 \pm 0.012$) with a fitted mass $M_{\rho(1450)} = (1380 \pm 24)$ MeV/c^2 when fixing the width at $\Gamma_{\rho(1450)} = 310$ MeV/c^2 [17]. No significant evidence of a $\rho(1700)$ contribution is found ($\gamma = -0.008 \pm 0.008$). The previous values are the weighted averages between the results of both fit types. Their errors account for statistical and systematic uncertainties coming from model dependence. It must be stated that the fitted $\rho(1450)$ parameters show large correlations with the corresponding $\rho(1450)$ width. In fact, fixing $\Gamma_{\rho(1450)} = 600$ MeV/c^2 leads to the averaged fit results: $\beta = -0.156$, $M_{\rho(1450)} = 1470$ MeV/c^2 and $\gamma = -0.030$ with a substantial improvement of the χ^2, *i.e.*, 56 (KS) and 51 (GS) over 65 degrees of freedom.

One could try to explain the enhancement of the pion form factor centered around 1200 MeV/c^2 as originating from an inelastic effect induced via unitarity by the opening of the $\omega\pi^0$ channel which occurs at 920 MeV/c^2 [203]. Although this effect is physically sound and should take place, the proposed description is not very predictive and requires a factor $(M_0^2/(M_0^2 - s - iM_0\Gamma_0))^{n_0}$ with three additional parameters M_0, Γ_0 and n_0 to be adjusted in the fit. However, the existence of a $\rho(1450)$ meson is already well established in the $\pi^+\pi\;\, 2\pi^0$ final state [204] and since the sensitivity of the data on the pion form factor is not sufficient to fit a larger number of parameters. the inelastic parametrisation is not used in the present analysis.

Fig. 8.4 shows the KS/GS-type fits using one and three Breit-Wigner amplitudes.

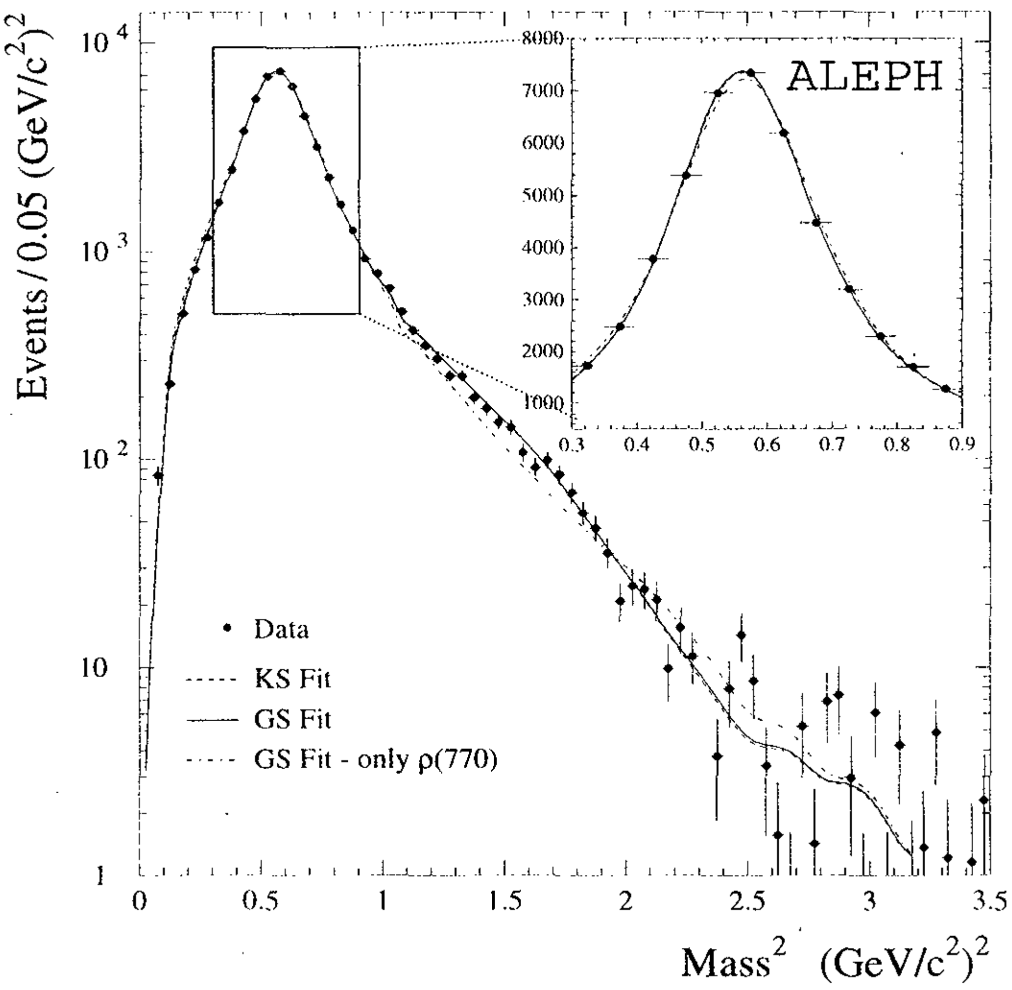

Figure 8.4: *Fit of the* $\tau^- \to \pi^-\pi^0\,\nu_\tau$ *invariant mass spectrum using the Kühn-Santamaria (KS) and the Gounaris-Sakurai (GS) parametrisation. The solid and dashed curves are the functions corresponding to the KS/GS-type form factor fits given in Table* 8.2. *They have been convolved with the detector resolution and the* τ *phase space. Due to statistical fluctuations in the detector response matrix, the functions are not smooth after convolution. The dashed-dotted line corresponds to a GS-type fit in which only the* $\rho(770)$ *contribution is taken into account.*

8.3.3 Combined Fit of τ and e^+e^- Data

The results of the combined τ and e^+e^- data fit with the KS and GS parametrisations are presented in Table 8.3. In these fits, the pion form factor is described by the ρ resonance with different parameters fitted for $\rho^\pm$ and ρ^0, while the much smaller $\rho(1450)$ and $\rho(1700)$ contributions are assumed to be isospin invariant. In this way, it is possible to directly compare, for the first time, in a model-independent way the parameters of the charged and the neutral ρ's. Due to the large number of degrees of freedom in the combined fits, all free parameters can be simultaneously determined with good precision. All presented fits resulted in significantly higher $\rho(770)$ masses than the value of $M_{\rho(770)} = (768.5 \pm 0.6)$ MeV/c^2 (average of $\rho^\pm$ and ρ^0) given by the PDG [17]. Within large uncertainties (about 8 MeV/c^2) essentially due to model dependence, the width $\Gamma_{\rho(770)}$ was found to be in agreement with the PDG value of $\Gamma_{\rho(770)} = (150.7 \pm 1.2)$ MeV/c^2. The additional fit parameter λ in the second type of fit is found to be $\lambda = 0.45 \pm 0.11$, *i.e.*, quite different from the fixed value $\lambda \equiv 1$ in the first type of fits. As can be expected, a different adjustment of λ has a considerable impact on the fitted mass and width of the $\rho(770)$. The mass of $M_{\rho(770)}^{(\lambda=0.45)} = 783.8$ is clearly larger then the peak value and, in fact, it is even larger the mass of the $\omega(783)$. Both τ and e^+e^- data are sensitive to the $\rho(1450)$ parameters. The $\rho(1450)$ width is found to be strongly model-dependent, but from all fit types its value is significantly higher than the PDG value of $\Gamma_{\rho(1450)} = (310 \pm 60)$ MeV/c^2 obtained from $e^+e^- \to \omega\pi$ data. This difference could be

Parameter	Kühn-Santamaria (KS)	Gounaris-Sakurai (GS)	
δ	$(1.91 \pm 0.15)\times10^{-3}$	$(1.97 \pm 0.10)\times10^{-3}$	$(1.97 \pm 0.15)\times10^{-3}$
$M_{\rho^\pm(770)}$	773.4 ± 0.9	775.7 ± 0.9	783.8 ± 3.0
$M_{\rho^0(770)}$	773.4 ± 0.7	775.7 ± 0.7	783.8 ± 3.0
$\Gamma_{\rho^\pm(770)}$	147.7 ± 1.6	150.8 ± 1.7	162.0 ± 5.3
$\Gamma_{\rho^0(770)}$	147.3 ± 1.3	150.8 ± 1.3	162.4 ± 5.0
β	-0.229 ± 0.020	-0.161 ± 0.010	-0.184 ± 0.010
$M_{\rho(1450)}$	1465 ± 22	1448 ± 19	1490 ± 23
$\Gamma_{\rho(1450)}$	696 ± 47	503 ± 38	591 ± 53
γ	0.075 ± 0.022	0.076 ± 0.009	0.074 ± 0.010
$M_{\rho(1700)}$	1760 ± 31	1757 ± 20	1799 ± 34
$\Gamma_{\rho(1700)}$	215 ± 86	237 ± 78	255 ± 39
λ	$\equiv 1.0$	$\equiv 1.0$	0.45 ± 0.11
χ^2/dof	190/195	194/195	193/194
$M_{\rho^\pm(770)} - M_{\rho^0(770)}$	0.0 ± 1.0	0.0 ± 1.0	0.0 ± 1.2
$\Gamma_{\rho^\pm(770)} - \Gamma_{\rho^0(770)}$	0.4 ± 1.8	0.0 ± 2.0	-0.4 ± 2.5

Table 8.3: *Results of the combined fit of the* $\pi^\pm\pi^0$ *and* $\pi^+\pi^-$ *resonance amplitudes according to the Kühn-Santamaria and the Gounaris-Sakurai model. In the second GS-type fit, the parameter* λ *introduced in Eq.* (8.13) *is additionally fitted. This leads to higher parameter errors with strong correlations among them.*

ALEPH	$M_\rho^\pm$	M_ρ^0	$\Gamma_\rho^\pm$	Γ_ρ^0
$M_\rho^\pm$	1	0.18	0.32	0.02
M_ρ^0	-	1	0.03	0.31
$\Gamma_\rho^\pm$	-	-	1	0.17

Table 8.4: *Average correlations found in the KS/GS-type fits (with fixed λ) between masses and widths of the charged and neutral $\rho^0(770)$.*

linked to the neglect of inelastic effects as discussed in the previous section. The fitted masses $M_{\rho(1450)}$ from all fit types are found to be in rather good agreement with the PDG average of $M_{\rho(1450)} = (1449 \pm 8)$ MeV/c^2. The information concerning the mass, width and relative amplitude of the $\rho(1700)$ is essentially extracted from the e^+e^- data and found to be in fairly good agreement with the PDG values.

Systematic uncertainties due to the energy scale in e^+e^- annihilation experiments are difficult to estimate as, in general, the publications do not refer to this point. In most cases, the experiments used the narrow $\phi(1020)$ resonance peak to calibrate the beam energy. Consequently, intrinsic uncertainties are introduced by slight modifications of the central ϕ mass value over the years, *e.g.*, $M_\phi = 1019.57$ MeV/c^2 in 1980 became $M_\phi = 1019.41$ MeV/c^2 in 1996. An additional systematic uncertainty of 0.3 MeV/c^2 is considered in the ρ^0 mass measurement.

Although the absolute values of the $\rho(770)$ masses and widths depend significantly on the KS- or GS-type of the fit and the parameter λ, their respective differences, *i.e.*, $\Delta M_{\rho(770)} = M_{\rho^\pm(770)} - M_{\rho^0(770)}$ and $\Delta\Gamma_{\rho(770)} = \Gamma_{\rho^\pm(770)} - \Gamma_{\rho^0(770)}$ are stable. Using the fit results from Table 8.3, one obtains the average

$$\begin{aligned} \Delta M_{\rho(770)} &= (0.0 \pm 1.0 \pm 0.1)\ \mathrm{MeV}/c^2 \\ \Delta\Gamma_{\rho(770)} &= (0.1 \pm 1.8 \pm 0.5)\ \mathrm{MeV}/c^2\ . \end{aligned}$$

The first errors are due to statistical and systematic uncertainties (including correlations between the fit parameters), while the second ones account for differences from the resonance parametrisations. Fig. 8.5 shows the results with its 39% CL error ellipse taking into account the correlations between the fit parameters given in Table 8.4.

A difference between $\Gamma_{\rho^\pm}$ and Γ_{ρ^0} could occur on one hand through electromagnetic isospin-violating decay modes such as $\rho \to \pi\pi\gamma$, which is observed at the 1% level for the ρ^0 [17]. On the other hand the dominant $\rho \to \pi\pi$ channel could also manifest some isospin violation. An obvious contribution comes from the observed $\pi^\pm - \pi^0$ and a potential $\rho^\pm - \rho^0$ mass differences which reflect into different values for the width according to (8.13). The ρ mass dependence is not completely clear: one could consider a variation given by

$$\Gamma_\rho \sim k^3(M_\rho^2)/M_\rho^2 \tag{8.18}$$

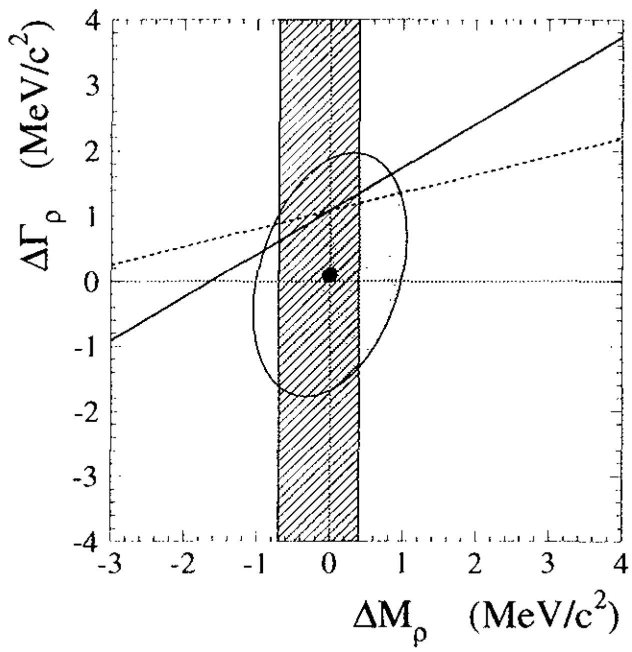

Figure 8.5: *Width difference* $\Delta\Gamma_{\rho(770)} = \Gamma_{\rho^\pm(770)} - \Gamma_{\rho^0(770)}$ *as a function of the difference in the* $\rho(770)$ *mass* $\Delta M_{\rho(770)} = M_{\rho^\pm(770)} - M_{\rho^0(770)}$. *The point is the measurement with its correlated one-sigma error ellipse. The dashed and solid lines show the expected dependences from Eqs.* (8.18) *and* (8.19), *respectively. The hatched area depicts the electromagnetic* ρ *mass difference predicted in* [206].

or, as argued in *Chiral Pertürbation Theory* [205],

$$\Gamma_\rho \sim k^3(M_\rho^2)\ . \qquad (8.19)$$

According to the charge of the ρ, the pion momentum in the ρ rest system is given by $2k(M_{\rho^0}^2) = (M_{\rho^0}^2 - 4m_{\pi^\pm}^2)^{1/2}$ for the neutral ρ^0 and $2k(M_{\rho^\pm}^2) = [M_{\rho^\pm}^2 - 2(m_{\pi^\pm}^2 + m_{\pi^0}^2) + (m_{\pi^\pm}^2 - m_{\pi^0}^2)^2/M_{\rho^\pm}^2]^{1/2}$ for the charged $\rho^\pm$, respectively. The dashed and solid lines in Fig. 8.5 give the functional dependence of the width difference $\Delta\Gamma_\rho$ on ΔM_ρ in the approximations of Eqs. (8.18) and (8.19), respectively, normalised to the fitted value of Γ_ρ. A further discussion of isospin (CVC) violating contributions to the respective Γ_ρ's is given in Section 9.1.

It is interesting to observe that the measured ΔM_ρ is significantly smaller than the mass difference between charged and neutral pions $\Delta M_\pi = M_{\pi^\pm} - M_{\pi^0} = (4.5936 \pm 0.0007)$ MeV/c^2 [17], where the dominant effect is understood to be of electromagnetic origin ($\Delta M_\pi^{\rm em} \simeq 4.5$ MeV/c^2 [79]). The ΔM_ρ measurement can be compared to the (model dependent) result of $\Delta M_\rho = (-0.3 \pm 2.2)$ MeV/c^2 [17] obtained in hadronic production, however in good agreement with this determination. The Mark III Collaboration exploited data on $J/\psi \to \pi^+\pi^-\pi^0$ decays, dominated by $J/\psi \to \rho\pi$, to measure the mass difference of the charged and neutral ρ's [207]. Their preliminary result is found to be in good agreement with the result presented here. Note that the value deduced from the difference in the mean values taken from Ref. [17] $\langle M_{\rho^\pm} \rangle - \langle M_{\rho^0} \rangle = (-1.8 \pm 1.4)$ MeV/c^2 is potentially unreliable as they both represent the weighted mean of independent measurements using not necessarily the same parametrisations. A theoretical electromagnetic ρ mass difference of -0.7 MeV/$c^2 < \Delta M_\rho < 0.4$ MeV/c^2 in agreement with the measurement has recently been evaluated in Ref. [206]. The measured difference $\Delta\Gamma_\rho$ is found to be consistent with the expected isospin violation from the $\pi^\pm - \pi^0$ and $\rho^\pm - \rho^0$ mass differences.

8.4 Conclusions

The CVC property of the Standard Model provides the possibility to identify the τ vector decay channels with the isovector components of the e^+e^- hadronic final states by means of isospin symmetry. The $\pi^+\pi^-$ and $\pi^+\pi^-\pi^+\pi^-$ cross sections measured in e^+e^- annihilation have been found to be in good agreement with the respective $\pi^-\pi^0$ and $\pi^-3\pi^0$ spectral functions. The $\pi^+\pi^-\pi^0\pi^0$ cross section has been compared to the corresponding linear combination of $\pi^-3\pi^0$ and $2\pi^-\pi^+\pi^0$ spectral functions from τ decays. Above 2 GeV/c^2, τ data points are significantly higher than the respective e^+e^- measurements (DM2). This is thought to be due to a disagreement in the non-resonant contribution as a good agreement with DM2 for the resonant ($\omega\pi$) part of the cross section has recently been found by the ALEPH Collaboration [5].

Fits of the pion form factor based on the Kühn-Santamaria [164] and the Gounaris-Sakurai [200] parametrisations have been performed. In this framework, the existence of an additional $\rho(1450)$ contribution is firmly established in τ decays. The fit using the GS parametrisation resulted in a better description of τ data yielding a χ^2 of 54 over 65 degrees of freedom. The parameters of the dominant $\rho(770)$ contribution found in this fit are: $M_{\rho^\pm(770)} = (776.4 \pm 0.9)$ MeV/c^2 and $\Gamma_{\rho^\pm(770)} = (150.5 \pm 1.6)$ MeV/c^2.

A combined fit to τ and e^+e^- data has been performed in order to measure the difference in mass and width between the dominant charged and neutral $\rho(770)$ amplitudes, expected to be generated by isospin-violating effects. The observed mass difference $M_{\rho^\pm(770)} - M_{\rho^0(770)} = (0.0 \pm 1.0)$ MeV/c^2 is significantly smaller than the corresponding value for the pions, while the width difference $\Gamma_{\rho^\pm(770)} - \Gamma_{\rho^0(770)} = (0.1 \pm 1.9)$ MeV/c^2 is consistent with isospin violation from the $\pi^\pm - \pi^0$ and $\rho^\pm - \rho^0$ mass differences.

Chapter 9

The Hadronic Contribution to the Muon $(g-2)$ and to $\alpha(M_Z^2)$

The contribution from hadronic loops to the muon anomalous magnetic moment and to the running of the QED fine structure constant α at low energy cannot be calculated with current QCD methods. Via dispersion relations these contributions are related to absorptive parts of current-current corelators which those are proportional to e^+e^- annihilation cross section measurements and τ vector spectral functions (see Section 1.3.3). The low energy hadronic contribution can therefore directly be computed from experimental data. By virtue of the good quality of τ spectral functions one can expect a considerable improvement in the precision of the above quantities when including τ data into the current analysis based on e^+e^- cross sections only. The results presented here are published in Ref. [208].

Introduction

The anomalous magnetic moment $a_\mu = (g-2)/2$ of the muon, defined through its deviation from the bare magnetic moment obtained for the spin half muon from the solution of the Dirac equation, is experimentally and theoretically known to very high accuracy. The contribution of heavier objects to a_μ relative to the anomalous moment of the electron scales as $(m_\mu/m_e)^2 \sim 4 \times 10^4$. These properties allow an extremely sensitive test of the validity of QED and of additional contributions from strong and electroweak interactions. In order to achieve a deeper understanding of SM input parameters like, *e.g.*, the fermion masses, theories have been proposed which include new particles such as additional gauge bosons, supersymmetric partners of the known fermions or exited leptons related to speculations about compositness. The muon anomaly provides a stringent test for new theories beyond the Standard Model, since any new field (particle) which couples to the muon must contribute to a_μ. In principle the existence of new, heavier particles can be detected through their effects via virtual radiative processes on the behaviour of lighter observed particles, *i.e.*, on the muon $(g-2)$.

The present value from the combined μ^+ and μ^- measurements [209],

$$a_\mu = (11\,659\,230 \pm 85) \times 10^{-10} , \tag{9.1}$$

should to be improved to a precision of at least 4×10^{-10} by a forthcoming Brookhaven experiment [210][1] (BNL-E821). It is convenient to separate the prediction from the Standard Model (SM) $a_\mu^{\rm SM}$ into its different contributions

$$a_\mu^{\rm SM} = a_\mu^{\rm QED} + a_\mu^{\rm had} + a_\mu^{\rm weak} , \tag{9.4}$$

where

$$\begin{aligned} a_\mu^{\rm QED} &= \frac{\alpha}{2\pi} + 0.765857381(51)\left(\frac{\alpha}{\pi}\right)^2 + 24.050531(40)\left(\frac{\alpha}{\pi}\right)^3 \\ &\quad +126.02(42)\left(\frac{\alpha}{\pi}\right)^4 + 930(170)\left(\frac{\alpha}{\pi}\right)^5 \\ &= (11\,658\,470.6 \pm 0.2) \times 10^{-10} , \end{aligned} \tag{9.5}$$

is the pure electromagnetic contribution (see [212] and references therein), $a_\mu^{\rm had}$ is the contribution from hadronic vacuum polarization, and $a_\mu^{\rm weak} = (15.1 \pm 0.4) \times 10^{-10}$ [212, 213, 214] accounts for corrections due to the exchange of the weak interacting bosons up to two loops. Using the recent analysis of S. Eidelman and F. Jegerlehner [179] that found $a_\mu^{\rm had} = (702.4 \pm 15.3) \times 10^{-10}$, and applying fourth order corrections due to the exchange of additional photons and electron or quark loops (summarized by T. Kinoshita *et al.* [215] to $(-4.1 \pm 0.7) \times 10^{-10}$) one finds

$$a_\mu^{\rm SM} = (11\,659\,184 \pm 16) \times 10^{-10} . \tag{9.6}$$

---

[1] The principle of the measurement is simple: a muon beam is injected into a storage ring. The time dilatation provides an increase of the muon lifetime which allows a high number of orbits before the muons decay into electrons. The difference between the orbital cyclotron frequency ω_c and the spin precession frequency ω_s defines the precession frequency ω_a of the muon spin relative to its momentum which is proportional to the anomalous magnetic moment: $\omega_a = (eB/mc)a_\mu$. In accelerators where both magnetic and electric fields are present the precession frequency is given by

$$\omega_a = \frac{e}{mc}\left[a_\mu \mathbf{B} - \left(a_\mu - \frac{1}{\gamma^2 - 1}\right)\boldsymbol{\beta} \times \mathbf{E}\right] , \tag{9.2}$$

which is independent of the electric field $\mathbf{E}$ at the "magic" γ factor

$$\gamma = \sqrt{\frac{1}{a_\mu} + 1} \simeq 29.3 . \tag{9.3}$$

i.e., $|p_\mu| = 3.094$ GeV$/c$. One can thus achieve vertical focusing with electrostatic quadrupoles, and build the storage ring magnet to have a uniform dipole magnetic field to determine a_μ. This elimination of the magnetic field gradient (already established in the most recent CERN experiment [211]) which previously was required for focusing, permits a significant improvement in accuracy. The spin precession ω_a is reconstructed from the direction and the number of electrons emitted from the decaying muons as a function of the time and the muon lifetime. It is of crucial importance for the subsequent determination of a_μ to precisely know the value of the magnetic field B to an accuracy better than 4×10^{-7}!

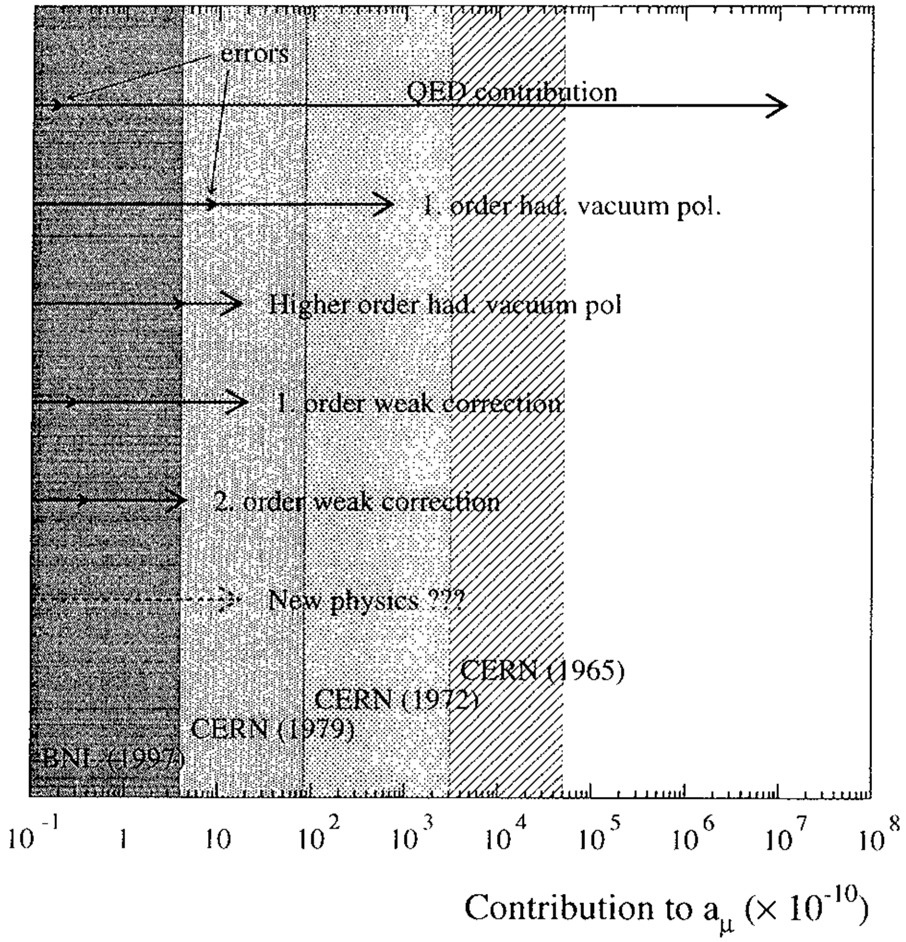

Figure 9.1: *Contributions and uncertainties to* a_μ *from pure QED, QCD and electroweak interactions, where for the hadronic contribution the result obtained in this analysis is used. The shaded areas depict the sensitivities of past CERN experiments and the design value of BNL-E821.*

Comparing the errors of the respective contributions to $a_\mu^{\rm SM}$ reveals that its total uncertainty is clearly dominated by the leading order vacuum polarization correction $a_\mu^{\rm had}$, originating from a quark-loop insertion into the muon vertex correction diagram as shown in Figure 9.2. The different contributions to a_μ and their uncertainties are shown in Fig. 9.1. In particular, it is annoying that the error on the hadronic contribution is of the same order of magnitude as $a_\mu^{\rm weak}$ which to test is the aim of the BNL-E821 experiment.

In this chapter, a new evaluation of the hadronic vacuum polarization contribution to a_μ and also to the running of the QED fine structure constant $\alpha(s)$ from low energy to the mass of the Z boson is presented. In addition to using the complete and in comparison with previous analyses slightly enlarged experimental information on e^+e^- annihilation data, the new data from hadronic τ decays are incorporated which provide a more precise description of the hadronic contributions at energies less than 1.5 GeV. Attention is brought to the straightforward and statistically well-defined averaging procedure and error propagation used, which takes into account full systematic correlations between the cross section measurements. Much care has been put into the treatment of unmeasured final states which are bound via isospin constraints.

9.1 Hadronic Vacuum Polarization in γ and W propagators

As QCD is a non-Abelian theory with massless gauge bosons, its perturbative expansion at low energies is not well-behaved and non-perturbative effects lead to currently unpredictable long distance resonance phenomena in quark interactions. Fortunately, cross sections measured in e^+e^- annihilation and spectral functions from τ decays provide an experimental access to the hadronic vacuum polarization: from unitarity, the hadronic cross section of e^+e^- annihilation is related to the absorptive part of the vacuum polarization correlator via the optical theorem.

Similarly, hadronic spectral functions from τ decays are directly related to the isovector vacuum polarization currents when isospin invariance (CVC) and unitarity hold. For this purpose one has to worry whether the breakdown of CVC due to quark mass effects ($m_u \neq m_d$ generating $\partial_\mu J^\mu \sim (m_u - m_d)$ for a charge-changing hadronic current J^μ between u and d quarks) or unknown isospin-violating electromagnetic decays has non-negligible contributions within the present accuracy. However, the CVC predictions of τ branching ratios evaluated in Section 8.2 show reasonable agreement within about 5% experimental accuracy over the full range of exclusive vector hadronic final states. Expected deviations from CVC due to so-called *second class currents* as, *e.g.*, the decay $\tau^- \to \pi^- \eta \, \nu_\tau$ where the corresponding e^+e^- final state $\pi^0\eta$ (C=+1) is strictly forbidden, have estimated branching fractions of order of $(m_u - m_d)^2 \simeq 10^{-5}$ [216], while the experimental upper limit amounts to $\mathrm{B}(\tau \to \pi^- \eta \, \nu_\tau) < 1.4 \times 10^{-4}$ [17] with 95% CL. Another classical test is the pion β-decay, yielding a sensitivity to CVC violation of 3%: the CVC hypothesis relates the isovector, vector matrix element of the (severely suppressed) decay $\pi^- \to \pi^0 e^- \bar{\nu}_e$ (no axial-vector part) to the electromagnetic form F_π factor of the pion

$$\begin{aligned} \langle \pi^0(k')|J^\mu|pi^-(k)\rangle &\overset{\mathrm{CVC}}{=} -V_{ud}\sqrt{2}\langle \pi^0(k')|j^\mu_{\mathrm{em}}|pi^-(k)\rangle \\ &= -V_{ud}\sqrt{2}F_\pi\left((k-k')^2\right)(k+k')^\mu \ . \end{aligned} \tag{9.7}$$

The small mass difference of $m_{\pi^-} - m_{\pi^0} \simeq 4.6 \ \mathrm{MeV}/c^2$ permits to equate $F_\pi\left((k-k')^2\right) \simeq F_\pi(0) = 1$. The β-decay branching ratio can then be calculated with kinematic variables. Taking into account electromagnetic radiative corrections of order 1% one obtains the theoretical prediction [217] of $B_{\mathrm{CVC}}(\pi^- \to \pi^0 e^- \bar{\nu}_e) = (1.0482 \pm 0.0048) \times 10^{-8}$ which is in agreement with the most precise measurement [218] of $B(\pi^- \to \pi^0 e^- \bar{\nu}_e) = (1.026 \pm 0.039) \times 10^{-8}$.

An estimate of a possible CVC violation can be obtained in the $\pi\pi$ final state which is dominated by the $\rho(770)$ resonance. $SU(2)$ symmetry breaking can occur in the $\rho^\pm$ ρ^0 masses and widths caused by electromagnetic interactions. Hadronic contributions

Final states	$\frac{\Gamma_{\rho^\pm}-\Gamma_{\rho^0}}{\Gamma_\rho}$ $(\times 10^3)$	Ref.
$\pi\omega \to \pi\pi^0\gamma$	0.32	[219]
$\pi\gamma$	-0.34 ± 0.21	[17]
$\eta\gamma$	-0.38 ± 0.07	[17]
$\ell^+\ell^-$	-0.091 ± 0.004	[17]
$m_{\pi^\pm} - m_{\pi^0}$, $m_{\rho^\pm} - m_{\rho^0}$	6.3 ± 2.5	[17, 206]
$\pi\pi\gamma$	-3 ± 3	[219]
Sum	2.8 ± 3.9	

Table 9.1: *Expected CVC violation from electromagnetic interactions in $\rho^\pm$-ρ^0 decays.*

to the $\rho^\pm$-ρ^0 width difference are expected to be much smaller since they are proportional to $(m_u - m_d)^2$. The different electromagnetic contributions to the width are listed in Table 9.1: radiative transitions introduce a negligible effect, while the dominant contribution comes from the $\pi^\pm$-π^0 mass difference. A recent theoretical analysis [206] indicates that the $\rho^\pm$ and ρ^0 masses are in fact equal within 0.5 MeV/c^2: $m_{\rho^\pm} - m_{\rho^0} = -(0.15 \pm 0.55)$ MeV/c^2. This prediction has been verified in Section 8.3.3 with the result: $m_{\rho^\pm} - m_{\rho^0} = -(0.0 \pm 1.0)$ MeV/c^2. Since the π^- and π^0 mass difference is known experimentally [17] to be $m_{\pi^\pm} - m_{\pi^0} = (4.5936 \pm 0.0005)$ MeV/c^2 and understood theoretically [79] to be almost completely from electromagnetic origin, it is expected that the total $\rho^\pm$ and ρ^0 widths should be different even in the limit where hadronic interactions are $SU(2)$-invariant (this includes the chiral limit). An additional point concerns contributions from photon bremsstrahlung. While the infrared divergences in $\rho \to \pi\pi\gamma$ decays vanishes when including the vertex correction graphs, finite terms are expected to contribute differently to the widths of the charged and the neutral ρ. The corresponding bremsstrahlung graphs have been calculated in Ref. [219]. The width contributions from finite terms to both the $\rho^\pm$ and the ρ^0 turn out to be negative. The estimate of the width difference given in Tab. 9.1 assumes finite contributions to the widths from loop corrections to be small.

The total expected $SU(2)$ violation in the ρ width is finally computed from the above considerations to be

$$\frac{\Gamma_{\rho^\pm} - \Gamma_{\rho^0}}{\Gamma_\rho} = (2.8 \pm 3.9) \times 10^{-3} , \tag{9.8}$$

where the error comes essentially from the estimate of the $\rho^\pm$ ρ^0 mass difference and of the $\pi\pi\gamma$ contribution. This effect introduces corrections for a_μ^{had} and the running of $\alpha(s)$ when including τ data (see Section 9.6).

$$\delta a_\mu^{\mathrm{had}} = -(1.3 \pm 2.0) \times 10^{-10} \tag{9.9}$$

in the a_μ^{had} calculation from the $\tau^- \to \pi^-\pi^0\nu_\tau$ spectral function which is applied in the present analysis. Corrections from the higher mass resonances $\rho(1450), \rho(1700)$ are

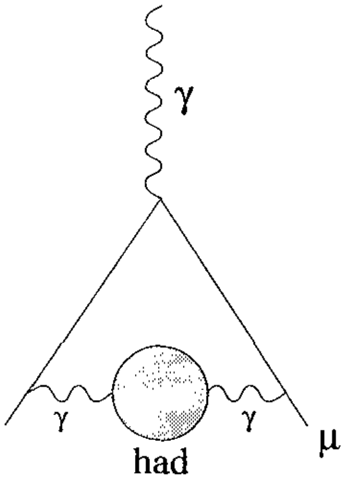

Figure 9.2: *Leading order hadronic vacuum polarization contribution to* a_μ.

expected to be negligible. Similarly a correction of

$$\delta\Delta\alpha_{\rm had}^{(5)}(M_Z^2) \; = \; -(0.09 \pm 0.12) \times 10^{-4} \tag{9.10}$$

is introduced in the calculation of the running of α.

From a more qualitative point of view, one should keep in mind that in this analysis the CVC hypothesis is applied at a very low energy scale where the absorptive parts of the matrix elements are largely dominated by non-perturbative QCD which are expected to factorize from their respective W or γ excitation.

However, electroweak radiative corrections must be taken into account. Their dominant contribution comes from the short distance correction to the effective four-fermion coupling $\tau^- \to (d\bar{u})^- \nu_\tau$. The radiative corrections are absorbed into an overall multiplicative factor $S_{\rm EW} = 1.0194 \pm 0.0040$ introduced in the definition of the spectral functions (1.22). The origin of $S_{\rm EW}$ and its error are discussed in Section 1.3.2 of Chapter 1.

9.1.1 Muon Magnetic Anomaly

By virtue of the analyticity of the vacuum polarization correlator, the contribution of the hadronic vacuum polarization to a_μ can be calculated via the dispersion integral [220]

$$a_\mu^{\rm had} \; = \; \frac{1}{4\pi^3} \int\limits_{4m_\pi^2}^{\infty} ds\, \sigma_{\rm had}(s)\, K(s) \; . \tag{9.11}$$

Here $\sigma_{\rm had}(s)$ is the total $e^+e^- \to$ hadrons cross section as a function of the c.m. energy-squared s, and $K(s)$ denotes the QED kernel

$$K(s) \; = \; x^2\left(2 - \frac{x^2}{2}\right) + (1+x)^2\left(1 + \frac{1}{x^2}\right)\left(\ln(1+x) - x + \frac{x^2}{2}\right) + \frac{(1+x)}{(1-x)}x^2 \ln x \tag{9.12}$$

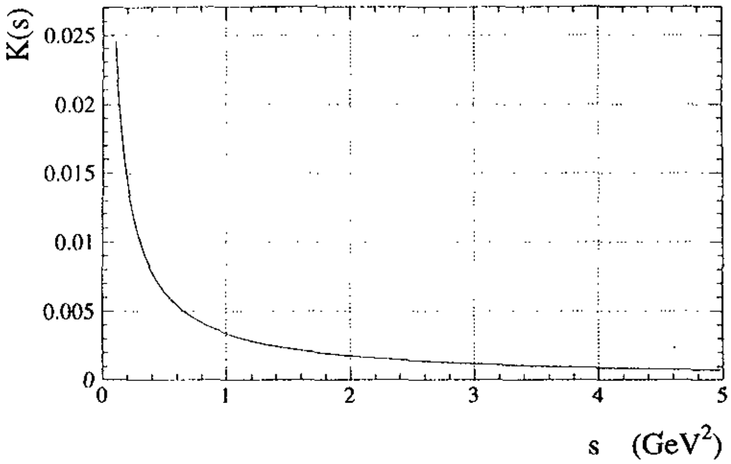

Figure 9.3: *Electromagnetic kernel-function $K(s)$ multiplying the cross section in the dispersion integral* (9.11).

with $x = (1-\beta_\mu)/(1+\beta_\mu)$ and $\beta = (1-4m_\mu^2/s)^{1/2}$ (see also remarks concerning the numerical stability of $K(s)$ in Ref. [179]). The function $K(s)$ decreases monotonically with increasing s (Fig. 9.3). It gives a strong weight to the low energy part of the integral (9.11). About 91% of the total contribution to $a_\mu^{\rm had}$ is accumulated at c.m. energies $\sqrt{s}$ below 2.1 GeV while 72% of $a_\mu^{\rm had}$ is covered by the two-pion final state which is dominated by the $\rho(770)$ resonance. The precise spectrum of the two-pion final state from τ data as well as new input for the more controversial four-pion final states should therefore help to significantly improve the $a_\mu^{\rm had}$ determination.

9.1.2 Running of the QED Fine Structure Constant

In the same spirit one can evaluate the hadronic contribution $\Delta\alpha(s)$ to the renormalized vacuum polarization function $\Pi'_\gamma(s)$ which governs the running of the electromagnetic fine structure constant $\alpha(s)$. For the spin 1 photon, $\Pi'_\gamma(s)$ is given by the Fourier transform of the contraction of the electromagnetic currents $j^\mu_{\rm em}(s)$ in the vacuum $(q^\mu q^\nu - q^2 g^{\mu\nu})\,\Pi'_\gamma(q^2) = i\int d^4x\, e^{iqx}\langle 0|T(j^\mu_{\rm em}(x)j^\nu_{\rm em}(0))|0\rangle$. With $\Delta\alpha(s){=}-4\pi\alpha\,{\rm Re}\left[\Pi'_\gamma(s) - \Pi'_\gamma(0)\right]$, one has

$$\alpha(s) = \frac{\alpha(0)}{1-\Delta\alpha(s)}\,, \qquad (9.13)$$

where $4\pi\alpha(0)$ is the square of the electron charge in the long-wavelength Thomson limit. The contribution $\Delta\alpha(s)$ can naturally be subdivided in a leptonic and a hadronic part. Furthermore, at $s = M_Z^2$ it is appropriate to separate the leading vacuum polarization contribution involving the five light quarks u, d, s, c, b from the top quark contribution since the latter cannot be calculated in the light fermion approximation.

The leading order leptonic contribution is given by

$$\Delta\alpha_{\rm lep}(M_Z^2) = \frac{\alpha(0)}{3\pi}\sum_\ell \frac{\alpha}{3\pi}\left[-\frac{5}{3} + \beta_\ell^2 - \frac{1}{2}\beta_\ell(3-\beta_\ell^2)\ln\left(\frac{1-\beta_\ell}{1+\beta_\ell}\right)\right]$$

$$\begin{aligned} &= \frac{\alpha(0)}{3\pi} \sum_{\ell} \left[\ln \frac{s}{m_\ell^2} - \frac{5}{3} + \mathcal{O}\left(\frac{m_\ell^2}{s}\right) \right] \\ &= 314.2 \times 10^{-4} \quad (s \equiv M_Z^2) \; . \end{aligned} \tag{9.14}$$

Using analyticity and unitarity, the dispersion integral for the contribution from the light quark hadronic vacuum polarization $\Delta\alpha^{(5)}_{\rm had}(M_Z^2)$ reads [221]

$$\Delta\alpha^{(5)}_{\rm had}(M_Z^2) = -\frac{M_Z^2}{4\pi^2\alpha} \, {\rm Re} \int\limits_{4m_\pi^2}^{\infty} ds \, \frac{\sigma_{\rm had}(s)}{s - M_Z^2 - i\epsilon} \; , \tag{9.15}$$

where $\sigma(s) = 16\pi^2\alpha^2(s)/s \cdot {\rm Im}\Pi'_\gamma(s)$ from the optical theorem, and ${\rm Im}\Pi'_\gamma$ stands for the absorptive part of the hadronic vacuum polarization correlator. In contrast to $a_\mu^{\rm had}$, the integration kernel favours cross sections at higher masses. Hence, the improvement when including τ data is expected to be small.

The top quark contribution can be calculated using the next-to-next-to-leading order α_s^3 prediction of the total inclusive cross section ratio R, defined as

$$R(s) = \frac{\sigma_{\rm tot}(e^+e^- \to \text{hadrons})}{\sigma(e^+e^- \to \mu^+\mu^-)} = \frac{3s}{4\pi\alpha^2}\sigma_{\rm tot} \; , \tag{9.16}$$

from perturbative QCD using $\overline{\rm MS}$ [95, 179]:

$$\begin{aligned} R_{\rm pert}(s) = {} & 3\sum_f \left[Q_f^2 \left(1 - \frac{4m_f^2}{s}\right)^{1/2} \left(1 + \frac{2m_f^2}{s}\right) \right] \left[1 + \frac{\alpha_s(s)}{\pi} + F_3 \left(\frac{\alpha_s(s)}{\pi}\right)^2 + F_4 \left(\frac{\alpha_s(s)}{\pi}\right)^3 \right] \\ & - \left(\sum_f Q_f\right)^2 F_4' \left(\frac{\alpha_s(s)}{\pi}\right)^3 \; . \end{aligned} \tag{9.17}$$

The coefficients F_3 and F_4 are taken from Eqs. (2.65) for n_f active flavours. The last term $\sim F_4(\sum_f Q_f)^2$ with $F_4' = 1.2395$ stems from "light-by-light" scattering diagrams with three internal photon lines. The m_f dependent factors in Eq. (9.17) accounts for phase space suppression near the $f\bar{f}$ production threshold. The evaluation of the integral (9.15) with $m_{\rm top} = 175$ GeV and the running strong coupling constant fixed at $\alpha_s(M_Z^2) = 0.121$ yields $\Delta\alpha_{\rm top}(M_Z^2) = -0.6 \times 10^{-4}$.

Using $\Delta\alpha^{(5)}_{\rm had}(M_Z^2) = (280 \pm 7) \times 10^{-4}$ [179], one obtains

$$\alpha^{-1}(M_Z^2) = 128.890 \pm 0.090 \; . \tag{9.18}$$

Again, the error is dominated by the hadronic vacuum polarization part that is not calculable within perturbative QCD.

9.2 The Integration Procedure

The information used for the evaluation of the integrals (9.11) and (9.15) comes mainly from direct measurements of the cross sections in e^+e^- annihilation and via CVC from

τ spectral functions. The integrals themselves are evaluated using the trapezoidal rule, *i.e.*, combining adjacent measurement points by straight lines. Even if this method is straightforward and free from theoretical constraints (other than CVC in the τ case), its numerical calculation requires special care. The combination of measurements from different experiments taking into account correlations – both inside each data set and between different experiments are subjected to additional studies and discussions.

9.2.1 Averaging Data from different Experiments

In order to exploit the maximum information, weighted averages of different experiments at a given energy are calculated instead of evaluating separately the integrals for every experiment and finally averaging them[2]. Generally, if different measurements at a given c.m. energy show inconsistencies, *i.e.*, their χ^2 per degree of freedom (dof) is larger than one, the error of their weighted average is rescaled with $\sqrt{\chi^2/\mathrm{dof}}$.

The solution of the averaging problem is found using a correlated χ^2 minimization, defining

$$\chi^2 = \sum_{n=1}^{N_{\rm exp}} \sum_{i,j=1}^{N_n} (x_i^n - k_i)\,(C_{ij}^n)^{-1}\,(x_j^n - k_j)\ , \tag{9.19}$$

where x_i^n is the ith cross section measurement of the nth experiment in a given final state, C_{ij}^n is the covariance between the ith and the jth measurement and k_i is the unknown distribution. The covariance matrix C^n is given by

$$C_{ij}^n = \begin{cases} (\Delta_{i,\rm stat}^n)^2 + (\Delta_{i,\rm sys}^n)^2 & \text{for } i = j \\ \Delta_{i,\rm sys}^n \cdot \Delta_{j,\rm sys}^n & \text{for } i \neq j \end{cases} \quad , \quad i,j = 1,\ldots,N_n\ , \tag{9.20}$$

where $\Delta_{i,\rm stat}^n$ ($\Delta_{i,\rm sys}^n$) denotes the statistical (systematic) error of x_i^n. The systematic errors of the e^+e^- annihilation measurements are essentially due to luminosity and efficiency uncertainties. The minimum condition $d\chi^2/dk_i = 0$, $\forall i$ leads to the linear equation problem

$$\sum_{n=1}^{N_{\rm exp}} \sum_{j=1}^{N_n} (x_j^n - k_j)\,(C_{ij}^n)^{-1} = 0\ , \qquad i = 1,\ldots,N_n\ . \tag{9.21}$$

The inverse covariance $\tilde{C}_{ij}^{-1}$ between the solutions k_i, k_j is the sum over the inverse covariances of every experiment

$$\tilde{C}_{ij}^{-1} = \sum_{n=1}^{N_{\rm exp}} (C_{ij}^n)^{-1}\ . \tag{9.22}$$

---

[2] One could imagine two experiments a and b, each with two independent measurements $a_1(E_1) \pm \Delta a_1$, $a_2(E_2) \pm \Delta a_2$ and $b_1(E_1) \pm \Delta b_1$, $b_2(E_2) \pm \Delta b_2$ at energies $E_1 \neq E_2$. Setting $\Delta a_1 = \Delta a_2 = \Delta b_1 = \Delta b_2$ leads to identical errors in both integration methods. However, non-symmetric errors as, *e.g.*, $\Delta a_1/2 = 2\Delta a_2 = 2\Delta b_1 = \Delta b_2/2$ propagate a 53% larger uncertainty when calculating independently the sum over the points (trivial integration) of the experiments a, b and averaging afterwards rather than averaging $\langle a_1, b_1\rangle$ and $\langle a_2, b_2\rangle$ first, *i.e.*, keeping the energy information of the respective points in the average.

One should be aware of a potential bias when using least squared minimization techniques in the presence of overall normalization uncertainties [202] (see Section 8.3). In order to demonstrate that the solutions k_i of the linear equation (9.21) are unbiased, consider the following situation: two experiments X, Y have each measured two cross sections x_1, x_2 and y_2, y_3, where x_2 and y_2 overlap at the same energy and are going to be averaged. The solution distribution k_i therefore contains three measurements $i = 1, 2, 3$ which consists essentially of the points x_1, y_3 and the average $\langle x_2, y_2\rangle$. The covariance matrices of the experiments, taken from Eq. (9.20) are ($a \equiv x,\ y$)

$$C^a = \begin{pmatrix} \Delta a_{1,\mathrm{stat}}^2 + \Delta a_{1,\mathrm{sys}}^2 & \Delta a_{1,\mathrm{sys}}\,\Delta a_{2,\mathrm{sys}} \\ \Delta a_{1,\mathrm{sys}}\,\Delta a_{2,\mathrm{sys}} & \Delta a_{2,\mathrm{stat}}^2 + \Delta a_{2,\mathrm{sys}}^2 \end{pmatrix}, \tag{9.23}$$

so that the solutions k_i of (9.21) for the three remaining measurements take the form

$$\begin{aligned} k_1 &= x_1 + (y_2 - x_2)\,\frac{\Delta x_{1,\mathrm{sys}}\,\Delta x_{2,\mathrm{sys}}}{\delta_{2,\mathrm{tot}}^2} \\ k_2 &= x_2\,\frac{\Delta y_{2,\mathrm{stat}}^2 + \Delta y_{2,\mathrm{sys}}^2}{\delta_{2,\mathrm{tot}}^2} + y_2\,\frac{\Delta x_{2,\mathrm{stat}}^2 + \Delta x_{2,\mathrm{sys}}^2}{\delta_{2,\mathrm{tot}}^2} \\ k_3 &= y_3 + (x_2 - y_2)\,\frac{\Delta y_{3,\mathrm{sys}}\,\Delta y_{2,\mathrm{sys}}}{\delta_{2,\mathrm{tot}}^2} \end{aligned} \tag{9.24}$$

with $\delta_{2,\mathrm{tot}}^2 = \Delta x_{2,\mathrm{stat}}^2 + \Delta x_{2,\mathrm{sys}}^2 + \Delta y_{2,\mathrm{stat}}^2 + \Delta y_{2,\mathrm{sys}}^2$. Eq. (9.24) becomes the simple uncorrelated solution if systematic errors are absent. Due to the initial correlation between the measurements, the averaging of x_2 and y_2 readjusts the points x_1, y_3 too. One concludes from Eq. (9.24) that the presence of correlated systematic errors naturally influences the solution, but does not bias it.

However, direct correlations from normalization uncertainties occurring between the experiments as described in the next paragraph would indeed bias the averaging procedure. They are therefore subsequently added into the solution covariance matrix (9.22).

9.2.2 Correlations between Experiments

Eq. (9.22) provides the covariance matrix needed for the error propagation when calculating the integrals over the solutions k_i from Eq. (9.21). Up to this point, $\tilde{C}_{ij}$ only contains correlations between the systematic uncertainties within the same experiment. However, due to commonly used simulation techniques for acceptance and luminosity determinations as well as state-of-the-art calculations of radiative corrections, systematic correlations from one experiment to another cannot be excluded. It is clearly a difficult task to reasonably estimate the amount of such correlations as they depend on the capabilities of the contributing experiments and one's theoretical understanding of the dynamics of the respective final states. In general, one can state that in older experiments, where only parts of the total solid angle were covered by the detector acceptance, individual experimental limitations should dominate the systematic uncertainties. Potentially common systematics, such as radiative corrections or efficiency, acceptance and luminosity calculations based on the Monte Carlo simulation, play only minor roles. The correlations between systematic errors below 2 GeV c.m. energy are therefore estimated to be between 10% and 30%, with the exception of the $\pi^+\pi^-$ final state, where a 40% correlation due to the easier experimental situation and the better knowledge of the dynamics is imposed, which leads to non-negligible systematic contributions from the uncertainties of the radiative corrections. At energies above 2.1 GeV the experiments measured the total inclusive cross section ratio R. Between 2.1 and 3.1 GeV, individual technical problems dominate the systematic uncertainties. At higher energies, new experiments provide nearly full geometrical acceptance which decreases the uncertainty of efficiency estimations. Radiative corrections as well as theoretical errors of the luminosity determination give important contributions to the final systematic errors quoted by the experiments. The correlations between the systematic errors of the experiments are therefore estimated to be negligible between 2 GeV and 3 GeV, 20% between 3 GeV and 10 GeV, and 30% above 10 GeV.

These correlation coefficients are added to all those entries of $\tilde{C}_{ij}$ from Eq. (9.22) which involve two different experiments.

9.2.3 Inclusion of τ Data

In this analysis, data from the τ decays $\tau^- \to \pi^-\pi^0\,\nu_\tau$, $\tau^- \to \pi^-3\pi^0\,\nu_\tau$ and $\tau^- \to 2\pi^-\pi^+\pi^0\,\nu_\tau$ are used in addition to the common e^+e^- data sets. Assuming isospin invariance to hold, the corresponding e^+e^- isovector cross sections are calculated via the CVC relations (8.1), (8.2) and (8.3). The τ spectral functions v_1, defined in Eq. 1.22, are given as binned continous distributions of the mass-squared s. In each bin i, the spectral function $v_1(s_i)$ contains the (normalized) invariant mass spectrum $\Delta N_i/N$, integrated over the bin width ds_i. On the contrary e^+e^- cross sections are measured at discrete energy settings. To each e^+e^- measurement is associated a τ cross section value obtained by interpolating between adjacent bins. This interpolation takes into account the correlations between the bins and is achieved imposing a functional form obtained from a fit to Breit-Wigner resonances using the Gounaris-Sakurai parametrization [200] (see Section 8.3). However, the fit function is renormalized in each bin so that its integral over the width of each bin corresponds to the measured CVC cross section for that bin. All the data points – τ, e^+e^- and interpolated τ values – are injected with their correlations into Eqs. (9.21) and (9.22).

Due to the high bin-to-bin correlations of the τ data and the significant normalization uncertainty coming from the τ hadronic branching ratios, biases of the least-square minimization (see Section 8.3) cannot be excluded. The average solution is therefore calculated twice, *i.e.*, with and without correlations, taking the mean value of both integrations as the result and adding half of the total difference as systematic error. This is done in all cases where τ data are involved. The effect amounts to about 10% of the total error.

9.2.4 Evaluation of the Integral

The procedure described above provides the weighted average and the covariance of the cross sections from different experiments contributing to a certain final state in a given range of c.m. energies. Now, the trapezoidal rule is applied. In order to perform the integrations (9.11) and (9.15), the integration range is subdivided into N_H sufficiently small energy steps and the corresponding covariance is calculated for each of these steps (where additional correlations induced by the trapezoidal rule has to be taken into account). The new high-binned covariance matrix C^H reads then

$$C_{kl}^{H} = \sum_{i,j=1}^{N-1} D_{k,i}\tilde{C}_{ij}D_{l,j} \ , \quad k,l = 1,\ldots,N_H \ , \tag{9.25}$$

with the derivatives

$$\left.\begin{array}{rcl} D_{k,i} & = & (\tilde{s}_{i+1} - s_k^H)/(\tilde{s}_{i+1} - \tilde{s}_i) \\ D_{k,i+1} & = & -(\tilde{s}_i - s_k^H)/(\tilde{s}_{i+1} - \tilde{s}_i) \end{array}\right\} \ \forall k : \ \tilde{s}_i \leq s_k^H < \tilde{s}_{i+1} \tag{9.26}$$

and $D_{k,i} = 0$ elsewhere. $\tilde{C}_{ij}$ is the average covariance matrix (9.22) and the $\tilde{s}_i$ are the energies corresponding to the entries in $\tilde{C}_{ij}$, while the s_k^H denote the energies corresponding to the new high-binned covariance matrix C_{kl}^H. This procedure yields error envelopes between adjacent measurements as depicted by the shaded bands in Figs. 9.6 and 9.7. The integrals (9.11) and (9.15) can now easily be calculated from the new high-binned distribution and their errors are obtained by gaussian propagation of the covariance matrix C^H.

9.3 Radiative Corrections

Higher order radiative corrections bias the measurements of both cross sections in e^+e^- annihilation and invariant mass spectra from τ hadronic decays. The e^+e^- experiments generally correct the measured cross section for QED effects, including bremsstrahlung, vacuum polarization and higher order self-energy graphs (see references in [179]). Following the prescription of Ref. [179], all inclusive cross section measurements R at masses below the J/ψ resonance are multiplied by the (small) correction factor $(1 + \Delta\alpha_{\rm lep}(s))(\alpha/\alpha(s))^2$ in order to account for the missing correction for hadronic vacuum polarization.

In τ decays, final state radiation from the τ itself or from its decay products can influence the invariant mass measurement. Due to the high mass of the τ lepton, the bremsstrahlung graph is largely suppressed. Both types of radiation are included in the Monte Carlo simulation program KORALZ [140, 141, 142], used to unfold the measured distributions from detector resolution and physical (higher order) effects. Even if the actual frequency with which final state radiation occurs or if its energy was not well simulated in the Monte Carlo, reconstructed photons found to originate from radiation of the τ decay [24] are included in the invariant mass determination, and thus do not bias the measurement.

Electroweak radiative corrections are applied through the CVC correction factor $S_{\rm EW}$ defined in Eq. (1.25).

9.4 The Origin of the Data

The exclusive low energy e^+e^- cross sections have mainly been measured by experiments working at e^+e^- colliders in Novosibirsk and Orsay. Due to the high hadron multiplicity at energies above 2.5−−3.1 GeV, the exclusive measurement of the respective hadronic final states is not practicable. Consequently, the experiments at the high energy colliders DORIS and PETRA (DESY) and PEP (SLAC) have measured the total inclusive cross section ratio R. Some of the e^+e^- data used have here already been mentioned in Section 8.1. Nevertheless, for sake of completeness they are contained in the following compilation:

> The $e^+e^- \to \pi^+\pi^-$ measurements are taken from OLYA [169, 170], TOF [171], NA7 [172], CMD [169], DM1 [173] and DM2 [174]. In addition, the new $\pi^-\pi^0$ τ spectral function is used, normalized to the world average branching ratio $\mathrm{B}(\tau^- \to \pi^-\pi^0\,\nu_\tau) = (25.24 \pm 0.16)\%$ [17]. According to Eq. (8.1), τ data provide only the dominant isovector part of the total two-pion cross section. A correction due to the small isospin-violating isoscalar $\omega \to \pi^+\pi^-$ final state, which interferes with the isovector amplitude, is applied. A small correction for the missing, *i.e.*, unmeasured decay modes $\rho \to \pi^0\gamma$ (only for e^+e^- data) and $\rho \to \eta\gamma$, is added.
>
> The reaction $e^+e^- \to \pi^+\pi^-\pi^0$ is dominated by ω and ϕ intermediate resonances. In the peak region of these resonances analytic parametrizations of the cross sections are used. The non-resonant data are taken from ND [182], M2N [191], M3N [190], DM1 [222] and DM2 [223]. Corrections for the missing ω and ϕ decay modes are applied.
>
> The $e^+e^- \to \pi^+\pi^-\pi^0\pi^0$ data are available from OLYA [181], ND [182], M2N [191], DM2 [187, 194, 188, 189] and M3N [190]. According to Eq. (8.3), a linear combination of both four-pion τ decay channels connects the corresponding spectral functions with the above e^+e^- final state. The branching ratios $\mathrm{B}(\tau^- \to 2\pi^-\pi^+\pi^0\,\nu_\tau) = (4.25 \pm 0.09)\%$ and $\mathrm{B}(\tau^- \to \pi^-3\pi^0\,\nu_\tau) = (1.14 \pm 0.14)\%$ [17] are used as respective normalizations.
>
> The reaction $e^+e^- \to \omega\pi^0$ is mainly reconstructed in the $\pi^+\pi^-\pi^0\pi^0$ final state. It was studied by the collaborations ND [182] and DM2 [188]. Corrections for the missing ω decay modes are applied.
>
> The $e^+e^- \to \pi^+\pi^-\pi^+\pi^-$ final state was studied by the experiments OLYA [181], ND [182], MEA [183], CMD [184], DM1 [185, 186], DM2 [187, 188, 189] and M3N [190]. The corresponding spectral function from $\tau^- \to \pi^-3\pi^0\,\nu_\tau$ (according to Eq. (8.2)) is also used.
>
> The $e^+e^- \to \pi^+\pi^-\pi^+\pi^-\pi^0$ final state is taken from M3N [190] and CMD [184]. The other five-pion mode $e^+e^- \to \pi^+\pi^-3\pi^0$ can be accounted for using the rigourous isospin relation $\sigma_{\pi^+\pi^-3\pi^0} = 0.5 \times \sigma_{\pi^+\pi^-\pi^+\pi^-\pi^0}$.

For the reaction $e^+e^- \to \omega\pi^+\pi^-$, measured by the groups DM1 [185] and DM2 [184], a correction for ω decays other than into three pions which appear in the five-pion final state is applied.

The $e^+e^- \to \pi^+\pi^-\eta$ data were studied by ND [182] and DM2 [192]. One must subtract from the cross section the contributions which are already counted in the $\pi^+\pi^-\pi^+\pi^-\pi^0$ and $\pi^+\pi^-3\pi^0$ finale states.

The cross sections of the six-pion final states $3\pi^+3\pi^-$ and $2\pi^+2\pi^-2\pi^0$ were measured by DM1 [193], M3N [190] CMD [184] and DM2 [194]. In Section 8.1 an upper limit for the unknown $\pi^-\pi^+4\pi^0$ cross section of $\sigma_{\pi^+\pi^-4\pi^0} \leq (3/2) \times \sigma_{2\pi^-2\pi^+2\pi^0} - (9/24) \times \sigma_{3\pi^-3\pi^+}$ was derived using isospin constraints. Half of this upper limit is taken as the estimated contribution, with an error of 100%.

The $e^+e^- \to \mathrm{K}^+\mathrm{K}^-$ and $e^+e^- \to \mathrm{K}^0_\mathrm{S}\mathrm{K}^0_\mathrm{L}$ cross sections are taken from OLYA [224], DM1 [225] and DM2 [226].

The reactions $e^+e^- \to \mathrm{K}^0_\mathrm{S}\,\mathrm{K}^+\pi^-$ and $e^+e^- \to \mathrm{K}^+\mathrm{K}^-\pi^0$ were studied by DM1 [199, 227] and DM2 [187]. Using isospin symmetry the cross section of the final state $\mathrm{K}^0_\mathrm{S}\mathrm{K}^0_\mathrm{L}\pi^0$ is obtained from the relation $\sigma_{\mathrm{K}^0_\mathrm{S}\mathrm{K}^0_\mathrm{L}\pi^0} = \sigma_{\mathrm{K}^+\mathrm{K}^-\pi^0}$.

The inclusive reaction $e^+e^- \to \mathrm{K}^0_\mathrm{S}+X$ was analyzed by DM1 [198]. From it, one can estimate the total $\mathrm{K}\bar{\mathrm{K}}\pi\pi$ contribution (this time for both $I = 1$ and $I = 0$) as described in Section 8.1.

At higher energy the total cross section ratio R is measured inclusively. Data provided by the experiments $\gamma\gamma2$ [228], MARK I [229], DELCO [230], DASP [231], PLUTO [232], LENA [233], Crystal Ball [234], MD-1 [235], CELLO [236], JADE [237], MARK-J [238], TASSO [239], CLEO [240], CUSB [241] and MAC [242] are used in this analysis. Above 3.5 GeV the measurements of the MARK I Collaboration are significantly higher than those from LENA, PLUTO and Crystal Ball. In addition, the QCD prediction of R, which should be reliable in this energy regime, favours lower values. In agreement with Ref. [179], MARK I data are neglected above this energy threshold.

Although small, the enhancement of the cross section due to $\gamma - \mathrm{Z}$ interference is corrected for c.m. energies above the J/ψ mass. Using the factorial ansatz according to Ref. [243, 179], yields a negligible contribution to a_μ^{had} and a -0.30×10^{-4} shift of $\Delta\alpha^{(5)}_{\mathrm{had}}(M_Z^2)$.

Fig. 9.4 shows as an example the cross sections for the three-, five- and six-pion final states and for $e^+e^- \to \mathrm{K}^+\mathrm{K}^-$. The inclusive crossection ratio R is plotted in Fig. 9.5 together with the QCD perturbative prediction from Eq. 9.17 for $\alpha_s(M_Z)$=0.1200 ± 0.0013.

9.5 Analytical Contributions

In some energy regions where data information is scarce and/or reliable theoretical predictions are available, analytical contributions to extend the experimental integral are

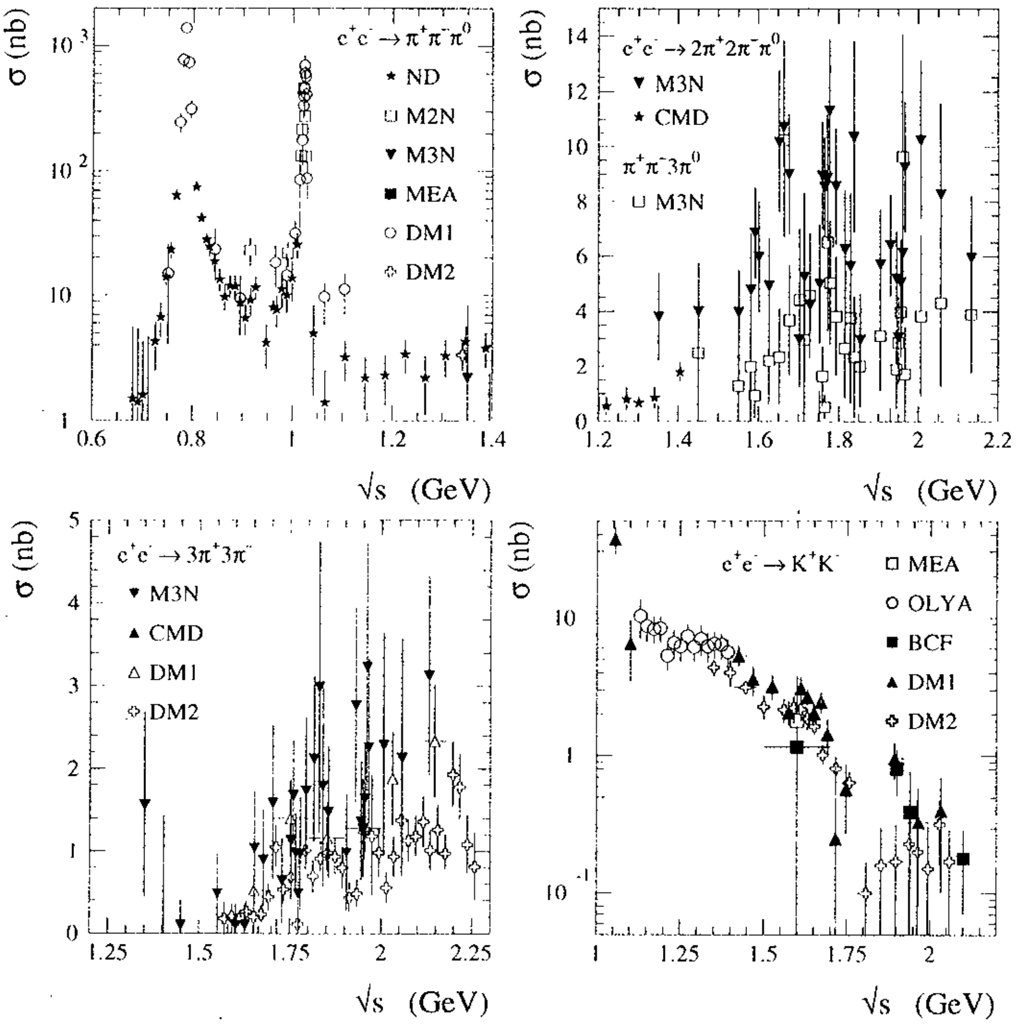

Figure 9.4: *Cross sections of the e^+e^- final states $\pi^+\pi^-\pi^0$, $(5\pi)^0$, $3\pi^+3\pi^-$ and K^+K^- versus the c.m. energy $\sqrt{s}$. From isospin symmetry one expects $\sigma_{\pi^+\pi^-3\pi^0} = 0.5\times\sigma_{\pi^+\pi^-\pi^+\pi^-\pi^0}$ (upper right hand plot).*

used.

9.5.1 The $\pi^+\pi^-$ Threshold Region

To overcome the lack of data at threshold energies, the second order expansion Eq. (8.4) obtained from *Chiral Perturbation Theory* [178] is used as a description of the pion form factor F_π (which is connected with the two-pion cross section via Eq. (1.31).

9.5.2 Narrow Resonances

The e^+e^- annihilation cross section involves narrow resonances such as the $\omega(782)$ and $\phi(1020)$ at low energies, the J/ψ and Υ resonances at the $c\bar{c}$ and $b\bar{b}$ quark thresholds,

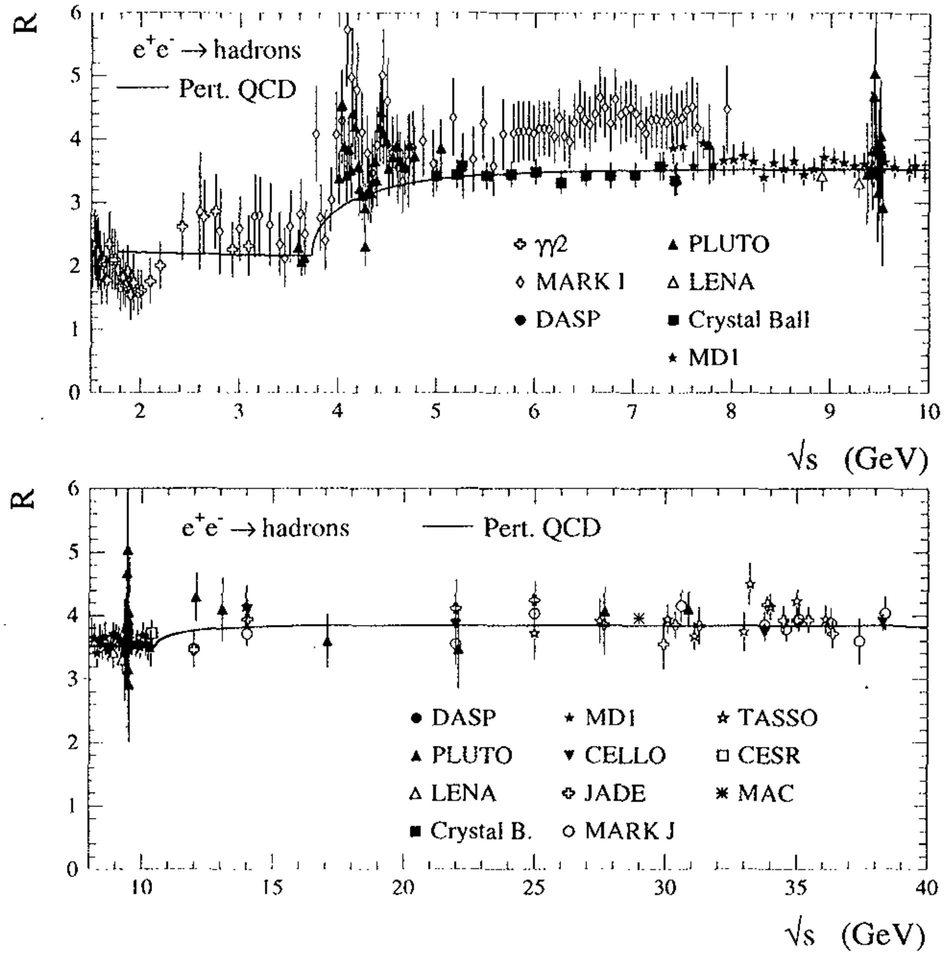

Figure 9.5: *Inclusive hadronic Cross sections ratio in* e^+e^- *annihilation versus the c.m. energy* $\sqrt{s}$. *The QCD perturbative prediction Eq.* (9.17) *inputs* $\alpha_s(M_Z) = 0.1200$. *At the* $c\bar{c}$ *and* $b\bar{b}$ *production thresholds, the cross sections are dominated by non-perturbative contributions.*

respectively, as well as their excited spectroscopic states. It is safe to parametrize these states using relativistic Breit-Wigner resonance shapes with an s-dependent width. The expression

$$\sigma(s) = \frac{12\pi}{M_P^2}\frac{\Gamma_{ee}}{\Gamma_P}\frac{M_P^2\Gamma_P\Gamma(s)}{(s-M_P^2)^2+M_P^2\Gamma^2(s)}\,, \tag{9.27}$$

is used for the cross section of a resonance P with the s-dependent width [179]

$$\Gamma(s) = \frac{s}{M_P^2}\sum_i B(P\to X_i)\frac{F_{X_i}(s)}{F_{X_i}(M_P^2)}\,. \tag{9.28}$$

The above sum is over all branching ratios of the resonance P with the respective phase space factors $F_{X_i}(s)$ given, *e.g.*, for a spinless two-body decay $X = P_1P_2$ by $F_{P_1P_2} = (1-(m_{P_1}+m_{P_2})^2/s)^{3/2}$. The physical input values of the parametrizations and their errors are taken from Ref. [17]. The total parametrization errors are then calculated by gaussian error propagation.

9.5.3 High Energy Tail

At energies sufficiently above the Υ resonance family, the perturbative QCD prediction of R with five active quarks is supposed to be reliable. In agreement with Ref. [179], $R_{\rm pert}(s)$ from Eq. (9.17) is applied for $\sqrt{s} \geq 40$ GeV.

9.6 Results

The integrals (9.11) and (9.15) are evaluated exclusively, *i.e.*, for every contributing final state, up to the c.m. energy of 2.125 GeV. Even if some particular modes have been measured up to somewhat higher energies, one has to worry about unmeasured exclusive modes and therefore use the total R measurement above this threshold. Both energy regions are assumed to be uncorrelated. Because the contributions of the exclusive channels at low energy are simply summed up, their respective covariances must be estimated when propagating the error: in general, unmeasured final states whose contributions are deduced from measured ones via isospin are set to be 100% correlated with these. Also different detectors performing the same measurement are correlated through the sharing of commonly used simulation techniques to calculate acceptance and selection efficiency which depend on the assumed underlying physical dynamics. Contributions from resonances that are analytic are globally assumed to have 20% correlations due to modelling uncertainties. Between purely measured final states the correlations are estimated depending on the number of common experiments that contribute to their measurements and on the common energy region, as well as according to the relative importance of their statistical and systematic errors. In general the estimation yields a correlation between 10% and 20%. This treatment is different from that of Ref. [244] where a 100% correlation was assumed.

As described in Section 1.3.3, corrections to the charged $\rho^{\pm}$ width have to be applied to account for small CVC-violating effects. The magnitude of the width difference Eq. (9.8) translated into $a_\mu^{\rm had}$ and $\Delta\alpha_{\rm had}^{(5)}(M_Z^2)$ is evaluated using the fitted GS parametrization of the ρ line shape (Section 8.3). One obtains the additive corrections

$$\begin{aligned} \delta a_\mu^{\rm had} &= -(1.3 \pm 2.0) \times 10^{-10} \\ \delta\Delta\alpha_{\rm had}^{(5)}(M_Z^2) &= -(0.09 \pm 0.12) \times 10^{-4} \end{aligned} \qquad (9.29)$$

for the $\tau^- \to \pi^-\pi^0\,\nu_\tau$ spectral function which is applied in the present analysis. Corrections from the higher mass resonances $\rho(1450), \rho(1700)$ are expected to be negligible.

The two- and four-pion cross sections (incl. the τ contribution) in different energy regions are depicted in Figs. 9.6 and 9.7. The bands are the results within (diagonal) error-envelopes of the averaging procedure and the application of the trapezoidal rule described in Section 9.2.

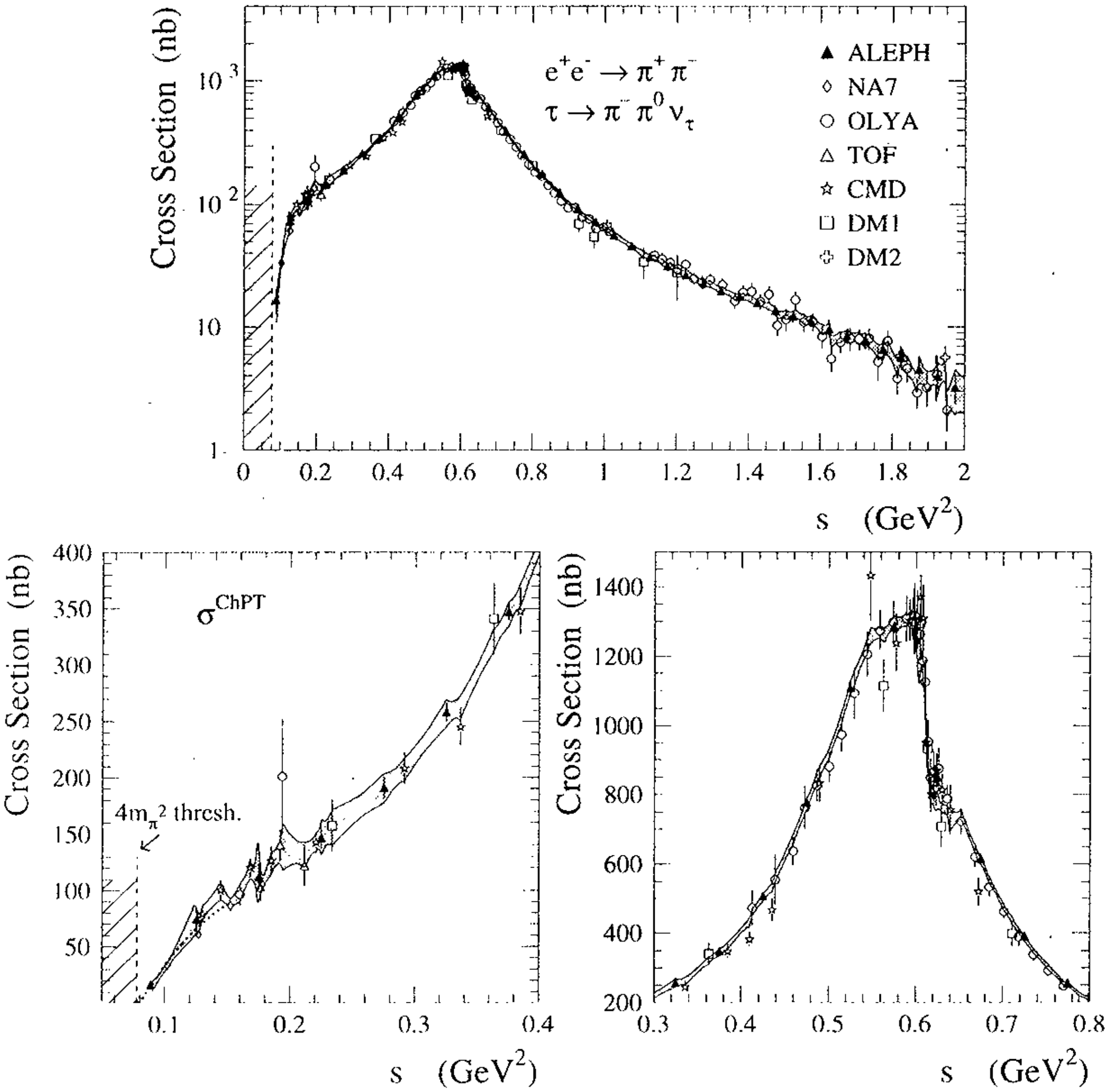

Figure 9.6: *Two-pion cross section as a function of the c.m. energy-squared. The band represents the result of the averaging procedure described in the text within its diagonal errors. The lower left hand plot shows the chiral expansion of the two-pion cross section obtained from expression* (8.4).

Final states	$a_\mu^{\rm had}$ ($\times 10^{10}$)	$\Delta\alpha_{\rm had}^{(5)}(M_{\rm Z}^2)$ ($\times 10^4$)	Energy (GeV)
$\pi^+\pi^-$ threshold	2.30 ± 0.05	0.04 ± 0.00	$4m_\pi^2$ – 0.320
$\pi^+\pi^-$	495.86 ± 12.46	34.01 ± 0.87	0.320 – 2.125
$\pi^+\pi^-$ (incl. τ data)	500.81 ± 6.03	34.31 ± 0.38	0.320 – 2.125
$\rho(\pi^0\gamma + \eta\,\gamma)$ (1)	0.30 ± 0.05	0.02 ± 0.01	0.298 – 2.125
ω	37.09 ± 1.07	2.97 ± 0.09	0.420 – 0.810
$\omega \to \pi\gamma$, neutrals (1)	0.03 ± 0.01	< 0.01	0.810 – 2.125
Φ	39.23 ± 0.94	5.18 ± 0.12	1.000 – 1.055
$\Phi \to \eta\,\gamma$, $\pi^0\gamma$ (1)	0.09 ± 0.01	0.01 ± 0.00	1.055 – 2.125
$\pi^+\pi^-\pi^0$ (below Φ)	4.12 ± 0.41	0.42 ± 0.04	0.810 – 1.000
$\pi^+\pi^-\pi^0$ (above Φ)	1.90 ± 0.72	0.46 ± 0.26	1.055 – 2.125
$\pi^+\pi^-2\pi^0$	21.41 ± 2.36	5.82 ± 0.63	0.910 – 2.125
$\pi^+\pi^-2\pi^0$ (incl. τ data)	22.26 ± 1.53	6.16 ± 0.49	0.897 – 2.125
$\omega\,\pi^0(\omega \to \pi\gamma$, neutr.) (1)	0.88 ± 0.11	0.18 ± 0.02	0.930 – 2.125
$\pi^+\pi^-\pi^+\pi^-$	15.90 ± 1.34	4.61 ± 0.39	0.983 – 2.125
$\pi^+\pi^-\pi^+\pi^-$ (incl. τ data)	16.50 ± 0.98	4.76 ± 0.31	0.794 – 2.125
$\pi^+\pi^-\pi^+\pi^-\pi^0$	4.02 ± 0.51	1.51 ± 0.20	1.019 – 2.125
$\pi^+\pi^-3\pi^0$ (2)	2.01 ± 0.26	0.75 ± 0.10	1.019 – 2.125
$\omega\,\pi^+\pi^-$ ($\omega \to \pi\gamma$, neutr.) (1)	0.07 ± 0.02	0.03 ± 0.01	1.340 – 2.125
$\pi^+\pi^-\pi^+\pi^-\pi^+\pi^-$	0.47 ± 0.14	0.19 ± 0.04	1.350 – 2.125
$\pi^+\pi^-\pi^+\pi^-2\pi^0$	3.32 ± 0.36	1.35 ± 0.14	1.350 – 2.125
$\pi^+\pi^-4\pi^0$ (2)	2.40 ± 2.40	0.98 ± 0.98	1.350 – 2.125
$\eta\,\pi^+\pi^-$ (3)	0.51 ± 0.14	0.16 ± 0.05	1.075 – 2.125
$\rm K^+K^-$	4.30 ± 0.58	0.85 ± 0.10	1.055 – 2.055
$\rm K_S^0K_L^0$	1.20 ± 0.42	0.23 ± 0.08	1.090 – 2.125
$\rm K_S^0K^+\pi^-$ (+ $\rm K_L^0K^-\pi^+$ (2))	2.04 ± 0.36	0.70 ± 0.12	1.340 – 2.125
$\rm K^+K^-\pi^0$	0.42 ± 0.29	0.15 ± 0.10	1.440 – 2.125
$\rm K_S^0K_L^0\pi^0$ (2)	0.42 ± 0.29	0.15 ± 0.10	1.440 – 2.125
$\rm KK\pi\pi$ (all modes)	4.52 ± 1.65	1.82 ± 0.66	1.441 – 2.125
J/ψ(1S,2S,3770)	8.04 ± 0.52	9.97 ± 0.68	3.096 – 3.800
Υ(1S,2S,3S,4S,10860,11020)	0.10 ± 0.01	1.18 ± 0.08	9.460 – 11.20
R	41.64 ± 3.61	164.31 ± 5.59	2.125 – 40.0
R (perturbative) (4)	0.16 ± 0.00	42.82 ± 0.10	40.0 – ∞
$\sum$ ($e^+e^- \to$ hadrons)	695.0 ± 15.0	280.9 ± 6.3	$4m_\pi^2$ – ∞
$\sum$ ($e^+e^- \to$ hadrons) (incl. τ data)	701.1 ± 9.4	281.7 ± 6.2	$4m_\pi^2$ – ∞

[1] Correction for missing modes (see text).

[2] Deduced from isospin relations (see text).

[3] Without contribution from $\eta \to \pi^+\pi^-\pi^0$ and $\eta \to 3\pi^0$.

[4] Values are taken from [179].

Table 9.2: *Summary of the $a_\mu^{\rm had}$ and $\Delta\alpha_{\rm had}^{(5)}(M_Z^2)$ contributions from e^+e^- annihilation and τ decays. The line "$\pi^+\pi^-$ threshold" contains the results from the integral over expression* (8.4) *at threshold energies.*

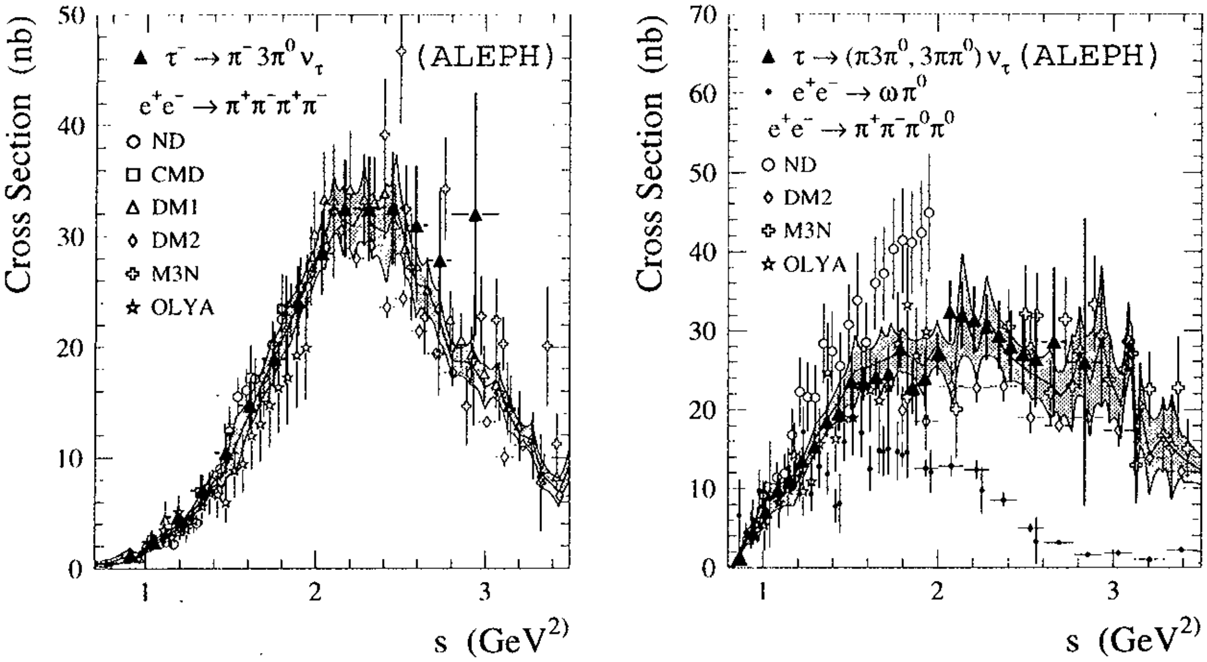

Figure 9.7: *Four-pion cross section as a function of the c.m. energy-squared. The band represents the result of the averaging procedure described in the text within its diagonal errors. The right-hand plot shows additionally the* $e^+e^- \to \omega\pi^0$ *amplitude (small points).*

9.6.1 Lowest Order Hadronic Contributions

The results of the exclusive contributions to $a_\mu^{\rm had}$ and $\Delta\alpha_{\rm had}^{(5)}(M_Z^2)$ are presented in Table 9.6. After the inclusion of the τ data, the error of $a_\mu^{\rm had}$ is dominated much less by the uncertainty of the two-pion contribution. Other important sources are the contradictory $\pi^+\pi^-2\pi^0$ data, as well as the unmeasured $\pi^+\pi^-4\pi^0$ final state. In the latter case, limits can be set only by using very conservative isospin arguments. As shown in Section 8.1 the large upper limit comes from the assumption of a dominant σ_{411} class accompanied by a vanishing σ_{321} contribution. Both classes occur in $\pi^+\pi^-\pi^+\pi^-2\pi^0$, while none contributes to $\pi^+\pi^-\pi^+\pi^-\pi^+\pi^-$ and only σ_{411} is part of $\pi^+\pi^-4\pi^0$ (see Section 1.4). The measured cross section of $\pi^+\pi^-\pi^+\pi^-2\pi^0$ is clearly higher than the corresponding $\pi^+\pi^-\pi^+\pi^-\pi^+\pi^-$ final state hence guaranteeing a leading contribution from one of the classes mentioned if isospin invariance holds. Since those classes correspond to eigenstates, a resonance analysis of the measured six-pion data would reveal important properties of the class structure of the respective modes which thus could give more constraining isospin bounds.

Another large uncertainty comes from the $K\bar{K}\pi\pi$ final states. The measurement of the $K^+K^-\pi^+\pi^-$ mode alone does not allow one to calculate isospin bounds for all possible contributions. Fortunately, it is possible to extract the complete $K\bar{K}\pi\pi$ contribution on the basis of a DM1 measurement of the inclusive channel K_S^0+X [198]. Nevertheless, large experimental uncertainties prevent a precise determination of the corresponding integrals.

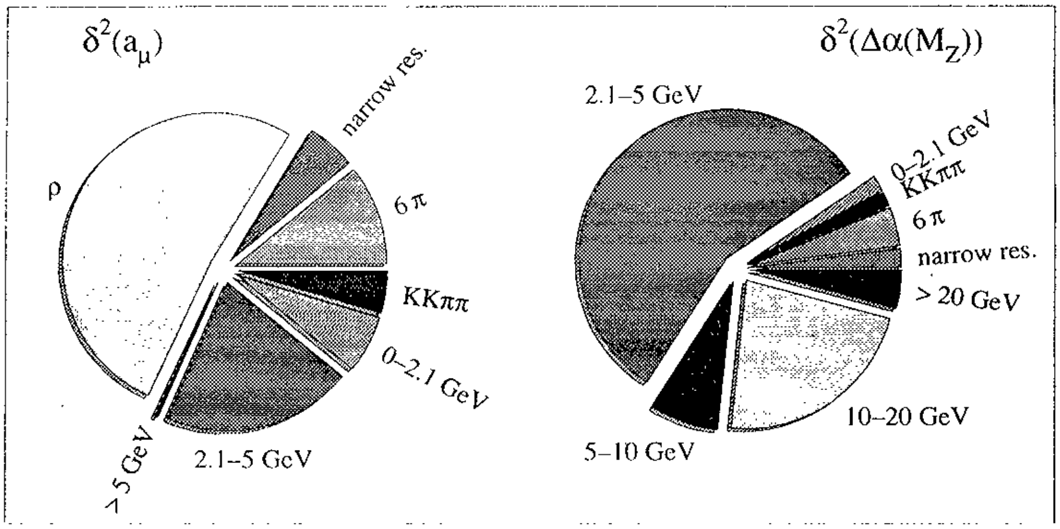

Figure 9.8: *Quadratic contribution of the various error sources to* $a_\mu^{\rm had}$ *(left hand plot) and* $\Delta\alpha_{\rm had}^{(5)}(M_Z^2)$ *(right hand plot) after the inclusion of* τ *data. In the energy region* 0 2.1 *GeV all exclusive contributions that are not given separately are included.*

The last important error source, especially for $\Delta\alpha_{\rm had}^{(5)}(M_Z^2)$, comes from the integral over the measured high energy inclusive cross section ratio R. The reliability of the QCD perturbative expansion for energies sufficiently above the still unpredictable resonance phenomena has been proven in many cases (see, *e.g.*, α_s measurements from different energy scales at LEP, HERA and from τ decays). Thus, theoretical input at energies lower than 40 GeV should be reliable and could significantly help to reduce the integration uncertainties [245, 246]. However, this has not been used in the present analysis which relies on experimental data as far as possible.

The squared contributions of the various final states and energy regimes to the errors of $a_\mu^{\rm had}$ and $\Delta\alpha(M_Z^2)$ are depicted in Fig. 9.8. Only the results after the inclusion of τ data are shown. One obtains for the lowest order hadronic vacuum polarization diagram of the muonic anomalous magnetic moment the contributions

$$\begin{aligned} a_\mu^{\rm had} &= (695.0 \pm 15.0) \times 10^{-10} \quad (e^+e^- \text{ data only}) \\ a_\mu^{\rm had} &= (701.1 \pm 9.4) \times 10^{-10} \quad (\text{combined } e^+e^- \text{ and } \tau \text{ data}) \end{aligned}$$

and for the running of α at M_Z^2

$$\begin{aligned} \Delta\alpha_{\rm had}^{(5)}(M_Z^2) &= (280.9 \pm 6.3) \times 10^{-4} \quad (e^+e^- \text{ data only}) \\ \Delta\alpha_{\rm had}^{(5)}(M_Z^2) &= (281.7 \pm 6.2) \times 10^{-4} \quad (\text{combined } e^+e^- \text{ and } \tau \text{ data}) \,. \end{aligned}$$

Fig. 9.9 shows a compilation of published results. The inclusion of the new τ data yields a large improvement in the precision of the $a_\mu^{\rm had}$ determination. The difference in $a_\mu^{\rm had}$ between the exclusive e^+e^- analyses of [179] and this work is mainly due to a disagreement in the two-pion integral where significantly lower values are obtained here.

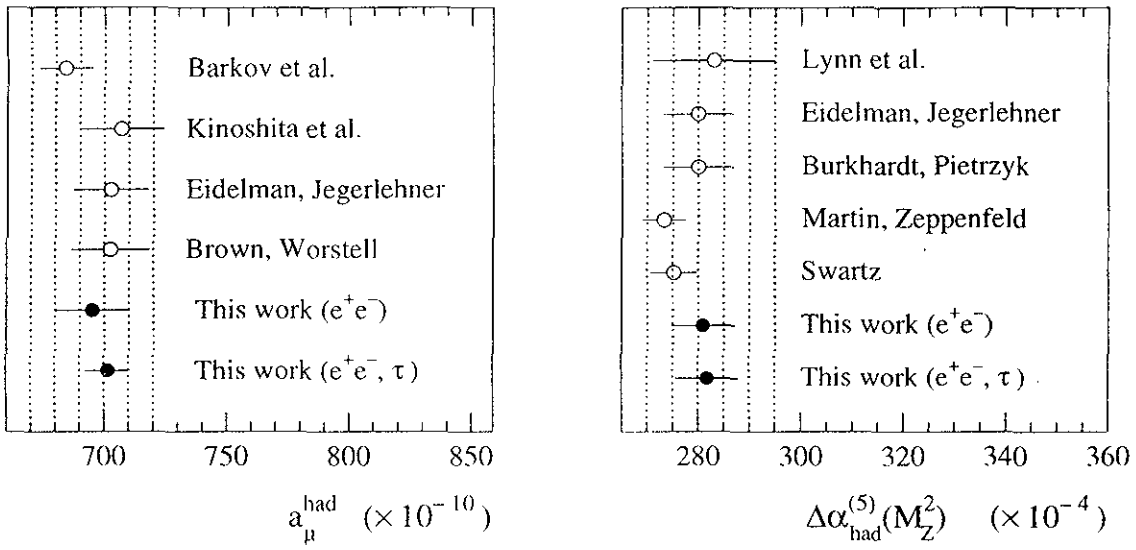

Figure 9.9: *Comparison of estimates of $a_\mu^{\rm had}$ (lowest) and $\Delta\alpha_{\rm had}^{(5)}(M_Z^2)$. The numbers are taken from Refs.* [169, 215, 179, 244, 247, 248, 245, 249].

In addition, differences in the handling of unmeasured modes generate inconsistent results. The results of Ref. [215] cannot easily be compared to the newer ones as the data set did not include the recent DM2 results. The differences in the final errors of $a_\mu^{\rm had}$ in the exclusive e^+e^- analysis of this work compared to Ref. [179, 244] is mainly caused by different techniques in the handling of the data and their errors. The detailed study of the origin of correlations, their propagation, as well as the rigourous use of isospin constraints to bound unmeasured modes yield slightly smaller errors here. As expected, the gain in the precision of $a_\mu^{\rm had}$ coming from τ data is significant whereas it is very small for $\Delta\alpha_{\rm had}^{(5)}(M_Z^2)$ since the dominant contributions and uncertainties come from energies above the τ mass.

9.6.2 Higher Order Contributions

In the famous paper of Kinoshita *et al.* [215], higher order contributions to the muon hadronic vacuum polarization graph, such as additional lepton or quark loops inserted in the diagram of Fig. 9.2 and the so-called light-by-light scattering graph, have been evaluated. The latter has been recomputed by different groups obtaining $(-5.2 \pm 1.8) \times 10^{-10}$ [250] and $(-9.2 \pm 3.2) \times 10^{-10}$ [251] with large uncertainties compared to the designed experimental accuracy of $\Delta a_\mu \simeq 4.0 \times 10^{-10}$ of the forthcoming BNL experiment. The conservative average of $(-6.2 \pm 4.0) \times 10^{-10}$ is used in the following with an enlarged error to account for inconsistencies.

The calculation of the higher order $\mathcal{O}(\alpha/\pi)^3$ loop diagrams is accomplished and partly corrected in a recent work [252], where second order kernel functions $K^{(2)}(s)$ are provided. These are used to calculate the corresponding contributions in the same spirit as the dominant lowest order graph by virtue of the dispersion integral (9.11). The numerical evaluation in Ref. [252] was performed on the basis of the data sample used by Ref. [179]. This exercise is repeated here in order to check the consistency of the results. For the contribution of diagrams with additional photon exchanges, *e.g.*, the fourth order muon vertex correction, the kernel labeled $K^{(2a)}(s)$ in [252] is used which gives $a_\mu^{(2a)} = (-20.9 \pm 0.4) \times 10^{-10}$. The diagrams with an electron loop inserted in one of the photon lines of Fig. 9.2 (kernel $K^{(2b)}(s)$ in Ref. [252]) contribute to $a_\mu^{(2b)} = (10.6 \pm 0.2) \times 10^{-10}$, where the asymptotic expansion, the analytical and numerical solutions provided in Ref. [252] lead to very similar results. Finally, the insertion of two hadronic loops in the muon vertex correction graph (kernel $K^{(2c)}(s)$ in Ref. [252]) results in $a_\mu^{(2c)} = (0.27 \pm 0.01) \times 10^{-10}$. The contributions $a_\mu^{(2a,b,c)}$ are found to be in agreement with Ref. [252]. All higher order results given here are computed from the e^+e^- data set only.

The compilation of the hadronic higher order parts (including light-by-light scattering) yields $a_\mu^{\rm had}[(\alpha/\pi)^3] = (-16.2 \pm 4.0) \times 10^{-10}$.

9.6.3 Results for $a_\mu^{\rm had}$ and $\alpha(M_Z^2)$

Collecting all contributions, one obtains for the anomalous magnetic moment of the muon

$$\begin{aligned} a_\mu &= (11\,659\,164.5 \pm 15.6) \times 10^{-10} \quad (e^+e^- \text{ data only}) \\ a_\mu &= (11\,659\,170.6 \pm 10.2) \times 10^{-10} \quad (\text{combined } e^+e^- \text{ and } \tau \text{ data}) \,, \end{aligned}$$

where the errors of the lowest order calculation $a_\mu^{\rm had}$ and $a_\mu^{(2a,b,c)}$ are added linearly.

The inverse of the fine structure constant at M_Z^2 is found to be

$$\begin{aligned} \alpha^{-1}(M_Z^2) &= 128.882 \pm 0.087 \quad (e^+e^- \text{ data only}) \\ \alpha^{-1}(M_Z^2) &= 128.878 \pm 0.085 \quad (\text{combined } e^+e^- \text{ and } \tau \text{ data}) \,. \end{aligned}$$

One may use the latter (combined) result for $\alpha(M_Z^2)$ to improve the constraint on the mass of the standard model Higgs boson $M_{\rm Higgs}$ inferred from a global electroweak fit (see also Section 2.6). This is done by utilizing current available electroweak data [112, 111] and the ZFITTER electroweak library [253]. It requires M_Z^2, $m_{\rm top}$, and $\alpha(M_Z^2)$ as input parameters, which are allowed to vary within their experimental accuracies. The additional parameters $M_{\rm Higgs}$ and the strong coupling constant at M_Z^2, $\alpha_s(M_Z^2)$, are freely adjusted in the fit. It is found to be $\alpha_s(M_Z^2) = 0.1201 \pm 0.0033$ which is in perfect agreement with the experimental value of 0.122 ± 0.006 [129] from the analyses of QCD observables in hadronic Z decays at LEP. The fitted Higgs boson mass is 138^{+137}_{-76} GeV, compared to 149^{+148}_{-82} GeV when using the previous value of $\alpha(M_Z^2)$ from Eq. (9.18). An additional error of 50 GeV should be added to account for theoretical uncertainties [253].

Fig. 9.10 depicts the variation of χ^2 as a function of the Higgs boson mass for the new and previously used values of $\alpha(M_Z^2)$ (the latter taken from [179]). The upper limit for $M_{\rm Higgs}$ is 516 GeV at 95% CL. The correlation contours between the fit parameter $\alpha_s(M_Z)$ and $M_{\rm Higgs}$ is shown in Fig. 9.11.

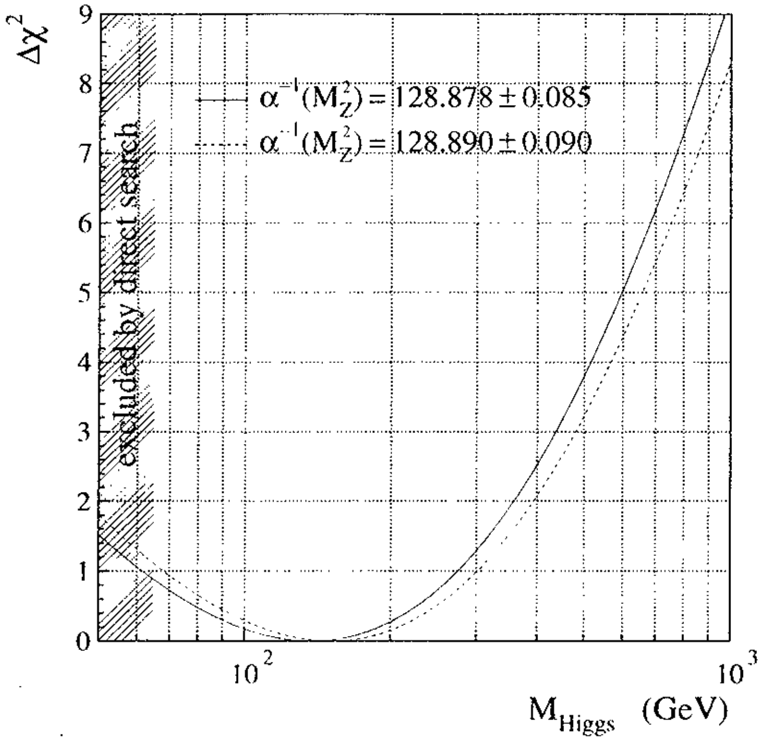

Figure 9.10: *Constraint fit results for the previous and the new value of $\alpha(M_Z^2)$ as a function of the Higgs mass.*

9.7 Conclusions

In this chapter, the hadronic vacuum polarization contribution to $(g-2)$ of the muon and to the running of the QED fine structure constant $\alpha(s)$ at $s = M_Z^2$ has been reevaluated using τ vector spectral functions in addition to slightly enlarged e^+e^- annihilation cross section data sets in order to improve the precision of the corresponding integrals. The results are, to lowest order, $a_\mu^{\rm had} = (701.1 \pm 9.4) \times 10^{-10}$ yielding $a_\mu = (11\,659\,170.6 \pm 10.2) \times 10^{-10}$ and $\Delta\alpha_{\rm had}^{(5)}(M_Z^2) = (281.7 \pm 6.2) \times 10^{-4}$, propagating $\alpha^{-1}(0)$ to $\alpha^{-1}(M_Z^2) = (128.878 \pm 0.085)$. The improvement coming from τ data is small in the $\Delta\alpha_{\rm had}^{(5)}(M_Z^2)$ case which is dominated by high energy contributions. However, it causes a 37% reduction in the error on $a_\mu^{\rm had}$.

In the near future, new low energy e^+e^- annihilation data are expected to be produced by the CMD-2 Collaboration [254] at Novosibirsk. In addition, new results for the $\tau^- \to \pi^-\pi^0\nu_\tau$ spectral function with a precision comparable to the ALEPH data were recently presented by the CLEO Collaboration [255]. Significant improvement is also expected from energy scans at the future high-luminosity e^+e^- collider DAΦNE in Frascati.

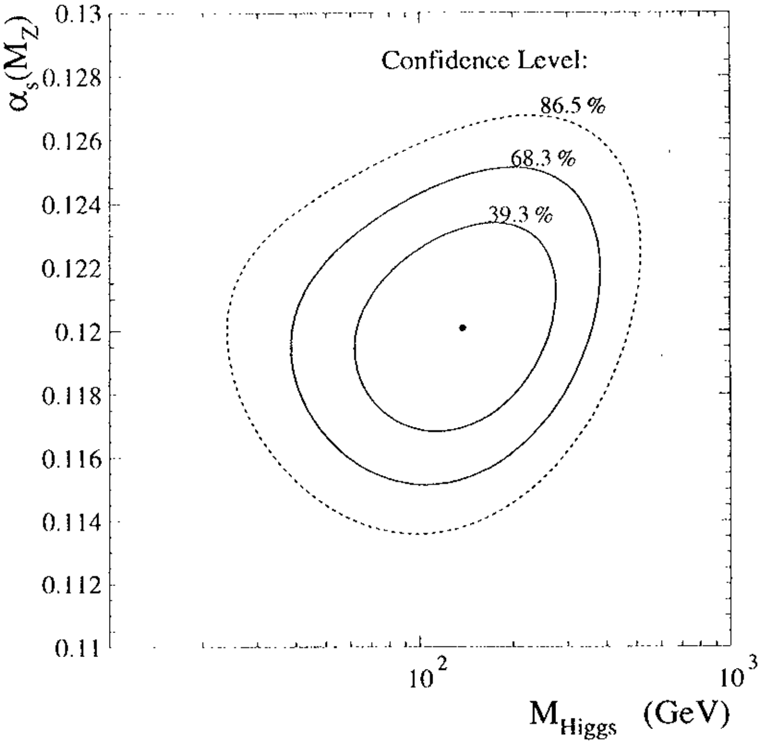

Figure 9.11: *Correlation between* $\alpha_s(M_Z)$ *and the Higgs mass* M_{Higgs} *simultaneously obtained from the global electroeak fit. The contours denote the respective confidence regimes.*

Chapter 10

τ Spectral Functions and QCD

The theoretical basis of the following phenomenological QCD analysis using vector and axial-vector spectral functions has been outlined in Chapter 2. The subject of the studies are QCD sum rules obtained in the environment of chiral symmetry, and the measurement of $\alpha_s(M_\tau)$ and non-perturbative contributions to the hadronic width of the τ.

10.1 QCD Chiral Sum Rules

As seen in Section 2.4, the application of chiral symmetry, *i.e.*, neglecting quark masses allows the computation of interesting low energy sum rules involving the difference of vector and axial-vector spectral functions. By virtue of the identity (1.27), the formulae Eqs. (2.36), (2.37), (2.39) and (2.40), expressed as functions of the vector and axial-vector spectral functions defined in Eq. (1.22), read

$$\frac{1}{4\pi^2}\int_0^{s_0\rightarrow\infty} ds\,\frac{1}{s}\,[v_1(s)-a_1(s)] \;=\; f_\pi^2\frac{\langle r_\pi^2\rangle}{3} - F_A\;, \tag{10.1}$$

$$\frac{1}{4\pi^2}\int_0^{s_0\rightarrow\infty} ds\,[v_1(s)-a_1(s)] \;=\; f_\pi^2\;, \tag{10.2}$$

$$\frac{1}{4\pi^2}\int_0^{s_0\rightarrow\infty} ds\,s\,[v_1(s)-a_1(s)] \;=\; 0\;, \tag{10.3}$$

$$\frac{1}{4\pi^2}\int_0^{s_0\rightarrow\infty} ds\,s\ln\frac{s}{\Lambda^2}\,[v_1(s)-a_1(s)] \;=\; -\frac{4\pi f_\pi^2}{3\alpha}\left(m_{\pi^\pm}^2-m_{\pi^0}^2\right)\,. \tag{10.4}$$

Eq. (10.1) is known as the Das-Mathur-Okubo (DMO) sum rule [6]. It relates the given integral ($I_{\rm DMO}$) to the square of the pion decay constant $f_\pi = (92.4 \pm 0.26)$ MeV [17] obtained from the decays $\pi^- \rightarrow \mu^-\bar\nu_\mu$ and $\pi^- \rightarrow \mu^-\bar\nu_\mu\gamma$; to the pion axial-vector form factor F_A for radiative decays[1] $\pi^- \rightarrow \ell^-\bar\nu_\ell\gamma$; and to the pion charge radius-squared

---

[1] In cases where it is a real radiative photon the differential decay rate can be written as

$$\frac{d^2\Gamma_{\pi\rightarrow\ell\nu\gamma}}{dE_\gamma dE_\ell} = \frac{d^2(\Gamma_{\rm IB}+\Gamma_{\rm SD}+\Gamma_{\rm INT})}{dE_\gamma dE_\ell}\;. \tag{10.5}$$

$\langle r_\pi^2 \rangle = (0.431 \pm 0.026)$ fm^2 [53]. The error of $\langle r_\pi^2 \rangle$ includes theoretical uncertainties. For completeness the results on the pion polarizability (see next section) will be also expressed in terms of the standard value $\langle r_\pi^2 \rangle = (0.439 \pm 0.008)$ fm^2 obtained from a one parameter fit to the same space-like data [180]. Eqs (10.2) and (10.3) are the first and second Weinberg sum rules (WSR) [7], where the pion pole in (10.2) is already integrated out. When switching quark masses on, only the first WSR remains valid while the second WSR breaks down due to contributions from the difference of non-conserved vector and axial-vector currents of order m_q^2/s, leading to a quadratic divergence of the integral (see Section 2.4.1). Eq. (10.4) represents the electromagnetic splitting of the pion masses [83]. Although apparently containing an arbitrary energy scale Λ, the sum rule is actually independent of Λ by virtue of the second WSR (10.2). However, for finite s_0, Eq. (10.4) maintains its Λ dependence.

The above integrals are calculated with variable upper integration bounds $s_0 \leq M_\tau^2$ using the spectral functions and their respective covariance matrices in order to provide a straightforward gaussian error propagation taking into account the strong bin-to-bin correlations of the spectral functions. In general, clearly, an integral of the above type is evaluated as

$$I(s_0) \;=\; \int\limits_0^{s_0} ds\, W(s)\,[v_1(s) - a_1(s)] \;=\; \sum_{i=1}^{N_{\rm bin}(s_0)} W(s_i)\,[v_{1,i} - a_{1,i}] \;, \qquad (10.6)$$

and its squared error reads

$$\Delta^2 I(s_0) \;=\; \sum_{i,j=1}^{N_{\rm bin}(s_0)} W(s_i)\left[C_{ij}^V + C_{ij}^A\right] \;, \qquad (10.7)$$

where the anticorrelations between v_1 and a_1 due to the estimates of the vector/axial-vector parts of the final states $\mathrm{K\bar{K}}\pi$ and $\mathrm{K\bar{K}}\pi\pi$ are reabsorbed in the respective covariance matrices $C^{V/A}$ so that v_1 and a_1 are now uncorrelated.

Fig. 10.1 shows the vector minus axial-vector distribution obtained from τ decays in addition to two times the vector spectral function v_{1,e^+e^-} from e^+e^- annihilation (see Section 8.1) data minus the inclusive $(v_1 + a_1)$ measurement, yielding a corresponding $(v_1 - a_1)$ spectral function with a slightly better precision at the end of the τ phase space. This treatment is of course not free from ambiguities as an eventual conceptual disagreement (*e.g.*, undetected systematic uncertainties) between the τ vector spectral function v_1 which is included in the $(v_1 + a_1)$ spectral function and v_{1,e^+e^-} translates into the difference $(v_1 - a_1)$ which then is inconsistent. Inferences from results obtained in such a way should therefore be handled with prudence.

The sum rules (10.1)–(10.4) versus the upper integration bound $s_0 \leq M_\tau^2$ are plotted in Figs. 10.2a–d. In addition to the the τ spectral functions, again the contribution from e^+e^- annihilation combined with the $(v_1 + a_1)$ inclusive measurement are shown. The

---

where $\Gamma_{\rm IB}$, $\Gamma_{\rm SD}$ and $\Gamma_{\rm INT}$ are the contributions from inner bremsstrahlung, structure-dependent radiation and there interference. The structure-dependent term is parametrized by using vector and axial-vector form factors $F_{V/A}$ (for the complete expression see Ref. [17]).

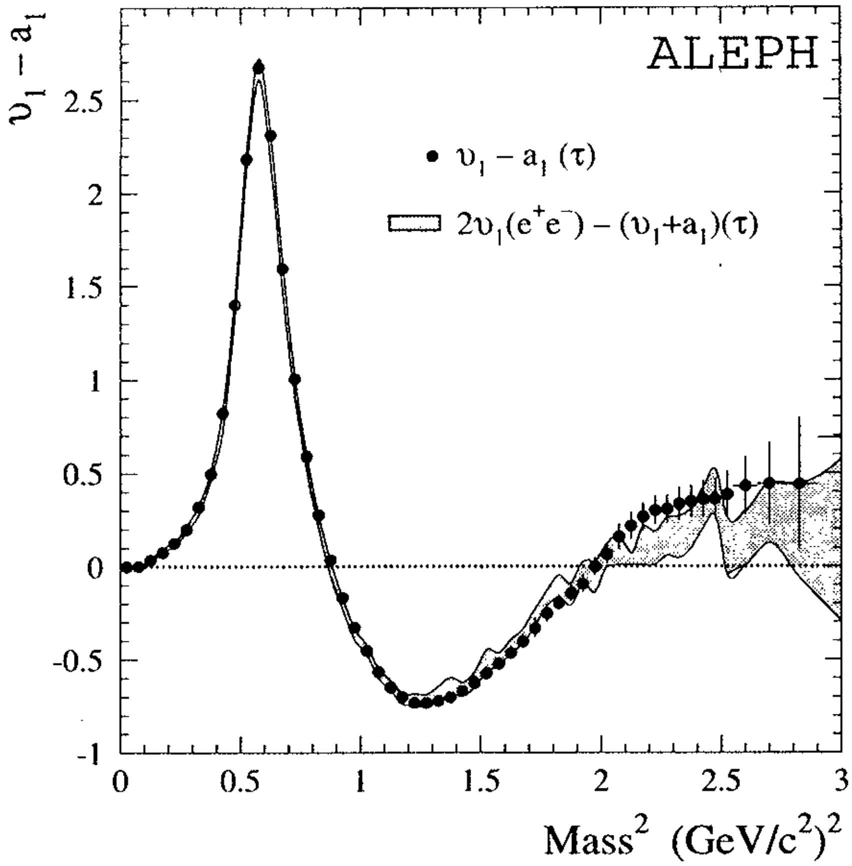

Figure 10.1: *Vector minus axial-vector ($v_1 - a_1$) spectral function. The band shows the corresponding spectral function using two times the vector spectral function from e^+e^- annihilation data minus the inclusively measured ($v_1 + a_1$) spectral function from τ decays.*

horizontal band depicts the respective chiral prediction of the integrals taken from [48]. One observes that only for the DMO sum rule (Fig. 10.2a), where contributions from higher mass-squares are suppressed, does the saturation within the one sigma error seem to occur at the τ mass scale. The other sum rules (Fig. 10.2b–c) are apparently not saturated at M_τ^2 as indicated by the non-vanishing ($v_1 - a_1$) spectral function at the end of the τ phase space (Fig. 10.1) and its still oscillating behaviour.

A way to improve the saturation of finite energy sum rules is to apply the Borel-transformed formulae (Section 2.3.2) emphasizing the lower resonances of the spectra. On the other hand, Borel-transformed sum rules give rise to non-perturbative corrections from quark condensates and non-vanishing quark masses scaling with the Borel parameter M^2. For example, the Borel-transformed first WSR reads [77]

$$\frac{1}{4\pi^2}\int\limits_0^{s_0\to\infty} ds\, e^{-s/M^2}\,[v_1(s) - a_1(s)] \;=\; f_\pi^2$$

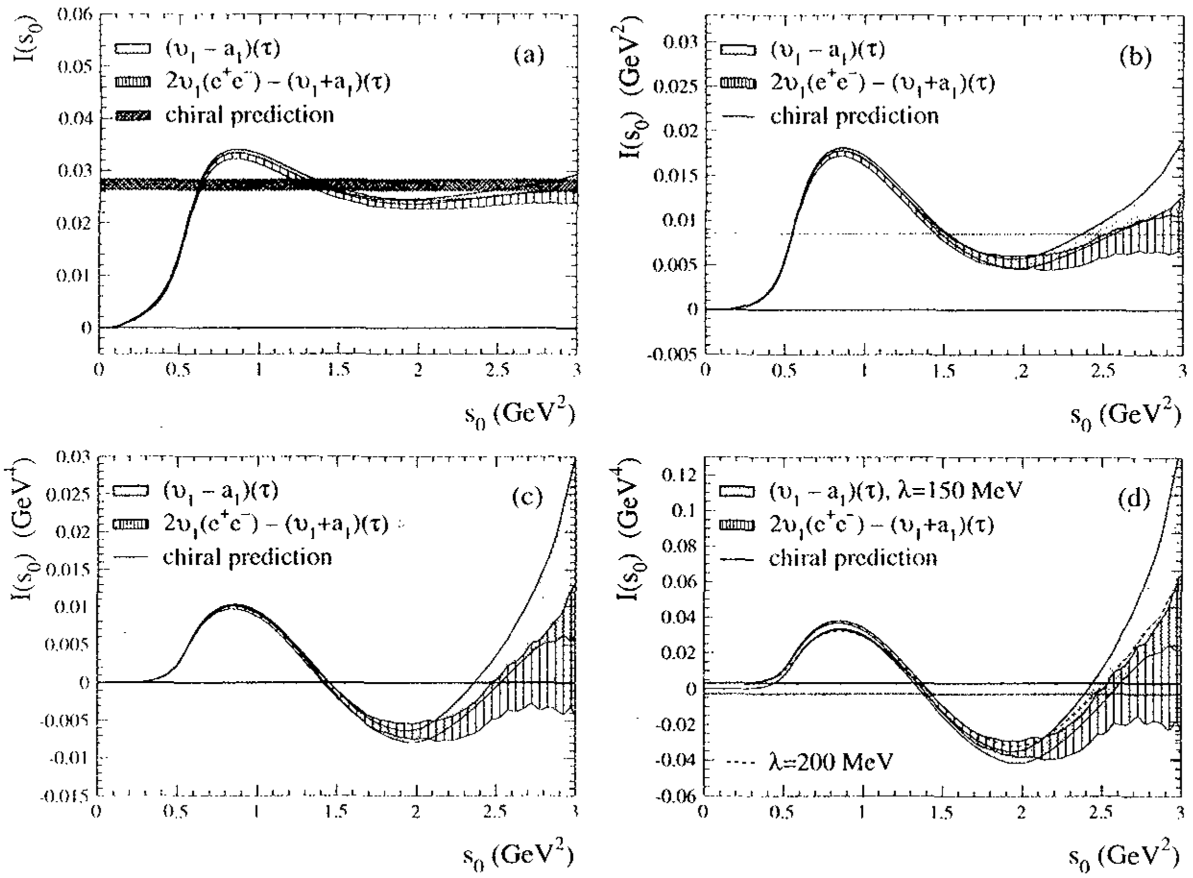

Figure 10.2: *Sum rules corresponding to Eqs* (10.1)–(10.4) *(plots: a–d) versus the upper integration bound s_0.*

$$+\frac{\alpha_s(M^2)}{2\pi}\left[-\frac{m_u(M^2)m_d(M^2)}{\pi^2}-\frac{8}{3}\frac{f_\pi^2 m_\pi^2}{M^2}-\frac{32\pi}{9}\frac{(\langle 0|\bar{q}q|0\rangle)^2}{M^4}+\ldots\right], \qquad (10.8)$$

where the current algebra expression $f_\pi^2 m_\pi^2 = -(m_u+m_d)\langle 0|\bar{u}u|0\rangle$ obtained from Eqs. (2.30) and (2.31) are used, $m_u(M^2)$ and $m_d(M^2)$ denote the running quark masses described by Eq. (2.15). The Borel integral (10.8) is plotted in Fig. 10.3 for $M^2 = 1$ GeV^2. The comparison with Fig. 10.2d makes the gain in precision *and* asymptoticness obvious. The chiral prediction is taken from the r.h.s. of Eq (10.8) setting f_π as defined above, $\alpha_s(1\ \mathrm{GeV}) = 0.59 \pm 0.07$ evolved from $\alpha_s(M_\tau) = 0.35 \pm 0.02$ (Section 10.2), $m_u(1\ \mathrm{GeV}) = 5 \pm 3\ \mathrm{MeV}/c^2$, $m_d(1\ \mathrm{GeV}) = 10 \pm 5\ \mathrm{MeV}/c^2$ [17] and neglecting higher order non-perturbative contributions $\mathcal{O}(M^{-6})$ and contributions other than quark condensates. One thus obtains $(8.44 \pm 0.17) \times 10^{-3}$ GeV^2, while the integral over τ data at $s_0 \sim 3$ GeV^2 reads $(7.61 \pm 0.26) \times 10^{-3}$ GeV^2, somewhat lower than the chiral prediction so that further non-perturbative terms need to be added. Anyway, the precision obtained is remarkable and such constraints can be used in order to measure higher order non-perturbative contributions or — if these are known from other sources — one might even get limits on the light quark masses?

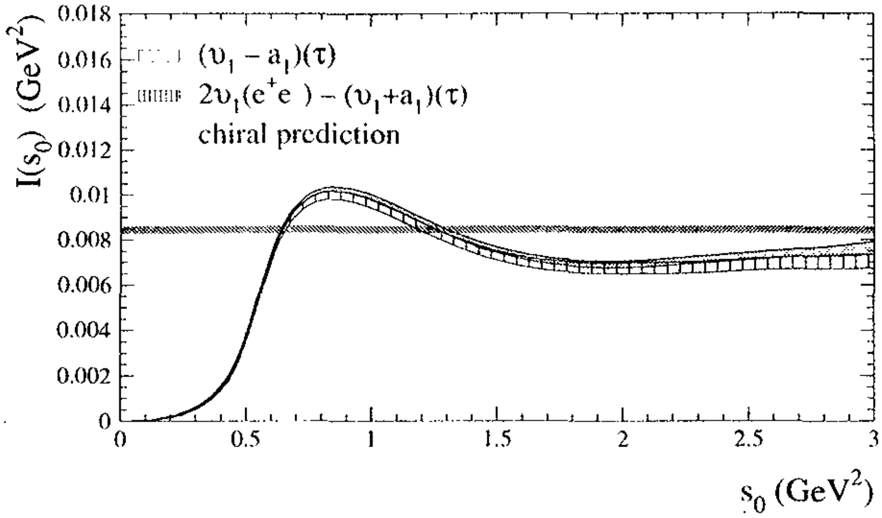

Figure 10.3: *Borel-transformed first WSR with $M^2 = 1$ GeV^2. The chiral prediction is given by the r.h.s of Eq.* (10.8).

10.1.1 The Polarizability of the Pion

In order to quantify the actual precision of the sum rules, the electric polarizability of the pion[2], given by [256]

$$\alpha_{\rm E} = \frac{\alpha F_A}{m_\pi f_\pi^2}, \tag{10.9}$$

is determined in this section utilizing the DMO sum rule $I_{\rm DMO}$ (10.1) as proposed in [257]. The computation of the pion axial-vector form factor F_A is most accurate using the measurement of the ratio $\gamma \equiv F_A/F_V$ obtained from radiative pion decays $\pi^- \to e^-\bar{\nu}_e\gamma$. Using the weighted average $\gamma = 0.46 \pm 0.05$ of the measurements [258] as well as the CVC relation between the pion vector form factor and the π^0 lifetime $|F_V| = (1/\alpha)(2\pi\tau_{\pi^0}m_{\pi^0})^{-1/2} = 0.0132 \pm 0.0005$ [259, 17] leads to

$$\alpha_{\rm E}^{\rm theo} = (2.86 \pm 0.33) \times 10^{-4}\ {\rm fm}^3\,, \tag{10.10}$$

as a theoretical prediction.

Using the τ $(v_1 - a_1)$ spectral functions, the DMO integral at the τ mass scale gives $I^{\tau}_{\rm DMO} = (28.0 \pm 1.6 \pm 1.1) \times 10^{-3}$, where the first error is the directly propagated integration error using the covariance matrices of the spectral functions. The second error is a systematic error which accounts for missing asymptoticness because the integration stops at $\sim s_0 = 3$ GeV^2 (it is not performed to exactly M_τ^2 since the error of the spectral functions blows up at the very end of the τ phase space). For the $2v_1(e^+e^-)-(v_1+a_1)(\tau)$ spectral function one obtains $I^{\tau,e^+e^-}_{\rm DMO} = (25.2 \pm 1.3 \pm 0.4) \times 10^{-3}$ with a $\chi^2 = 2.7/1$ when

---

[2] The electric polarizability $\alpha_{\rm E}$ of a physical system can be understood classically as the proportionality constant which governs the induction of the dipole moment $\mathbf{p}$ of a system in the presence of an external electric field $\mathbf{E}$: $\mathbf{p} = \alpha_{\rm E}\mathbf{E}$. The polarizability is an important quantity to characterize a particle, *i.e.*, in probing its inner structure.

compared to the above pure τ result, assuming both measurements conservatively to be 50% correlated (the actual correlation is lower since the inclusive $(v_1 + a_1)$ and the exclusive v_1 and a_1 τ spectral functions have large uncorrelated parts). The weighted average (taking into account the correlation) is

$$\langle I_{\rm DMO} \rangle = (26.4 \pm 1.5) \times 10^{-3} \, . \tag{10.11}$$

According to the prescription of Ref. [17], the error is increased by $\sqrt{\chi^2/1}$ to account for some inconsistency. Combining (10.1) and (10.9) with the assumption that the contribution to (10.1) for $s_0 > M_\tau^2$ is negligible, *i.e.*, the integral is saturated, one finds that the pion polarizability is

$$\alpha_{\rm E}^{\rm exp} = (2.40\,[2.68] \pm 1.14\,[0.76]) \times 10^{-4}\ {\rm fm}^3 \, . \tag{10.12}$$

The figures in brackets give the corresponding result if the standard value of $\langle r_\pi^2 \rangle = (0.439 \pm 0.008)\ {\rm fm}^2$ [180] is used for the pion charge radius-squared. Both results (10.12) are in agreement with the chiral prediction (10.10).

The authors of [257] (see also [260, 85]) used the first WSR (10.2) as an additional constraint to considerably improve the precision and the reliability of the $I_{\rm DMO}$ evaluation as it naturally reduces the sensitivity to the saturation assumption.

Another approach to the solution of (10.1) deals with the Borel-transformed DMO sum rule, which suppresses the high energy tail of the spectral function in order to improve saturation at M_τ^2 and to increase the precision of the integral [257, 261]:

$$\begin{aligned} \hat{I}_{\rm DMO}(M^2) &= \frac{1}{4\pi^2} \int\limits_0^{s_0 \to \infty} ds\, e^{-s/M^2}\, \frac{v_1(s) - a_1(s)}{s} \\ &\qquad + \frac{f_\pi^2}{M^2} - \frac{C_6 \langle \mathcal{O}(6) \rangle}{6M^6} - \frac{C_8 \langle \mathcal{O}(8) \rangle}{24 M^8} \end{aligned} \tag{10.13}$$

where $\hat{I}_{\rm DMO}(M^2) = I_{\rm DMO}$ in the limit $M^2 \to \infty$. At sufficiently high M^2 the impact of the dimension $D = 6$ and dimension $D = 8$ non-perturbative terms on $\hat{I}_{\rm DMO}(M^2)$ is small. One may use projecting sum rules with improved saturation to determine the corresponding phenomenological operators:

$$4\pi^2 C_6 \langle \mathcal{O}(6) \rangle \simeq \int\limits_0^{s_0} ds\, s^2\, [v_1(s) - a_1(s)] - \beta_1 s_0 \int\limits_0^{s_0} ds\, s\, [v_1(s) - a_1(s)] \, , \tag{10.14}$$

$$-4\pi^2 C_8 \langle \mathcal{O}(8) \rangle \simeq \int\limits_0^{s_0} ds\, s^3\, [v_1(s) - a_1(s)] - \beta_2 s_0^2 \int\limits_0^{s_0} ds\, s\, [v_1(s) - a_1(s)] \, . \tag{10.15}$$

Eqs. (10.14) and (10.15) hold for $s_0 \to \infty$ since the second term on the r.h.s. vanishes in the chiral limit by virtue of the second WSR (10.3). Unfortunately, the gain in convergence of the sum rules obtained from the insertion of the (even less convergent) second WSR is not very successful as it is accompanied by large additional errors. The coefficients $\beta_{1/2}$ in (10.14) and (10.15) depend on the high energy tail of the $(v_1 - a_1)$ spectral function

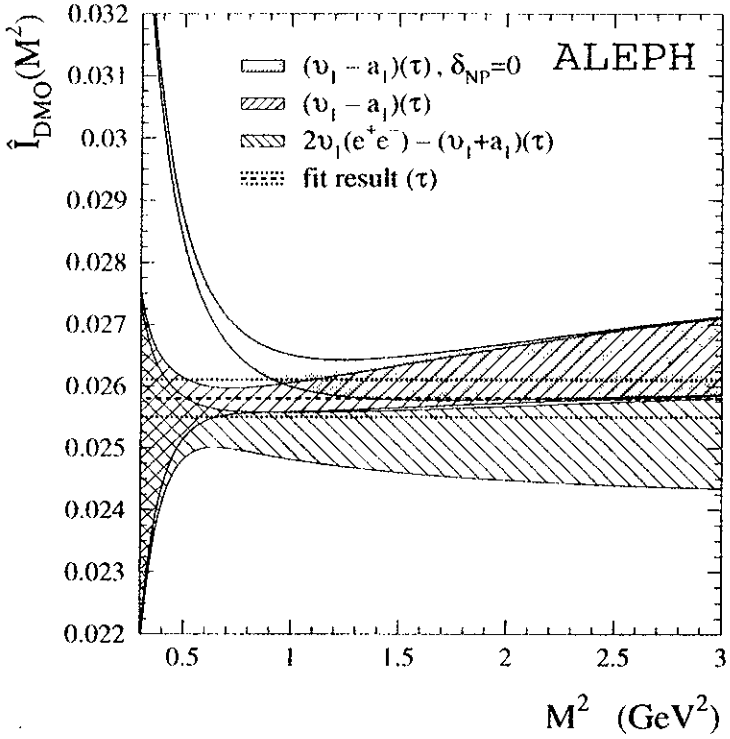

Figure 10.4: Laplace-transformed DMO sum rule $\hat{I}_{\rm DMO}$ as a function of the Borel parameter M^2 for the exclusive τ and the combined e^+e^-, τ $(v_1 - a_1)$ spectral function. The shaded area depicts the τ integral without the non-perturbative contributions. It diverges hyperbolically at small M^2.

which can be expanded in powers of s_0. They are estimated to be $\beta_1 \approx 1.5$ and $\beta_2 \approx 2.8$. This gives for the non-perturbative contributions the extremely rough estimates (using τ data only): $C_6\langle\mathcal{O}(6)\rangle = -0.025 \pm 0.027$ GeV^6 and $C_8\langle\mathcal{O}(8)\rangle = -0.15 \pm 0.16$ GeV^8, which yields the most precise value of $\hat{I}_{\rm DMO}$=(26.3 ± 0.6) for τ spectral functions at (high) $M^2 = 2.6$ GeV^2 enabling one to avoid the large errors of the inaccurate operator terms at low energy.

A more promising solution of Eq. (10.13) lies in a simultaneous fit of $\hat{I}_{\rm DMO}$ and the non-perturbative terms by means of moments on the Borel parameter M^2. A χ^2 fit is performed using the (strongly correlated) moments $M^2 = 0.2, 0.7, 1.2, \ldots, 3.7$ GeV^2 in order to guarantee sufficient information for the constraint of the dimension $D = 6$ and $D = 8$ operators at low M^2 and non-biased, purely perturbative contributions at high M^2 to fix $\hat{I}_{\rm DMO}$ through the Borel-transformed DMO integral in (10.13). The fit converges with a $\chi^2 = 2.3$ over 5 degrees of freedom, yielding (for τ data)

$$\hat{I}_{\rm DMO} = (25.8 \pm 0.3 \pm 0.1) \times 10^{-3} \, , \qquad (10.16)$$

which is in agreement with (10.11). The second error accounts for estimated uncertainties induced by the saturation assumption. From the fit, the non-perturbative contributions are $C_6\langle\mathcal{O}(6)\rangle$=$0.0029 \pm 0.0002$ GeV^6 and $C_8\langle\mathcal{O}(8)\rangle$=$-0.0015 \pm 0.0003$ GeV^8 with an anticorrelation of nearly 100%.

Fig. 10.4 depicts $\hat{I}_{\rm DMO}$ as a function of M^2 for the pure τ and the combined τ and e^+e^- annihilation $(v_1 - a_1)$ spectral functions. In this case, the pure τ spectral function provides smaller errors because of the more accurate two-pion contribution in τ decays which is strongly weighted in (10.13). The shaded band shows the τ result without the non-perturbative terms. Non-perturbative contributions dominate the integral at $M^2 < 1$ GeV^2 and become negligible for $M^2 > 2.5$ GeV^2 as the comparison between the shaded and the hatched bands demonstrates. Using (10.16) the electric polarizability is

$$\alpha_{\rm E}^{\rm exp} = (2.68\,[2.96] \pm 0.91\,[0.32]) \times 10^{-4}\ {\rm fm}^3 \tag{10.17}$$

with significantly lower errors compared to (10.12) due to the improved convergence of the Laplace-transformed DMO sum rule. Again the figures in brackets give the corresponding result when using the standard value of $\langle r_\pi^2 \rangle$.

10.2 The Measurement of $\alpha_s(M_\tau)$

The measurement of $\alpha_s(M_\tau)$ presented in this section adopts a method based on a simultaneous fit of the hadronic τ decay rate and spectral moments, which was proposed by F. Le Diberder and A. Pich [13], and was already employed in previous analyses by the ALEPH [8] and CLEO [9] Collaborations. The theoretical framework, relevant formulae and definitions of the observables are given in Section 2.5

10.2.1 R_τ and the Moments

Computing the ratio of the inclusive vector and axial-vector branching fractions, taken from Tabs. 6.1 and 6.2, to the electronic branching fraction Eq. (1.7) yields the semileptonic widths

$$\begin{aligned} R_{\tau,V} &= 1.782 \pm 0.018\,, && (10.18)\\ R_{\tau,A} &= 1.710 \pm 0.018\,, && (10.19)\\ R_{\tau,V+A} &= 3.492 \pm 0.015\,, && (10.20)\\ R_{\tau,V+A+S} &= 3.649 \pm 0.013\,. && (10.21) \end{aligned}$$

The inclusive sum $R_{\tau,V+A}$ has a much lower error than the exclusive $R_{\tau,V/A}$ since the latter suffers from anti-correlations between the branching ratios of "adjacent" τ decay channels, *i.e.*, those which differ by only one additional π^0. This is taken into account in the calculation of the error. However, these anti-correlations disappear when there is no need to separate the V, A components. Clearly, the value obtained and the error for $R_{\tau,V+A}$ must correspond to $R_{\tau,V+A+S} - R_{\tau,S}$, where $R_{\tau,S} = 0.156 \pm 0.008$ [90] is the strange hadronic width (of $\bar{u}s$ quark currents), because of the overall branching ratio normalisation to one. Thus, it serves as a good cross check of the correlations intervening into the calculation. The above strange quark inclusive width was used in Ref. [90] to infer a measurement of the strange quark mass at the τ mass scale of $m_s(M_\tau) = 212^{+30}_{-35}$ MeV$/c^2$ which is dominated by uncertainties of experimental origin. Thus, there is no advantage in including $R_{\tau,S}$ (or equivalently $R_{\tau,V+A+S}$) in this analysis, as the improvement in experimental precision is

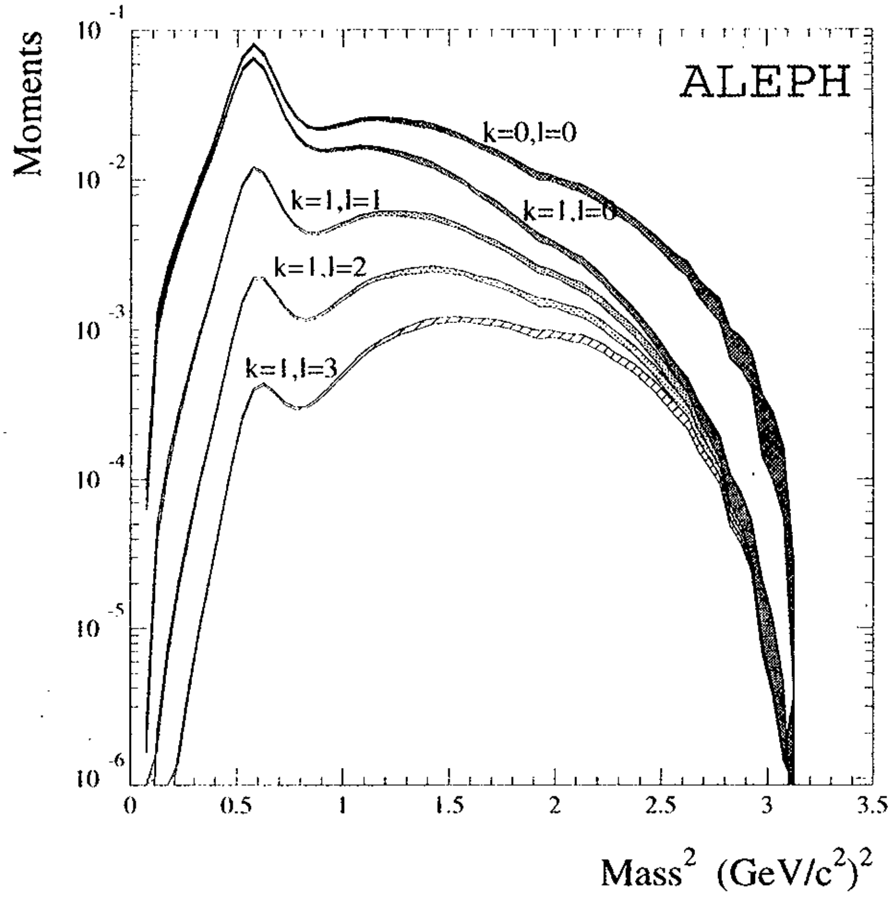

Figure 10.5: *Distribution of the* $(V + A)$ *spectral moments* $k = 1$, $l = 0, \ldots, 3$ *(without pion pole) according to the integrand in Eq.* (10.22).

then entirely effaced by the m_s uncertainty of the theoretical prediction.

To separate the measurement from theoretical constraints on the non-perturbative contributions to the OPE, spectral moments are computed from the invariant mass spectra of vector and/or axial-vector final states. The normalisation according to Eq. (2.89) reduces considerably the correlation between the τ hadronic width and the moments. It is completely negligible in the $(V + A)$ case where $R_{\tau,V+A}$ is calculated from the difference $R_\tau - R_{\tau,S}$, which has no correlations with the hadronic invariant mass spectrum. The correlations between $R_{\tau,V/A}$ and the corresponding moments are estimated to be 30%, where they are positive between $R_{\tau,V/A}$ and $D^{10}_{V/A}$ and negative for $D^{1l>0}_{V/A}$. Fig. 10.5 shows the distribution of the integrand in

$$D^{kl}_{\tau,V/A} \equiv \int\limits_0^{M_\tau^2} ds \left(1 - \frac{s}{M_\tau^2}\right)^k \left(\frac{s}{M_\tau^2}\right)^l \frac{1}{N_{V/A}} \frac{dN_{V/A}}{ds} , \qquad (10.22)$$

which corresponds to Eq. (2.89), for $k = 1$, $l = 0, \ldots, 3$. As can be concluded from Eq. (2.88), higher moments in l, projecting on higher squared masses, determine higher dimensional OPE terms. The effect of an α_s and, *e.g.*, $\delta^{(8)}$ variation on $R_{\tau,V}$ and the

ALEPH	$l=0$	$l=1$	$l=2$	$l=3$
D_V^{1l}	0.7159	0.1689	0.0532	0.0227
$\Delta^{\exp} D_V^{1l}$	0.0034	0.0006	0.0007	0.0006
D_A^{1l}	0.7205	0.1471	0.0639	0.0303
$\Delta^{\exp} D_A^{1l}$	0.0033	0.0009	0.0005	0.0004
D_{V+A}^{1l}	0.7177	0.1581	0.0585	0.0265
$\Delta^{\exp} D_{V+A}^{1l}$	0.0022	0.0006	0.0004	0.0004

Table 10.1: *Spectral Moments of vector (V), axial-vector (A) and vector plus axial-vector ($V+A$) inclusive τ decays. The errors give the total experimental uncertainties including statistical and systematic effects.*

ALEPH	$D_{\tau,V}^{10}$	$D_{\tau,V}^{11}$	$D_{\tau,V}^{12}$	$D_{\tau,V}^{13}$
$D_{\tau,V}^{10}$	1	−0.215	−0.862	−0.947
$D_{\tau,V}^{11}$		1	0.636	0.394
$D_{\tau,V}^{12}$			1	0.959
$D_{\tau,V}^{13}$				1

ALEPH	$D_{\tau,A}^{10}$	$D_{\tau,A}^{11}$	$D_{\tau,A}^{12}$	$D_{\tau,A}^{13}$
$D_{\tau,A}^{10}$	1	−0.377	−0.766	−0.951
$D_{\tau,A}^{11}$		1	0.843	0.479
$D_{\tau,A}^{12}$			1	0.871
$D_{\tau,A}^{13}$				1

ALEPH	$D_{\tau,V+A}^{10}$	$D_{\tau,V+A}^{11}$	$D_{\tau,V+A}^{12}$	$D_{\tau,V+A}^{13}$
$D_{\tau,V+A}^{10}$	1	−0.320	−0.862	−0.950
$D_{\tau,V+A}^{11}$		1	0.614	0.247
$D_{\tau,V+A}^{12}$			1	0.896
$D_{\tau,V+A}^{13}$				1

Table 10.2: *Experimental correlations between the moments $D_{\tau,V/A}^{kl}$.*

moments, which demonstrates the constraints of the measured observables on the QCD quantities, is shown in Fig. 10.6. The central points are the theoretical prediction of R_τ, V and the moments for some input values $\alpha_s(M_\tau)$, $\delta^{(4)}$, $\delta^{(6)}$ and $\delta^{(8)}$. The stars depict the deviation when changing $\alpha_s \to \alpha_s + 2\Delta\alpha_s$, while the triangles show what happens when shifting $\delta^{(8)} \to \delta^{(8)} + 2\Delta\delta^{(8)}$. One observes that α_s is determined from $R_{\tau,V}$ and the first moments D_V^{10}, D_V^{11}, but little effect is seen for the higher moments D_V^{12}, D_V^{13}. On the other hand, these moments determine the high dimensional non-perturbative power term, while the sensitivity from $R_{\tau,V}$ is weak. The measured values of the moments for V, A and $(V+A)$ spectral functions are given in Tab. 10.1; for their correlation matrices see Tab. 10.2. The correlations between the moments are computed analytically from the contraction of the derivatives of two involved moments with the covariance matrices of the respective normalized invariant mass-squared spectra. In all cases, the negative sign between the $k=1, l=0$ and the $k=1, l>0$ moments is understood to be due to the ρ and the π, a_1 peaks which determine the major part of the respective $k=1, l=0$ moments. They are much less important for higher moments as one can

Error source	$D^{10}_{\tau,V}$	$D^{11}_{\tau,V}$	$D^{12}_{\tau,V}$	$D^{13}_{\tau,V}$	Section
Statistical error	0.17	0.20	0.25	0.56	6
Fake photons	0.05	0.08	0.10	0.14	7.1.1
ECAL energy calibration	0.10	0.09	0.17	0.39	7.1.2
ECAL energy resolution	0.10	0.03	0.25	0.65	7.1.3
Photon likelihood: ref. distributions	0.07	0.09	0.12	0.41	7.1.4
Photon likelihood: cut on estimator	0.01	0.05	0.09	0.08	7.1.4
Photon min. energy threshold	0.09	0.10	0.14	0.28	7.1.5
Cut on distance: photon track	0.01	0.05	0.11	0.14	7.1.6
Energy dependence of reconstr. m_{π^0}	0.03	0.03	0.04	0.09	7.1.7
TPC momentum calibration	0.01	0.01	0.03	0.05	7.2.1
TPC momentum resolution	0.01	0.01	0.01	0.02	7.2.2
Unfolding: variation of ξ	0.04	0.10	0.35	0.58	7.3
Unfolding: difference test true	0.06	0.06	0.23	0.37	7.3
MC statistics	0.13	0.09	0.21	0.66	7.4
Branching ratios	0.34	0.20	1.02	1.85	7.4
Non-τ background	0.03	0.02	0.18	0.36	7.4
Separation V-A	0.17	0.08	0.49	0.94	6.1
MC distributions	0.05	0.04	0.17	0.30	6.1
Total	0.48	0.37	1.33	2.59	

Table 10.3: *Relative experimental errors (in %) to the vector moments. The last column indicates the reference section where the specific error sources are described.*

see in Fig. 10.5. Consequently, the amount of the negative correlation increases with $l = 1, \ldots, 3$. This also explains the large (and increasing) positive correlations between the $k = 1, l > 0$ moments, in which, with growing l, the high energy tail becomes more and more important counterbalancing the low energy peaks. The individual contributions to the total errors are listed in Tab. 10.3 for the vector case. One clearly sees the dominance from the branching ratio uncertainties which is also the only error contributing to $R_{\tau,V/A}$. An improvement of the branching ratio measurement is therefore of utter importance and expected, in particular, from a forthcoming ALEPH analysis including all LEP I data.

This measurement of the spectral moments can be compared to previous publications which are available from ALEPH and CLEO (Fig. 10.7). One observes a clear shift of the first moment $k = 1, l = 0$ to lower values and, corresponding to their anti-correlations, larger values for the $k = 1, l > 0$ moments in the new analysis when compared to the

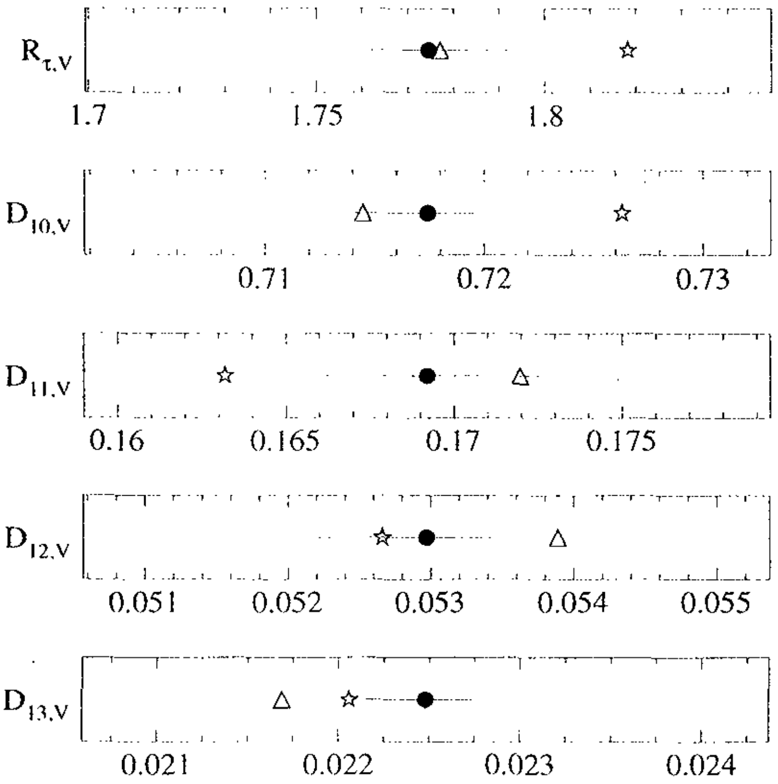

Figure 10.6: *Effect of a $\alpha_s \to \alpha_s + 2\Delta\alpha_s$ (hollow stars) and $\delta^{(8)} \to \delta^{(8)} + 2\Delta\delta^{(8)}$ (hollow triangles) shift on $R_{\tau,V}$ and the vector moments. The points in the centres give the unshifted values.*

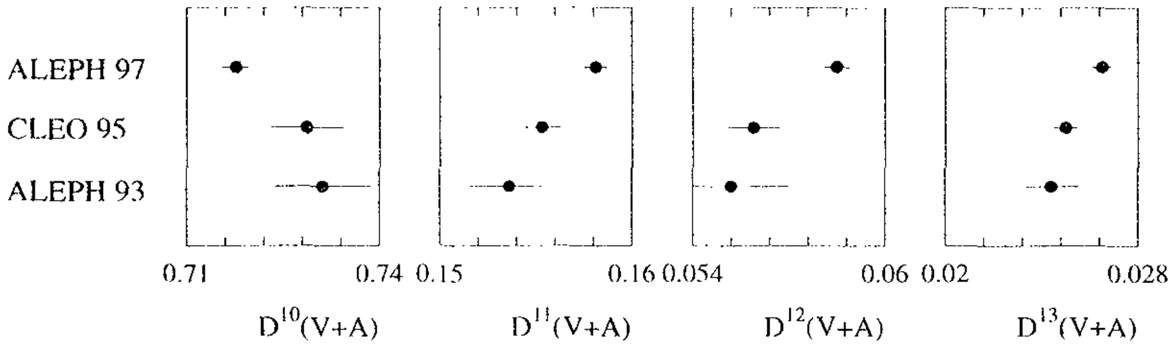

Figure 10.7: *Measured spectral moments D^{kl}_{V+A} in comparison to results obtained in previous analyses by CLEO* [9] *and ALEPH* [8]. *Note the strong correlations between the respective moments $l = 0, \ldots, 3$.*

former ones. This is to a large extent explained by the different τ branching ratios used and the consideration of K$\bar{\text{K}}$, K$\bar{\text{K}}\pi$ and K$\bar{\text{K}}\pi\pi$ contributions in this measurement.

10.2.2 Theoretical Prediction and Uncertainties

The combined fit for V, A and $(V + A)$ performed here adjusts the parameters $\alpha_s(M_\tau)$, $\langle(\alpha_s/\pi)GG\rangle$ (from Eq. (2.82)), $\rho\alpha_s\langle\bar{q}q\rangle^2_{V/A}$ from (Eq. (2.83)) and $\langle\mathcal{O}_8\rangle_{V/A}$ of the OPE in the theoretical predictions of $R_{\tau,V/A}$ (2.54) and the spectral moments (2.85). Clearly one has to worry about the theoretical uncertainties affecting these predictions. They do not differ qualitatively for either $R_{\tau,V/A}$ or the moments. However, quantitatively, one expects larger effects, *e.g.*, from uncertainties in the perturbative series, on the τ hadronic widths or lower moments ($l \simeq 0,1$). Instead, uncertainties from non-perturbative contributions (other than those which are fitted) should affect higher moments ($l \simeq 3,4$) more than lower ones. The translation from theoretical errors on $R_{\tau,V/A}$ to $\alpha_s(M_\tau)$ can be easily performed using Eq (2.54) and Tab. 2.1 (the third line corresponds to the method used here) and calculating the derivative. One obtains (with $K_4 = 25$)

$$\begin{aligned} \Delta\alpha_s(M_\tau) &= \frac{\Delta R_{\tau,V/A}}{0.633 + 0.743\alpha_s(M_\tau) + 1.323\alpha_s^2(M_\tau) + 1.822\alpha_s^3(M_\tau)} \qquad (10.23) \\ &\simeq 0.88\Delta R_{\tau,V/A} \;, \qquad \text{for} : \alpha_s(M_\tau) = 0.35 \;, \end{aligned}$$

and $\Delta\alpha_s(M_\tau) = 0.44\Delta R_{\tau,V+A}$. Note that this dependence is larger than what one would expect from the naive Taylor expansion (2.70) which leads to $\Delta\alpha_s \simeq 0.58\Delta R_{\tau,V/A}$.

The following list compiles the uncertainties entering into the theoretical predictions. The errors used and their impact on $R_{\tau,V/A}$ and $\alpha_s(M_\tau)$ are explicitly given in Tab. 10.4, while the total theoretical errors on $R_{\tau,V/A}$ and the moments are presented in Tab. 10.5 and finally the correlation matrix of the theoretical errors between $R_{\tau,V+A}$ and the $(V+A)$ moments is given in Tab. 10.6.

Physical constants: relevant physical constants are

(a) the CKM matrix element $|V_{ud}|$,
(b) the electroweak radiative correction factor $S_{\rm EW}$,
(c) light quark masses m_u, m_d.

Errors from the light quark masses are negligible (as the light quark mass contribution at all), while the others, in particular $\Delta S_{\rm EW}$, must be taken into account (see Tab. 10.4).

Perturbative series: errors in the truncated perturbative expansion originate mainly from the unknown higher order expansion coefficient K_4. Motivated by the works presented in Refs. [262, 263], K_4 is chosen to be $K_4 = K_3(K_3/K_2) \simeq 25$, obtained assuming an algebraic growth of the perturbation series, with an error of 50. This point is further discussed in a later paragraph.

Error source	Value $\pm\,\Delta$	$\Delta R_{\tau,V+A}$	$\Delta\alpha_s(M_\tau)$	$\Delta\alpha_s(M_Z)$
S_{EW}	1.0194 ± 0.0040	0.014	0.006	0.0006
V_{ud}	0.9752 ± 0.0007	0.005	0.002	0.0002
K_4	$K_3(K_3/K_2) \pm 50$	0.028	0.012	0.0013
β_3	$0 \pm \beta_3(\beta_3/\beta_2)$	0.003	0.001	0.0001
R-scheme (RS)	$\beta_2^{\overline{\rm MS}} \to \beta_2^{\rm RS} = 2\beta_2^{\overline{\rm MS}}$	0.004	0.002	0.0002
R-scale $\mu = \xi M_\tau^2$	$M_\tau + 0.7$	0.011	0.005	0.0005
Total errors		0.034	0.015	0.0016

Table 10.4: *Sources of theoretical uncertainties and its impact on $R_{\tau,V+A}$ and $\alpha_s(M_\tau)$ for $\alpha_s(M_\tau) = 0.35$ and evolved to $\alpha_s(M_Z)$. The origins of the different errors are explained in the text. The effects on $R_{\tau,V/A}$ are one-half of $R_{\tau,V+A}$, while V and A are degenerated.*

ALEPH	R_τ	D_τ^{10}	D_τ^{11}	D_τ^{12}	D_τ^{13}
V	0.017	0.0040	0.0034	0.0004	0.0002
A	0.016	0.0040	0.0030	0.0004	0.0003
$(V+A)$	0.034	0.0040	0.0031	0.0004	0.0003

Table 10.5: *Total theoretical errors for the vector, axial-vector and $(V+A)$ hadronic widths and moments.*

Another important point is the renormalization scale (μ) dependence of the prediction. It is governed by the parameter $\xi = \mu/M_\tau$ where ideally the final observables are independent of ξ. This fact is expressed in the RGE which governs the running of α_s. Formally, the integrals (2.67) in Eq. (2.66) also obey the RGE [86]:

$$\xi\frac{\partial A^{(n)}\left(\alpha_s(-\xi^2 s)\right)}{\partial\xi} = n\sum_{k=1}\beta_k A^{(n+k)}\left(\alpha_s(-\xi^2 s)\right) . \qquad (10.24)$$

In a truncated series the renormalisation scale dependence remains and is therefore an intrinsic uncertainty of the theoretical prediction. On the other hand, there is no reason to believe that the renormalisation scale should deviate very much from the energy scale at which QCD is applied. In order to get an estimate of the associated uncertainty, μ is varied from M_τ ($\xi = \mu/M_\tau = 1$), which is the standard value to $\mu = 2.5$. When changing the μ-scale, the coefficients $\tilde{K}_n(\xi)$ of the perturbative expansion, as well as α_s, have to be reexpressed according to the RGE. The ξ dependence of the coefficients is explicitely given in Eq. (2.63).

In addition to the renormalisation scale dependence, the arbitrariness of the choice of the renormalisation scheme (RS) leaves an ambiguity. The effect of this ambiguity is tested by changing $\beta_2^{\overline{\rm MS}}$ into an arbitrary $\beta_2^{\rm RS} = 2\beta_2^{\overline{\rm MS}}$ and recomputing α_s and the $\tilde{K}_n$ in the new scheme.

As can be seen in Tab. 10.4, the uncertainty from the missing β_3 coefficient is negligibly small. The implementation of the new value for β_3 from Eq. (2.19) has

ALEPH	$R_{\tau,V+A}$	$D^{10}_{\tau,V+A}$	$D^{11}_{\tau,V+A}$	$D^{12}_{\tau,V+A}$	$D^{13}_{\tau,V+A}$
$R_{\tau,V+A}$	1	0.879	−0.856	−0.539	−0.800
$D^{10}_{\tau,V+A}$		1	−0.992	−0.507	−0.874
$D^{11}_{\tau,V+A}$	–	–	1	0.396	0.810
$D^{12}_{\tau,V+A}$	–	–	–	1	0.842
$D^{13}_{\tau,V+A}$	–	–	–	–	1

Table 10.6: *Theoretical correlations between $R_{\tau,V+A}$ and the moments $D^{kl}_{\tau,V+A}$.*

no impact on this analysis.

- **Non-perturbative operators** in the OPE power terms of dimensions $D = 4, 6, 8$ have no theoretical errors since they are free varying parameters of the fits and will be determined experimentally. Contributions from higher orders have not been calculated yet. Their Wilson coefficients carry a large number of non-trivial quark-quark, quark-gluon and gluon-gluon dynamical effects. Fortunately, as concluded from Eq. (2.57), they can only contribute indirectly via a logarithmic dependence on s, *i.e.*, they are proportional to α_s^2. The subsequent operator of dimension $D = 10$ is then suppressed by $\alpha_s^2/M_\tau^{10} \simeq 4 \times 10^{-4}$, and thus neglected in this analysis. Also neglected is any additional dimension $D = 2$ term (except the quark masses). $D = 2$ terms cannot be generated by a dynamical QCD action and are therefore absent in the SVD approach. But they are not ruled out experimentally and are still controversial theoretically. A possible $D = 2$ contribution from ultraviolet renormalons is of perturbative origin as it is caused by the truncation of the perturbative series. This is further discussed in the following paragraph.

By far the most critical error sources are effects from the truncated perturbative expansion at order α_s^3, since one could expect some convergence problems at $\alpha_s(M_\tau)/\pi \sim 1$. It is natural to express the corresponding uncertainty through the size of the first neglected term, *i.e.*, K_4 in Eq. (2.66) (or $\tilde{K}_4$ which takes into account the RS dependence). No explicit calculation of K_4 exists but several estimates are available:

A.L. Kataev and V. Starshenko [262] advocated the prescription of the principle of minimal sensitivity (PMS) [264], which allows the computation of an RS with optimal convergence, *i.e.*, with minimal dependence on higher order corrections. Actually, the difference between an observable calculated in the RS using the PMS and the ordinary RS, say $\overline{\text{MS}}$, provides an estimate of the missing terms accumulated in K_4. The estimation yields $\delta R_{\tau,V/A} \simeq 53(\alpha_s(M_\tau)/\pi)^4$ which is $K_4 \simeq 36$. To stress the success of this approach, the authors refer to several calculations including that of the four-loop correction to the electronic $(g-2)_e$, which previously has been correctly estimated by means of the same method [265].

F. Le Diberder [263] performed an experimental estimate of K_4 using the *a priori* freedom of choice of the renormalisation scale $\mu = \xi M_\tau$ (insofar as all physical observables are reexpressed in μ and thus obey the RGE). The sensitivity at $\mu = M_\tau$ is naturally

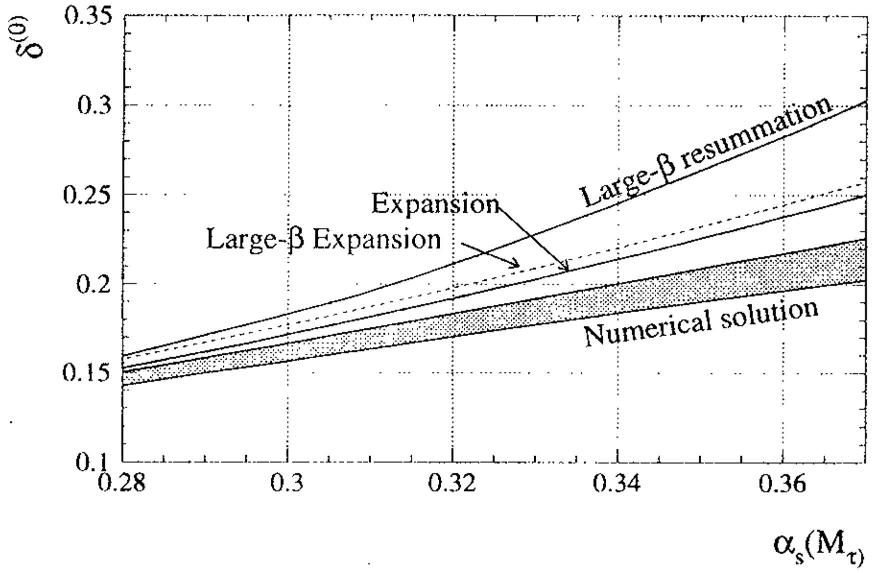

Figure 10.8: *Perturbative contribution $\delta^{(0)}$ to $R_{\tau,V/A}$ with different approaches. The "expansion", the "numerical solution" and the "large-β expansion" are given for $K_4 = K_3(K_3/K_2) \simeq 25$. The shaded band depicts the response to the variation $\Delta K_4 = \pm 50$.*

small. α_s measurements from other scales which are less precise than the one obtained from τ decays (with a large error on K_4) are additional inputs into the experimental fit. However, reducing μ increases the sensitivity dramatically, giving rise to the precise determination $K_4 = 27 \pm 5$ at $\mu \simeq 1$ GeV.

These consistent estimations are rather encouraging. Nevertheless, calculations of higher order renormalon chains also indicate comparable values of K_4 but they predict an oscillating behaviour of the series, *i.e.*, small K_n coefficients for n-even and large K_n for n-odd. One therefore has to worry about important contributions from the K_5 term which was found to be 788 in Ref [89]. On the other hand, by virtue of the implicit resummation of the α_s Taylor expansion in the $A^{(n)}$ integrals, the perturbative series (2.66) converges more rapidly than the naive guess $\sim (\alpha_s/\pi)$. For $\alpha_s(M_\tau) = 0.35$, one has in fourth order $A^{(4)} = 18.92 \times 10^{-5}$, and at higher orders $A^{(5)} = 1.436 \times 10^{-5}$ and $A^{(6)} = 0.073 \times 10^{-5}$. Thus even an extremely large $K_5 \approx 800$ produces an effect of $\Delta R_{\tau,V/A} \simeq 0.017$, which is still covered by the systematic uncertainty listed in Tab. 10.4. In Ref. [89], R_τ and the spectral moments have been calculated employing a renormalon resummation of the Adler function (2.58) in the large-β_0 limit. The resummation is performed by evaluating the integral of the Borel transform in the large-β_0 limit, where IR and UV singularities ("renormalons") appear in the new Borel plane as mentioned in the brief introduction Section 2.5.3. The UV renormalons, situated outside the integration range, have alternating signs and can be resummed. However, the IR renormalons lie inside the integration range on the positive axis and give rise to non-perturbative power contributions which are absorbed in the OPE. Fig. 10.8 depicts the results for $\delta^{(0)}$ using the different methods to evaluate the perturbative series. The large-β_0 limit resummed perturbative prediction is taken from Ref. [89]. Expanding α_s in the large-β_0 Borel integral in a Taylor series up to α_s^4 and setting $K_4 = 25$ yields the curve labeled "large-β expansion" [89]. The "expansion" corresponds to the naive Taylor expansion Eq. (2.70) and the numerical solution is Eq (2.66) with a numerical evaluation of the $A^{(n)}$ integrals. One observes an important discrepancy between the large-β_0 limit and the numerical solution employed in this analysis. However, experiences from other applications indicate that the estimates from the large-β_0 limit are most probably oversized [266] and will probably be reduced when including additional renormalon chains which are neglected in the present calculation. This point receives additional support from the comparison between the known (exact) K_n values and the results from the large-β_0 expansion [89]:

order	K_n(exact solution)	K_n(large $-\ \beta$ limit)
$n = 1$	1	1
$n = 2$	1.6398	1.5565
$n = 3$	6.3711	15.711
$n = 4$	...	24.83
$n = 5$	...	787.8

While the agreement in second order is acceptable, it is very bad in third order. The resummed solution shows an oscillating behaviour with large n-odd values and relatively small n-even coefficients. Even if the individual K_n coefficients of the large-β expansion do not fit to the exact solutions, the total $(K_n + g_n)$ contributions to $\delta^{(0)}$ shows a much better agreement.

Finally, the uncertainty chosen for the fourth order perturbative coefficient is $\Delta K_4 = \pm 50$ and should be a conservative estimate.

No additional uncertainty is introduced to cover as the possible existence of a $\delta^{(0)} \sim (\Lambda^2/s)$ term, because it is understood that such a contribution could only exist as a consequence of the truncation of the perturbative series (Section 2.5.3), whose uncertainties are already embedded in the ΔK_4 consideration.

10.2.3 Results of the Combined Fits

The fit program, written by F. Le Diberder, is the same as used in the first ALEPH analysis of α_s from τ decays in 1993 [8]. The fit minimizes a χ^2, calculated in the usual manner through the contraction of the differences between measured and fitted quantities with the inverse of the sum of the experimental and theoretical covariance matrices taken from Tabs. 10.2 and 10.6.

The results of the various fits are listed in Tab. 10.7. Tab. 10.8 gives the corresponding correlation matrices between the fitted parameters. The limited number of observables and the high correlations between the spectral moments explain the large correlations observed especially between the fitted non-perturbative operators. Taking into account these correlations, one obtains for the total non-perturbative contributions $\delta_{\mathrm{NP,V}} = 0.019 \pm 0.005$, $\delta_{\mathrm{NP,A}} = -0.022 \pm 0.003$ and $\delta_{\mathrm{NP,V+A}} = -0.002 \pm 0.004$, respectively.

One notices a remarkable agreement between the $\alpha_s(M_\tau)$ values of the different columns. On the other hand, the conformity of the results is not "too good" from the statistical point of view, when taking into account that the large correlations between the columns

ALEPH	Vector (V)	Axial-Vector (A)	$V + A$
$\alpha_s(M_\tau)$	$0.349 \pm 0.015 \pm 0.015$	$0.350 \pm 0.019 \pm 0.015$	$0.348 \pm 0.008 \pm 0.015$
$\delta^{(0)}$	0.201 ± 0.016	0.202 ± 0.018	0.200 ± 0.013
$\delta^{(2)}$	$-(0.7 \pm 0.3)\times 10^{-3}$	$-(0.7 \pm 0.3)\times 10^{-3}$	$-(0.7 \pm 0.3)\times 10^{-3}$
$\delta^{(4)}$	$(0.1 \pm 0.4)\times 10^{-3}$	$(-1.1 \pm 0.7)\times 10^{-3}$	$-(0.9 \pm 0.8)\times 10^{-3}$
$\delta^{(6)}$	0.029 ± 0.004	-0.028 ± 0.004	0.001 ± 0.005
$\delta^{(8)}$	-0.009 ± 0.001	0.008 ± 0.001	-0.001 ± 0.001
Total $\delta_{\rm NP}$	0.019 ± 0.005	-0.022 ± 0.003	-0.002 ± 0.004
χ^2/d.o.f.	0.4/1	0.1/1	0.2/1

Table 10.7: *Fit results of $\alpha_s(M_\tau)$ and the OPE non-perturbative contributions from vector, axial-vector and $(V + A)$ combined fits using the hadronic widths and the corresponding spectral moments as input parameters. Where two errors are given they denote experimental (first number) and theoretical uncertainties (second number). The total non-perturbative contribution is the sum $\delta_{\rm NP} = \sum_{n=2,4,6,8} \delta^{(n)}$.*

ALEPH	$\alpha_s(M_\tau)$	$\delta_V^{(4)}$	$\delta_V^{(6)}$	$\delta_V^{(8)}$
$\alpha_s(M_\tau)$	1	-0.334	-0.224	-0.142
$\delta_V^{(4)}$		1	0.765	0.973
$\delta_V^{(6)}$			1	0.972
$\delta_V^{(8)}$				1

ALEPH	$\alpha_s(M_\tau)$	$\delta_A^{(4)}$	$\delta_A^{(6)}$	$\delta_A^{(8)}$
$\alpha_s(M_\tau)$	1	-0.570	0.571	-0.508
$\delta_A^{(4)}$		1	-0.849	0.903
$\delta_A^{(6)}$			1	-0.972
$\delta_A^{(8)}$				1

ALEPH	$\alpha_s(M_\tau)$	$\delta_{V+A}^{(4)}$	$\delta_{V+A}^{(6)}$	$\delta_{V+A}^{(8)}$
$\alpha_s(M_\tau)$	1	0.033	0.146	0.060
$\delta_{V+A}^{(4)}$		1	-0.680	0.773
$\delta_{V+A}^{(6)}$			1	-0.939
$\delta_{V+A}^{(8)}$				1

Table 10.8: *Correlation matrices according to the fits presented in Tab. 10.7 for vector (upper left table), axial-vector (upper right) and $(V + A)$ (lower table).*

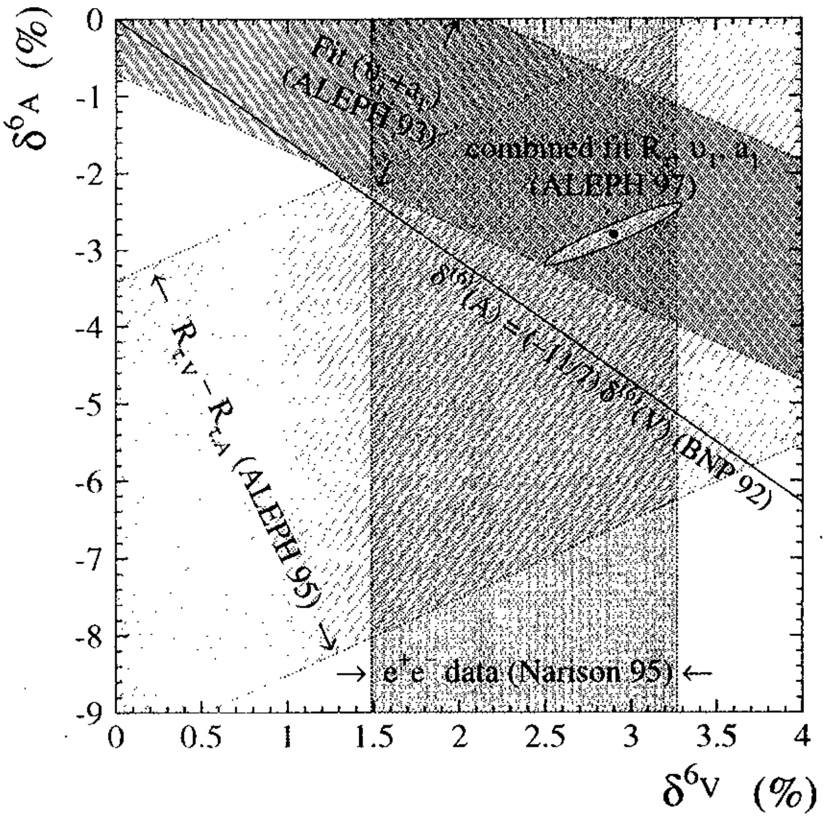

Figure 10.9: *Non-perturbative contribution $\delta^{(6)}$ to the inclusive vector and axial-vector τ hadronic widths. The ellipse depicts the new ALEPH result. The strong correlations of about 90% between $\delta_V^{(6)}$ and $\delta_A^{(6)}$ are found in an additional fit in which the exclusive vector and axial-vector widths and moments were combined.*

of Tab. 10.7 stem from theoretical uncertainties of common origin. The same argument, *i.e.*, strong correlations between the input observables, renders the small χ^2's obtained in the individual fits harmful, due to the fact that the "real" degree of freedom must be smaller than one. The results can be compared to those obtained in the previous ALEPH analysis [8] where the strong coupling was measured to be $\alpha_s(M_\tau) = 0.330 \pm 0.046$ using a much smaller data set of 8500 τ decays.

The individual as well as the total non-perturbative power contributions to the inclusive $R_{\tau,V+A}$ are all compatible with zero, while the uncertainty of the total contribution amounts to only 0.4%, which is much smaller than the error coming from the perturbative term. The gain from the separation of vector and axial-vector channels compared to the inclusive $(V + A)$ fit becomes obvious in the adjustment of the leading non-perturbative contributions of dimension $D = 6$ and $D = 8$, which cancel in the inclusive sum. The information for their accurate determination comes mainly from the high $l = 3, 4$ moments. Certainly, this cancellation of the non-perturbative terms puts a premium on the $\alpha_s(M_\tau)$ determination from the inclusive $(V + A)$ observables, and is reassuring even though one knows OPE to be well-behaved. The contributions from mass terms $\delta^{(2)}$, which behave

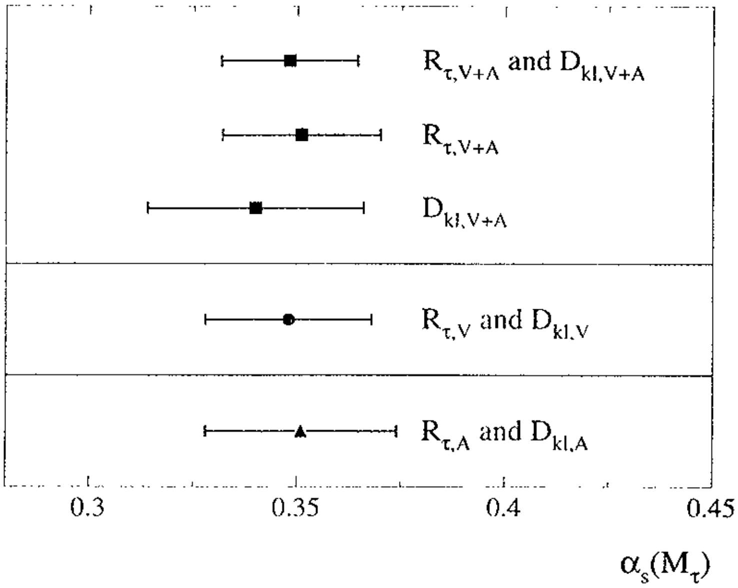

Figure 10.10: *Results for $\alpha_s(M_\tau)$ using $R_{\tau,V+A}$ only, the moments D^{kl}_{V+A} only and the combined information from vector and axial-vector τ decays. Note that the measurements are very correlated due to the dominant theoretical errors.*

like $m^2_{u/d}$, are below the 0.1% level. The gluon condensate governing the $\delta^{(4)}$ contributions is undetectable in all cases which agrees well with the fact that it is suppressed to second order α_s^2 (see Eq. (2.57) and Eq. (2.82)). Another interesting observation is the alternating sign in both vector and axial-vector cases between the $\delta^{(6)}$ and $\delta^{(8)}$ terms. This is connected with the special form of the shape of the vector (axial-vector) hadronic width as a function of the τ mass s_0, represented by the spectral moments in the above fits. The shape grows faster (slower) than the perturbative prediction with decreasing $s_0 < M_\tau^2$ giving rise to the balancing $\delta^{(6)}$ addition. It then abruptly explodes in the opposite direction, due to strong influences from low energy poles (resonances), which are qualitatively described by the opposite sign of the $\delta^{(8)}$ contribution. These properties will be discussed in detail in the next section. Fig. 10.9 depicts the measured $\delta_A^{(6)}$ versus $\delta_V^{(6)}$ in comparison with other estimations of both experimental and theoretical origin. The solid line corresponds to Eq. (2.83). The references are: "ALEPH 93" [8], "ALEPH 95" [24], "Narison 95" [267] and "BNP 92" [12].

In order to check the consistency of the different approaches one can use either the normalisation, *i.e.*, the τ hadronic width obtained from the hadronic branching ratios or the explicit form of the spectral functions, *i.e.*, the spectral moments. $\alpha_s(M_\tau)$can then be determined using variables coming only from one of these inputs. This is done for the $(V + A)$ case where contributions from non-perturbative terms are very small, so that the effect of additional theoretical assumptions are minimized. The results of these fits are shown in Fig. 10.10. They are in perfect agreement.

The evolution of the "best" and most robust $\alpha_s(M_\tau)$ measurement from the inclusive $(V + A)$ observables based on the Runge-Kutta integration of the differential equation to

N^{3}LO (Section 2.2.2) yields

$$\boxed{\begin{aligned} \alpha_s(M_\tau) &= 0.348 \pm 0.008_{\rm exp} \pm 0.015_{\rm theo} \\ \alpha_s(M_Z) &= 0.1211 \pm 0.0008_{\rm exp} \pm 0.0016_{\rm theo} \pm 0.0010_{\rm evol} \end{aligned}} \qquad (10.25)$$

The first error accounts for the experimental uncertainty, the second number gives the uncertainty of the theoretical prediction of R_τ and the spectral moments, and the last error stands for possible ambiguities in the evolution due to uncertainties in the matching scales of the quark thresholds (0.0010). Effects associated with the truncation of the RGE at $\mathcal{O}(\alpha_s^5)$ are small (the new N^{3}LO order gives a tiny contribution of $\alpha_s(M_Z)_{3.\,\rm order} - \alpha_s(M_Z)_{4.\,\rm order} = 0.00034$).

Using Eq. (2.13) one can express the value of $\alpha_s(M_\tau)$ in terms of the $\overline{\rm MS}$ renormalization scale $\Lambda_{\overline{\rm MS}}$ at three loop level. For the result (10.25) at $\mu = M_\tau$ with three active flavours one has

$$\Lambda^{(3)}_{\overline{\rm MS}} = (397 \pm 14_{\rm exp} \pm 27_{\rm theo})\ {\rm MeV}\ . \qquad (10.26)$$

10.2.4 The Running of $\alpha_s(s)$

The analysis presented in the preceeding section provides precise measurements of $\alpha_s(M_\tau)$. So far, there have been no major obstacles and consequently the perturbative expansion and the OPE approach used to build the theoretical prediction of the observables are believed to describe nature – at least phenomenologically. Nevertheless, by means of the exclusive measurement of the vector and axial-vector spectral functions, it becomes possible to deepen the QCD analysis as the spectral functions contain the entire phenomena of QCD physics at low energy. When decreasing the energy scale, non-perturbative effects become larger, a fact characterized by the appearence of high-peaked resonances in the spectral functions, especially the $a_1(1260)$, the $\rho(770)$ and the π-pole. However, not only non-perturbative contributions arise, but also the perturbative prediction increases with decreasing energy and one might expect convergence problems of the perturbative series at $\alpha(s_0)/\pi > 0.1$ [86].

Using the spectral functions, one can simulate the physics of a hypothetical τ lepton with a mass $\sqrt{s_0}$ smaller than M_τ. As defined in Eq. (2.50), the τ hadronic width $R_\tau(s_0)$ is then calculated by convoluting the spectral functions with the kinematical factor[3] $(1-s/s_0)^2(1+2s/s_0)/s_0$ corresponding to the new "τ mass" $\sqrt{s_0}$. The evolution of $R_\tau(s_0)$ provides a direct test of the running of $\alpha_s(\sqrt{s_0})$, governed by the RGE β-function. In addition, results, whether or not they are consistent with QCD, ought to prove the proper use of the OPE approach in τ decays, and thus confirm the astonishing precision of the $\alpha_s(M_\tau)$ measurement. A similar study was presented in Ref. [268]. A fit of the theoretical prediction $R_{\tau,V/A}(s_0)$, especially $R_{\tau,V+A}(s_0)$, to the data over a reasonable range

---

[3] Note that at small "τ masses" s_0, the different kinematical factor for vector and scalar particles becomes non-negligible.

$s_0^{\rm min} \leq s_0 \leq M_\tau^2$ in which the OPE is valid will provide an important consistency check of the results for $\alpha_s(M_\tau)$ and the non-perturbative contributions obtained in Section 10.2.3 using R_τ and the spectral moments. Again, in these studies one is very lucky to have separated vector and axial-vector channels, which now permits one to cancel the degenerated perturbative series by using $R_{\tau,V-A}(s_0)$ in order to directly investigate its consistency with the OPE prediction, *i.e.*, testing the power law that the experimental data obey.

It is convenient to exhibit the important questions and problems concerning the α_s determination and the use of the OPE in order to attempt to get answers or at least some hints from the respective $R_{\tau,V/A}(s_0)$ distributions:

1. Down to which $s_0^{\rm min}$ is the OPE valid? The regime of validity is then assigned by $s_0^{\rm min} \leq s \leq M_\tau^2$.
2. Is $s_0^{\rm min}$ identical in the V, A and $(V+A)$ case?
3. Can one distinguish two and three active quark flavours in the RGE?
4. What is the dominating power of the OPE in the region of its validity, *i.e.*, $s_0 \geq s_0^{\rm min}$?
5. Do the dimensions $D = 6, 8$ describe the non-perturbative spectrum? Does the inclusion of $\delta^{(8)}$ allow to decrease $s_0^{\rm min}$?
6. Can one constrain K_4 or an eventual dimension $D = 2$ term?
7. What follows for the theoretical errors?

The functional dependence of the respective $R_{\tau,V/A}$ hadronic widths are plotted in Fig 10.11 and Fig 10.12 together with the results from the direct χ^2 fits and the moments fit from Tab. 10.7. Also shown are the experimental errors, attached to the data distributions, and the theoretical uncertainties. The correlations between two adjacent bins $s_1 < s_2$ are huge as the only different, *i.e.*, new, information is provided by the bin at s_2. They are even reinforced by the genuine experimental and theoretical correlations. The correlations are calculated analytically from the respective derivatives of Eq. (2.50) using the identity Eq. (1.27), and are packed into an overall covariance matrix that is used to calculate the χ^2, which is minimized in the fit. Fig. 10.13 shows the plot corresponding to Fig. 10.11, translated into the running of $\alpha_s(s_0)$. Also plotted is the evolution using only two quark favours. No significant deviation is found, *i.e.*, experimentally one cannot distinguish if two or three flavours are involved.

The values obtained for the parameters are compatible with those given in Tab. 10.7. For example in the case of $(V+A)$ the direct $R_{\tau,V+A}(s_0)$ fit yields: $\alpha_s(M_\tau) = 0.354 \pm 0.017$, $\delta^{(6)}_{V+A} = -0.005 \pm 0.005$ and $\delta^{(8)}_{V+A} = (0.9 \pm 1.3) \times 10^{-3}$, while there is a negligible dependence on the gluon condensate (which therefore has been fixed in the fit). The curve blows up at decreasing s_0 due to the pion pole which, at high phase space suppression, becomes very strong (see also for $R_{\tau,A}(s_0)$ in Fig. 10.12). In the pure vector case, there is no pseudoscalar contribution to counterbalance the ρ. Thus $R_{\tau,V}(s_0)$ decreases dramatically after passing the peak of the resonance. One observes an energy shift between the

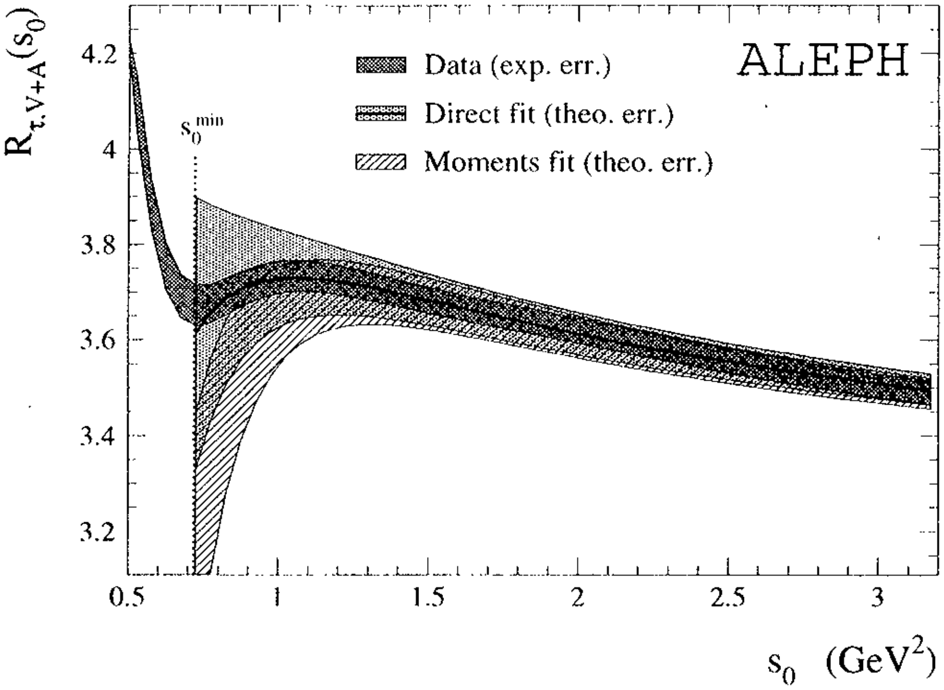

Figure 10.11: $(V+A)$, V *and* A *hadronic widths versus the square "τ mass" s_0. All curves is plotted as error bands to emphasize their strong point-to-point correlations in s_0. The shaded band (with a solid line in the centre) "direct fit" depicts the result of the direct adjustment of the theoretical prediction to the data curve shown. The "moments fit" is the evolution of the theoretical prediction using the results for $R_{\tau,V+A}$ and the non-perturbative terms from Tab. 10.7.*

occurrence of an object (peak) in the spectral functions and its effect on the τ hadronic width. For example, the ρ peak at 0.6 GeV^2 gives rise to a maximum of $R_{\tau,V}(s_0)$ around $s_0 = 1.5$ GeV^2. This is due to a large phase space suppression when the object has a mass comparable to the "τ mass" s_0.

For $R_{\tau,V+A}(s_0)$, the regime of validity of the OPE is clearly above $s_0^{\min} \simeq 0.7$, and may reach down to $s_0^{\min} \approx 1.7$ for $R_{\tau,V/A}(s_0)$. So far, the inclusive sum $(V+A)$ is much better behaved than the individual contributions, although the OPE seems to be valid in all three cases. The experimental fact that the non-perturbative contributions (inside present accuracy) exactly cancel over the whole range $1.2 \leq s_0 \leq M_\tau^2$ appears almost magic. It is the deeper reason why the α_s determination from the inclusive $V+A$ data is so robust. Below 1 GeV^2 the error of the theoretical prediction of $R_{\tau,V+A}(s_0)$ starts to diverge due to the large uncertainty at this energy from the non-perturbative terms (these errors are not contained in the theoretical error band of the moments fit result).

One may refer to Question 4 and wonder whether the powers $D = 6$ and $D = 8$ of the OPE are the genuine powers of the non-perturbative terms arising in $R_{\tau,V}(s_0)$ and $R_{\tau,A}(s_0)$. Fortunately, as a trick, one can use the difference $R_{\tau,V-A}(s_0)$, which is free from

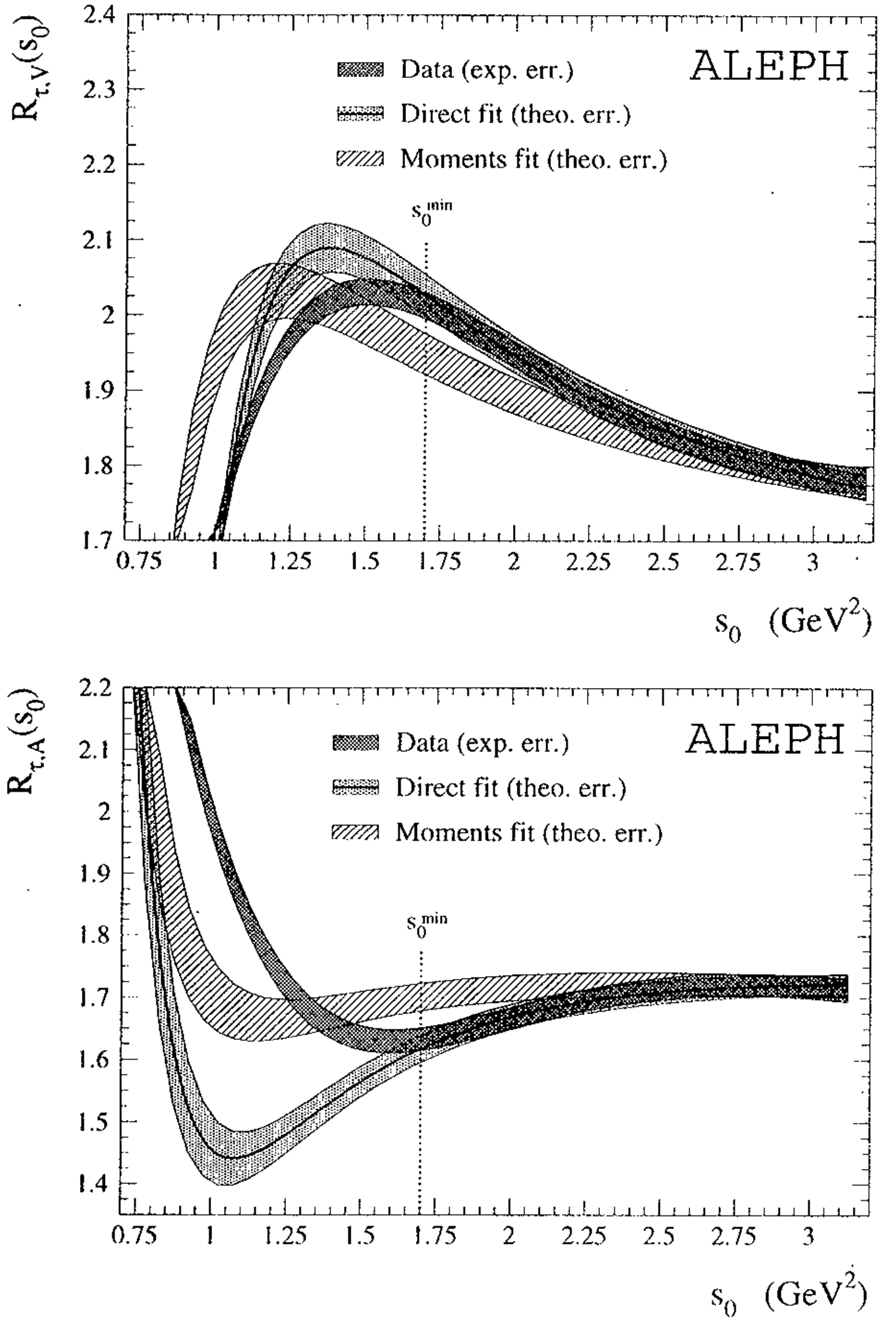

Figure 10.12: *Vector and axial-vector hadronic widths versus the square "τ mass" s_0. The limits of the OPE validity are pushed to much larger energies compared to the more inclusive ($V + A$) case.*

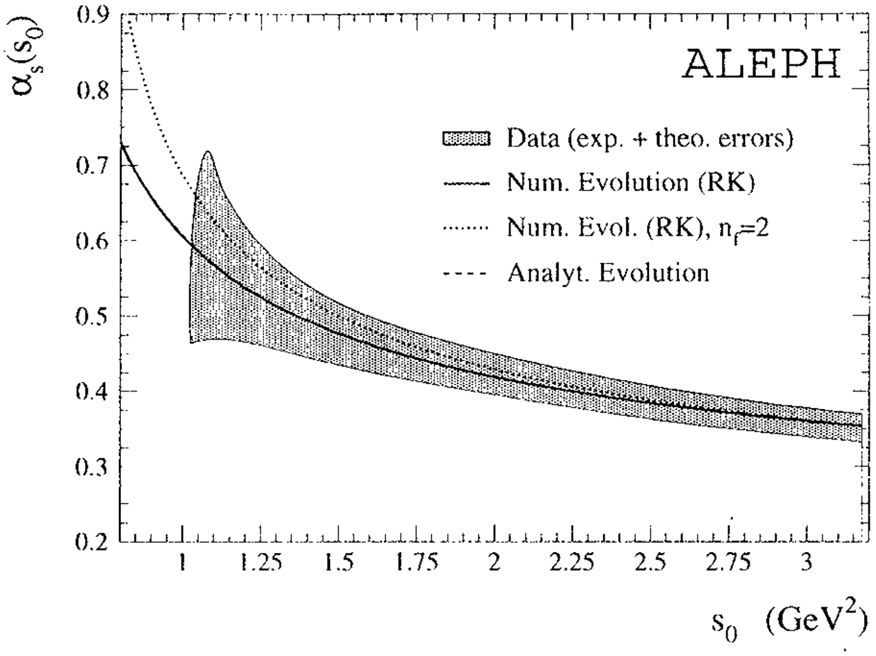

Figure 10.13: *The running of $\alpha_s(s)$ as obtained from the fit of $R_{\tau,V+A}(s_0)$ to the theoretical prediction. the shaded band shows the data including experimental and theoretical errors. The lines depict the different methods to solve the RGE. The analytical method corresponds to Eq. (2.13). The numerical method uses Runge-Kutta integration (up to four loops of the β-function) to solve the differential equation. Both curves are identical. Also shown is the solution with two active flavours only. The blowing up of the error at small s_0 stems from the uncertainties in the non-perturbative dimension $D = 6$ and $D = 8$ terms that become dominant for $s_0 < 1$.*

any perturbative contribution for this inspection. Fig. 10.14 depicts $R_{\tau,V-A}$ versus s_0. One observes that it is clearly positive at M_τ^2. The regime of validity for the OPE has again become smaller, *i.e.*, s_0^{min} is located around 2 GeV, a fact that is actually trivial as deviations from the OPE are reinforced in $(V - A)$ compared to V, A. Two fits have been performed in order to test the underlying power law:

$$(1): \quad R_{\tau,V-A}(s_0) = \frac{3}{2} V_{ud}^2 S_{\mathrm{EW}} \left(\frac{C_D \langle \mathcal{O}_D \rangle}{s_0^{D/2}} \right) \, , \quad 2\ \mathrm{GeV}^2 \le s_0 \le M_\tau^2 \, , \tag{10.27}$$

$$(2): \quad R_{\tau,V-A}(s_0) = \frac{3}{2} V_{ud}^2 S_{\mathrm{EW}} \left(\frac{C_6 \langle \mathcal{O}_6 \rangle}{s_0^3} + \frac{C_8 \langle \mathcal{O}_8 \rangle}{s_0^4} \right) \, , \quad 1.2\ \mathrm{GeV}^2 \le s_0 \le M_\tau^2 \tag{10.28}$$

The first fit Eq. (10.27), which has as free parameters the dimension D and the complete term $C_D\langle \mathcal{O}_D \rangle$, serves to fix the "genuine" power law, while the second fit adjusts the two dimension $D = 6, 8$ operators in order to test the compatibility of the OPE approach with the non-perturbative shape of the data. The results are $D = 6.9 \pm 0.5$ and $C_D\langle \mathcal{O}_D \rangle = 2.2 \pm 0.6$ for the fit Eq. (10.27) and $C_6\langle \mathcal{O}_6 \rangle = 4.24 \pm 0.16$ and $C_8\langle \mathcal{O}_8 \rangle = -4.83 \pm 0.17$ for Eq. (10.28) with, in both fits, strong anti-correlations between the fitted quantities of 97.5% and 98.7%, respectively. Thus, the dominating power of dimension $D = 6$ can

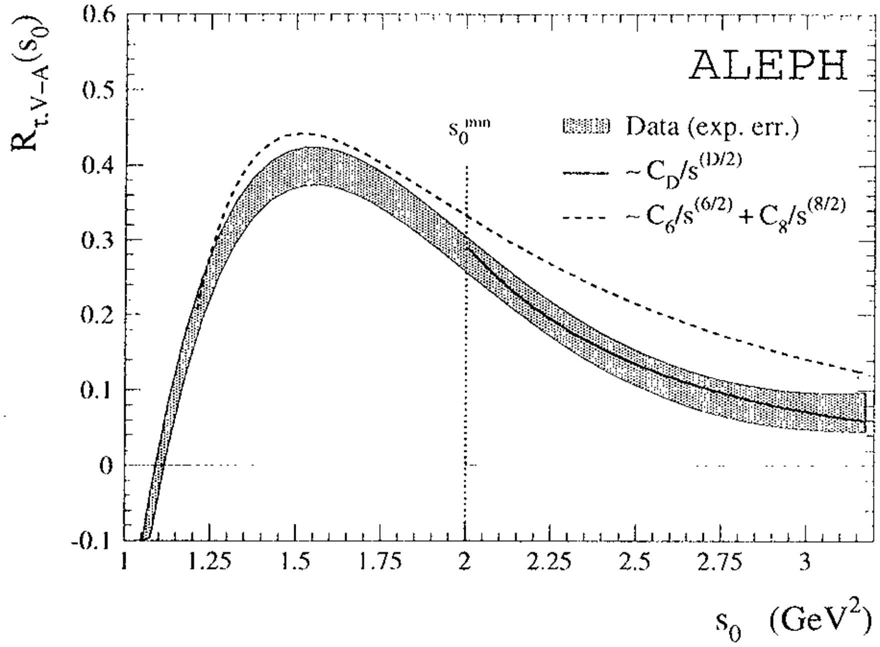

Figure 10.14: *Difference of vector and axial-vector hadronic width $R_{\tau,V-A}$ versus the "τ mass" s_0. The solid/dashed line corresponds to the fit Eq. (10.27)/(10.28).*

be confirmed, which supports the SVZ approach [11]. On the other hand, the second fit reveals that the inclusion of an additional $D = 8$ power term in the OPE does not quantitatively improve the agreement between the theoretical prediction (OPE) and the data. The point of inflexion at about 2 GeV^2, which causes the break down of the pure dimension $D = 6$ OPE, is not governed by a power $D = 8$ but rather by $D \simeq 10$. This suggests that prudence is required in the interpretation of the excellent precision obtained for the dimension $D = 8$ operators in the vector and axial-vector fits of Tab. 10.7, *i.e.*, for a term which is actually not quite meaningful.

Looking at Fig. 8.3 in Section 8.1 one may consider that additional insight into the non-perturbative power law ought to be obtained from an inclusion of e^+e^- annihilation vector data at energies above the τ. This is the same exercise already performed in Section 10.1 in order to provide a comparison to τ data. However, when becoming quantitative one has to be careful about the consistent treatment of the different data sets to avoid differences between τ vector and e^+e^- isovector spectral functions from being falsely interpreted as contributions to $(V - A)$. Therefore, the major part, in particular the ρ resonance where τ and e^+e^- data show some disagreement in the normalisation, is still entirely taken from τ $(V - A)$ data. Beyond $s_0 = 2.7$ GeV^2 (where τ and e^+e^- data agree for the vector spectral function), a combination of $R_{\tau,V+A}(s_0)$, obtained from the QCD fit (Tab. 10.7), and two times the vector part from e^+e^- annihilation data are used. The $R_{\tau,V+A}(s_0)$ theoretical prediction has proved in Fig. 10.11 to be very reliable down to values of $s_0 \simeq 1$ GeV^2 because non-perturbative contributions cancel out. Therefore, it should be therefore even more stable for energies above M_τ. In addition to

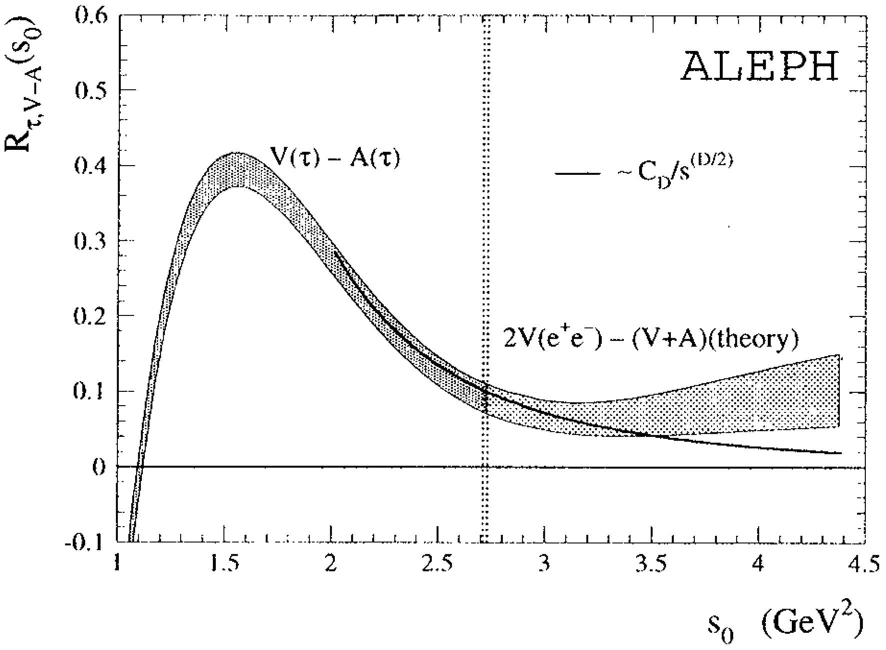

Figure 10.15: *Difference of vector and axial-vector hadronic width $R_{\tau,V-A}$ obtained from τ spectral functions (left side) and a combination of e^+e^- annihilation data and the QCD theoretical prediction (right side) versus s_0. The solid line corresponds to the fit Eq. (10.27).*

this, the $R_{\tau,V+A}(s_0)$ theoretical prediction is normalised at $s_0 = M_\tau^2$ to the measurement Eq. (10.20). Fig. 10.15 depicts the corresponding $R_{\tau,V-A}(s_0)$ distribution. The plotted function is Eq (10.27) extended to masses $s_0 > M_\tau^2$. The result seems to be a bit discouraging as it is hardly compatible with a pure dimension $D = 6$ contribution[4] This inconsistency with the OPE approach could be another hint (see Section 8.2) of an overestimation of the vector part, possibly due to an axial-vector dominance of the $\mathrm{K}\bar{K}\pi$ final states. This is still rather speculative and must be cleared up in forthcoming analyses. It should be strongly emphasized that these difficulties do not affect the inclusive $(V+A)$ measurement on which the $\alpha_s(M_\tau)$ determination is based. However, again one sees that results based on pure vector (or pure axial-vector) should be handled with particular care as the applicability of the OPE approach is not yet on solid ground.

The last point to be discussed here is concerned with Question 6, *i.e.*, does the study of the running provide additional constraints on K_4 or an operator of dimension $D = 2$? The problem associated with these two quantities insomuch as they are degenerate with α_s is that a simultaneous determination of them *and* α_s is not practicable. Using α_s measurements from other experiments as input is actually not more meaningful as the precision is insufficient to obtain informative constraints. One possibility is to advocate the method of Ref. [263] which determines K_4 at a renormalisation scale $\mu \simeq 1$ GeV,

---

[4] Note that the strong correlations allow indeed easily a vertical shift of the total curve but the direction, *i.e.*, the slope is well determined.

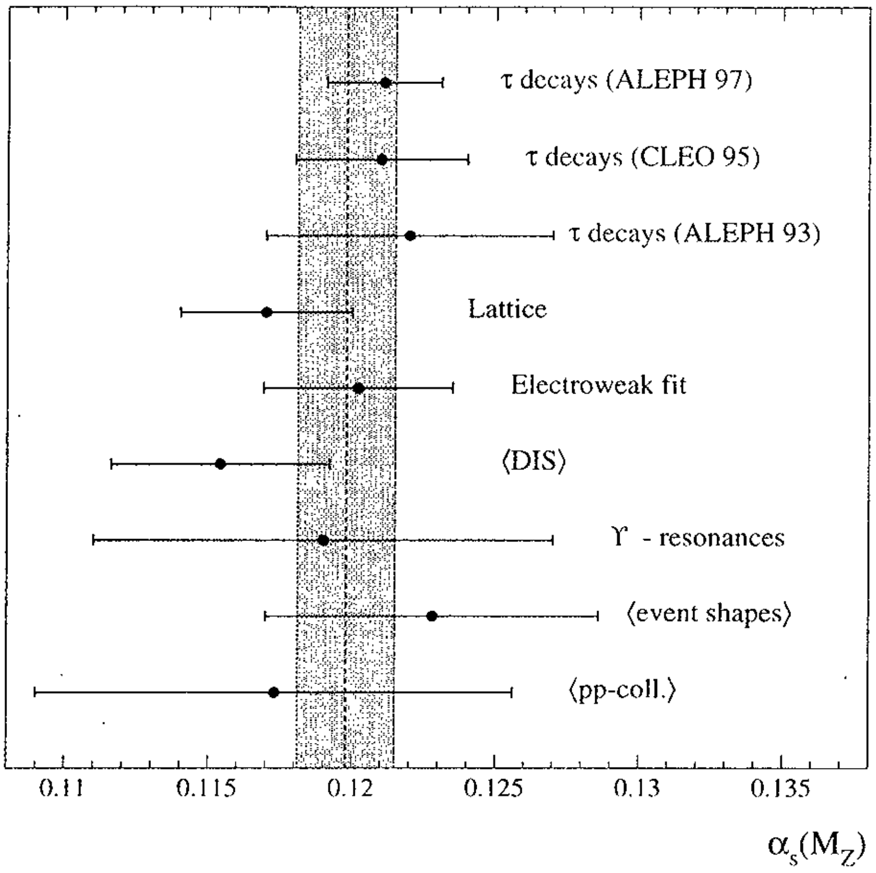

Figure 10.16: *Compilation of α_s measurements evolved to M_Z. The shaded band depicts the new world average. The CLEO 95 and ALEPH 93 measurements have been rescaled by the current B_ℓ world average.*

i.e., significantly lower than the τ mass, in order to increase the sensitivity. The value obtained is very precise, but theoretically questioned [266]. The degeneracy between α_s and the $D = 2$ term is even larger and all attempts to obtain a limit will usually fail. In addition, $D = 2$ terms, which might arise from the truncation of the perturbative series (Section 2.5.3), are of perturbative origin and should therefore cancel in $R_{\tau,V-A}$. Upper limits, obtained from the V, A or $(V + A)$, reach 5%.

10.2.5 A New World Average

Following the summary of α_s measurements presented in Section 2.6, a new world average can be computed using the present measurement Eq. (10.25), which turns out to yield the most precise individual $\alpha_s(M_Z)$ determination. Fig. 10.16 presents the new value for $\alpha_s(M_\tau)$ in comparison to older ones taken from Refs. [8] and [9] (renormalised to the new massless leptonic branching ratio — see footnote in Section 2.6). Also shown are other precise measurements from Lattice QCD [119] and the overall electroweak fit [112] (the corresponding values are given in Tab. 2.2 Section 2.6). and the average over all other measurements not exclusively presented here (flagged "yes" in Tab. 2.2). The shaded band depicts the new world average that is found, using the mathematics of Section 2.6, to be

$$\langle \alpha_s(M_Z) \rangle = 0.1198 \pm 0.0017 , \tag{10.29}$$

with a χ^2/d.o.f. = 3.9/6 assuming a correlation of 30% due to the theoretical input into the analyses. Only the new $\alpha_s(M_\tau)$ result is used in the average.

10.3 Comments and Conclusion

The preceeding sections dealt with two important (one might say *genuine*) applications of the τ spectral functions to QCD: chiral sum rules are exploited in order to test vector/axial-vector saturation at M_τ. It could be shown that even if the actual precision of the spectral functions at the end of the τ phase space is rather weak, the application of Borel transformed sum rules significantly improves their asymptoticness and allows one to obtain accurate results. The main point of this analysis is that a measurement of α_s at M_τ has been performed using a fit of non-perturbative operators and $\alpha_s(M_\tau)$ to the τ hadronic width and spectral moments, where the latter were taken from the τ spectral functions. The result obtained for $\alpha_s(M_\tau)$ is currently the most precise experimental determination (Section 2.6). It is dominated by theoretical errors. Consistency checks concerning the running of $\alpha_s(s_0)$ and the non-perturbative contribution to the hadronic width were performed. Due to the suppression of non-perturbative terms, the theoretical prediction of $R_{\tau,V+A}(s_0)$ was shown to be in perfect agreement with the data down to the ρ region. It has further been shown that the dominant power law of the non-perturbative part is compatible with a dimension $D = 6$. Additional insight into the non-perturbative behaviour became possible beyond M_τ by using the $(V + A)$ theoretical prediction and data from e^+e^- annihilation. With increasing $s_0 > M_\tau^2$, the non-perturbative contribution flattens significantly around $R_{\tau,V-A}(s_0) \simeq 0.1$, which is in disagreement with the OPE expectation. However, this is a small effect in the $(V - A)$ part, which emphasizes the non-perturbative contribution, by a factor of larger than 10 compared to the $(V + A)$ part which is used to determine α_s and where the non-perturbative contributions are negligibly small. The fact that the value of $\alpha_s(M_\tau)$ determined here allows one to reproduce the behaviour of $R_{\tau,V+A}$ down to ~ 0.7 GeV^2 is a rather unexpected result and puts the α_s determination at the τ scale on a very solid ground.

Conclusions and Outlook

Conclusions and Outlook

The experimental aim of the analysis presented in this thesis is the measurement of the non-strange vector and axial-vector spectral functions of semi-hadronic τ decays. The principal ingredients of the spectral functions are the invariant mass-squared spectra of the hadronic final states normalized to their respective branching ratios. The latter are mainly taken from the comprehensive ALEPH analysis of Ref. [24], while rare or unknown decay channels are bound using isospin symmetry arguments.

For each event passing τ pair selection, charged track identification and τ hadronic decay classification, the critical steps of the invariant mass-squared measurement are the energy and momentum calibration and the rejection of fake photons. In addition, the unfolding of detector effects, which is necessary in order to obtain the physical mass-squared spectra, demands particular care. A new experimental method is employed based on a singular value decomposition of the detector response matrix and a regularization of its inverse.

Extensive systematic comparisons of Monte Carlo simulation to the data are performed to ensure the high precision of the spectral function measurement. For the π^0 reconstruction is especially important: the study and correction of fake photons, the ECAL energy calibration and resolution, the photon reconstruction efficiency and the π^0 mass measurement. The track reconstruction is also investigated: the momentum calibration and resolution as well as the reconstruction efficiency and the effect of secondary nuclear interactions. The unfolding method, the limited Monte Carlo statistics and the branching ratios as well as the non-τ background are all considered. It turns out that the fake photon rejection, the branching ratios and the unfolding procedure yield the dominant systematic error sources.

The spectral function analysis opens a wide range of interesting applications on phenomenological QCD and provides important information about an energy region which is out of reach of present theoretical predictions. The hypothesis of conserved vector currents (CVC) associates the τ vector spectral functions with the cross sections of corresponding isovector final states of e^+e^- annihilation experiments. Comparisons are performed between the two- and four-pion channels as well as between the total vector and isovector spectral functions from τ decays and e^+e^- data. The compilation of the total spectral functions both in τ decays and e^+e^- annihilation requirs particular care. Additional information from isospin symmetry regarding unknown or unmeasured final states is necessary. Conversely, the CVC predictions of the vector τ branching ratios from e^+e^- cross sections are compared to measured quantities from τ decays. In general, good agreement is found between e^+e^- and τ data, where in many cases τ data are more accurate. A combined fit of the pion form factor using phenomenological formula based on vector resonances is performed in order to extract the difference in mass and width between the charged $\rho^\pm$ (from τ decays) and the neutral ρ^0 (in e^+e^- annihilation). They are found to be

$$\begin{aligned} \Delta M_{\rho(770)} &= (0.0 \pm 1.0 \pm 0.1)\ \mathrm{MeV}/c^2 \\ \Delta \Gamma_{\rho(770)} &= (0.1 \pm 1.8 \pm 0.5)\ \mathrm{MeV}/c^2 , \end{aligned}$$

where the first errors are the direct fit uncertainties and the second errors account for model dependencies. The fit result is found to be in agreement with a theoretical estimate of the electromagnetic ρ mass difference.

In the ρ dominated two-pion final state, the precision of τ spectral functions exceeds the accuracy of e^+e^- cross section measurements. This is exploited to improve the calculation of the hadronic contributions to the muon $(g-2)$ and to the running of the fine structure constant, $\alpha(M_Z^2)$. These hadronic contributions dominate the present accuracy of the two basic physical observables. Both contributions are evaluated by means of a dispersion integral over experimental data in an energy regime that is deeply non-perturbative, and therefore not predictable with current QCD methods. Data from τ spectral functions are included via CVC for the most precise two- and four-pion final states. Since the particular accuracy of the two-pion integral reaches a precision of the order of one per cent, a detailed study of CVC violating electromagnetic effects is performed. It provides a small correction to the measured contribution from τ decays of about -0.3%. The hadronic contributions obtained from the respective integrals are for the muonic $(g-2)$

$$\begin{aligned} a_\mu^{\rm had} &= (695.0 \pm 15.0) \times 10^{-10} \quad (e^+e^- \text{ data only}) \\ a_\mu^{\rm had} &= (701.1 \pm 9.4) \times 10^{-10} \quad (\text{combined } e^+e^- \text{ and } \tau \text{ data}) \end{aligned}$$

and for the running of α at M_Z^2

$$\begin{aligned} \Delta\alpha_{\rm had}^{(5)}(M_Z^2) &= (280.9 \pm 6.3) \times 10^{-4} \quad (e^+e^- \text{ data only}) \\ \Delta\alpha_{\rm had}^{(5)}(M_Z^2) &= (281.7 \pm 6.2) \times 10^{-4} \quad (\text{combined } e^+e^- \text{ and } \tau \text{ data}) \ . \end{aligned}$$

A global electroweak fit, performed with the new determination (incl. τ data) of $\alpha^{-1}(M_Z^2) = 128.878 \pm 0.085$, leads to a Higgs boson mass of 138^{+137}_{-76} GeV.

The difference of vector and axial-vector spectral functions offers insight into the low energy behaviour of QCD and the applicability of chiral symmetry. The DMO sum rule, the first and second Weinberg sum rules, as well as the sum rule related to the electromagnetic pion mass splitting, all relate integrals with infinite upper ranges to precise predictions obtained using chiral symmetry, *i.e.*, using massless light quarks. It is shown in this analysis that at the τ mass scale these integrals are not saturated, *i.e.*, they are still oscillating, so that an evaluation of the sum rules cannot be performed easily. However, the application of finite energy sum rule techniques considerably improves the convergence of the integrals, and allows for the evaluation of the pion polarizability by means of the DMO sum rule:

$$\alpha_E = (2.68 \pm 0.91) \times 10^{-4} \text{ fm}^3 \ .$$

The error includes experimental and systematic uncertainties.

An important application of hadronic τ decays to QCD is the determination of the strong coupling constant $\alpha_s(M_\tau)$. The principle of the measurement is based on a fit of the theoretical prediction for an inclusive observable to the data, where $\alpha_s(M_\tau)$ is a free parameter. Since QCD is applied here at a low energy scale, one has to worry whether non-perturbative effects play a role. This is accounted for by the use of the low energy Operator Product Expansion (OPE), which organizes the non-perturbative contributions as an expansion in powers of the τ mass and coefficients which can be fitted simultaneously with $\alpha_s(M_\tau)$. The observables used are the τ hadronic width and spectral moments, which are complementary to each other in the sense that they use information from the normalization (R_τ) and the form of the spectral functions only (moments). The best and most robust determination of $\alpha_s(M_\tau)$ is obtained from the inclusive $(V + A)$ fit that yields

$$\alpha_s(M_\tau) = 0.348 \pm 0.008_{\rm exp} \pm 0.015_{\rm theo} \ .$$

This value evolved to the Z mass scale gives

$$\begin{aligned} \alpha_s(M_Z) &= 0.1211 \pm 0.0008_{\rm exp} \pm 0.0016_{\rm theo} \pm 0.0010_{\rm evol} \ , \\ &= 0.1211 \pm 0.0021 \ . \end{aligned}$$

Expressed in terms of the $\overline{\rm MS}$ renormalization scale at $\mu = M_\tau$ with three active flavours at three loop level one has

$$\Lambda^{(3)}_{\overline{\rm MS}} = (397 \pm 14_{\rm exp} \pm 27_{\rm theo}) \ {\rm MeV} \ .$$

The result is dominated by theoretical uncertainties, whose evaluation is still delicate. The total non-perturbative contribution to $R_{\tau,V+A}$ is found to be compatible with zero and negligibly small. However, the same fit using the exclusive vector and axial-vector hadronic widths and moments revealed that the non-perturbative contributions, in particular of dimension $D = 6$, are large, but fortunately exactly cancel out in the inclusive sum, within present accuracy.

The spectral function measurement opens the possibility to measure the τ hadronic width as a function of a variable "τ mass" $s_0 \leq M_\tau^2$, taking advantage of the universal nature of the measured spectral functions. This provides a direct test of the running of $\alpha_s(s_0)$ which governs the evolution of the theoretical prediction to values smaller than the τ mass. A perfect agreement between the measured $R_{\tau,V+A}(s_0)$ and theory is found for the whole range of $0.7 \ {\rm GeV}^2 \leq s_0 \leq M_\tau^2$. At $0.7 \ {\rm GeV}^2$, $R_{\tau,V+A}(s_0)$ starts to blow up due to the influence of the ρ peak and the pion pole which are of non-perturbative origin. A direct fit of the data and theory in the valid region yields the result $\alpha_s(M_\tau) = 0.354 \pm 0.017$, including experimental and theoretical uncertainties, and very small contributions of non-perturbative origin. The above value is consistent with the result for $\alpha_s(M_\tau)$ obtained in the fit of $R_{\tau,V+A}(M_\tau^2)$ and the moments. The same direct fit is performed for the exclusive vector and axial-vector $R_{\tau,V/A}(s_0)$, where a worse agreement between experiment and theory is found, and strong non-perturbative contributions cause theory to break down much earlier, *i.e.*, at larger s_0. The evolution of the non-perturbative contributions as a function of s_0 is accessed directly by considering the difference $R_{\tau,V-A}(s_0)$ in which perturbative contributions cancel to all orders of the perturbative expansion. The fit of a free dimensional operator to $R_{\tau,V-A}(s_0)$ in order to test the dominant non-perturbative OPE dimension leads to

$$D = 6.9 \pm 0.5 \ .$$

This is in astonishing agreement with the assumption of a dominant $D = 6$ contribution made in the SVZ approach. A fit of $R_{\tau,V-A}(s_0)$ to an operator $D = 6$ plus an operator $D = 8$ indicates that the addition of the $D = 8$ term does not quantitatively improve the validity of the OPE. Data from e^+e^- annihilation in combination with the theoretical prediction of $R_{\tau,V+A}(s_0)$ could be used to extend the OPE analysis to masses greater than M_τ and to elucidate the asymptotic behaviour of the non-perturbative contributions.

Future work must be done in both the experimental and the theoretical domains. Experimentally it has been shown that most of the physical observables calculated using the τ spectral functions as input are limited by the uncertainties in the hadronic branching ratios and in the separation of vector and axial-vector final states. The accuracy of the hadronic branching ratios is expected to be improved substantially by means of a forthcoming ALEPH analysis which will include the whole LEP I data set from 1990–1995. An improvement in the simulation of fake photons or the fake photon suppression in data will provide a higher precision of the low mass-squared tail of the $\pi^-\pi^0$ spectral function, which is important in the evaluation of the hadronic contribution to the muon $(g-2)$. A better knowledge of the dynamics and the branching ratios of multi-pion and $K\bar{K}$ final states is necessary in order to extract more accurate information about their G-parity and/or contributions from eventual isospin violating decays of intermediate states. A more detailed experimental and theoretical analysis of CVC violating effects occurring in τ decays and e^+e^- annihilation would improve the accuracy and reliability of all comparisons and calculations based on the CVC hypothesis. Clearly, the evaluation of the hadronic contribution to the running of the QED fine structure constant at M_Z can be improved using additional theoretical input for energy scales lower than 40 GeV from perturbative, and even non-perturbative, QCD. The QCD analysis of the τ spectral functions revealed that at the order of the τ mass scale QCD already describes the data well. Additional interesting results are expected from a deeper study of the Borel transformed finite energy sum rules. Optimistically, one might obtain constraints on the light u, d quark masses using fits to moments of the Borel parameter M^2. The measurement of the strange spectral function and, even more powerful, the separation of strange vector and axial-vector components would give rise to tests of further sum rules involving, *e.g.*, the difference between non-strange and strange vector spectral functions, which could receive significant contributions from the mass of the strange quark.

Theoretically, a primary goal is to achieve a better understanding of the higher order N^{3}LO perturbative contribution to the τ hadronic width. If a direct calculation of the first unknown coefficient K_4 is currently out of reach, more detailed studies of contributions from so-called renormalization chains seem to be necessary. In addition, the claimed non-existence of a dimension $D = 2$ contribution to R_τ is still discussed among theorists and requires further work. It is not unreasonable to hope to obtain answers from experiment to these primarily theoretical problems.

Bibliography

[1] M.L. Perl *et al.*, *Phys. Rev. Lett.* **35** (1975) 1489.

[2] Y.S. Tsai, *Phys. Rev.* **D4** (1971) 2821.

[3] H. Albrecht *et al.* (ARGUS Collaboration), *Phys. Lett.* **B185** (1987) 223.

[4] W.T. Ford, *Nucl. Phys.* **B40** (Proc. Suppl.) (1995) 191.

[5] D. Buskulic *et al.* (ALEPH Collaboration), CERN PPE/96-103 (1996).

[6] T. Das, V.S. Mathur and S. Okubo, *Phys. Rev. Lett.* **19** (1967) 895.

[7] S. Weinberg, *Phys. Rev. Lett.* **18** (1967) 507.

[8] D. Buskulic *et al.* (ALEPH Collaboration), *Phys. Lett.* **B307** (1993) 209.

[9] T. Coan *et al.* (CLEO Collaboration), *Phys. Lett.* **B356** (1995) 580.

[10] L. Duflot, *Nucl. Phys.* **B40** (Proc. Suppl.) (1995) 37.

[11] M.A. Shifman, A.L. Vainshtein and V.I. Zakharov, *Nucl. Phys.* **B147** (1979) 385, 448, 519.

[12] E. Braaten, S. Narison and A. Pich, *Nucl. Phys.* **B373** (1992) 581.

[13] F. Le Diberder and A. Pich, *Phys. Lett.* **B289** (1992) 165.

[14] S.L. Glashow, *Nucl. Phys.* **22** (1961) 579;
S. Weinberg, *Phys. Rev. Lett.* *19* (1967) 1264.
A. Salam, Proceedings of the Eigth Nobel Symposium, Ed. N. Svartholm, Wiley Interscience, N.Y. 1968, 367.

[15] M. Kobayashi and T. Maskawa, Prog. Theor. Phys. **49** (1973) 652;
N. Cabibbo, *Phys. Rev. Lett.* **10** (1963) 531.

[16] D. Abbaneo *et al.* (LEP Electroweak Working Group), CERN PPE-96-183 (1996).

[17] R.M. Barnett *et al.* (Particle Data Group), *Phys. Rev.* **D54** (1996) 1.

[18] M.L. Perl, Lectures given at 20th SLAC Summer Institute on Particle Physics, Stanford, California 1992, SLAC PUB-6071.

[19] J.Z. Bai *et al.* (BES Collaboration), *Phys. Rev.* **D53** (1996) 20.

[20] H. Albrecht *et al.* (ARGUS Collaboration), *Phys. Lett.* **B292** (1993) 221.

[21] R. Barate *et al.* (ALEPH Collaboration), CERN PPE/97-016 (1997);
D. Buskulic *et al.* (ALEPH Collaboration), *Z. Phys.* **C70** (1996) 549;
D. Decamp *et al.* (ALEPH Collaboration), *Phys. Lett.* **B279** (1992) 411;
D. Buskulic *et al.* (ALEPH Collaboration), *Phys. Lett.* **B279** (1992) 432.

[22] P. Weber, 'Review of τ lifetime measurements', Talk given at the TAU96 Conference, Colorado, 1996.

[23] D. Buskulic *et al.* (ALEPH Collaboration), *Z. Phys.* **C70** (1996) 561.

[24] D. Buskulic *et al.* (ALEPH Collaboration), *Z. Phys.* **C70** (1996) 579.

[25] W. Marciano and A. Sirlin, *Phys. Rev. Lett.* **61** (1988) 1815; *Phys. Rev. Lett.* **61** (1986) 1815.

[26] M. Davier, L. Duflot, F. Le Diberder and A. Rougé, *Phys. Lett.* **B306** (1993) 411.

[27] I. Nikolic, Thesis, Université de Paris-Sud, Report LAL 96-27 (1996).

[28] J.H. Christenson *et al.*, *Phys. Rev. Lett.* **13** (1964) 138.

[29] W. Bernreuther and O. Nachtmann, *Phys. Lett.* **63** (1989) 2787.

[30] R. Akers *et al.* (OPAL Collaboration), *Z. Phys.* **C66** (1995) 31.

[31] N. Wermes, 'CP Tests and Dipole Moments in τ Pair Production Experiments', Talk given at the TAU96 Conference, Colorado, 1996.

[32] C. Bouchiat and L. Michel, *Phys. Rev.* 106 (1957) 170.

[33] M. Chadha, 'Measurement of Michel Parameters at CLEO', Talk given at the TAU96 Conference, Colorado, 1996.

[34] Chorus Proposal, CERN SPSLC/90-42 (1990);
M. de Jorg *et al.* (CHORUS Collaboration), CERN PPE/93-131 (1993).

[35] NOMAD proposal and addenda, CERN SPSLC/91-21, /91-48, /91-53, /93-19, 94-21, 94-28 (1991-94);
A. Rubbia (NOMAD Collaboration), *Nucl. Phys.* **B40** (Proc. Suppl.) (1995) 93.

[36] D. Cinabro *et al.* (CLEO II Collaboration), *Phys. Rev. Lett.* **70** (1993) 3700.

[37] R. Akers *et al.* (OPAL Collaboration), *Z. Phys.* **C65** (1995) 183.

[38] D. Buskulic *et al.* (ALEPH Collaboration), *Phys. Lett.* **B349** (1995) 585.

[39] G. Alexander *et al.* (OPAL Collaboration), *Z. Phys.* **C72** (1996) 231.

[40] A. Höcker, LAL Report in preparation.

[41] R. McNaulty, Talk given at APSDPF96, Minneapolis, August 1996.

[42] L. Passalacqua, 'Direct Bounds on the Tau Neutrino Mass from LEP', Talk given at the TAU96 Conference, Colorado, 1996.

[43] S. Gentile and M. Pohl, *Phys. Rep.* **274** (1996) 287.

[44] J.H. Kühn and E. Mirkes, *Z. Phys.* C56 (1992) 661.

[45] E. Braaten and C.S. Li, *Phys. Rev.* **D42** (1990) 3888.

[46] A. Höcker, 'Vector and Axial-Vector Spectral Functions and QCD', Talk given at the TAU96 Conference, Colorado, 1996.

[47] P.L. Campana, 'Branching fractions for modes involving kaons', Talk given at the TAU96 Conference, Colorado, 1996.

[48] J.F. Donoghue and E. Golowich, *Phys. Rev.* **D49** (1994) 1513.

[49] R. Decker and M. Finkemeier, *Nucl. Phys.* **B438** (1995) 17.

[50] M. Finkemeier, W. Marciano and A. Pich, *private communications* (Nov. 1996).

[51] A. Pich, *Nucl. Phys.* **B39** (Proc. Suppl.) (1995) 326.

[52] A. Pàis, *Ann. Phys.* **9** (1960) 548.

[53] G. Colangelo, M. Finkemeier and R. Urech, *Phys. Rev.* **D54** (1996) 4403.

[54] A. Rougé, *Z. Phys.* **C70** (1996) 65.

[55] R.J. Sobie, *Z. Phys.* **C69** (1995) 99.

[56] J.D. Bjorken, *Phys. Rev.* **179** (1969) 1547;
C.N. Yang, in *High Energy Collisions* (Gordon & Breach, N.Y.), (1969) 509.

[57] R. Feynman, *Phys. Rev. Lett.* **23** (1969) 1415;
S.D. Drell and T.M. Yan, *Ann. Phys.* **66** (1971) 578.

[58] H.D. Politzer, *Phys. Rev. Lett.* **30** (1973) 1346;
D. Gross and F. Wilczek, *Phys. Rev. Lett.* **30** (1973) 1343.

[59] M. Gell-Mann, *Phys. Lett.* **8** (1964) 214;
G. Zweig CERN TH/401 and TH/412 (1964).

[60] H. Fritzsch, M. Gell-Mann and H. Leutwyler, *Phys. Lett.* **B47** (1973) 365.

[61] R. Brandelik *et al.* (TASSO Collaboration), *Phys. Lett.* **B86** (1979) 243;
D.P. Barber *et al.* (MARK J Collaboration), *Phys. Rev. Lett.* **43** (1979) 830;
Ch. Berger *et al.* (PLUTO Collaboration), *Phys. Lett.* **B86** (1979) 418;
W. Bartel *et al.* (JADE Collaboration), *Phys. Lett.* **B91** (1980) 142.

[62] P.M. Zerwas and H.A. Kastrup, eds., 'QCD 20 Years Later' World Scientific, Singapore 1993.

[63] T. Pich, Lectures given at 1994 European School of High Energy Physics, Sorrento, Italy 1994, FTUV-95-19 (1995).

[64] R.L. Mills and C.N. Yang, *Phys. Rev.* **96** (1954) 191.

[65] G. t'Hooft and M. Veltman, *Nucl. Phys.* **B44** (1972) 189.

[66] G. t'Hooft and M. Veltman, *Nucl. Phys.* **B44** (1972) 189;
W.A. Bardeen, A.J. Buras, D.W. Duke and T. Muta, *Phys. Rev.* **D18** (1978) 3998.

[67] T. Appelquist and J. Carazzone, *Phys. Rev.* **D11** (1975) 2856.

[68] W. Bernreuther, *Ann. Phys.* **151** (1983) 129.

[69] W. Bernreuther, W. Wetzel, *Nucl. Phys.* **B197** (1982) 228;
W. Wetzel, *Nucl. Phys.* **B196** (1982) 259;
W. Bernreuther, Talk given at Workshop on QCD at LEP, Aachen, Germany 1994, PITHA-94-31 (1994).

[70] S.A. Larin, T. van Ritbergen and J.A.M. Vermaseren, *Nucl. Phys.* **B438** (1995) 278.

[71] W. Bernreuther, *private communication*, April 1997.

[72] F.B. Hildebrandt, 'Introduction to numerical analysis', McGraw-Hill, N.Y. 1956, Sect. 6.16.

[73] T. van Ritbergen, J.A.M. Vermaseren and S.A. Larin, UM-TH-97-01, NIHHEF-97-001, e-Print Archive: hep-ph/9701390 (1997).

[74] L.J. Reinders, H. Rubinstein and S. Yazaki, *Phys. Rep.* **127** (1985) 1.

[75] K.G. Wilson, *Phys. Rev.* **179** (1969) 1499.

[76] D.J. Broadhurst and S.C. Generalis, *Phys. Lett.* **B165** (1985) 175.

[77] E. Floratos, S. Narison and E. de Rafael, *Nucl. Phys.* **B155** (1979) 115.

[78] S. Narison, 'QCD Spectral Sum Rules', World Scientific Lecture Notes in Physics – Vol. 26, World Scientific, Singapore 1989.

[79] J. Gasser and H. Leutwyler, *Phys. Rep.* **87** (1982) 77.

[80] J. Goldstone, *Nuovo Cim.* **19** (1961) 154;
J. Goldstone, A. Salam and S. Weinberg, *Phys. Rev.* **127** (1962) 965;
Y. Nambu and G. Jona-Lasinio, *Phys. Rev.* **122** (1961) 345.

[81] A. Pich, CERN TH/93-6978 (1993).

[82] R.D. Peccei and J. Solà, *Nucl. Phys.* **B281** (1987) 1.

[83] T. Das, G.S. Guralnik, V.S. Mathur, F.E. Low and J.E. Young, *Phys. Rev. Lett.* **18** (1967) 759.

[84] K. Kawarabayashi and M. Suzuki, *Phys. Rev. Lett.* **16** (1966) 225; K. Riazzuddin and M. Fayazuddin, *Phys. Rev.* **147** (1966) 1071.

[85] V.G. Kartvelishvili and M.V. Margvelashvili, *Z. Phys.* **C55** (1992) 83.

[86] F. Le Diberder and A. Pich, *Phys. Lett.* **B286** (1992) 147;

[87] S. Narison and A. Pich, *Phys. Lett.* **B211** (1988) 183.

[88] S. Narison, *Nucl. Phys.* **B40** (Proc. Suppl.) (1995) 47; G. Altarelli, P. Nason and G. Ridolfi, *Z. Phys.* **C68** (1995) 257; P.A. Rączka and A. Szymacha, *Z. Phys.* **C70** (1996) 125.

[89] M. Neubert, *Nucl. Phys.* **B463** (1996) 511.

[90] M .Davier, 'τ decays into strange particles and QCD', Talk given at the TAU96 Conference, Colorado, 1996.

[91] E. Braaten, *Phys. Rev. Lett./* **60** (1988) 1606.

[92] K.G. Chetyrkin and A. Kwiatkowski, *Z. Phys.* **C59** (1993) 525.

[93] S. Adler, *Phys. Rev.* **D10** (1974) 3714.

[94] K.G. Chetyrkin, A.L. Kataev and F.V. Tkachov, *Phys. Lett.* **85** (1979) 277.

[95] S.G. Gorishny, A.L. Kataev and S.A. Larin, *Phys. Lett.* **B259** (1991) 144;
L.R. Surguladze and M.A. Samuel, *Phys. Rev. Lett.* **66** (1991) 560.

[96] P. Ball, M. Beneke and V.M. Braun, *Nucl. Phys.* **B452** (1995) 563.

[97] G. Altarelli, P. Nason and G. Ridolfi, *Z. Phys.* **C68** (1995) 257.

[98] A.H. Mueller, 'The QCD Perturbation Series', in 'QCD 20 Years Later', Aachen 1992, ed. P. Zerwas and H.A. Kastrup, World Scientific, Singapore 1993, Vol. 1, 162.

[99] M. Beneke and V.I. Zakharov, *Phys. Rev. Lett.* **69** (1992) 2472; M. Beneke, *Nucl. Phys.* **B385** (1992) 452.

[100] C. Becchi, S. Narison, E. de Rafael and F.J. Yndurain, *Z. Phys.* **C8** (1981) 335;
D.J. Broadhurst, *Phys. Lett.* **B101** (1981) 423;
S.C. Generalis, *J. Phys.* **G15** (1989) L225.

[101] K.G. Chetyrkin, S.G. Gorishny and V.P. Spiridonov, *Phys. Lett.* **B160** (1985) 149.

[102] D.J. Broadhurst and S.C. Generalis, *Phys. Lett.* **165** (1985) 175.

[103] S. Bethke *et al.* (JADE Collaboration), *Phys. Lett.* **B213** (1988) 235.

[104] R. Ball and S. Forte, *Phys. Lett.* **B358** (1995) 365.

[105] J. Ellis and M. Karliner, *Phys. Lett.* **B341** (1995) 397.

[106] J. Chyla and A.L. Kataev, *Phys. Lett.* **B297** (1992) 385.

[107] M. Schmelling, Talk given at the International Conference on High Energy Physics, Warsaw 1996.

[108] Y.L. Dokshitzer, Workshop on Jets and HERA, Durham (1990).

[109] W. Bartel *et al.* (JADE Collaboration), *Z. Phys.* **C33** (1986) 23.

[110] T. Hebbeker *et al.*, *Phys. Lett.* **B331** (1994) 165.

[111] R. Clare *et al.* (LEP Electroweak Working Group), LEP EWWG/96-01 (1996); Talk given at the International Conference on High Energy Physics, Warsaw 1996.

[112] A. Blondel, W. de Boer, Talks given at the International Conference on High Energy Physics, Warsaw 1996.

[113] F. Abe *et al.* (CDF Collaboration), *Phys. Rev. Lett.* **68** (1992) 1104.

[114] W.T. Giele, E.W.N. Glover and J. Yu, *Phys. Rev.* **D53** (1996) 120.

[115] C. Albajar *et al.* (UA1 Collaboration), *Phys. Lett.* **B369** (1996) 46.

[116] M. Jamin and A. Pich, IFIC/97-06, FTUV/97-06, HD-THEP-96-55 (1997).

[117] M.B. Voloshin, *Int. J. Mod. Phys.* **A10** (1995) 2865.

[118] M. Shifman, *Int. J. Mod. Phys.* **A11** (1996) 3195.

[119] J. Flynn, Talk given at the International Conference on High Energy Physics, Warsaw 1996.

[120] P.Z. Quintas *et al.* (CCFR Collaboration), *Phys. Rev. Lett.* **71** (1993) 1307.

[121] M. Virchaux and A. Milsztajn, *Phys. Lett.* **B274** (1992) 221.

[122] T. Ahmed *et al.* (H1 Collaboration), *Phys. Lett.* **B346** (1995) 415;
M. Derrick *et al.* (ZEUS Collaboration), *Phys. Lett.* **B363** (1995) 201.

[123] M. Kobel, Proc. of the XXVII Rencontre de Moriond, Les Arcs, France 1992.

[124] D. Haidt, 'Directions in High Energy Physics', Vol. 14, Precision Tests of the Standard Electroweak Model, ed. P. Langacker, World Scientific Company, 1993.

[125] S. Bethke, Proc. of the Workshop on the Standard Model at the Energy of Present and Future Accelerators, Budapest 1989, LBL-28112 (1989).

[126] Y. Ohnishi *et al.* (TOPAZ Collaboration), *Phys. Lett.* **B313** (1993) 475.

[127] R. Barate *et al.* (ALEPH Collaboration), CERN PPE/96-186 (1996).

[128] G. Ballocchi *et al.* (UA6 Collaboration), *Phys. Lett.* **B317** (1993) 250.

[129] S. Bethke, *Nucl. Phys.* **B39** (Proc. Suppl.) (1995) 198.

[130] S. Bethke, Proc. of QCD'96, Montpellier, France 1996.

[131] J. Shigemitsu, Talk given at Lattice 96; International Symposium on Lattice Field Theory, St. Louis, MO, 1996.

[132] D. Buskulic *et al.* (ALEPH Collaboration), 'ALEPH Handbook Vol. 1', ed. by C. Bowdery, 1995.

[133] D. Decamp *et al.* (ALEPH Collaboration), *Nucl. Inst. Meth.* **A294** (1990) 121.

[134] D. Buskulic *et al.* (ALEPH Collaboration), *Nucl. Inst. Meth.* **A360** (1995) 481.

[135] D. Buskulic *et al.* (ALEPH Collaboration), *Z. Phys.* **C62** (1994) 539.

[136] D. Buskulic *et al.* (ALEPH Collaboration), *Phys. Lett.* **B297** (1992) 459.

[137] R. Della Marina (ALEPH Collaboration), `ALEPH internal note 92-022 PHYSIC 92-019` (1992).

[138] J.C. Brient and H. Videau (ALEPH Collaboration), `ALEPH internal note 94-088 PHYSIC 94-076` (1994).

[139] R. Brun *et al.*, GEANT3.15, CERN DD/EE/84-1.

[140] S. Jadach, J.H. Kühn and Z. Wąs, *Comp. Phys. Comm.* **64** (1991) 275.

[141] S. Jadach, B.F.L. Ward and Z. Wąs, *Comp. Phys. Comm.* **79** (1994) 503.

[142] S. Jadach *et al.*, *Comp. Phys. Comm.* **76** (1993) 361.

[143] D. Buskulic *et al.* (ALEPH Collaboration), *Z. Phys.* **C62** (1994) 539.

[144] P. Abreu *et al.* (DELPHI Collaboration), *Phys. Lett.* **B372** (1996) 172.

[145] H.J. Park, Ph.D. Thesis, Université de Paris-Sud, Report LAL 95-08 (1995) 245.

[146] D. Decamp *et al.* (ALEPH Collaboration), *Z. Phys.* **C54** (1992) 211.

[147] J.C. Brient, S. Orteu, A. Rougé and M. Verderi (ALEPH Collaboration), `ALEPH internal note 93-107 PHYSIC 93-088` (1993);
A. Rougé (ALEPH Collaboration), `ALEPH internal note 94-051 PHYSIC 94-051` (1994).

[148] D. Buskulic *et al.* (ALEPH Collaboration), *Nucl. Inst. Meth.* **A360** (1995) 481.

[149] V. Blobel, 'Unfolding methods in high-energy physics experiments', DESY 84-118 (1984).

[150] A. Höcker and V. Kartvelishvili, *Nucl. Inst. Meth.* **A372** (1996) 469.

[151] G. D'Agostini, 'A multidimensional Unfolding Method Based on Bayes' Theorem', DESY 94-099 (1994).

[152] G.E.Forsythe, M.A.Malcolm and C.B.Moler, 'Computer Methods for Mathematical Computations', Prentice-Hall Inc., Englewood Cliffs, 1977.

[153] C.E.Lawson and R.J.Hanson, 'Solving Least Square Problems', Prentice-Hall Inc., Englewood Cliffs, 1974.

[154] M.Schmelling, *Nucl. Inst. Meth.* **A340** (1994) 400.

[155] D. Gibaut *et al.* (CLEO Collaboration), *Phys. Rev. Lett.* **73** (1994) 934.

[156] R. Balest *et al.* (CLEO Collaboration), *Phys. Rev. Lett.* **75** (1995) 3809.

[157] M. Artuso *et al.* (CLEO Collaboration), *Phys. Rev. Lett.* **69** (1992) 3278.

[158] T.E. Coan *et al.*(CLEO-Collaboration), *Phys. Rev.* **D53** (1996) 6037.

[159] S. Towers (for the OPAL Collaboration), 'Tau decays involving neutral kaons'; R. Kass (for the CLEO Collaboration), 'Three-prong tau decays with kaons', Talks given at the TAU96 Conference, Colorado, 1996.

[160] G. Mills *et al.*(DELCO Collaboration), *Phys. Rev. Lett.* **54** (1985) 624.

[161] D. Bauer *et al.* (TPC/2γ Collaboration), *Phys. Rev.* **D50** (1994) R13.

[162] D. Buskulic *et al.* (ALEPH Collaboration), *Phys. Lett.* **B332** (1994) 209.

[163] V. Shelkov (for the CLEO Collaboration), 'Tau decays involving η mesons and $\tau^- \to f_1 \pi^- \nu_\tau$ from CLEO', Talk given at the TAU96 Conference, Colorado, 1996.

[164] J.H. Kühn and A. Santamaria, *Z. Phys.* **C48** (1990) 445.

[165] H. Videau (ALEPH Collaboration) `ALEPH internal note 94-087, PHYSIC 94-075` (1994).

[166] R. Barate *et al.* (ALEPH Collaboration), CERN PPE/97-013 (1997).

[167] S. Eidelman and V.N. Ivanchenko, *Phys. Lett.* **B257** (1991) 437.

[168] S. Eidelman and V.N. Ivanchenko, *Nucl. Phys.* **B40** (Proc. Suppl.) (1995) 131.

[169] L.M. Barkov *et al.* (OLYA, CMD Collaboration), *Nucl. Phys.* **B256** (1985) 365.

[170] I.B. Vasserman *et al.* (OLYA Collaboration), *Sov. J. Nucl. Phys.* **30** (1979) 519.

[171] I.B. Vasserman *et al.* (TOF Collaboration), *Sov. J. Nucl. Phys.* **33** (1981) 709.

[172] S.R. Amendolia *et al.* (NA7 Collaboration), *Phys. Lett.* **B138** (1984) 454.

[173] A. Quenzer *et al.* (DM1 Collaboration), *Phys. Lett.* **B76** (1987) 512.

[174] D. Bisello *et al.* (DM2 Collaboration), *Phys. Lett.* **B220** (1989) 321.

[175] B. Esposito *et al.* (MEA Collaboration), *Phys. Lett.* **B67** (1977) 239; *Lett. Nuovo Cim.* **28** (1980) 337.

[176] D. Bollini *et al.* (BCF Collaboration), *Lett. Nuovo Cim.* **14** (1975) 418.

[177] M. Bernardini *et al.* (BCF Collaboration), *Phys. Lett.* **B46** (1973) 261.

[178] J. Gasser and U.G. Meissner, *Nucl. Phys.* **B357** (1991) 90.

[179] S. Eidelman and F. Jegerlehner, *Z. Phys.* **C67** (1995) 585.

[180] S.R. Amendolia *et al.* (NA7 Collaboration), *Nucl. Phys.* **B277** (1986) 168.

[181] L.M. Kurdadze *et al.* (OLYA Collaboration), *JETP Lett.* **43** (1986) 643.

[182] S.J. Dolinsky *et al.* (ND Collaboration), *Phys. Rep.* **C202** (1991) 99.

[183] B. Esposito *et al.* (MEA Collaboration), *Lett. Nuovo Cim.* **28** (1980) 195.

[184] L.M. Barkov *et al.* (CMD Collaboration), *Sov. J. Nucl. Phys.* **47** (1988) 248.

[185] A. Cordier *et al.* (DM1 Collaboration), *Phys. Lett.* **B109** (1981) 155.

[186] A. Cordier *et al.* (DM1 Collaboration), *Phys. Lett.* **B81** (1979) 389.

[187] D. Bisello (for the DM2 Collaboration), *Nucl. Phys.* **B21** (Proc. Suppl.) (1995) 111.

[188] D. Bisello *et al.* (DM2 Collaboration), Report LAL 90-35, Orsay (1990).

[189] L. Stanco (for the DM2 Collaboration), Proceedings of Hadron-91 (World Scientific ed. 1992) 84.

[190] G. Cosme *et al.* (M3N Collaboration), *Nucl. Phys.* **B152** (1979) 215; C. Paulot, Thesis, Report LAL 79-14, Orsay (1979).

[191] G. Cosme *et al.* (M2N Collaboration), *Phys. Lett.* **B63** (1976) 349; G. Parrour *et al.* (M2N Collaboration), *Phys. Lett.* **B63** (1976) 357.

[192] A. Antonelli *et al.* (DM2 Collaboration), *Phys. Lett.* **B212** (1988) 133.

[193] D. Bisello *et al.* (DM1 Collaboration), *Phys. Lett.* **B107** (1981) 145.

[194] M. Schioppa (DM2 Collaboration), Thesis, Universita di Roma “La Sapienza” (1986).

[195] A. Dobado, M.J. Herrero, T.N. Truong, *Phys. Lett.* **B235** (1990) 134.

[196] F. Mane *et al.* (DM1 Collaboration), *Phys. Lett.* **B112** (1982) 178.

[197] D. Bisello *et al.* (DM2 Collaboration), *Z. Phys.* **C52** (1991) 227.

[198] F. Mané (DM1 Collaboration), Thesis, Université de Paris-Sud, Report LAL 82/46 (1982).

[199] A. Cordier *et al.* (DM1 Collaboration), *Phys. Lett.* **B110** (1982) 335.

[200] G.J. Gounaris and J.J. Sakurai, *Phys. Rev. Lett.* **21** (1968) 244.

[201] M. Benayoun *et al.*, *Z. Phys.* **C58** (1993) 31.

[202] G. D'Agostini, *Nucl. Inst. Meth.* **A346** (1994) 306.

[203] B. Costa de Beauregard, T.N. Pham and T.N. Truong, *Phys. Lett.* **B67** (1977) 213.

[204] A.B. Clegg and A. Donnachie, *Z. Phys.* **C62** (1994) 455.

[205] K. Huber and H. Neufeld, *Phys. Lett.* **B357** (1995) 221.

[206] J. Bijnens and P. Gosdzinsky, **Phys. Lett. B388** (1996) 203.

[207] L.P. Chen and W. Dunwoodie (for the MARK III Collaboration), Proceedings of Hadron-91 (World Scientific ed. 1992) 100.

[208] R. Alemany, M. Davier and A. Höcker, Report LAL 97-02 (1997), submitted to *Z. Phys.*.

[209] J. Bailey *et al.*, *Phys. Lett.* **B68** (1977) 191.
F.J.M. Farley and E. Picasso, 'The muon $(g-2)$ Experiments', Advanced Series on Directions in High Energy Physics - Vol. 7 Quantum Electrodynamics, ed. T. Kinoshita, World Scientific 1990.

[210] B. Lee Roberts, *Z. Phys.* **C56** (Proc. Suppl.) (1992) 101.
See also http://www.phy.bnl.gov/g2muon/home.html.

[211] J. Bailey, *Nucl. Phys.* **B150** (1979) 1.

[212] A. Czarnecki, B. Krause and W.J. Marciano, *Phys. Rev. Lett.* **76** (1995) 3267; *Phys. Rev.* **D52** (1995) 2619;

[213] T.V. Kukhto, E.A. Kuraev, A. Schiller and Z.K. Silagadze, *Nucl. Phys.* **B371** (1992) 567.

[214] R. Jackiw and S. Weinberg, *Phys. Rev.* **D5** (1972) 2473.

[215] T. Kinoshita, B. Nižić and Y. Okamoto, *Phys. Rev.* **D31** (1985) 2108.

[216] S. Tisserant and T.N. Truong, *Phys. Lett.* **B115** (1982) 264;
A. Pich, *Phys. Lett.* **B196** (1987) 561;
H. Neufeld and H. Rupertsberger, *Z. Phys.* **C68** (1995) 91.

[217] A.W. Thomas, Talk given at the Int. Symposium on Non-Nucleonic Degrees of Freedom Detected in the Nucleus, Osaka, Japan 1996.

[218] W.K. McFarlane *et al.*, *Phys. Rev.* **D32** (1985) 547.

[219] P. Singer, *Phys. Rev.* **130** (1963) 2441; Erratum: **161** (1967) 1694.

[220] M. Gourdin and E. de Rafael, *Nucl. Phys.* **B10** (1969) 667.

[221] N. Cabbibo and R. Gatto, *Phys. Rev. Lett.* **4** (1960) 313; *Phys. Rev.* **124** (1961) 1577.

[222] A. Cordier *et al.* (DM1 Collaboration), *Nucl. Phys.* **B172** (1980) 13.

[223] A. Antonelli *et al.* (DM2 Collaboration), *Z. Phys.* **C56** (1992) 15.

[224] P.M. Ivanov *et al.* (OLYA Collaboration), *Phys. Lett.* **B107** (1981) 297;
P.M. Ivanov *et al.* (OLYA Collaboration), *JETP. Lett.* **36** (1982) 112.

[225] D. Bisello *et al.* (DM1 Collaboration),
Reports LAL 80-35, LAL 80-36, LAL 80-37, Orsay (1980).

[226] D. Bisello *et al.* (DM2 Collaboration), *Z. Phys.* **C39** (1988) 13.

[227] F. Mané *et al.* (DM1 Collaboration), *Phys. Lett.* **B112** (1982) 178.

[228] C. Bacci *et al.* ($\gamma\gamma2$ Collaboration), *Phys. Lett.* **B86** (1979) 234.

[229] J.L. Siegrist *et al.* (MARK I Collaboration), *Phys. Rev.* **D26** (1982) 969.

[230] W. Bacino *et al.* (DELCO Collaboration), *Phys. Rev. Lett.* **40** (1978) 671.

[231] R. Brandelik *et al.* (DASP Collaboration), *Phys. Lett.* **B76** (1978) 361;
H. Albrecht *et al.* (DASP Collaboration), *Phys. Lett.* **B116** (1982) 383.

[232] J. Burmester *et al.* (PLUTO Collaboration), *Phys. Lett.* **B66** (1977) 395;
C. Berger *et al.* (PLUTO Collaboration), *Phys. Lett.* **B81** (1979) 410;
L. Criegee and G. Knies (PLUTO Collaboration), *Phys. Rep.* **C83** (1982) 151.

[233] B. Niczyporuk *et al.* (LENA Collaboration), *Z. Phys.* **C15** (1982) 299.

[234] Z. Jakubowski *et al.* (Crystal Ball Collaboration), *Z. Phys.* **C40** (1988) 49;
C.Edwards *et al.* (Crystal Ball Collaboration), SLAC-PUB-5160 (1990).

[235] A.E. Blinov *et al.* (MD-1 Collaboration), *Z. Phys.* **C49** (1991) 239;
A.E. Blinov *et al.* (MD-1 Collaboration), *Z. Phys.* **C70** (1996) 31.

[236] H.J. Behrend *et al.* (CELLO Collaboration), *Phys. Lett.* **B183** (1987) 400.

[237] W. Bartel *et al.* (JADE Collaboration), *Phys. Lett.* **B129** (1983) 145;
W. Bartel *et al.* (JADE Collaboration), *Phys. Lett.* **B160** (1985) 337;
B. Naroska (JADE Collaboration), *Phys. Rep.* **C148** (1987) 67.

[238] B. Adeva *et al.* (MARK-J Collaboration), *Phys. Rev. Lett.* **50** (1983) 799;
B. Adeva *et al.* (MARK-J Collaboration), *Phys. Rev. Lett.* **50** (1983) 2051;
B. Adeva *et al.* (MARK-J Collaboration), *Phys. Rep.* **C109** (1984) 131;
B. Adeva *et al.* (MARK-J Collaboration), *Phys. Rev.* **D34** (1986) 681.

[239] R. Brandelik *et al.* (TASSO Collaboration), *Phys. Lett.* **B113** (1982) 499;
M. Althoff *et al.* (TASSO Collaboration), *Phys. Lett.* **B138** (1984) 441.

[240] R. Giles *et al.* (CLEO Collaboration), *Phys. Rev.* **D29** (1984) 1285;
D. Besson *et al.* (CLEO Collaboration), *Phys. Rev. Lett.* **54** (1985) 381.

[241] E. Rice *et al.* (CUSB Collaboration), *Phys. Rev. Lett.* **48** (1982) 906.

[242] E. Fernandez *et al.* (MAC Collaboration), *Phys. Rev.* **D31** (1985) 1537.

[243] H. Burkhardt, F. Jegerlehner, G. Penso and C. Verzegnassi, *Z. Phys.* **C42** (1989) 497.

[244] D.H. Brown and W.A. Worstell, *Phys. Rev.* **D54** (1996) 3237.

[245] A.D. Martin and D. Zeppenfeld, *Phys. Lett.* **B345** (1995) 558.

[246] K. Adel and F.Y. Ynduráin, FTUAM 95-32, hep-ph/9509378 (1995).

[247] B.W. Lynn, G. Penso and C. Verzegnassi, *Phys. Rev.* **D35** (1987) 42.

[248] H. Burkhardt and B. Pietrzyk, *Phys. Lett.* **B356** (1995) 398.

[249] M.L. Swartz, *Phys. Rev.* **D53** (1996) 5268.

[250] M. Hayakawa, T. Kinoshita and A.I. Sanda, *Phys. Rev.* **D54** (1996) 3137; M. Hayakawa, T. Kinoshita and A.I. Sanda, *Phys. Rev. Lett.* **75** (1995) 790.

[251] J. Bijnens, E. Pallante and J. Prades, *Nucl. Phys.* **B474** (1996) 379.

[252] B. Krause, 'Higher-Order Hadronic Contributions to the Anomalous Magnetic Moment of Leptons', (Karlsruhe Univ., ITTP), TTP96-26 (1996).

[253] 'Reports of the working group on precision calculations for the Z resonance', Ed. D. Bardin et al., CERN-PPE 95-03.

[254] S. Eidelman, 'CVC and Hadronic Decays of τ Lepton', Talk given at the TAU96 Conference, Colorado, 1996.

[255] J. Urheim (for the CLEO Collaboration), 'Spectral Functions of $\tau^- \to \pi^-\pi^0\nu_\tau$ and $\bar{K}^0\pi^-\nu_\tau$', Talk given at the TAU96 Conference, Colorado, 1996.

[256] M.V. Terent'ev, *Sov. J. Nucl. Phys.* **16** (1973) 87; B.R. Holstein, *Comm. Nucl. Part. Phys.* **19** (1990) 221.

[257] V. Kartvelishvili, M. Margvelashvili and G. Shaw, 'Pion Polarisability and Hadronic τ Decays', Talk given at the QCD96 Conference, Montpellier, 1996.

[258] L.E. Piilonen *et al.*, *Phys. Rev. Lett.* **57** 1402; A. Bay *et al.*, *Phys. Lett.* **B174** (1986) 445; V.N. Bolotov *et al.*, **B243** (1990) 308.

[259] D.A. Bryman *et al.*, *Phys. Rep.* **88** (1982) 151.

[260] V. Kartvelishvili, *Phys. Lett.* **B287** (1992) 159; V. Kartvelishvili and M. Margvelashvili, *Z. Phys.* **C55** (1992) 83.

[261] M.V. Margvelashvili, *Phys. Lett.* **B215** (1988) 763.

[262] A.L. Kataev, V.V. Starshenko, *Mod. Phys. Lett.* **A10** (1995) 235; *Nucl. Phys.* **B39** (Proc. Suppl.) (1995) 312.

[263] F. Le Diberder, *Nucl. Phys.* **B39** (Proc. Suppl.) (1995) 318; LAL 94-43 (1994).

[264] P.M. Stevenson, *Phys. Rev.* **D23** (1981) 2916.

[265] T. Kinoshita and W.B. Lindquist, *Phys. Rev.* **D42** (1990) 636;
J. Kubo and S. Sakakibara, *Z. Phys.* **C14** (1982) 345.

[266] M. Beneke, M. Neubert and A. Pich, *private communication*, Feb. 13th, 1997.

[267] S. Narison, *Phys. Lett.* **B361** (1995) 121.

[268] M. Girone and M. Neubert, *Phys. Rev. Lett.* **76** (1996) 3061.

Remerciements

Un chapitre sympathique, sachant que ceux qui seront les premiers à le lire considèrent qu'ils ont participé à cette œuvre – ceci est une observation qui me regarde également, bien entendu. Sachant que par conséquent ils commenceront tous leur lecture ici, on est logiquement tenté de les remercier tous. C'est clair et net. Surtout avec l'espoir de figurer un jour, inattendu, parmi les remerciements de l'un ou de l'autre... cela est comme le dîner dont on régale des gens afin de s'inviter soi-même ultérieurement chez eux, ce qui revient toujours à faire une bonne affaire. D'un autre côté, ces remerciements ont tout de même une prétention sérieuse, un désir: une thèse cela signifie une longue et intensive période dans un bureau, passée avec d'autres qui vivent également dans des bureaux, tout une foule de bureaucrates comme les primitifs dans leurs grottes. Dans une telle situation, le voisin du bureau, la dame qui loge proche de l'imprimante ou son propre patron, à l'improviste, deviennent *les* véritables compagnons avec qui, dans l'ambiance crépusculaire, on s'entretient des faux photons ou de la mutilation de certaines séries perturbatives – ce qui doit paraître un chuchotement intime aux profanes... Lorsque l'on s'éveille, on se posera peut-être des questions: peut-on entrer dans une relation intime avec un faux photon? Peut-on discuter ce genre de choses avec son amie? A-t-on, après tout, encore besoin d'une amie? Pourtant, je ne m'éveillerai qu'*après* la thèse et c'est pour cela que je ne connais pas encore les réponses. Ce qui est clair: pendant les deux années passées, par moments, la physique est devenue ma vie et grâce à mon chef, Michel Davier, ceci ne perdait jamais l'apparence d'une vraie vie. Mon expérience dans le monde de physique est beaucoup trop petite pour me permettre d'estimer toute l'importance de Michel pour l'avancée des particules mais, sans aucun doute, le progrès de nos recherches communes porte son écriture, sa stimulation et ses idées – partout.

Je remercie sincèrement et chaleureusement Michel Davier de m'avoir introduit au LAL et de m'avoir guidé dans ce travail de recherche, dont nous sommes – comme je l'espère – tous les deux un peu fiers. Je l'assure de toute ma gratitude.

Superbe, la coutume francaise de se tutoyer entre collègues! Depuis toujours, j'avais eu un rapport problématique avec la hiérarchie, que je tâchais d'ignorer – un comportement tout à fait transparent et logique lorsque l'on est étudiant. Les relations respectueuses et amicales entre les membres du groupe ALEPH-LAL ainsi que celles qui règnent dans tout le LAL et au CERN, certainement dûes pour une bonne part au cosmopolitisme, m'ont profondément aidé dans mes tentatives de m'intégrer à l'étranger – en France – et de l'aimer. Je remercie cordialement Philippe Heusse, sage dirigeant du groupe, toujours pleine de compréhension pour ses enfants qui, parfois, arrivent mal rasés et l'air renfrogné en retard à sa réunion du mardi architôt. Je remercie aussi les autres membres du groupe: J. Boucrot, O. Callot, S. Chen, L. Duflot, J.F. Grivaz, A. Jacholkowska, P. Janot, M. Kado, D.W. Kim, F. Le Diberder, J. Lefrançois, A.M. Lutz, I. Nikolic, M.H. Schune, L. Serin, I. Videau (je la remercie, même si elle n'arrêtait pas de m'énerver en me proposant de faire du body-building bien que j'étais persuadé d'avoir déjà vu des muscles attachés à ma stature svelte) et D. Zerwas. Je remercie en particulier Jean-Jacques Veillet pour les bonnes heures que l'on a passées ensemble, lui, moi et un de mes tas de ferrailles.

Appartiens-je encore aux jeunes? Afin de me faciliter le choix, j'ai rangé quelques demi-jeunes dans le groupe suivant ce qui personnellement me rend la vie plus gaie... Je tiens à remercier François Le Diberder pour de nombreuses discussions très importantes, pour son soutien et sa motivation et pour m'avoir introduit dans le fonctionnement miraculeux du "world of MINVAR". Je remercie bien sûr Laurent Duflot, qui connaît toujours la réponse et sait adroitement se guider dans l'univers piégé de la statistique. Je remercie Ricard Alemany et Irena Nikolic pour la bonne collaboration dans la maison τ et je remercie Edwige, Irena, Dirk, Laurent, Marumi et Ricard pour leur amitié.

Merci beaucoup à Anne-Marie Lutz et Sumit Sen de m'avoir facilité l'usage du francais et de l'anglais, qui malheureusement, avec tous leurs mystères, me sont restés des langues étrangères.

Je tiens à remercier Antonio Pich et Ryszard Stroynowski d'avoir pris le temps d'être les rapporteurs de cette thèse et de l'attention qu'ils m'ont donnés, de leurs conseils et leurs commentaires qui m'ont aidé à en améliorer la qualité. Je remercie également Luigi Rolandi et André Rougé de participer à mon jury. Je remercie Jacques Lefrançois de m'avoir accueilli dans son laboratoire et de présider cette thèse.